POLITECNICO DI TORINO

I Facoltà di Ingegneria

Thesis submitted in partial fulfillment of the requirements for the degree of

Doctor of Philosophy

In the Department of Mechanical and Aerospace Engineering

2D/3D Nonlinear and Non-Hertzian Tooth Deflection Analysis for Compliant Gear Dynamics

Fabio Bruzzone

Supervisor: Prof. Carlo Rosso

ScuDo
Scuola di Dottorato ~ Doctoral School
WHAT YOU ARE, TAKES YOU FAR

May 2020

DISCLAIMER:

This document is strictly private, confidential and personal to its recipients and should not be copied, distributed, reproduced in whole or in part, nor shared to any third party without the written express consent of Politecnico di Torino and GeDy TrAss s.r.l. under penalty of law.

AVVERTENZA:

Questo documento è strettamente privato, confidenziale e personale per i suoi destinatari e non deve essere copiato, distribuito, riprodotto nella sua interezza o in parte, e nemmeno condiviso con alcuna terza parte senza l'espresso consenso scritto del Politecnico di Torino e di GeDy TrAss s.r.l. sotto la pena prevista dalla legge.

Ringraziamenti

Abstract

One of the most reliable ways to transmit mechanical power is to use geared mechanisms and gears have indeed been used since ancient times in the most different fields. In recent years, and especially in the aeronautical and aerospace industry, an ever growing need to reduce the weight of the components and increase the transmitted power density trough the increase of the rotational velocity has become evident. This trend has led engineers to experience complex dynamic phenomena that could lead to failures if not properly accounted for in the design phase, which has become ever more complex in terms of the contradictory balance between robustness and low weight to be achieved for optimal results and a lot of research has been done to understand those phenomena.

Aim of this work is to develop a dynamic model able to integrate the instantaneous contact conditions between the flanks and the compliances of the gear webs and shafts in a numerically efficient way, so that this approach could be effectively used in the design or verification phase of the engineering process. During gear engagement the main source of dynamic excitation is the time-varying mesh stiffness and thus the first step of this work is the development of a method to determine it. This is done through an algorithm that takes into account the flexibilities of the different parts of the gears, such as the web, the rim, the fillet, and the involute profile. A nonlinear step is considered to find the actual contact point as it moves due to the deflection of the engaging profiles. To correctly estimate the mesh stiffness an accurate description of the contact is needed and therefore a 2D rough frictionless contact model is introduced and the effects of tip-corner contact and some profile modifications are highlighted. Most of the profile modifications applied to gears during manufacturing are also done along the facewidth and as such cannot be studied with a 2D

approach. For this reason, 3D rough frictionless contact is introduced coupled with a detailed description of the gear geometry through the use of 3D solid finite elements and the effects of profile modifications on the static transmission error and mesh contact stiffness are discussed.

In order to validate the results obtained from the presented approaches an experimental test bench to measure the quasi static transmission error is presented and the computational results are compared against the experimental ones. This test bench features an innovative design especially regarding the measurement, since the angular encoders reading the deformations are mounted so that the tangential displacements are uncoupled from the radial and axial ones, ensuring accurate readings.

Next, a time domain dynamic model is presented, which includes the results of the contact analyses and 3D finite element discretization to capture the flexible behavior of gears during engagement with fast computational times. This is achieved through the use of reduced order models, rotations of the results obtained at the previous time step and a series of expansions and reductions of the degrees of freedom to simulate the motion of the gears and the travelling load as the teeth enter and leave contact. The nonlinear mesh stiffness included is both time and load dependent. Models with different web designs are analyzed with this method and the results obtained are discussed for different conditions and also tooth profile modifications. Finally, the strengths and weaknesses of the proposed method are discussed, and the possibility of further improvement is commented upon.

Sommario

Uno dei modi più affidabili per trasmettere potenza nei sistemi meccanici è quello di usare trasmissioni con ruote dentate che infatti sono state usate fin dai tempi antichi nei più diversi ambiti di applicazione. Negli ultimi anni, specialmente nell'industria aeronautica ed aerospaziale, si è manifestato un sempre crescente bisogno di ridurre le masse in gioco e incrementare la densità di potenza trasmessa attraverso l'aumento della velocità di rotazione dei componenti. Questa tendenza ha portato gli ingegneri a scontrarsi con fenomeni dinamici complessi che potrebbero portare a cedimenti se non debitamente considerati in fase di progettazione, che è diventata anche più complessa in termini della ricerca del contradditorio equilibrio tra robustezza e leggerezza da ottenere per risultati ottimali e molta ricerca si è svolta per comprendere questi fenomeni.

Obbiettivo di questo lavoro è quello di sviluppare un modello capace di integrare le condizioni istantanee del contatto tra i fianchi delle ruote e le cedevolezze della cartella e dell'albero in una maniera numericamente efficiente, per fare in modo che questo approccio possa essere usato efficacemente nella fase di progettazione o verifica. Durante l'ingranamento la principale sorgente di eccitazione dinamica proviene dalla variazione nel tempo della rigidezza di ingranamento, perciò il primo passo di questo lavoro è lo sviluppo di un metodo per determinarla. Questo è ottenuto attraverso un algoritmo che tiene in considerazione le flessibilità delle diverse parti delle ruote dentate, quali la cartella, la corona, il raccordo e il profilo a involute. Un approccio nonlineare è incluso per ottenere il punto di contatto reale dato che questo si sposta a causa della deformazione dei profili a contatto. Per ottenere una rigidezza di ingranamento precisa è necessaria un'accurata descrizione del contatto e per fare questo un modello bidimensionale è introdotto e gli effetti del contatto tra gli spigoli delle

dentature sono analizzati insieme ad alcune modifiche di profilo. Tuttavia, la maggior parte delle modifiche di profilo effettuate sulle ruote durante la produzione sono create lungo la larghezza di fascia e quindi non posso essere studiate solamente con un approccio bidimensionale. Per questo motivo un modello di contatto tridimensionale è stato introdotto, accoppiato al calcolo delle cedevolezze coerente con questa modifica e gli effetti di questo tipo di modifiche di profilo sull'errore statico di trasmissione e di rigidezza di contatto sono discussi.

Per validare i risultati con gli approcci presentati un banco sperimentale per la misura dell'errore di trasmissione quasi statico è presentato e i risultati computazionali sono comparati con quelli sperimentali. Questo banco di prova introduce caratteristiche innovative specialmente per quanto riguarda il sistema di misura, dato che gli encoder angolari che leggono le deformazioni sono montati in modo che le deformazioni tangenziali siano disaccoppiate dalle deformazioni radiali e assiali, in modo da assicurare misure precise.

Successivamente, un modello dinamico nel dominio del tempo con tempi di calcolo molto rapidi è presentato, che incorpora i risultati delle analisi del contatto precedenti e una discretizzazione ad elementi finiti per catturare il comportamento flessibile della ruota durante l'ingranamento. La velocità del modello è ottenuta tramite l'uso di modelli di ordine ridotto, rotazione dei risultati ottenuti all'istante di tempo precedente e una serie di espansioni e riduzioni dei gradi di libertà per simulare il movimento delle ruote durante l'ingranamento e lo spostamento dei punti di applicazione del carico mentre i denti entrano e lasciano il contatto. La rigidezza di contatto inclusa nel modello è sia dipendente dal tempo che dal carico. Diversi modelli con diverse tipologie di cartella sono analizzati attraverso questo modello e i risultati ottenuti sono confrontati anche con diverse modifiche di profilo. Per concludere, i punti di forza e di debolezza di questo metodo sono discussi insieme alle possibilità di miglioramento dello stesso.

Table of Contents

List of figures

List of tables

I. Introduction

Gears are widely used mechanisms employed to transmit power and motion between different mechanical components. For their comprehensive study, several aspects need to be considered which considerably complicates the design process. During this delicate phase, the designer needs to assess the various layout possibilities and verify that each of them respects the design failure criteria. Furthermore, in order to develop a reliable and low noise product, several other analyses must be carried out with several different tools to ensure correct engaging conditions, and this can lead to sub-optimal results achieved by the end product since many mistakes can be made in-between the analyses or the different software used. Aim of this work is to develop a methodology to analyze gears in their entirety as accurately as possible, while keeping the computational times short to allow for design explorations by varying several parameters, all in one environment. Several tools are available for the quick and rough dimensioning of gears but those often neglect important aspects such as the compliance of the different part of the gears or the contact mechanics involved in their meshing. On the contrary, software based on Finite Elements are also popular and include those aspects at the price of slow and cumbersome model creations and computations. In this work approaches able to capture those aspects with fast setup and computational times, both in two and three dimensions, will be detailed, but its application to parametric studies and failure criteria will not be discussed. Even if the wanted results in terms of performance and weight are obtained under static conditions gears and transmissions are inherently dynamic systems due to their natural fluctuations in stiffness and other parameters during their rotation. Those dynamic aspects are often neglected up until the moment when the transmission is tested and either high cycle fatigue phenomena or disturbing noises present themselves. At the test stage the characteristics of the product are well defined and only minor changes can be made to suppress those unwanted byproducts. The dynamic interaction between gears is usually neglected in most industrial settings during the design process since the available methods and software are usually either very simplified or they require computational times that cannot coexist with the industry need to satisfy the customers as soon as possible. For this reason, a method to perform rather quickly and simply this kind of dynamic analyses using a scheme employing reduced order models of fully flexible and compliant gears will be detailed and applied. This method is still young but has a great overlook since it will allow the study of the dynamic characteristics of a transmission already in the design phase, providing key information to the designers before actual tests in an amount of time short enough to be actually applicable in an industrial scenario.

II. State of the Art

II.1 History of the field

Gears are one of the most widely used methods to transmit motion and power, and they have been so since ancient times. Probably the oldest evidence of their use is the Antikythera mechanism which dates back to the 3rd century BC and was used as an astronomical calendar. The Chinese during the 3rd century developed a chariot with a differential mechanism with gears to keep the statue of the emperor pointing south as it travelled through the country. From the ancient ages the uses of gears have multiplied exponentially and as of today their uses ranges from super-heavy machinery, down to miniaturized high-precision applications like clocks and watches. Recently [1] it has also been discovered that a small insect in its juvenile state uses a geared mechanism to synchronize the movement of its legs during jumps to maximize accuracy and distance covered. This is the first occurrence of a natural geared mechanism ever found. Ideally gears could be considered as rigid bodies and as such, due to their properties and geometry, they should be able to transmit motion at a constant rate without introducing in the system that they're a part of further sources of dynamic excitations. This would mean that gears wouldn't be sources or victims of mechanical failures since those are most commonly caused by dynamic problems. Indeed, most of the damage mechanisms, such as fatigue and wear, and all the noise and harshness

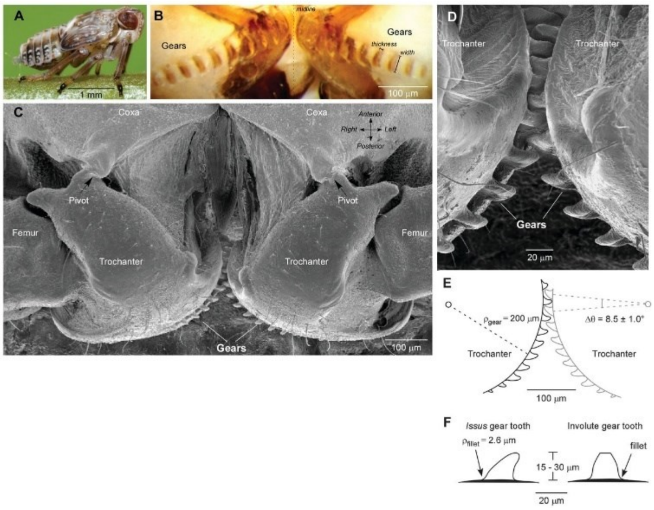

Figure 1: Naturally occurring geared mechanism from [1]

problems are due to the dynamic nature of the conditions in which the mechanical systems are operating. The large amount of literature related to engagement dynamics and gear dynamics in general ([2] [3] [4]) proves that this is not the case. This great amount of literature available is due to the various aspects and outputs the engineers are interested in, starting from the stresses in the gears, the cumulated damage, the efficiency of the power transmission, the noise and vibration emission and propagation, the loads on the supporting members such as the bearings and the gearbox casing, all the way to more complex problems like rotor dynamics and the final life assessment of the entire transmission. These dynamic effects are generated by the system kinematics, such as the cyclic variation of load due to gears rotation, and by the system flexibility. The first aspect could surely induce failure of the gears such as fatigue in the tooth root fillet or in the contact surface, but this is implicit in the nature of mating gears and unavoidable and therefore must be treated by a conventional fatigue approach as described in the consolidated standards like AGMA [5] or ISO [6]. Scientific analyses to reduce and mitigate problems related to the second aspect started in the Twenties and Thirties of the 20th century and they were related to the evaluation of the dynamic overloads due to teeth mating and studied which design changes could increase the lasting of the system by reducing noise and vibration. In the Fifties studies were conducted to understand the overload during engagement with the help of the first dynamic models. More complex models were then introduced in order to improve their accuracy and to take into account the effects of tooth tridimensionality and the nonlinearities of the main components and also due to the effects of friction and lubrication. The increase in computational power and availability the literature is enriched by complex Finite Element

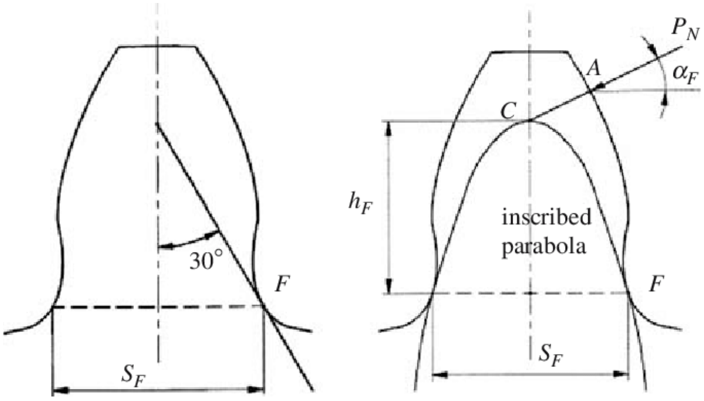

Figure 2: Tooth bending strength calculation according to AGMA [5] and ISO [6]

(FE) and Multibody models that also consider the micro and macro geometry of the gears, the overall deformations of the gearbox components and the evolution in time of the engagement. The goals of those studies also shifted with time. The earlier works are oriented towards the estimation of the Dynamic Factor which is the load increment due to the dynamics. Others are instead voted to engagement dynamics and they focus their attention on the compliance. Others are more system-oriented and they consider shaft and bearing clearances and flexibilities. With the rise of high spin speed system gyroscopic effects are also taken into account with complex rotor dynamics models of the geared system, while others are more focused on the noise and vibration aspects. This wide variety of goals and methods is justified by the objective complexity of those systems and reflects the difficulty of understanding and modeling the dynamic behavior of geared transmissions. In the early years the objective was to study and define a factor to scale the nominal forces to take into consideration the dynamics during the design of the gears, as is still done today according to [5] and [6]. The first works were mostly experimental and the first definition of the Dynamic Factor was obtained by comparing the nominal conditions to failure conditions by experimentally vary the spin speed and loads of a transmission and recording ruptures [2]. Failure conditions were then compared to nominal ones and the Dynamic Factor was computed. This clear dependency of the survival of the gears with spin speed and load conditions led Walker [7] to propose the first analytical expression. In that expression the Dynamic Factor was directly related to the tangential speed and the pitch diameter

$$DF = \frac{600 + v}{600} = \frac{dynamic\ load}{static\ load} \tag{2.1}$$

where v is the linear speed of the gear at the pitch diameter in feet per minute. This approach overestimated the dynamic contributions since it neglected a lot of parameters. A modification, which will become the starting point for the AGMA standard [5], was proposed in [8]:

$$DF = \frac{78 + \sqrt{v}}{78} = \frac{dynamic\ load}{static\ load} \tag{2.2}$$

The AGMA standard will later take into consideration the manufacturing quality in the expression of the Dynamic Factor K_v:

$$K_v = \left(\frac{C}{C + \sqrt{v}}\right)^{-B} = \frac{dynamic\ load}{static\ load} \tag{2.3}$$

where $C = 50 + 56(1 - B)$ and $B = 0.25(A_v - 5)^{2/3}$. Tuplin [9] is the first to also consider the errors due to gear manufacturing. He defines a natural frequency of the resonance phenomenon that could occur in a gear pair when a pitch error is present and the maximum load that the gear pair could experience. A sketch of this model is visible in Figure 4 and the accelerations $\ddot{x}_1$and $\ddot{x}_2$ can be computed solving the equations of motion where the external load is represented by the time variation of the distance between the gear m_2 and the stiffness k. Tuplin finds that the maximum load cannot exceed the value of the stiffness times the pitch error e. Harris [10] conducted a series of tests to understand the causes of gear vibration. Harris analyses the relative displacement as the variation in the velocity ratio at the pitch diameter for different gears and loads. He finds that the relative displacement at a

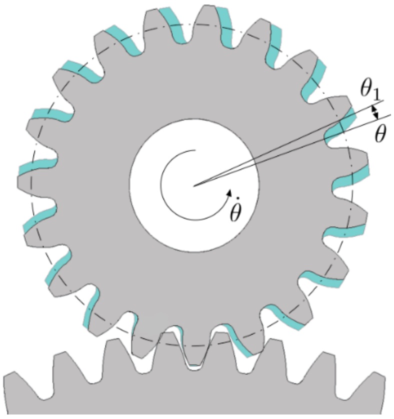

Figure 3: Visualization of the TE: In grey the ideal position, in cyan the actual one

precise load is strictly related to the static error at that loads and the curves he registers in the so called Harris map (Figure 5) are only related to the variation in stiffness. He therefore introduced the concept of the design load which corresponds to the particular torque for which the mesh excitations of a given gear are minimal. His findings were confirmed by numerous experiments and also proven theoretically for pinion-gear pairs [11] [12] and for multi-mesh systems [13], thus the importance of the Transmission Error (TE) was highlighted. If the gears are considered rigid, they form a perfect kinematic coupling and therefore the displacements along the line of action of the two mating gears are equal, so

$$\frac{d_{b,1}}{2}\theta_1 = \frac{d_{b,2}}{2}\theta_2 \tag{2.4}$$

where $d_{b,1}, d_{b,2}$ represent the base diameters of the two mating gears and θ_1, θ_2 their angular displacements. In actual conditions teeth are flexible, profiles are different from ideal and due to manufacturing and assembly errors the above relationship doesn't hold anymore. Therefore, the following general definition for the TE can be stated

$$TE = \frac{d_{b,1}}{2}\theta_1 - \frac{d_{b,2}}{2}\theta_2 \tag{2.5}$$

If conditions can be considered static or quasi-static this TE is often called Static Transmission error (STE) or Loaded Static Transmission Error (LSTE). When the TE is computed taking into considerations only the modifications from the ideal gears due to the manufacturing process then it's called Manufacturing Transmission Error (MTE). Those errors can be of shape, of pitch deviations or indexing and run-out. When the mounting deviations such as center distance variation, eccentricities, and misalignments but no loads are acting on the system then that is called the No Load Transmission Error (NLTE). Furthermore, due to dynamic effects, the instantaneous load changes and teeth could even lose contact and even have impacts on the coast side of the tooth profile and during rotation all of the above mentioned errors cumulate and the Dynamic Transmission Error (DTE) originates, which is hence a function of time, that can be expressed as

$$DTE = \frac{d_{b,1}}{2}\theta_1(t) - \frac{d_{b,2}}{2}\theta_2(t) \tag{2.6}$$

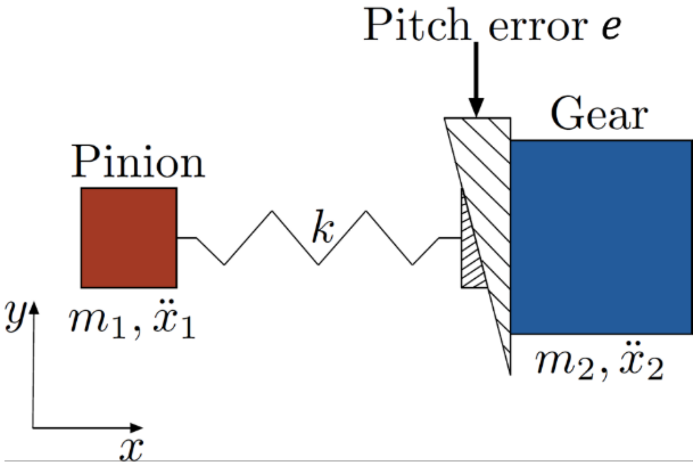

Figure 4: Tuplin dynamic model [9]

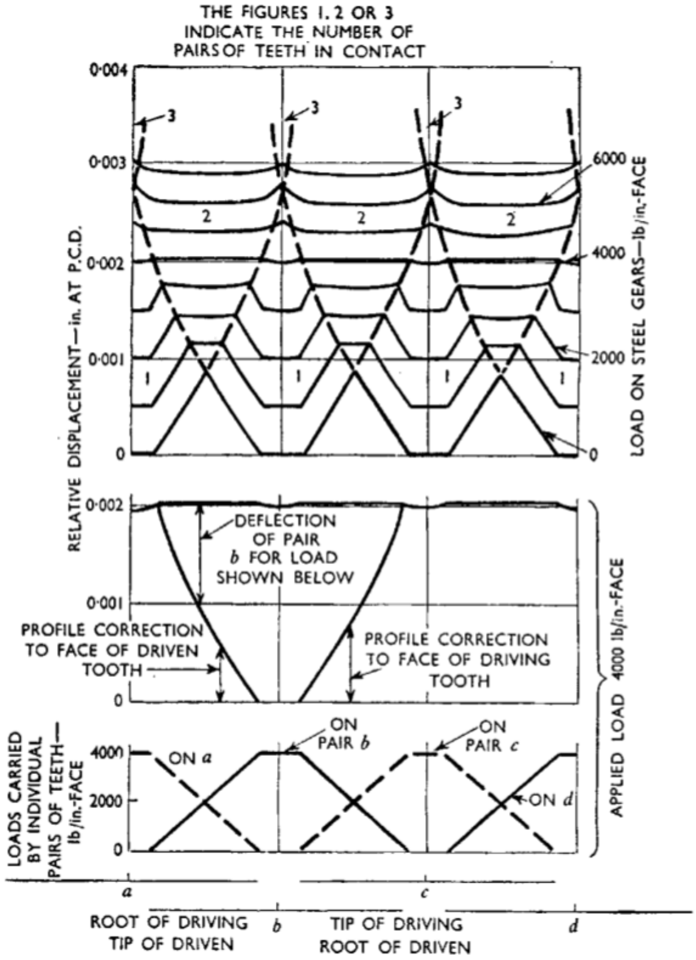

Figure 5: Harris map [10]

II.2 Sources of excitation

Evidently the calculation of those errors, especially the STE, is crucial in understanding the dynamic interaction in geared systems and obtaining the correct Dynamic Factor K_v and the DTE. The first works in this direction where based on analytical formulations and the first one is by Weber [14] and later by Weber and Banaschek [15]. These works are based on the superposition of the deformation due to the contact between teeth, the deflection of a clamped-free beam with the shape of the tooth and the ring compliance.

The compliance due to contact between teeth is analyzed using the bidimensional Hertz theory [16] for cylindrical contact, while Lundberg [17] proposed to consider a distribution of pressure at the surface of an elastic half plane. The clamped-free variable shape beam introduces the flexural, shear and normal compliances. The gear body is accounted for considering the tooth rigid and assuming the ring as an elastic semi-infinite plane where flexural, shear and normal effects are applied. Ishikawa [18], according to [19], improved the methodology by considering the tooth as a trapezoidal beam attached on top of a rectangular beam. Attia [20] introduced some modifications to Weber's model and a sketch for its application is visible in Figure 6 in which Y_A is the height from the root circle of the point of application of the load P, x_1 and x_2, are the distances between the beginning of the flank of tooth A and the centerlines of tooth B and C respectively, while x_3 and x_4 are the distances from those centerlines to the boundary of the considered gear portion of length

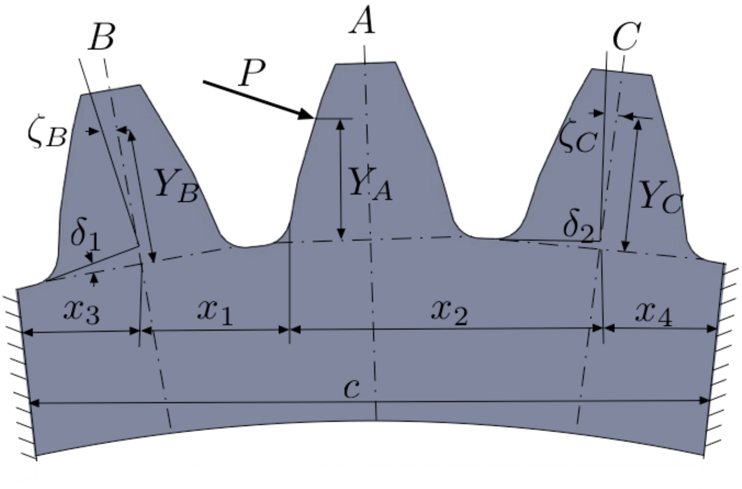

Figure 6: Sketch of Attia's model [20]

c.The angles δ_1 and δ_2 are the angular deflections of the unloaded teeth B and C while ζ_B and ζ_C are the corresponding angles computed at height Y_B and Y_C over the centerline of the respective tooth. due to the load applied on tooth A. Its main contribution is hence the inclusion of the deflection of the teeth close to the loaded one in the calculation of the static solution. Cornell [21] later used a discrete approach instead of Weber's integral approach to improve the feasibility of a computer implementation. O'Donnel [22] improved the model by implementing influence coefficients in the evaluation of tooth base stiffness. More recently Sainsot *et al.* [23] modified the approach to the compliance of the tooth base ζ''' from the semi-infinite plane of Weber to a semi-analytical formulation based on elastic rings which results in the following comprehensive formula:

$$y_A = \frac{F cos^2 \alpha}{bE} \cdot \left[L^*(h, \theta_f) \left(\frac{u}{s_f} \right)^2 + M^*(h, \theta_f) \frac{u}{s_f} + P^*(h, \theta_f) \cdot \left(1 + Q^*(h, \theta_f) tg^2 \alpha \right) \right] \tag{2.7}$$

where the coefficients L^*, M^*, P^* and Q^* are given as functions of the thickness of the tooth at the root and the ratio between the inner and outer radius of the gear rim and the other terms will be detailed in paragraph III.3.2. Other authors propose semi empirical models to describe the stiffness variation during the motion of the gear, such as the work of Cai and Hayashi [24]. In this paper the stiffness of the tooth is described as a function of time and contact ratio and the main parameters are the spin speed of the gear and the number of teeth that are contemporarily mating. For helical gears, Umezawa et al. ([25] , [26]) observed a logarithmic relationship between the stiffness and the position along the tooth face, and later Cai [27] proposed an improved function for the stiffness considering the contact ratio and addendum modifications. As the computational power increased many researchers started using the FE method, initially to compute the stress in the root fillet, but in [28] the FE was used instead to evaluate the dynamic behavior of the gear pair. An interesting validation of the FE approach is given in [29]. In that paper a comparison of 3D FE with experiments and other base theories is given. From that time many researchers started using FE analyses to calculate the stiffness of the teeth. Some of those consider only the effect of the tooth stiffness neglecting the contact, so the FE model is only related to the structural behavior of the tooth as in [30], [31] and [32]. Others consider separately the summation of Hertzian phenomena and the elastic behavior of the gear ([33], [34], [35], [36], [37], [38], [39]). An in-depth literature overview of the use of FE in the simulation of gear drives is given in [40]. Interestingly, Parker *et al.* [41] introduced a detailed semi-analytical contact mechanics model close to tooth surface, matched to a FE model of gear teeth and body that closely captures the non-linear dynamic response of spur gears, and another hybrid approach is presented in [42] . The effects of profile and lead modifications was investigated for helical gears in [43] and [44], where it was found that the meshing process can be modified by those since they affect the contact lines in the base plane and also the quality class of the gear was considered. Houser et al. [45] experimentally verified the strict correlation between the STE and the noise and vibration levels generated in operation. This relationship led researchers to minimize this source, first by investigating the corner contact [46], then suggesting algorithms to obtain the optimal microgeometries [47]. Other attempts at controlling the microgeometry can be found in [48], [49] for the improvement of the load distribution along the tooth flank, and in [50] to reduce the overloads. Recently [51] [52] [53] a set of analytical formulas was proposed which defines the optimal set of linear tip relief for spur and helical gears which minimizes the variance of the STE. The wide literature around these aspects highlights their importance and indeed Wang [54] [55] analyzes the effects of backlash and the STE in lightly loaded high speed gears. He concludes that *"the backlash alone is not a source of trouble, but backlash coupled with transmission errors can be"*. In [56] a study related to gear vibration is carried out using an analytical approach, considering the tooth stiffness variable along the tooth height and the position of the external force moves according to the engagement process.

II.3 Dynamic models

In the years between Tuplin [9] work and that of Bahgat *et al.* [56] a great number of studies were conducted and the extensive review by Ozguven and Houser [2] was surely the starting point for the model presented in [57], which is similar to the one in [26] but makes a distinction between STE and DTE and uses the former to compute the latter and was validated on the experimental results of dynamic root strains recorded in [58]. Figure 7 shows a representation of their proposed model in which two gears, characterized by equivalent inertias I_1, I_2 and base diameters $d_{b,1}$, $d_{b,2}$, are loaded by a driving T_1 and resisting torque T_2 and displace of quantities θ_1 and θ_2. The two are connected by a stiffness k_m and proportional damping c_m due to the meshing interaction, while the dynamic source of excitation is modeled by the time-varying quantity $e(t)$. Using a similar model, Kahraman and Singh in [59] study the dynamic behavior of a gear pair simplifying some aspects. For example, the STE is modeled as a sinusoidal quantity that varies with its own frequency and the fluctuation of the torque is characterized by a fundamental frequency different from the one of the STE, and those fluctuations make up the excitation sources. However, it introduces a non-linear trend of the elastic contribution to the force equilibrium, which is equal to zero when the displacement measured along the line of action is between the values of the backlash and is linear otherwise. This nonlinear trend is depicted in Figure 8 where q is the displacement along the line of action, b is half the backlash again measured on the line of action, k_m is the mesh stiffness and $F(q)$ is the resulting force contribution. The same authors later improved their model [60] by taking into account also the compliance of the shafts and the clearances in the bearings as well as the periodic variation of the mesh stiffness as a source term. Blankenship and Kahraman [61] later developed a test rig to verify the numerical results and they find that if a non-linear jump phenomenon occurs, its jump-up frequency is

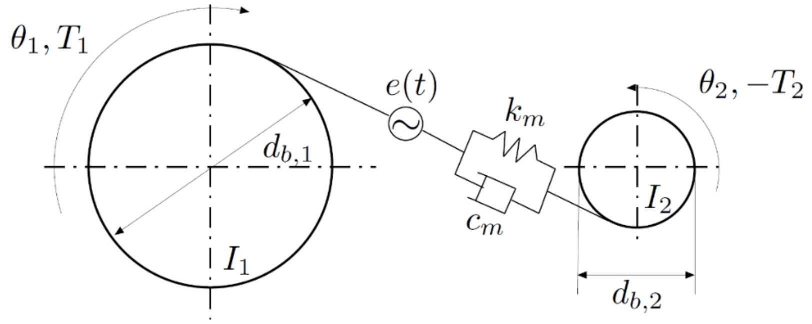

Figure 7: Ozguven and Houser model [57]

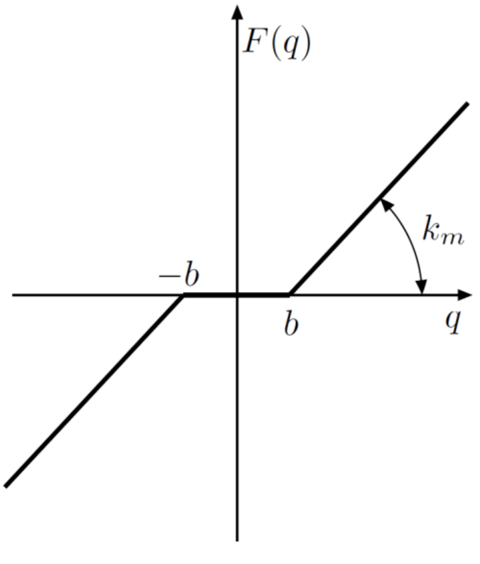

Figure 8: Nonlinear trend of the elastic contribution from [59]

independent of the load applied, while the jump-down frequency lowers as the load vanishes. A similar model can be found in [24], but they explicit the error contributions, and they are able to linearize the equations and express the error function in Fourier's series considering the effect of contact ratio and errors on the dynamic response of the gear pair. They then demonstrate that the presence of subharmonics in the response is mainly due to the error harmonics. In [62] the authors provide a detailed description of flank modifications, deviations from the theoretical one and mounting errors resulting in a general definition of the NLTE, which was first investigated in [63]. They apply this methodology on a system in which each gear is represented by 6 degrees of freedom, and it proves to represent well enough a unified approach. In [64] Theodossiades and Natsiavas consider the time-dependent mesh stiffness not as an external excitation, but as an intrinsic time-varying parameter of the system and they study the system's response with analytical and numerical methods analyzing the effects of backlash, damping and other parameters on the response and stability in several conditions highlighting the possibility of occurrence of crises and intermittent chaos for this kind of systems. The same researchers then improved their model [65] including also the non-linear characteristics of oil journal bearings and also proposing a reduced order model to take into account also the flexibilities of the shafts and their rotordynamic behavior showing that several possible branches of unstable periodic response are possible. Another approach detailed in [66] introduces nonlinearities also from bearings and by only specifying the external loads the existence of other chaotic phenomena is demonstrated. In [67] a modelling approach is developed to compute the kinematics and contact conditions for highly loaded gears in non-Newtonian mixed thermo-elastohydrodynamic conditions showing the influence of profile modifications on the contact and lubrication pattern and on the related power loss. Amabili and Rivola [68] proposed a modified non-linear model that takes into account also the non-linearity in damping and for its description they use the same approach as for the stiffness. NASA [69] published a report implementing the state of the art and focus on a parametric evaluation of the dynamic overload with respect to the contact ratio highlighting its importance in ruling gear dynamics. Kahraman and Blankenship [70] [71] experimentally investigated the relationship between the contact ratio and the magnitude of the dynamic overload and also the one between mesh stiffness variation and contact ratio. One of the first works that employs FE to evaluate gear dynamics is [72] in which different models of increasing complexity are studied and the influence of the engaging shifting due to teeth compliance on the dynamic overload is underlined. An interesting work focused on damping and friction was published by Vaishya and Sing in [73] and later in [74]. They consider the friction coefficient as an explicit function of time by taking into account the instantaneous sliding velocities between the surfaces due to the kinematics and the vibration. They highlight that friction damping is present also at pitch point where theoretically no sliding effects are present and that the absence of instabilities in most practical applications is due to this effect, but that this friction effect is a source of excitation for out of line actions. A further model improvement was published in [75] where the effects of profile modifications, backlash, tooth separation, mesh and bearing damping were included.

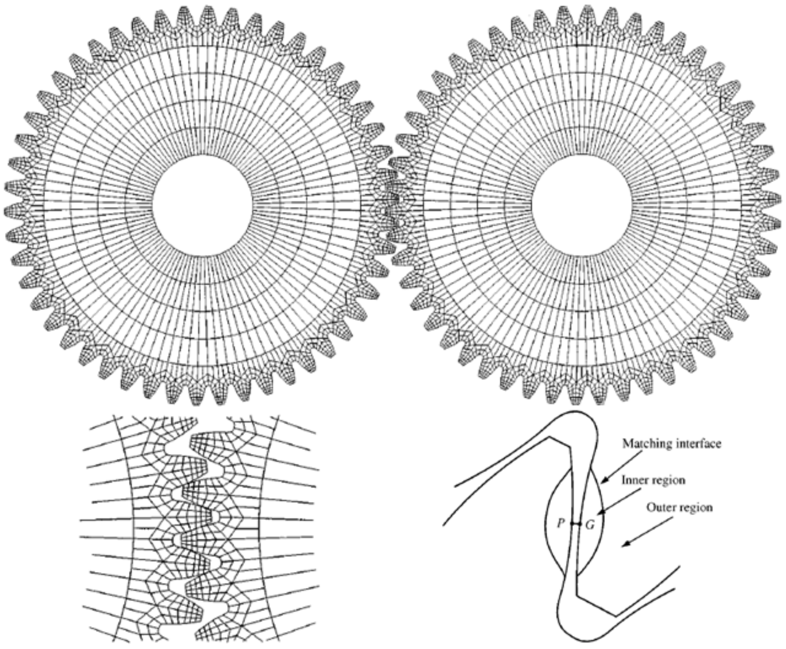

Figure 9: Coupled FE/Contact mechanics model from [41]

Parker and Vijayakar [41] removed the need to provide the mesh stiffness as in input by coupling a FE model with a detailed analytical contact model a got close agreement with experimental data on the dynamic response of spur gears and also compared to experimental tooth root strains in [76]. The same method was later extended to the frequency domain in [77]. This approach was even employed to applications in planetary gears [78] and experimental comparisons can be found in [79] also against simpler lumped parameters models. Further improvements to the method were introduced in [80] [81] [82] where the effects of compliant ring and sun gear was studied and it was shown that a higher flexibility of those components can improve the load sharing on the planets and the overall dynamic response. The effects of the presence of rolling elements was investigated in [83] using the same approach and comparing the results to those from a perturbation analysis. Improvements to reduce the computational effort were introduced in [84] [85] still considering several sources of non-linearities and the influence of flexibilities and also the effects of tooth profile modifications [86]. This model was the base upon which the Hybrid Analytical-Computational model was developed in [87]. The authors precompute a Force Deflection Function for various loads and apply that to a lumped parameters model obtaining extremely accurate results at a fraction of the computational time required by more complex analyses. Cooley and Parker also introduced an approach to the simulation of flexible gears by modeling a rotating elastic ring coupled to constant space-fixed foundations [88] [89] and a study on the parametric instabilities was later conducted introducing fluctuating values of the mesh stiffness [90]. The analytical nature of their model allows them to derive closed-form solutions for the eigenvalues including rotor dynamics effects and study in detail veering and instability phenomena. An interesting paper from Cooley *et al.* [91] analyzes two different methodologies to compute the mesh stiffness during the engagement and they

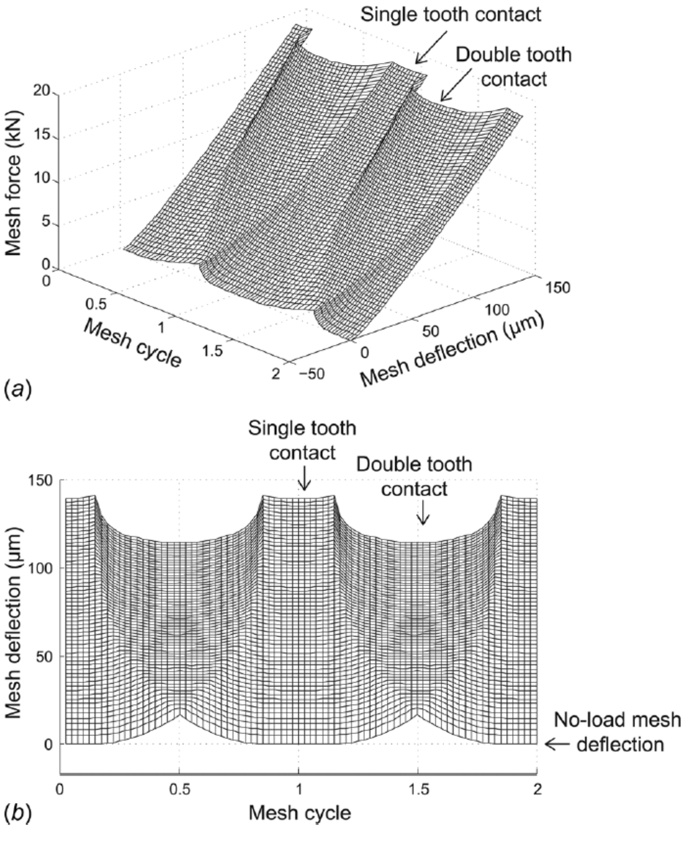

Figure 10: Force Deflection Function from [87]

show how to appropriately use it as input in lumped parameters or FE dynamic models. The first one is the *average slope approach* and it implies the calculation of the mesh stiffness simply dividing the load by the deflection during engagement:

$$k_a = \frac{F_m}{q_m} \tag{2.8}$$

where $q_m = \frac{d_{b,1}}{2}\theta_1 - \frac{d_{b,2}}{2}\theta_2 - \epsilon$ and F_m is the tooth mesh load. In this expression the loaded TE from (2.5) can be recognized and ϵ is the NLTE. The *local slope approach* contemplates the following instead:

$$k_l = \frac{F_m(q_m + \Delta q_m) - F_m(q_m - \Delta q_m)}{2\Delta q_m} \tag{2.9}$$

where Δq_m is a small variation in the mesh deflection. The authors find that using the *average slope approach* is correct for static analyses, but is incorrect for dynamic studies, where the *local slope approach* should be used instead, thus formulating the equations of motion as

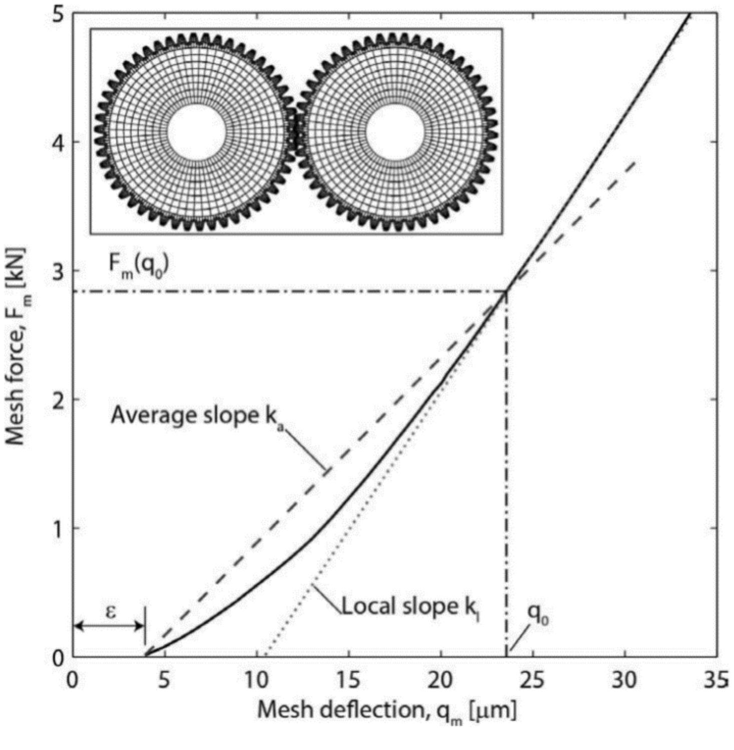

Figure 11: Average and Local slopes for the estimation of the mesh stiffness from [91]

$$m_e \ddot{q}_m + k_l(t) q_m = k_l(t) q_0(t) \tag{2.10}$$

where m_e is the equivalent mass of the system and therefore the excitation depends on the STE $q_0(t)$ which takes into account both the mean and the fluctuating components of the mesh stiffness. Hotait and Kahraman [92] went back and tried to experimentally deepen the understanding of the relationship between the DTE and the DF. They recorded for different torques and speeds the DF as the ratio between the tooth root strain under dynamic conditions and quasi-static ones (Figure 12):

$$DF = \frac{\left[\varepsilon_{dyn}(t)\right]_{max}}{\left[\varepsilon_{stat}(t)\right]_{max}} \tag{2.11}$$

At the same time, they recorded the DTE and found a strong relationship between the two factors finally formulating a linear relationship between them, allowing the estimation of one by knowing the other. Palermo et al. [93], starting from [41], proposed a scalable multibody model for spur and helical gears based on an instantaneous contact solution and considering also the effects of misalignments. Particularly interesting is the description of the shuttling, that is axial fluctuations due to mounting deviations, and its effects on the bearings loads and the dynamic moments along the plane of action. Lim and Singh [94] [95] [96] analyzed in detail the literature regarding the inclusion of the housing in the global

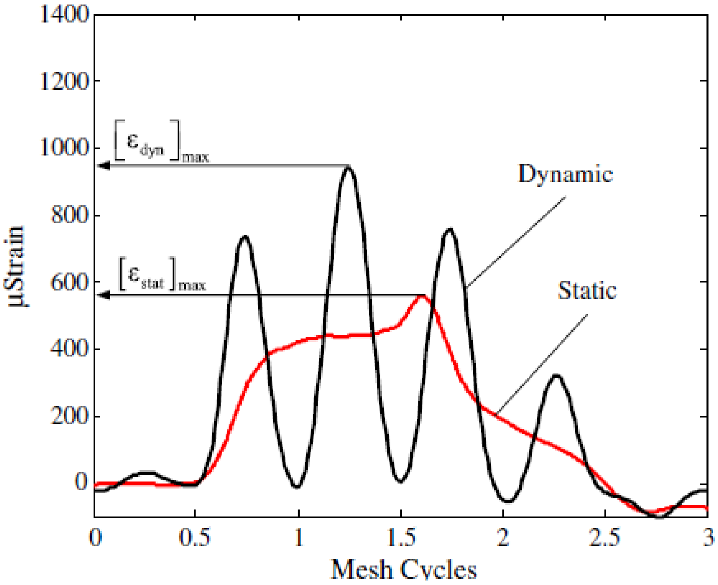

Figure 12: Static and dynamic tooth root strains during engagement from [92]

dynamic response and coupled the gearbox assembly with its gears and rolling elements to study the overall response. Rigaud and Sabot used a FE model of the gearbox [97] and showed the effects of the inclusion of all components of a gearbox, such as shafts, bearings, couplings and external inertias, on the overall dynamic response. In [98] a detailed FE model of the gearbox was used to compute its vibroacoustic response, but the dynamics of the gears was decoupled from the FE and only later the excitation through the bearings was applied to the casing. Instead in [99] the dynamics of the gears and the housing was coupled directly by a FE/contact mechanics model. In statics the rolling elements of the bearings were described in detail, while in dynamics they were included as an equivalent lumped-parameter model to reduce their otherwise enormous computational cost.

III. 2D teeth contact analysis

III.1 Introduction

In this chapter an algorithm for 2D teeth contact analysis and the calculation of STE of spur gears will be developed. First, the needed parameters relating to the geometry of the teeth defined to be used for the calculation of the deflections during engagement are defined. Next, the procedure to obtain the deflections under operation of the different contributions of the teeth and the gear body is shown and introduced in an nonlinear iterative algorithm which seeks equilibrium between the actual contact point considering the deformations and the actual load sharing factor between the engaged teeth pairs. Then a non-Hertzian contact model will be shown and the iterative contact detection taking into account tooth deformations under load will be introduced. The proposed model, as well as the 3D counterpart shown afterwards, will couple this precise non-Hertzian contact model in a nonlinear procedure in which both the actual contact point considering profile deformation and the load sharing coefficients will be iteratively sought. This is done without using finite elements or schemes such as the Lagrange multipliers method, but will use only semi-analytical formulations, resulting in a fast, detailed, and precise tool. The proposed model will be compared to a 2D FE model and against literature results. Finally, the notion of the tip relief tooth surface modification will be introduced, and its effects analyzed.

III.2 Parameters definition

The first step for an analysis is to determine the geometry and any spur gear can be defined by knowing the following parameters:

- number of teeth z
- modulus m
- face width b
- pressure angle α_P
- root fillet radius r
- addendum h_a (usually $h_a = m$)
- dedendum h_f (usually $h_f = 1.25m$)

The definition of the profiles of the teeth, namely the involute flank profile, the root fillets and the addendum and dedendum circles follows the well-established machine design criteria that can be found for example in [100]. Cornell [21] further specifies between two types of teeth profiles:

- Low Contact Ratio Gears (LCRG)
- High Contact Ratio Gears (HCRG)

The discriminant between the two types of gears lies in the position of the beginning of the tooth root fillet with respect to the base radius. Gears whose fillet radius begins above the base radius are called *"Standard gears"* and their profile is called *"form S"* and therefore they verify the following inequality:

$$(R_r^2 + 2r\, R_r) \geq\ R_B^2 \tag{3.1}$$

Where R_r is the radius of the root circle and $R_B$is the radius of the base circle defined as $R_B = R_P cos\alpha$ and R_P is the pitch radius defined as $R_P = z \cdot m$. If instead the tangent point of the fillet radius to the involute portion of the flank lies below the base circle, the gears are called *"Undercut tooth gears"* and their profile is called *"form A"* and verifies the following inequality:

$$(R_r^2 + 2r\, R_r) < R_B^2 \tag{3.2}$$

In Figure 13 are visualized the meanings of the terms mentioned above and others, while in Figure 14 the differences between *"form S"* and *"form A"* profiles can be appreciated. This distinction had to be specified since some of the parameters that will be detailed in the following will change depending on the tooth form. In Figure 14 it is also possible to observe the radius R_f which defines the beginning of the active portion of the involute profile. In the next paragraph the procedure to compute the deflections under load of a teeth will be carried out mostly according to the work of Cornell [21] and therefore it is better to define all the relevant parameters that will be used. Some of those are valid for the entire tooth and don't change depending on the point of the flank considered, while others do and will vary along the profile. Indeed, during the generation of the geometry of the teeth and the entire gears, which was omitted because trivial and extremely well established in literature, the profiles are discretized in a number of points N_i. The calculation procedure that will follow is

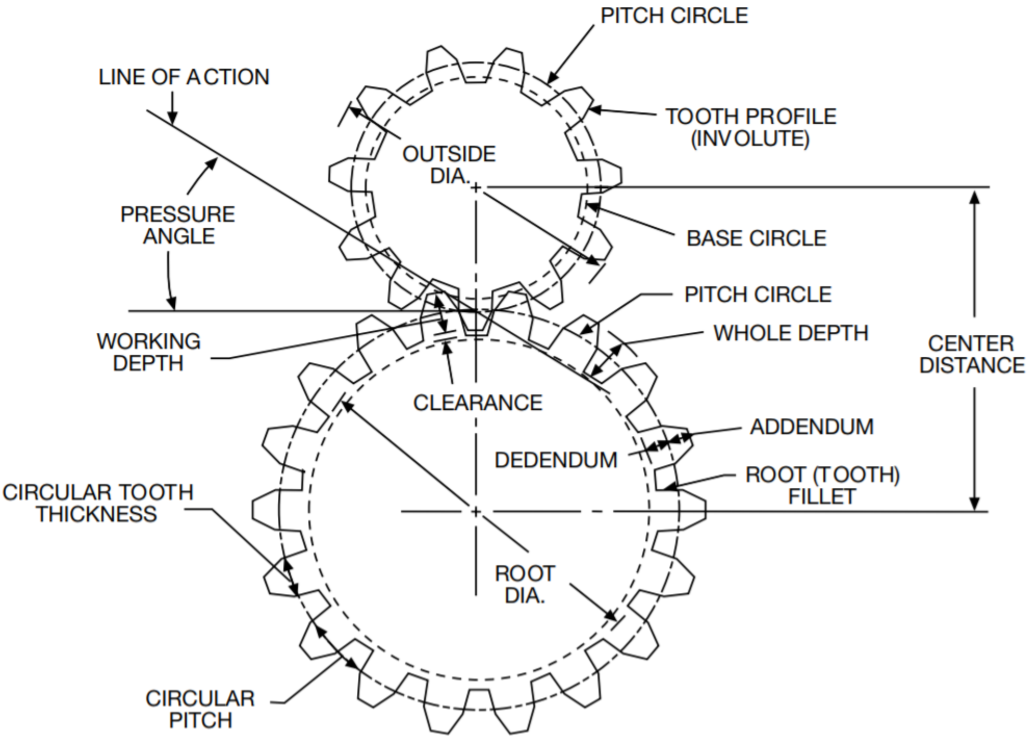

Figure 13: Main gear nomenclature

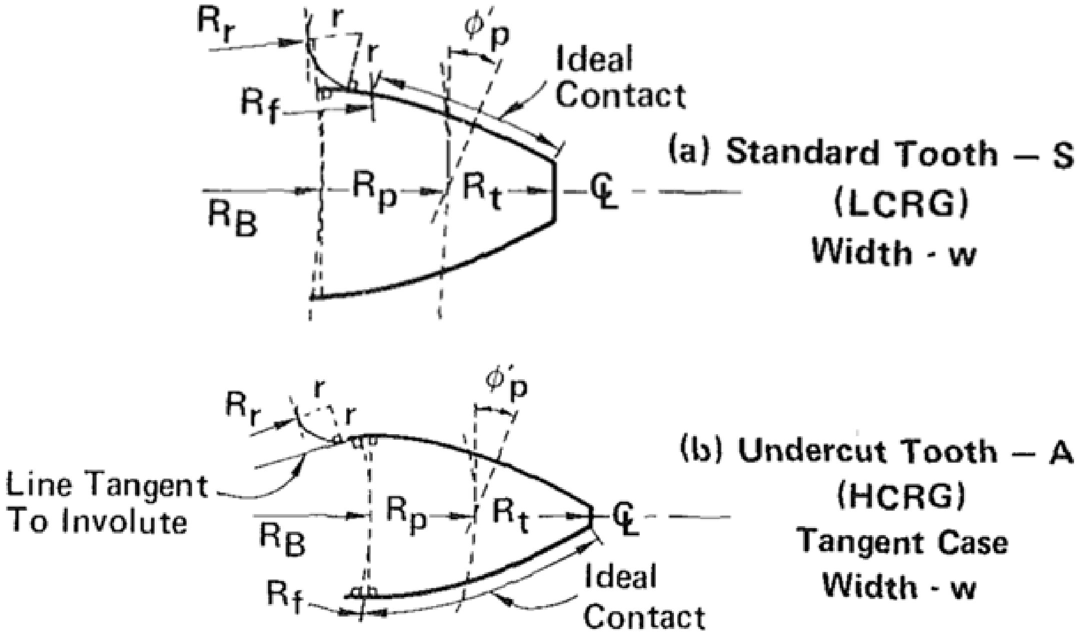

Figure 14: Form S and Form A differences from [21]

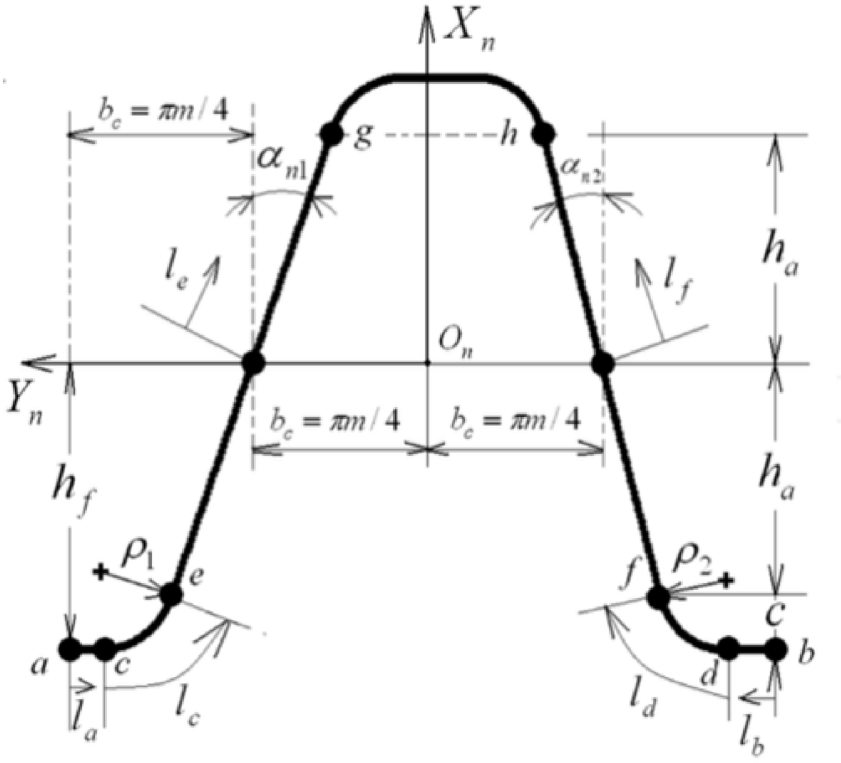

Figure 15: Parameters for the definition of the tooth fillet radius from [101]

computationally inexpensive and therefore N_i can as well be in the range of thousands, thus increasing the resulting accuracy since the non-Hertzian contact model that will be presented in III.4 and the iterative contact detection strongly rely on this discretization. The definition of the fillet radius and its geometry have been implemented by simulating the meshing action between a rack cutter and the generated gear according to [101] [102] and in Figure 15 are visible the main parameters needed, which are mainly the radii of curvatures ρ_1, ρ_2 for the drive and coast sides which define the beginning and end points (c, e and d, f respectively) and their arc length l_c and l_b if an asymmetric profile of the generating rack cutter is considered, while obviously $\rho_1 = \rho_2$ and $l_c = l_b$ for a symmetric one. For further details on the process of generating a profile from the simulation of the meshing action between a rack cutter and a workpiece the reader can refer to [101] and [102] or for a more comprehensive treaty to [103].In the following it is implied that the different parameters will depend upon the gear in consideration and therefore the suffix $j = 1{,}2$, where 1 indicates the pinion gear and 2 the driven gear (Figure 17), will be dropped where not explicitly needed. The parameters that do not change depending on the coordinates of the point considered are:

- t_p tooth thickness at pitch circle
- $\alpha_B = \frac{t_p}{2\,R_P} + \tan\alpha_P - \alpha_P$ (3.3) the angle between the midline of the tooth and the intersection point between the base circle and the flank, measured at the center of rotation of the gear
- $\bar{R} = \sqrt{(R_r + r)^2 - 2r\,\sqrt{(R_r + r)^2 - R_B^2} + r^2}$ (3.4) radius of the circle passing through the tangency point between the tooth flank and the fillet
- $\cos\bar{\phi} = {}^{R_B}/_{\bar{R}}$ (3.5)
- $\bar{\alpha} = \alpha_B - \tan\bar{\phi} + \bar{\phi}$ (3.6)
- $\bar{h} = 2\bar{R}\ \sin\bar{\alpha}$ (3.7) thickness of the tooth at radius $\bar{R}$
- $\bar{\gamma}$ angular extension of the tooth root fillet radius, defined as
- $\bar{\gamma} = \bar{\phi} - \bar{\alpha}$ (3.8) for "*form S*"teeth
- $\bar{\gamma} = \alpha_B$ (3.9) for "*form A*"teeth
- $\alpha_r = \sin^{-1}\left(\frac{r}{r+R_R}\right)$ (3.10) angle between the midline of the tooth and the center point of the root fillet, measured at the center of the gear and defined only for gears with "*form A*"teeth.

A visualization of those parameters is available in Figure 16. The parameters that instead change depending on which i^{th} node of the N_i discretizing the profile of the tooth are:

- R_{L_i}, *contact radius* defined as the radial position of the i^{th} point form the center of rotation of the gear
- $\phi_{L_i} = cos^{-1}\left(\frac{R_B}{R_{L_i}}\right)$ (3.11) *contact pressure angle*
- $\alpha_{L_i} = \alpha_B - \tan\phi_{L_i} + \phi_{L_i}$(3.12) *contact included tooth angle*
- $\phi'_{L_i} = \phi_{L_i} - \alpha_{L_i}$ (3.13) *contact load angularity with L*
- $R_{osc_i} = R_{L_i}\sin\phi_{L_i}$(3.14) curvature at the i^{th} point of the flank (radius of the osculating circle)

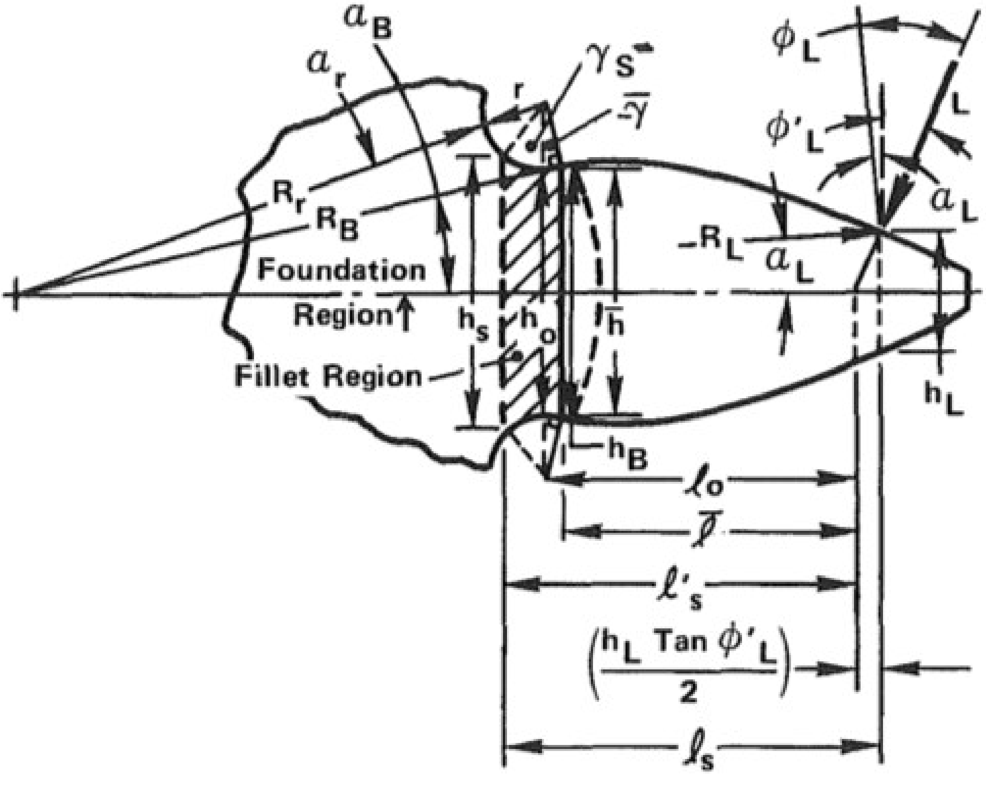

Figure 16: Tooth form depending parameters [21]

- $h_{L_i} = 2R_{L_i}\sin\alpha_{L_i}$(3.15) thickness of the tooth at the contact point
- $\bar{l}_i$ distance between the intersection of the line of action on the midline of the tooth and $\bar{R}$ projected on the midline:

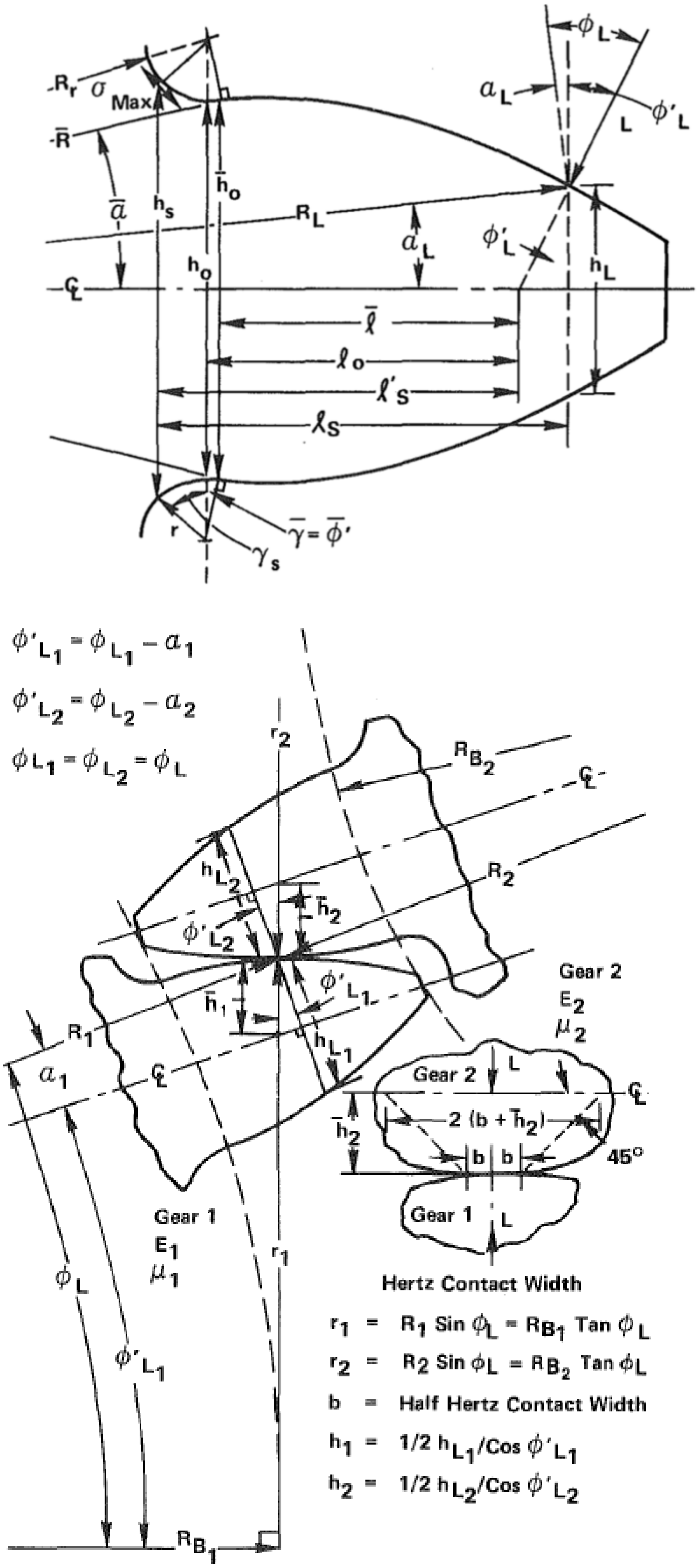

Figure 17: Definitions of the parameters changing for each i^{th} point on the flank of gear $j = 1{,}2$ from [21]

- $\bar{l}_i = R_{L_i} \cos \alpha_{L_i} - \frac{\left(h_{L_i} \tan \phi'_{L_i}\right)}{2} - \bar{R} \cos \bar{\alpha}$ (3.16) "*form S*"teeth
- $\bar{l}_i = R_{L_i} \cos \alpha_{L_i} - \frac{\left(h_{L_i} \tan \phi'_{L_i}\right)}{2} - (R_r + r) \cos(\alpha_B + \alpha_r) - r \sin \alpha_B \cos \alpha_B$ (3.17) "*form A*"teeth
- $\bar{h}_{Hertz,j} = \frac{{}^{1}/_{2} h_{L_{i,j}}}{\cos \phi'_{L_{i,j}}}$ (3.18)

The above-mentioned parameters are visible in Figure 17. The parameters of the material of the gears also needs to be specified, name the Young modulus E_j and the Poisson coefficient ν_j.

III.3 Operative deflections

Now that the constant and point-dependent parameters have been defined it is possible to proceed to the calculation of the deflections that the gear experiences under load. Those deformations can be distinguished between the one due to teeth flexibility and the ones of the gear body as will be detailed in the following.

III.3.1 Tooth deflections

The compliance of the tooth is due to three main contributions:

- The bending and shear deformation of the tooth y_B
- The deformation of the fillet region y_F
- The local deformation due to contact between teeth y_L

Using the superposition principle, the compliance of the tooth is given by

$$C = \frac{\left(y_{B,1} + y_{B,2}\right) + \left(y_{F,1} + y_{F,2}\right) + y_L}{L} \tag{3.19}$$

where L is the applied load. The bending and shear deformation of the tooth is computed assuming the tooth as a clamped-free beam using the analytical formula from Cornell [21] instead of the integral approach of Weber [14]. The expression is

$$y_B = \frac{L\ \cos^2 \phi_L'}{E} \cdot \sum_{i=1}^{n} \delta_i \cdot \left\{ \frac{l_i^2 - l_i \delta_i + \frac{1}{3} {\delta_i}^2}{\bar{I}_i} + \frac{2.4(1+\nu) + \tan^2 \phi_L'}{\bar{A}_i} \right\} \tag{3.20}$$

where δ_i is the thickness of the i^{th} slice of the tooth cross-section defined by the two consecutive points i and $i+1$ $(i = 1,2,\dots,N_i)$ of the discretization of the profile (Figure 18). Given that the coordinates X_{S_i} and Y_{S_i} of each of the profile nodes are known, the average area $\bar{A}_i$, the average moment of inertia $\bar{I}_i$, the thickness of the slice δ_i and its distance from the point of application of the load l_i are defined as:

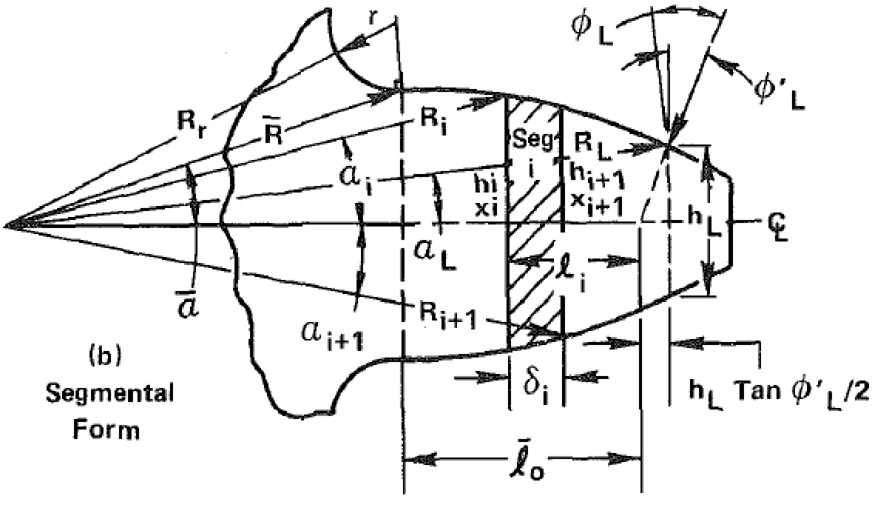

Figure 18: Clamped-free beam representation of the tooth cross-section from [21]

$$\bar{A}_i = \frac{4b \cdot 2Y_{S_{i+1}} \cdot 2Y_{S_i}}{Y_{S_{i+1}} + Y_{S_i}} \tag{3.21}$$

$$\bar{I}_i = \frac{b \cdot \left(2Y_{S_{i+1}}\right)^3 \cdot \left(2Y_{S_i}\right)^3}{6\left[\left(2Y_{S_{i+1}}\right)^3 + \left(2Y_{S_i}\right)^3\right]} \tag{3.22}$$

$$\delta_i = X_{s_{i+1}} - X_{s_i} \tag{3.23}$$

$$l_i = R_L \cdot \cos \alpha_L - \frac{1}{2} h_L \cdot \tan \phi'_L - X_{s_i} \tag{3.24}$$

The nodes above the point of application of the load L do not experience elastic deflections, just a rigid rotation of an angle α_{rg} whose expression is:

$$\alpha_{rg} = \tan^{-1}\left(\frac{y_{B,L} \cdot \cos \phi'_L}{\bar{l}}\right) \tag{3.25}$$

where $y_{B,L}$ is the deflection of the point where the load is applied. The contribution to the tooth deflection due to the presence of the fillet and the foundation takes into account the bending, shear and compression due to the applied load and is expressed as

$$\begin{aligned} y_F = & \frac{L \ \cos^2 \phi'_L}{bE} \cdot (1 - \nu^2) \\ & \cdot \left\{ \frac{16.67}{\pi} \left(\frac{l_F}{h_F}\right)^2 + 2\left(\frac{1 - \nu - 2\nu^2}{1 - \nu^2}\right)\left(\frac{l_F}{h_F}\right) \right. \\ & \left. + 1.534 \left(1 + \frac{\tan^2 \phi'_L}{2.4(1 + \nu)}\right) \right\} \end{aligned} \tag{3.26}$$

where:

$$l_F = \bar{l} + r \cdot (\sin \gamma_F - \sin \bar{\gamma}) \tag{3.27}$$

$$h_F = \bar{h} + 2r \cdot (\cos \bar{\gamma} - \cos \gamma_F) \tag{3.28}$$

The value of γ_F depends upon $\bar{l}/\bar{h}$, $\bar{r}/\bar{h}$, $\bar{\gamma}$ and ϕ'_L and is the one which maximizes the value of the deflection y_F and its value is interpolated based on the curves visible in Figure 19. This is one of the improvements in Cornell's model with respect to the one from O' Donnel [22]. Indeed, in his work O' Donnel fixed this angle to be $y_F = 75.5°$ but this underestimates the

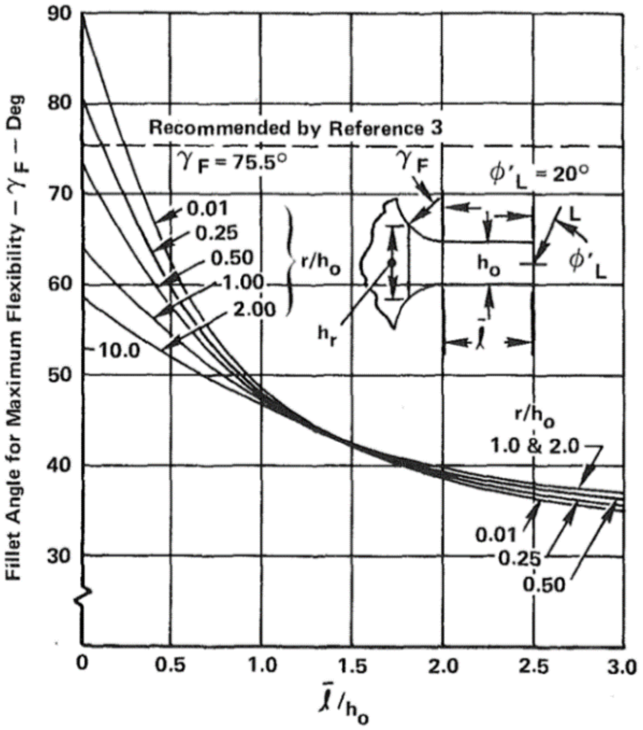

Figure 19: Curves for the determination of the angle γ_F from [21]

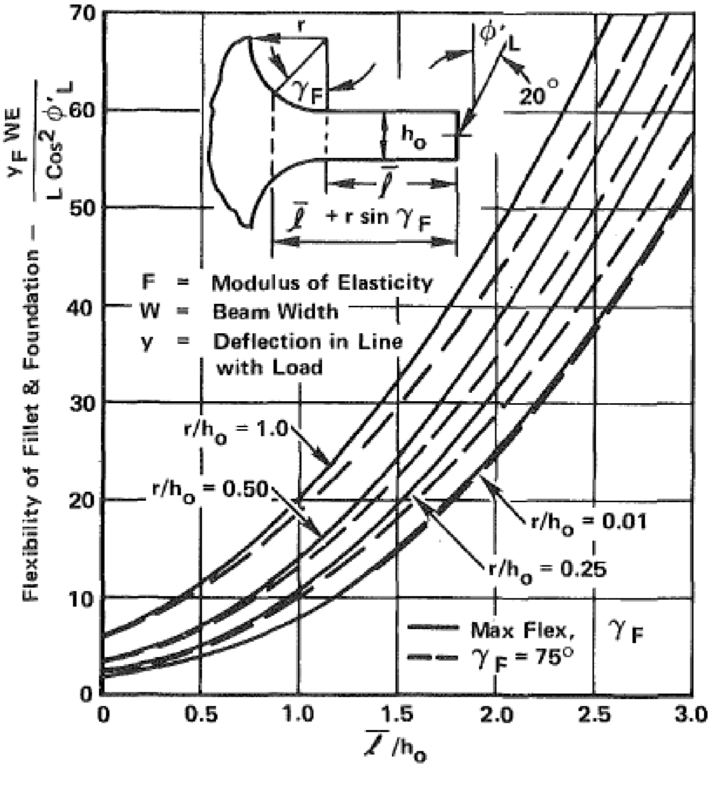

Figure 20: Variation of the flexibility y_F as a function of γ_F and $\bar{l}/\bar{h}$ from [21]

flexibility y_F especially for HCRG, characterized by high values of the ratio $\frac{\bar{l}}{\bar{h}}$ ($\frac{\bar{l}}{h_0}$ in Figure 19), while the approximation is close for LCRG. For completeness, the local deformation due to contact y_L as approximated by Cornell will be briefly discussed to further highlight the differences with the contact model that will be introduced in III.5. Due to their local nature however, these deformations will not be taken into account in the iterative calculations that will be detailed in paragraph III.4. His model is based on the classical Hertz theory for conforming elastic bodies and it is used to calculate the deformations of two contacting bodies. From Figure 21 it is possible to see that during contact under load, the rigid contact point P will displace based on the deformations α_1 and α_2 of the two bodies. The other points will first experience a rigid translation z_1 and z_2 and subsequently once adherence is reached a deformation w_1 and w_2. So, for a generic point in contact, the following equation is valid:

$$\alpha_1 + \alpha_2 = w_1 + w_2 + z_1 + z_2 \tag{3.29}$$

In Cornell's model the local deflection due to contact y_L is the sum of the contribution of the deformation due to Hertzian contact y_H and the local compression between the teeth y_C. At the rigid contact point P he expresses this deformation as:

$$\begin{aligned} y_L = y_H + y_C \approx \frac{2L}{\pi b} \left\{ \left(\frac{1-{\nu_1}^2}{E_1} \right) \cdot \left[\ln \frac{2\bar{h}_{Hertz,1}}{w} - \left(\frac{\nu_1}{2(1-\nu_1)} \right) \right] + \left(\frac{1-{\nu_2}^2}{E_2} \right) \cdot \right. \\ \left. \cdot \left[\ln \frac{2\bar{h}_{Hertz,2}}{w} - \left(\frac{\nu_2}{2(1-\nu_2)} \right) \right] \right\} \end{aligned} \tag{3.30}$$

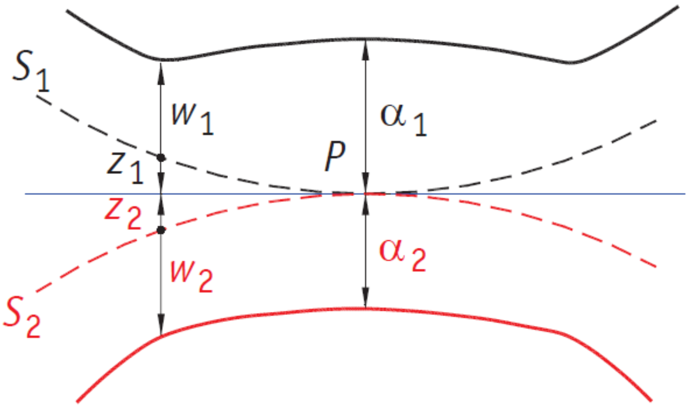

Figure 21: Displacements and deformations of the contact area

where w is the semi-width of the elliptical contact area computed as:

$$w = \sqrt{\frac{4L}{\pi b}\left[\left(\frac{1-{\nu_1}^2}{E_1}\right)+\left(\frac{1-{\nu_2}^2}{E_2}\right)\right]\Big/\left[\frac{1}{R_{osc_1}}+\frac{1}{R_{osc_2}}\right]} \tag{3.31}$$

The value of the deflection y_L is valid only for the contact point P, while the points that lie within a segment of length $2w$ and positioned so that the contact point P coincides with the mid-point of the segment, will deflect in a parabolically decreasing way from the maximum y_L, down to 0 at the extremes of the segment defining the contact area as visible in Figure 22. The simplifications of this model lie in the fact that only the radii of curvature R_{osc_1} and R_{osc_2} of the contact point P are considered, but the curvature of the involute profile changes continuously from root to tip and even inside the contact area and therefore cannot be considered constant. Furthermore, if the contact point P lies close to or at the tip of the tooth, up to w of the contact area computed in this way actually has no material underneath it, resulting in an erroneous pressure distribution and deflection. These limitations will be overcome in paragraph III.5.

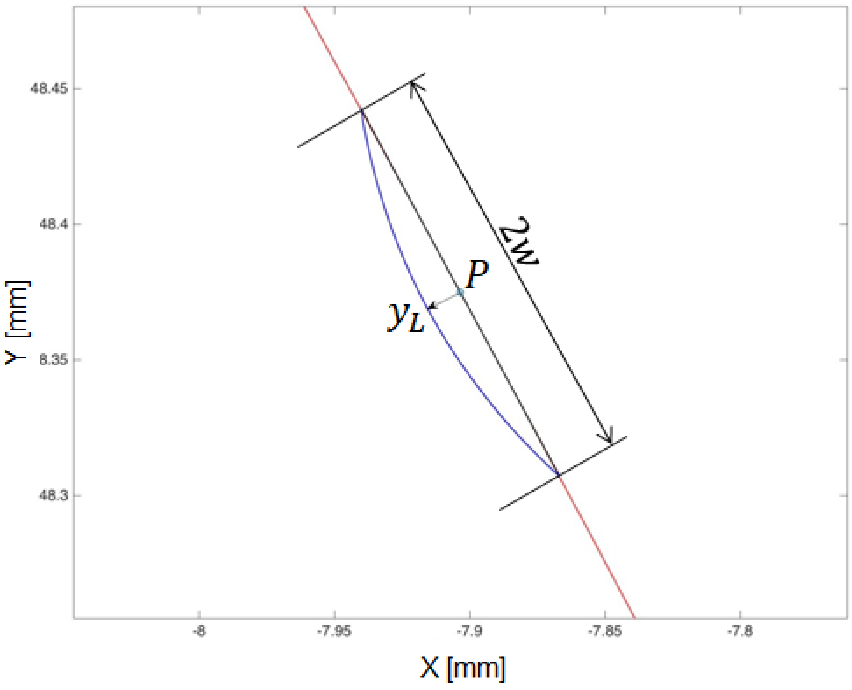

Figure 22: Local deflection in the contact area according Hertz theory

III.3.2 Gear body deflections

Under load the body of the gear deflects tangentially and this deformation influence also the unloaded teeth close to the loaded one and are defined in [20]. The tangential deflection can be calculated by observing an infinitesimally portion of the gear body with vertices A, B, C and D as defined in Figure 23. Under load this volume will undergo a rotation $\theta_{t,i}$ which will move it to the deformed configuration $A'B'C'D'$. The rotation can be expressed as

$$\theta_t = \frac{Q_p \cdot r}{4\pi b G} \cdot \left(\frac{1}{{r_s}^2} - \frac{1}{{r_f}^2}\right) \tag{3.32}$$

Where r is the radial distance from the center of the infinitesimal volume, r_s is the radius of the shaft on which the gear is mounted, r_f is the radius of the root circle, Q_p is the tangential load and G is the shear modulus

$$G = \frac{E}{2(1+\nu)} \tag{3.33}$$

Hence, the rotation of point P can be written as

$$\theta_{t,P} = \frac{Q_p \cdot {R_{L,P}}^2}{2\pi b E} \cdot (1+\nu) \cdot \left[\frac{1}{{r_s}^2} - \frac{z^2}{{r_p}^2(z-1{,}25)}\right] \tag{3.34}$$

and the displacement of any i^{th} point of the profile in the tangential direction is then

$$y_{GB,i} = \frac{L \cdot \cos\phi'_L \cdot R_{L,P}}{2\pi b E} \cdot (1+\nu) \cdot \left[\frac{1}{{r_s}^2} - \frac{z^2}{{r_p}^2(z-1{,}25)}\right] \cdot R_{L,i} \tag{3.35}$$

This approach however has been proven to not be accurate when compared with experimental measurements and therefore it will not be used. Instead, a more refined model proposed by Sainsot *et al.* [23] is here implemented to calculate the deflection of the gear body. Based on Muskhelishvili's theory applied to elastic rings they proposed the following formula for the gear body deflection:

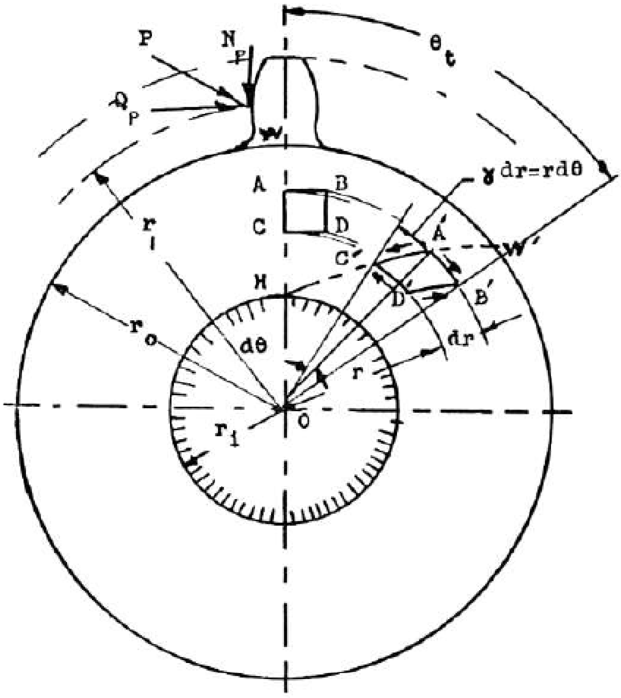

Figure 23: Tangential gear body deflections under load from [20]

$$y_A = \frac{Fcos^2\alpha}{bE} \cdot \left[L^*(h,\theta_f)\left(\frac{u}{s_f}\right)^2 + M^*(h,\theta_f)\frac{u}{s_f} + P^*(h,\theta_f) \cdot \left(1 + Q^*(h,\theta_f)tg^2\alpha\right)\right] \quad (3.36)$$

Where $h = r_o/r_i$ and θ_f is the angle between the tooth centerline and the junction with the root circle. The coefficients $L^*(h,\theta_f), M^*(h,\theta_f), P^*(h,\theta_f)$ and $Q^*(h,\theta_f)$ have been curve-fitted as polynomial functions of the form

$$X_i(h,\theta_f) = \frac{A_i}{\theta_f^2} + B_i h^2 + \frac{C_i h}{\theta_f} + \frac{D_i}{\theta_f} + E_i h + F_i \quad (3.37)$$

Where the constants A_i, B_i, C_i, D_i, E_i and F_i are listed in Table 1. The deflection of the teeth adjacent to the loaded one can be computed considering the portion of the gear rim connecting tooth B and C (Figure 24) as a beam on an elastic foundation subject to a normal load N and a bending moment M. The elastic deflection curve can be expressed as

Table 1: Constants for gear body contribution from [23]

	A_i	B_i	C_i	D_i	E_i	F_i
$L^*(h,\theta_f)$	-5.574e-5	-1.9986e-3	-2.3015e-4	4.7702e-3	0.0271	6.8045
$M^*(h,\theta_f)$	60.111e-5	28.100e-3	-83.431e-4	-9.9256e-3	0.1624	0.9086
$P^*(h,\theta_f)$	-50.952e-5	185.50e-3	0.0538e-4	53.300e-3	0.2895	0.9236
$Q^*(h,\theta_f)$	-6.2042e-5	9.0889e-3	-4.0964e-4	7.8297e-3	-0.1472	0.6904

$$EI\frac{d^4y}{d^4x} = -ky \tag{3.38}$$

where y is the deflection, x is the coordinate in the direction orthogonal to the line $\overline{O_1O_2}$ connecting the centers of rotation of the gears, I is the moment of inertia of rim and k is the stiffness of the foundation, defined

as

$$k = \frac{384EI}{x_1 + x_2 + x_3 + x_4} \tag{3.39}$$

x_1, x_2, x_3 and x_4 are visible in Figure 24. The general equation for solution of this problem is

$$y = e^{\beta x}(A \cdot \cos\beta x + B \cdot \sin\beta x) + e^{-\beta x}(C \cdot \cos\beta x + D \cdot \sin\beta x) \tag{3.40}$$

where

$$\beta = \left(\frac{k}{4EI}\right)^{\frac{1}{4}} \tag{3.41}$$

Applying the correct boundary conditions and solving (3.40) yields

$$y = \frac{e^{-\beta x}}{2\beta^3 EI} \cdot [N \cdot \cos\beta x - M \cdot (\cos\beta x - \sin\beta x)] \tag{3.42}$$

Therefore, the rigid rotations θ_B and θ_C that must be applied to teeth B and C respectively, knowing the intensity of the load

$$F = {}^{T}\!/_{R_B} \tag{3.43}$$

where T is the torque, can be computed as:

$$\theta_B = \tan^{-1}\left\{\frac{e^{-\beta x_1}}{2\beta^3 \cdot EI \cdot x_3} \cdot \left[\frac{F}{\cos\alpha} \cdot \sin\phi_L' \cdot \cos\beta x_1 - \beta Y_A \cdot \frac{F}{\cos\alpha} \cdot \cos\phi_L' \cdot (\cos\beta x_1 - \sin\beta x_1)\right]\right\} \tag{3.44}$$

$$\theta_C = \tan^{-1}\left\{\frac{e^{-\beta x_2}}{2\beta^3 \cdot EI \cdot x_4} \cdot \left[\frac{F}{\cos\alpha} \cdot \sin\phi_L' \cdot \cos\beta x_2 - \beta Y_A \cdot \frac{F}{\cos\alpha} \cdot \cos\phi_L' \cdot (\cos\beta x_2 - \sin\beta x_2)\right]\right\} \tag{3.45}$$

It is evident from Figure 24 that those rotations act in the opposite direction of application of the load, both for the pinion and the driven gear. The inclusion of this effect leads to an increase in the actual contact ratio $\varepsilon_{\alpha,act}$ due to the fact that the adjacent teeth come into, or lose, contact earlier or later than what could be predicted considering only the geometry of the engagement which is defined by the contact ratio ε_α. The iterative inclusion of this effect and the other contributions in the calculation of the gear's deformations will be discussed in the next paragraph.

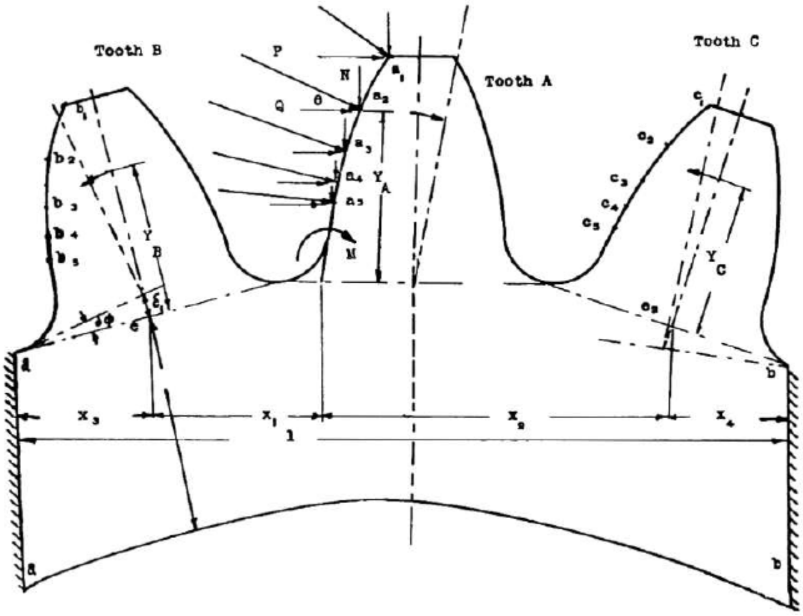

Figure 24: Quantities to define the effect of the loaded teeth on the adjacent ones from [20]

III.4 Iterative contact detection algorithm

Using the approach presented in the previous paragraph, neglecting for the moment the effect of the load on the adjacent teeth θ_A and θ_C, the deflection $y_{tot,i}$ of the gears could be computed using the superposition principle in the direction of the application of the load as

$$y_{tot,i} = y_{B,i} + y_{F,i} + y_{A,i} \tag{3.46}$$

In Figure 26 are visible the different contributions to the total deformation by applying the load $F = {}^{T}/_{R_B}$ to the geometrical contact point of a pinion, whose parameters are defined in Table 2, during single contact and ${}^{F}/_{2}$ in double contact. The distinction between single and double contact zones is visible in Figure 25. N_1 and N_2 are the tangency points between the base circles of the mating gears and the line of action inclined of the pressure angle α. Points B_1 and B_2 are defined by the intersections between the addendum circles and the line of action. Point E, marking the beginning of single tooth contact, is placed at a distance equal to the transversal base pitch $p_{b,t} = p_b \cdot \cos(\alpha) = m \cdot \pi \cdot \cos(\alpha)$ from point B_2, while the end of single tooth contact, point F is at the same distance from point B_1. Knowing the intersection points and the distances between those notable points the actual coordinates of the points can be easily found and the positions in which the rigid profiles are in single or double contact can be obtained. In Figure 26 the point of application of the load on the tooth moves from the beginning of the flank towards the tip and therefore the bending and shear deformation dramatically increase with the mesh angle due to the combined effect of the increase of the distance from the point of application of the load to the portion of the tooth which is considered clamped and the progressive reduction of cross-section of the tooth. The deformation due to local contact has a similar but less extreme trend, which is due to the decreasing trend of the radius of curvature R_{osc_1}. The effect of the fillet and foundation deflection increases as well, only due to the increasing distance of the application point of the load, while the gear body contribution stays constant since in this simple example only one tooth is considered. This is obviously a simplification and next the procedure for the calculation of the first iteration tentative load sharing coefficient will be described. When the system is in a single contact position it can be pictured as in Figure 27. Both the pinion (subscript p) and the driven gear (subscript g) can be seen as a series of springs each with its own stiffness. Starting from the center the stiffnesses of the gear bodies K_p and K_g are visible, then the global stiffness of the teeth $K_{t,p}$ and $K_{t,g}$ that include the bending of the teeth ($K_{B,g}$, $K_{B,p}$) and the effect of the fillet and foundation ($K_{FF,g}$, $K_{FF,p}$), and lastly the stiffness due to the local contact between the teeth K_c. The values of those stiffnesses come from the calculations of the deflections

Table 2: Example gear pair parameters

Parameter	Pinion	Gear
Number of teeth z [-]	20	20
Module m [mm]	3	3
Pressure angle α_P [°]	20	20
Face width b [mm]	23,5	23,5
Shaft radius r_s [mm]	10	10
Torque T [Nmm]	70000	70000
Young modulus E [MPa]	210000	210000
Poisson coefficent ν [-]	0,3	0,3

described in the previous paragraph, namely K_p and K_g from eq. (3.35), $K_{B,g}$ and $K_{B,p}$ from (3.20), $K_{FF,g}$ and $K_{FF,p}$ from (3.26) and lastly K_c from (3.30). Therefore, the system can be seen as a succession of springs in series that see the same force applied due to the torque transmitted, then global stiffness of the system during single contact can be written as

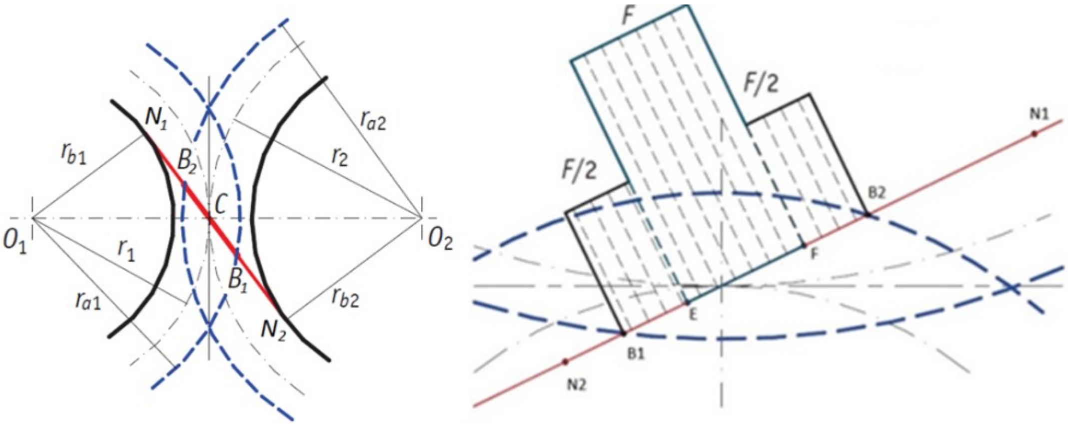

Figure 25: Geometrical distinction between single and double contact

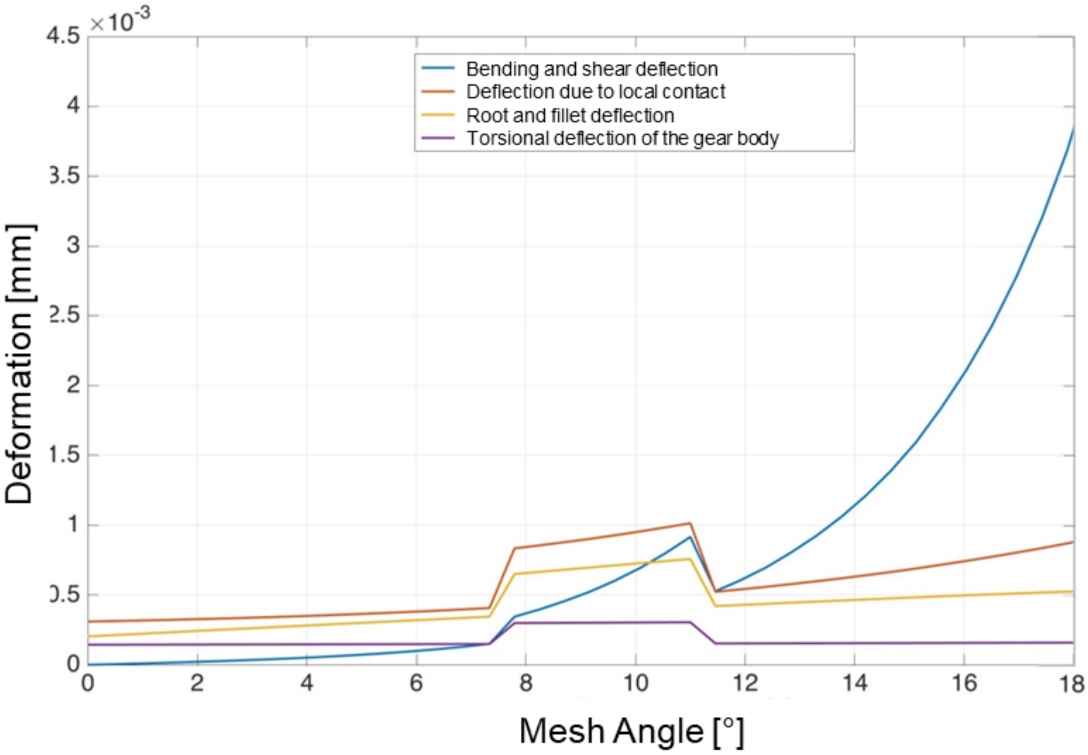

Figure 26: Contribution of the different effects to the total deformation

$$K_{TOT,1} = \frac{1}{{}^{1}/_{K_p} + {}^{1}/_{K_g} + {}^{1}/_{K_{FF,p}} + {}^{1}/_{K_{FF,g}} + {}^{1}/_{K_{B,p}} + {}^{1}/_{K_{B,g}} + {}^{1}/_{K_c}} \tag{3.47}$$

During double contact the stiffnesses of the gear bodies K_p and K_g remain unchanged, but the two pairs of teeth in contact can be represented by their mesh stiffnesses K_m^A and K_m^B for the pairs A and B in contact. A schematization is visible in Figure 28. The mesh stiffnesses K_m^A and K_m^B can be defined as

$$K_m^A = \left({}^{1}/_{K_{FF,p}}\right)_A + \left({}^{1}/_{K_{FF,g}}\right)_A + \left({}^{1}/_{K_{B,p}}\right)_A + \left({}^{1}/_{K_{B,g}}\right)_A \tag{3.48}$$

$$K_m^B = \left({}^{1}/_{K_{FF,p}}\right)_B + \left({}^{1}/_{K_{FF,g}}\right)_B + \left({}^{1}/_{K_{B,p}}\right)_B + \left({}^{1}/_{K_{B,g}}\right)_B \tag{3.49}$$

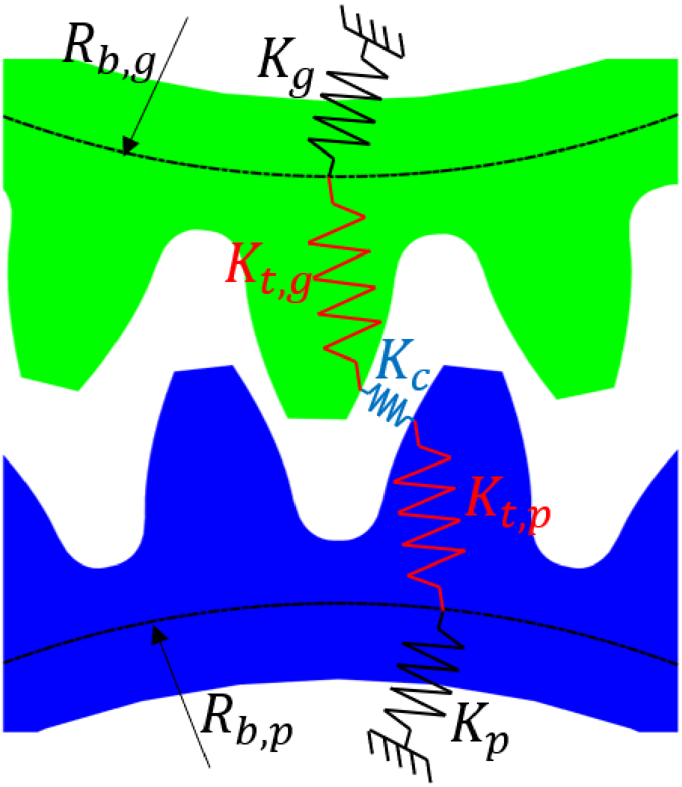

Figure 27: Series of springs during single contact

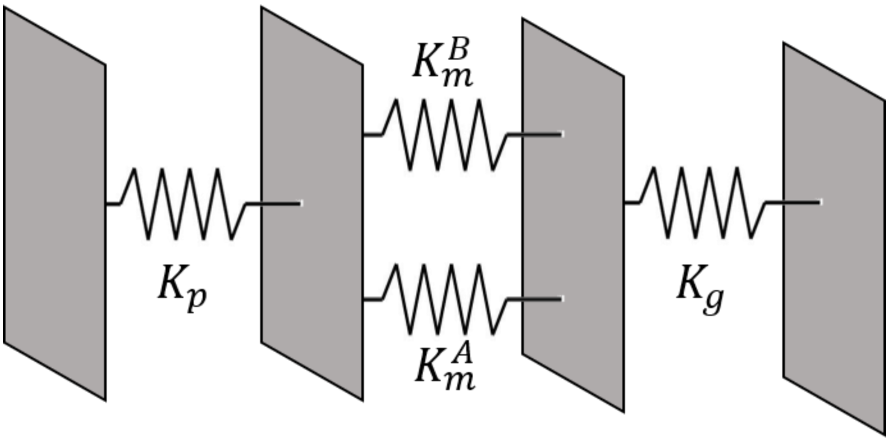

Figure 28: Series of springs during double contact

Therefore, the global stiffness during double contact can then be written as

$$K_{TOT,2} = \frac{1}{{}^{1}/_{K_p} + {}^{1}/_{K_g} + \frac{1}{K_m^A + K_m^B} + {}^{1}/_{K_c}} \quad [N/mm] \tag{3.50}$$

However, this is not a standard connection of springs in series where the two stiffnesses undergo the same deformation under the action of the applied load. Indeed, the two pairs of teeth at a given mesh angle have different contact points relative to their flank, and therefore they have different stiffnesses and deflections and hence also the load they will experience will be different. Namely the stiffer pair of teeth will take up most of the load, while the softer one a lower fraction of it. To quantify this relationship for each angular position in the mesh period considered the deflections of each pair of teeth in contact are computed considering a unit load at the instantaneous contact point, for the pinion and the driven gear as

$$y_{tot,P_{unit,p,k}} = y_{B,P_{unit,p,k}} + y_{F,P_{unit,p,k}} + y_{L,P_{unit,p,k}} + y_{Attia,P_{unit,p,k}} \tag{3.51}$$

$$y_{tot,P_{unit,g,k}} = y_{B,P_{unit,g,k}} + y_{F,P_{unit,g,k}} + y_{L,P_{unit,g,k}} + y_{Attia,P_{unit,g,k}} \tag{3.52}$$

where $k = 0, 1, 2$ for a standard spur gear application with $1 \leq \ \varepsilon_\alpha \ \leq 2$ and the meaning of k is explained in Figure 29. Therefore, for each pair of teeth in contact the following cumulative deflection can be considered

$$y_{tot,P_{unit,k}} = y_{tot,P_{unit,p,k}} + y_{tot,P_{unit,g,k}} \tag{3.53}$$

Hence, for the first iteration three different conditions can be defined, and their load sharing factor coefficient C_k can be specified:

- Case 1: $k = 1, 2$

$$C_1 = \frac{y_{tot,P_{unit,2}}}{y_{tot,P_{unit,1}} + y_{tot,P_{unit,2}}} \tag{3.54}$$

$$C_2 = \frac{y_{tot,P_{unit,1}}}{y_{tot,P_{unit,1}} + y_{tot,P_{unit,2}}} \tag{3.55}$$

- Case 2: $k = 0, 1$

$$C_1 = \frac{y_{tot,P_{unit,0}}}{y_{tot,P_{unit,1}} + y_{tot,P_{unit,0}}} \tag{3.56}$$

$$C_0 = \frac{y_{tot,P_{unit,1}}}{y_{tot,P_{unit,1}} + y_{tot,P_{unit,0}}} \tag{3.57}$$

- Case 3: $k = 1$ single contact

$$C_1 = 1 \tag{3.58}$$

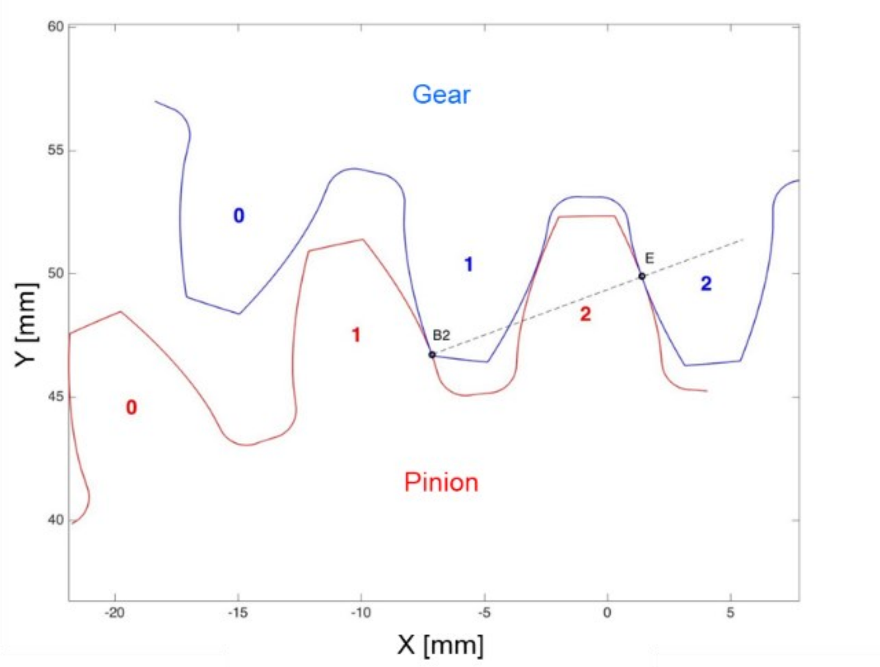

Figure 29: Numbering of teeth gear pairs k

This relationship for the 40 angular positions considered in the previous example, whose data is listed in Table 2, is visible in Figure 30 when contact at the geometric or rigid contact point, and therefore valid only for the first iteration, is considered. Similar considerations apply when $\varepsilon_\alpha > 2$ with minor adjustments to the conditions above. Furthermore, it is known that a deformation during contact between two bodies can shift the actual contact point from its location predictable by rigid body analysis, especially when bending deformations are involved as depicted in Figure 31. Indeed, if a rigid body is brought into contact via a vertical displacement with a flexible beam, the first point of contact is easily identifiable by rigid body kinematics. However, if the load is increased the point of contact will shift, thus changing the deformed shape of the beam. Numerically this results in an iterative search in which a natural equilibrium condition is sought for the load, the position of the contact point and the deformed shape of the beam as visible in Figure 31 a), while in b) the same concept is visualized for two teeth flank in contact. The rigid contact point on the left of the figure is visibly different from the actual contact point at equilibrium on the deformed profiles under load, both in terms of coordinates, since the profiles have undergone all deformations detailed earlier, but also in terms of position along the flanks. Indeed, the actual contact point is visibly further up on the profile of pinion since the flanks slide due to deformation against each other. In most applications this secondary effect is neglected if the deformations are not large. In gears however, this effect, combined with the influence of the load on one tooth on the adjacent teeth, can significantly alter the position of the actual contact point and particularly the number of teeth pairs currently engaged. To model these effects, in the present work an iterative contact detection algorithm has been implemented.

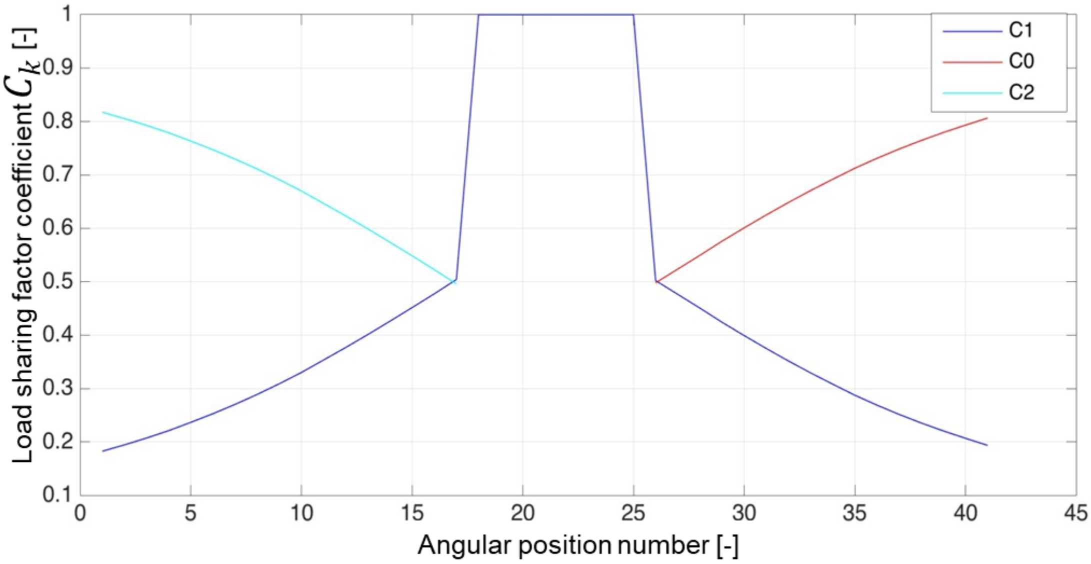

Figure 30: Load sharing factor coefficient C_k evolution

The start of the algorithm is the geometrical, or rigid, contact point, circled in green in Figure 32, which can be found either by finding the pair of points with the minimal angular distance between all the possible teeth pairs, or by intersecting the active portions of the profiles with the line of action of the gears. Next, the load is applied to the contact point just found and deformations of the teeth and the gear body are computed according to the methodology discussed in the previous paragraph, including the model from [20], and applied to the discretized geometry as in Figure 33 where the deformations have been amplified by a factor of 100 to make them more evident. At this point the iterative contact point detection takes place. From each of the points of the flank of the pinion teeth circular arcs with center in the center of rotation of the pinion are defined. Their radius is

$$r_i = \sqrt{x_i^2 + y_i^2} \tag{3.59}$$

Where x_i and y_i are the coordinates of the i^{th} point of the pinion flank after deformation. These arcs span an angle ϑ that is at least equal to the sum of the maximum angular deformation experienced by the profiles taking into account all contributions, to be sure that at least one of them will intercept the profile of the driven gear. An example of this process is visible in Figure 34. The arcs are discretized in m segments each spanning a sufficiently small

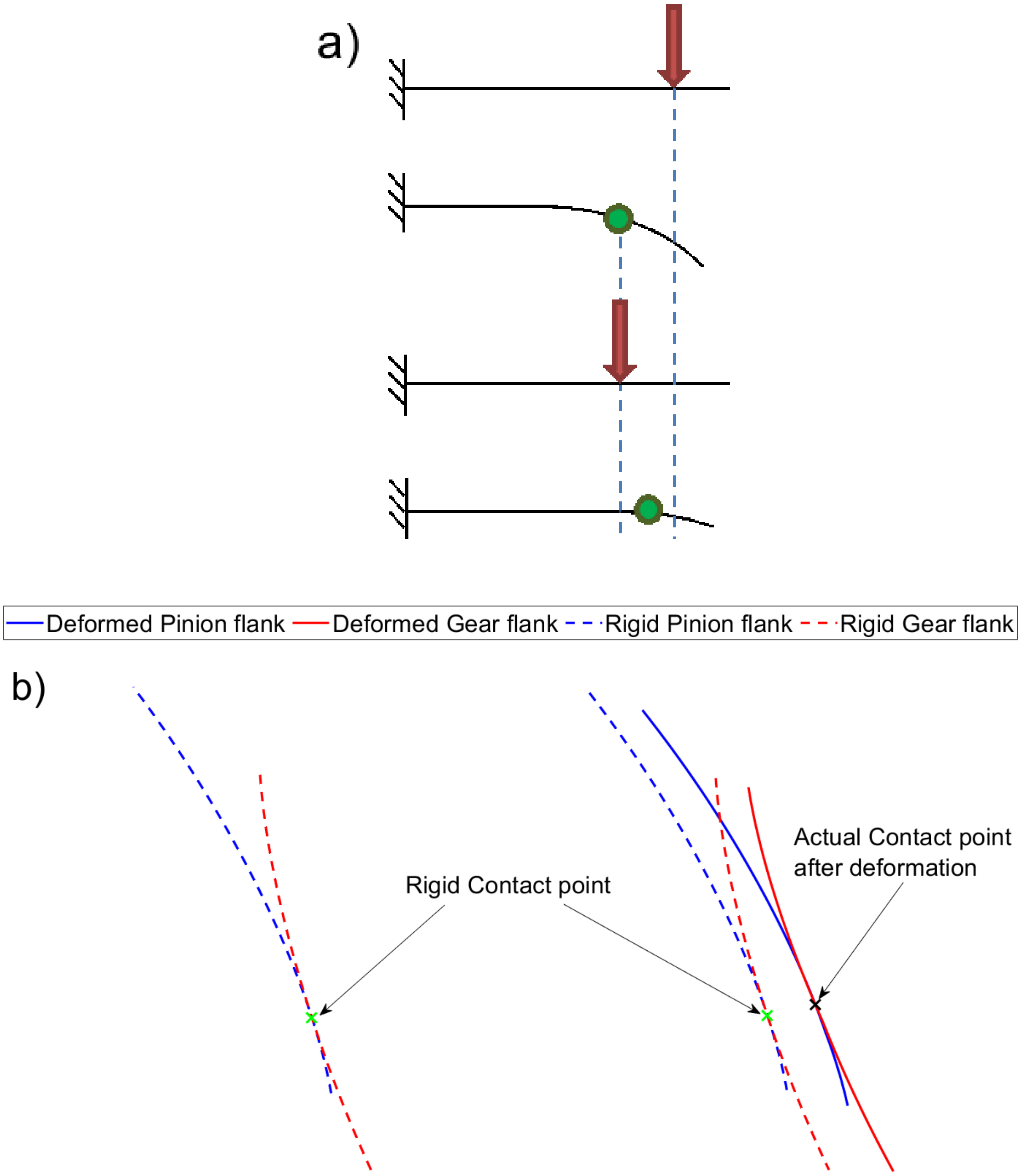

Figure 31: Shift of the actual contact point after deformation, a) example on a simple beam, b) actual contact point after deformation of a tooth pair in engagement

angle $\Delta\vartheta$, thus defining $m-1$ segments whose endpoints have coordinates $(x_k, y_k), (x_{k+1}, y_{k+1})$ where $k = 1, 2, \dots, m-1$. The new contact point will be the one where the intersection between the discretized arcs and the deformed profile of the driven gear forms the minimum angle. To find the intersections it is possible to write the following system of equations [104]

$$\begin{cases} (x_{g+1} - x_g) \cdot t_g = x_0 - x_g \\ (x_{k+1} - x_k) \cdot t_k = x_0 - x_k \\ \left(y_{g+1} - y_g\right) \cdot t_g = y_0 - y_g \\ \left(y_{k+1} - y_k\right) \cdot t_k = y_0 - y_k \end{cases} \tag{3.60}$$

where x_g, y_g are the coordinates of the driven gear profiles forming $N_i - 1$ segments whose endpoints are $\left(x_g, y_g\right)$, (x_{g+1}, y_{g+1}), while t_g and t_k are the distances from the starting point of the g, k segment from the intersection point (x_0, y_0) relative to the segment length

$$t_g = \sqrt{\left(x_g - x_0\right)^2 + \left(y_g - y_0\right)^2} \Big/ \sqrt{\left(x_g - x_{g+1}\right)^2 + \left(y_g - y_{g+1}\right)^2} \tag{3.61}$$

and similarly, for t_k. Rearranging (3.60) and writing it in matrix form yields

$$\begin{bmatrix} (x_{g+1} - x_g) & 0 & -1 & 0 \\ 0 & (x_{k+1} - x_k) & -1 & 0 \\ \left(y_{g+1} - y_g\right) & 0 & 0 & -1 \\ 0 & \left(y_{k+1} - y_k\right) & 0 & -1 \end{bmatrix} \begin{Bmatrix} t_g \\ t_k \\ x_0 \\ y_0 \end{Bmatrix} = \begin{Bmatrix} x_g \\ x_k \\ y_g \\ y_k \end{Bmatrix} \tag{3.62}$$

Or

$$\boldsymbol{A}\boldsymbol{t} = \boldsymbol{b} \tag{3.63}$$

If the segments are not parallel or overlapping, (3.63) can be simply solved as

$$\boldsymbol{t} = \boldsymbol{A}^{-1}\boldsymbol{b} \tag{3.64}$$

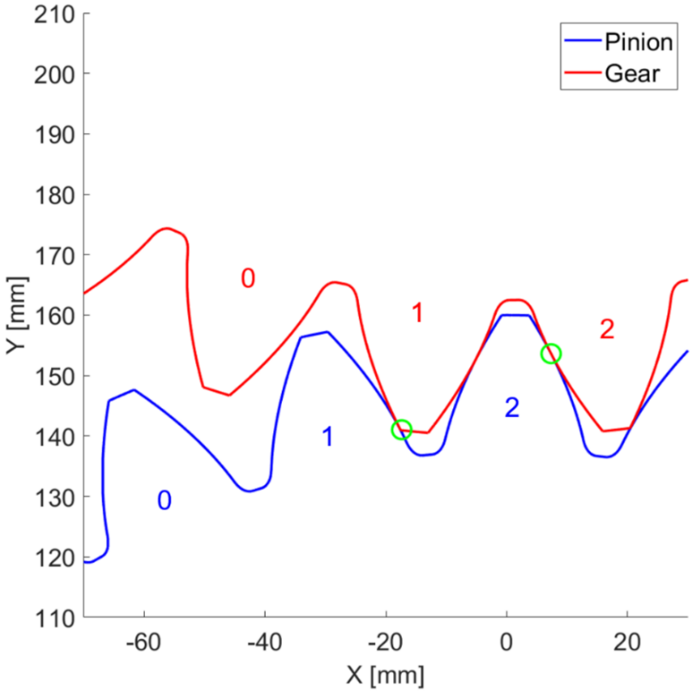

Figure 32: Rigid contact point detection

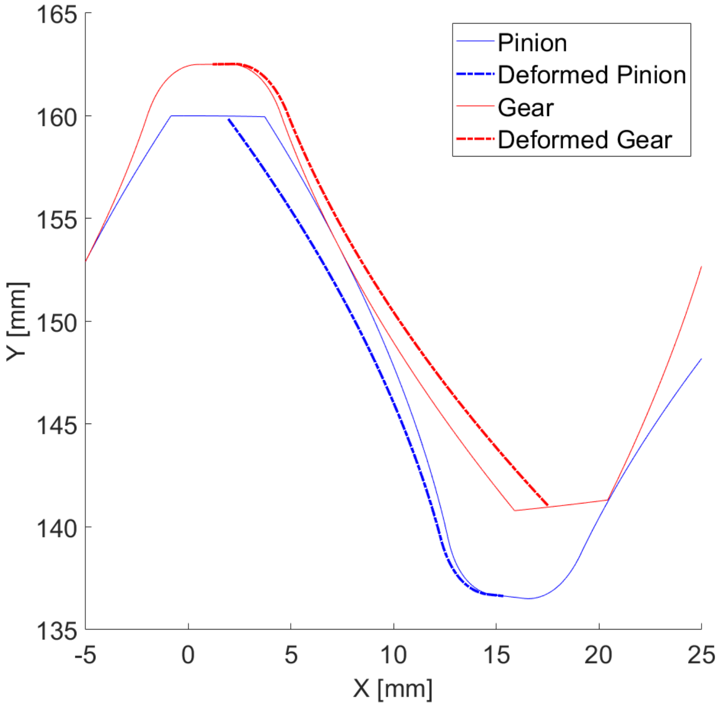

Figure 33: Profiles of teeth pair 2 after deformation. Note that the deformations have been amplified by a factor of 100.

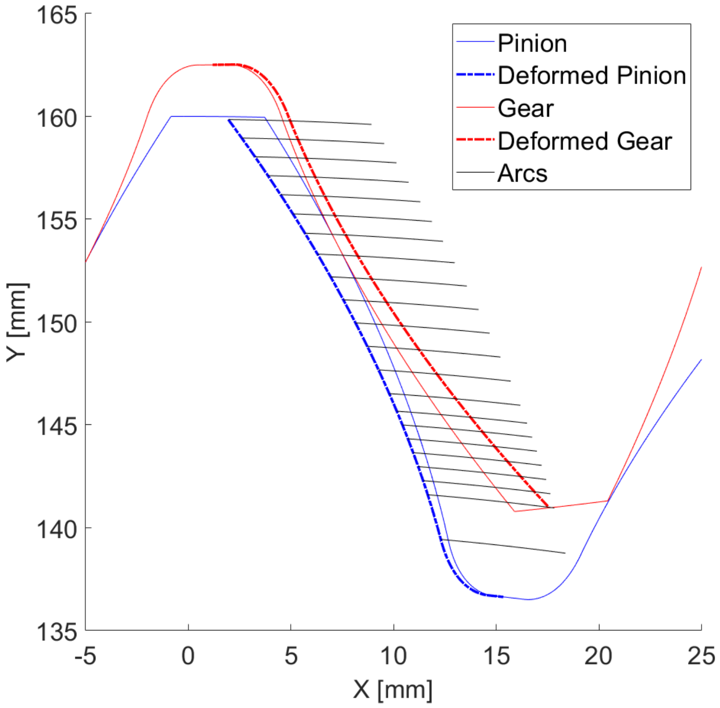

Figure 34: Arcs for iterative contact detection

An actual intersection between the segments is found only if the following conditions are simultaneously verified:

$$\begin{cases} 0 \leq t_g < 1 \\ 0 \leq t_k < 1 \end{cases} \tag{3.65}$$

Computationally, (3.64) would need to be solved $[(m-1)N_i] \cdot (N_i - 1)$ times, leading to a bottleneck in the calculations. This number can however be greatly reduced by considering only the segments that can potentially intersect checking if the smallest enclosing rectangles of each segment pair overlap. This produces the following set of inequalities

$$\min(x_g) \leq \max(x_k) \wedge \max(x_g) \geq \min(x_k) \wedge \min(y_g) \leq \max(y_k) \wedge \max(y_g) \geq \min(y_k) \tag{3.66}$$

thus reducing the number of solutions of (3.64) to less than $N_i - 1$. Of all the resulting intersection points (x_{0_i}, y_{0_i}) the one defining the new contact point (x_c, y_c) is found by

$$(x_c, y_c) = \left\{x_{0_i}, y_{0_i} \;\middle|\; min\left(\left|\tan^{-1}\left(\frac{y_i}{x_i}\right) - \tan^{-1}\left(\frac{y_{0_i}}{x_{0_i}}\right)\right|\right)\right\} = \{x_{0_i}, y_{0_i} \mid min(|\Delta\theta_i|)\} \tag{3.67}$$

which means looking for the contact point where the angle between the pinion flank and the intersection of the arc with the driven gear is minimum. Point (x_c, y_c) belongs to the profile of the driven gear and the closest point to it of the discretization of the flank is then chosen. For the pinion the new contact point is automatically determined by looking at the coordinates (x_i, y_i) from which the arc with the minimum $|\Delta\theta_i|$ was calculated. Since this is performed for each flank of the pinion, depending on the contact ratio of the gear and the angular position considered, multiple contact points will be found in general. However, not all those contact points that verify (3.67) are actual contact points. For a case with $\varepsilon_\alpha \leq 2$, considering the numbering of the flanks as shown in Figure 32, the $|\Delta\theta_i|$ of tooth 1 is compared with the ones eventually found for teeth 0 and 2. If those angles are lower or equal than the one for tooth 1 then those are actual contact points, otherwise are discarded and the corresponding tooth is the considered unloaded in the next iteration, and the load sharing factor coefficient is computed accordingly. This iterative process stops when between the coordinates of the contact point of previous iteration $iter - 1$ and the current one $iter$ change less than a tolerance value, so that

$$\left|x_{c,iter-1} - x_{c,iter}\right| \leq \ \varepsilon_x \ \wedge \ \left|y_{c,iter-1} - y_{c,iter}\right| \leq \ \varepsilon_y \tag{3.68}$$

where ε_x and ε_y are usually in the order of $10^{-3}\ mm$. Any 2D tooth profile modification or error can be included and taken into account into this process since no restriction has been specified for the shape on the teeth considered. Furthermore, in addition to the variation of the contact point, one must also consider a better approximation of the estimation of the load sharing coefficients to include the influence of the operative deflections. To do this, an approach as detailed in [105] is introduced. At each iterative step the deflection of the contact point in the direction of application of the load δ_i is registered, where i indicates the tooth pair considered and can be $i = 1{,}2$ for LCRG with $\varepsilon_\alpha \leq 2$ or $i = 1{,}2{,}3$ for HCRG with $\varepsilon_\alpha > 2$. In a general form, for a gear pair with N teeth pairs in engagement under the effect of gear deflections the load sharing factor Lsf_i for the i^{th} teeth pair in engagement ($i = 1{,}2{,}..N$) can be obtained as

$$Lsf_i = \frac{K_i}{\sum_{j=1}^{N} K_j}\left(\frac{1 + \sum_{j=1}^{N} K_j\, \tilde{E}_{ij}}{F}\right) \tag{3.69}$$

where $\tilde{E}_{ij} = \delta_i - \delta_j$ and $K_i = \frac{F_i}{\delta_i} = \frac{F \cdot Lsf_i}{\delta_i}$ at the previous iteration. The coefficients C_k that will multiply the total load F to be applied at each tooth pair considered can then be differentiate as before in various cases, yielding

- Case 1: $k = 1, 2$

$$C_1 = \frac{K_1}{K_1 + K_2}\left(\frac{1 + K_2\tilde{E}_{12}}{F}\right) \tag{3.70}$$

$$C_2 = 1 - C_1 = \frac{K_2}{K_1 + K_2}\left(\frac{1 - K_1\tilde{E}_{12}}{F}\right) \tag{3.71}$$

- Case 1: $k = 0{,}1$

$$C_1 = \frac{K_1}{K_1 + K_0}\left(\frac{1 + K_0\tilde{E}_{10}}{F}\right) \tag{3.72}$$

$$C_0 = 1 - C_1 = \frac{K_0}{K_1 + K_0}\left(\frac{1 - K_1\tilde{E}_{10}}{F}\right) \tag{3.73}$$

- Case 3: $k = 1$ single contact

$$C_1 = 1 \tag{3.74}$$

And similarly, for HCRG with $\varepsilon_\alpha \geq 2$. This iterative load variation doesn't add a convergence criterion since it's based on the deflections, hence if the deflections are the same as the previous step also the load sharing coefficient will be, and if the deflections are the same also the actual contact point will be the same, meaning that (3.68) is sufficient to reach convergence. Therefore, the algorithm just presented can be resumed in the following steps:

- Individuation of the rigid contact points and first estimation of the load sharing factor coefficient with the use of the correct equations between (3.54) trough (3.58)
- Calculation of the operative deflections on the loaded teeth as described in Chapter III.3 including the deformations of the adjacent teeth

- Calculation of the updated load sharing coefficients with the use of the correct equations between (3.70) and (3.74)
- Search of the new contact points between the deformed geometries with the arcs procedure described in this section
- Iteration of the above steps until the number of teeth pairs in contact doesn't change and (3.68) is verified
- After convergence is reached, analyze the contact using the deformed profiles with the approach detailed in the next paragraph
- Record the resulting STE by equation (2.5)

A visual representation of the above algorithm is visible in Figure 35.

III.5 2D Non-Hertzian contact model

As stated in paragraph III.3.1 the simplified contact model summarized by equations (3.30) and (3.31) cannot be used to effectively estimate the contact stiffness during engagement since it lacks the capability to correctly treat the complicated geometry involved. Firstly, the curvature of the teeth changes continuously, and the above-mentioned model only considers the curvature at the contact point. Furthermore, when tip corner contact occurs there is no practical way to limit the contact area to where there actually is material to support the pressure, and similar situations occur when tooth profile modifications are to be modeled, such as linear and parabolic tip relief that will be introduced later. To overcome these limitations and obtain accurate pressure distributions and surface displacements a frictionless non-Hertzian numerical 2D line contact model was implemented. The contact conditions can be expressed in the so called Hertz-Signorini-Moreau problem [106] [107] [108]

$$\boldsymbol{h} \geq 0,\ \boldsymbol{p_n} \geq 0,\ \boldsymbol{h} \cdot \boldsymbol{p_n} = 0 \tag{3.75}$$

The first condition enforces that no interpenetration can occur between the contact bodies and therefore the gap function $\boldsymbol{h}$, which measures the distances between the surfaces, can only be positive, or equal to $\mathbf{0}$ in the contact area. The second condition imposes that the

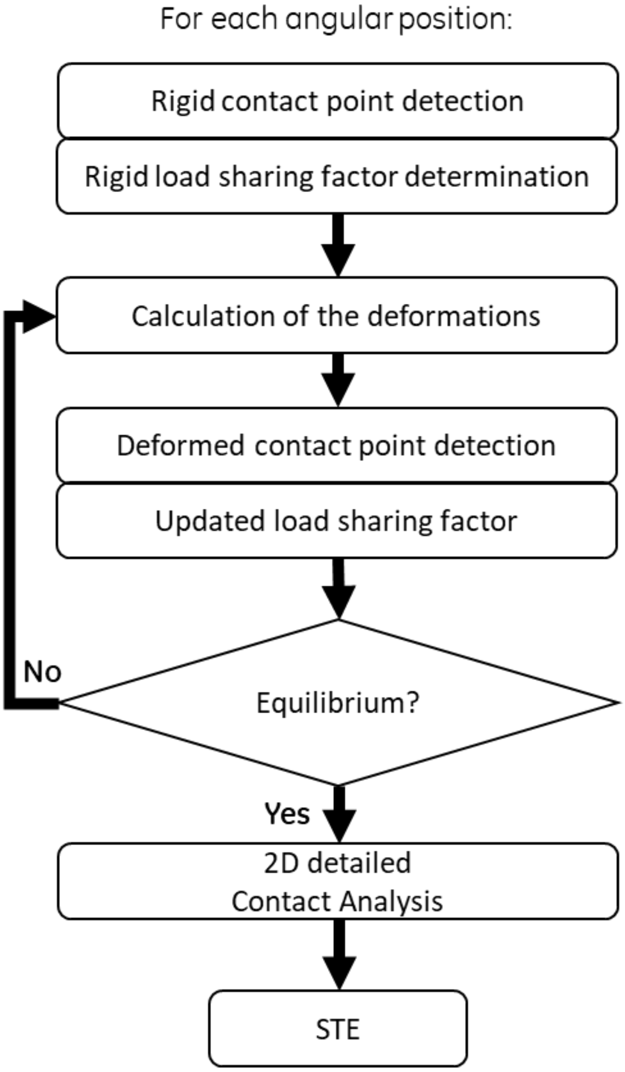

Figure 35: Pseudo-algorithm visualization

contact is non-adhesive and therefore no tension force must be present in the contact area, formulated from the normal stress

$$\boldsymbol{\sigma_n} = \boldsymbol{t} \cdot \boldsymbol{n} \tag{3.76}$$

where $\boldsymbol{t}$ is the traction force vector and $\boldsymbol{n}$ is the normal direction to the surface and $\boldsymbol{p_n} = -\boldsymbol{\sigma_n}$. The third condition enforces that the normal pressures can only be different from $\boldsymbol{0}$ inside the contact area where $\boldsymbol{h} = \boldsymbol{0}$ and null everywhere else. The gap function $\boldsymbol{h}$ is expressed as

$$\boldsymbol{h} = h_0 + \boldsymbol{g} + \boldsymbol{\delta} \tag{3.77}$$

where h_0 is the indentation between the profiles imposed as a rigid body motion, $\boldsymbol{g}$ is the initial separation of the contacting surfaces and represents it topography, while $\boldsymbol{\delta}$ represents the elastic deformation of the surfaces due to the applied normal pressure $\boldsymbol{p_n}$ and can be expressed as [109]

$$\boldsymbol{\delta} = \boldsymbol{C} \cdot \boldsymbol{p_n} \tag{3.78}$$

where $\boldsymbol{C}$ is a matrix of the influence coefficients which introduces the elasticity of the contacting surfaces. Its components C_{ij} $(i, j = 0,1, \dots N)$ relate the displacement δ_i at a point i due to the application of a unit pressure at point j. If a pressure profile $p_n(x)$ is assumed, the dimensionless elastic deformation $\delta^*(x)$ can be expressed as [110]

$$\delta^*(x) = -\frac{1}{\pi} \int_{x_a}^{x_b} ln|x_i - x|\, p_n(x)\, dx \tag{3.79}$$

If the pressure profile is approximated by a piecewise constant function $p_{n,j} = p_n(x_j)$ (Figure 36) in the considered region $x_j - \frac{\Delta x}{2} \le x \le x_j + \frac{\Delta x}{2}$ where Δx is the uniform mesh size $\Delta x = x_{j+1} - x_j$, then the deformation at a point $x_i = x_0 + i\Delta x$ can be written as

$$\delta^*(x_i) = -\frac{1}{\pi} \sum_{i=0}^{i=N} C_{ij}^*\, p_{n,j}\, dx \tag{3.80}$$

where

$$C_{ij}^* = \int_{x_j - \frac{\Delta x}{2}}^{x_j + \frac{\Delta x}{2}} ln|x_i - x|\, dx \tag{3.81}$$

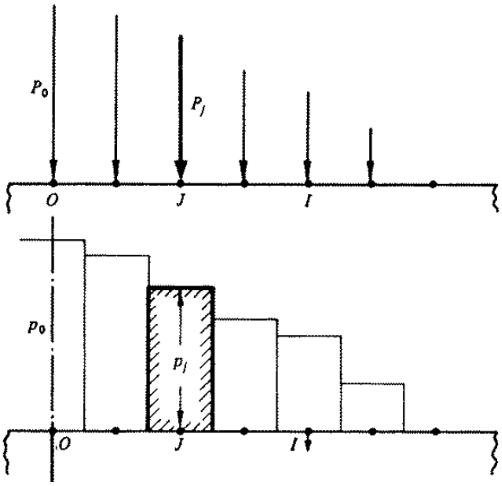

Figure 36: Piecewise constant pressure distribution

which can be solved analytically to yield

$$C_{ij}^{*} = \left(x_i - x_j + \frac{\Delta x}{2}\right) \cdot \left(ln\left|x_i - x_j + \frac{\Delta x}{2}\right| - 1\right) - \left(x_i - x_j - \frac{\Delta x}{2}\right) \cdot \left(ln\left|x_i - x_j - \frac{\Delta x}{2}\right| - 1\right) \tag{3.82}$$

Since a constant mesh size Δx has been chosen, (3.82) can be further simplified considering that

$$x_i - x_j = (i - j)\Delta x \tag{3.83}$$

Finally, the dimensional influence coefficients C_{ij} for unit thickness can be expressed as

$$C_{ij} = \frac{4}{E^{*}}\left[\left(i - j + \frac{1}{2}\right)\Delta x \cdot \left(ln\left|\left(i - j + \frac{1}{2}\right)\Delta x\right| - 1\right) - \left(\left(i - j - \frac{1}{2}\right)\Delta x\right) \cdot \left(ln\left|\left(i - j - \frac{1}{2}\right)\Delta x\right| - 1\right)\right] \tag{3.84}$$

where E^{*} is the effective elastic modulus considering the material properties of the bodies 1 and 2 in contact defined as:

$$\frac{1}{E^*} = \left(\frac{1-{\nu_1}^2}{E_1}\right) + \left(\frac{1-{\nu_2}^2}{E_2}\right) \tag{3.85}$$

To solve the problem stated in (3.75) and satisfy all conditions a sub-iterative process is needed. Firstly, only the values $h^{\tilde{n}}$ of the nodes $\tilde{n}$ belonging to the domain x that are in actual compenetration and hence satisfy

$$\tilde{n} = \{n \in x | h^n < 0\} \tag{3.86}$$

are selected to form the vector $\widetilde{\boldsymbol{h}}$ and consistently also the corresponding rows and columns of $\boldsymbol{C}$ are selected to form the matrix $\widetilde{\boldsymbol{C}}$**,** effectively setting all loads on nodes outside of the contact region to $\mathbf{0}$**.** The pressures $\widetilde{\boldsymbol{p}}$ pertaining to the compenetrating nodes are obtained by

$$\widetilde{\boldsymbol{p}} = \widetilde{\boldsymbol{C}}^{-\mathbf{1}}\widetilde{\boldsymbol{h}} \tag{3.87}$$

Next, the list of $\tilde{n}$ nodes is updated by removing those where tensile pressures are registered and those who are not compenetrating anymore due to the elastic deflection of the contacting surfaces, leaving then only those who satisfy

$$\tilde{n} = \{n \in x | \, \boldsymbol{p} > 0 \ \wedge \boldsymbol{C}\boldsymbol{p} < \boldsymbol{h}\} \tag{3.88}$$

This sub-iterative process stops when the list of $\tilde{n}$ nodes at the current sub-iterative step is the same as the previous one. Finally, given a certain h_0 after the solution of the sub-iterative procedure just explained, the load acting on the contacting bodies for unit thickness can be found as

$$f = \frac{\Delta x}{2} \sum_{i=0}^{i=N-1} (p_{n,i} + p_{n,i+1}) \tag{3.89}$$

which in general will be different from the imposed load $F = {}^{T}\!/_{R_B}$, hence further iterations are needed to obtain the correct h_0. As a first guess the value resulting from (3.30) is used as

$h_{0,1}$ for the first iteration, while for the k^{th} iteration the value $h_{0,k}$ to be used is estimated the previous iterations by

$$h_{0,k} = h_{0,k-1} + \frac{h_{0,k-1} - h_{0,k-2}}{f_{k-1} - f_{k-2}} (F - f_{k-1}) \tag{3.90}$$

with good convergence rates. The iterations stop when the residual

$$r_k = \frac{F - f_k}{F} \tag{3.91}$$

is below a certain tolerance value ε_F so that $r_k \leq \varepsilon_F$, where usually $\varepsilon_F = 1e - 4$. The elastic displacements of each contacting surface can be obtained by simply noting that

$$\frac{1}{E^*} = \left(\frac{1 - {\nu_1}^2}{E_1}\right) + \left(\frac{1 - {\nu_2}^2}{E_2}\right) = \frac{1}{E_1^*} + \frac{1}{E_2^*} \tag{3.92}$$

Therefore, $\boldsymbol{C}$ can be decomposed as

$$\boldsymbol{C} = \boldsymbol{C_1} + \boldsymbol{C_2} \tag{3.93}$$

where the influence coefficients of surfaces 1 and 2 are expressed by

$$\begin{aligned} C_{1,ij} = \frac{4}{E_1^*} \Bigg[&\left(i - j + \frac{1}{2}\right) \Delta x \cdot \left(ln \left| \left(i - j + \frac{1}{2}\right) \Delta x \right| - 1 \right) - \left(\left(i - j - \frac{1}{2}\right) \Delta x \right) \\ &\cdot \left(ln \left| \left(i - j - \frac{1}{2}\right) \Delta x \right| - 1 \right) \Bigg] \end{aligned} \tag{3.94}$$

$$\begin{aligned} C_{2,ij} = \frac{4}{E_2^*} \Bigg[&\left(i - j + \frac{1}{2}\right) \Delta x \cdot \left(ln \left| \left(i - j + \frac{1}{2}\right) \Delta x \right| - 1 \right) - \left(\left(i - j - \frac{1}{2}\right) \Delta x \right) \\ &\cdot \left(ln \left| \left(i - j - \frac{1}{2}\right) \Delta x \right| - 1 \right) \Bigg] \end{aligned} \tag{3.95}$$

The elastic displacements are finally obtained

$$\boldsymbol{h_k} = \boldsymbol{C_k p} \tag{3.96}$$

where $k = 1{,}2$. The above method is valid for rough frictionless non-Hertzian contact, but it's still valid also for Hertzian problems, which allows a comparison. Two cylinders of radii $r_1 = 100\,mm$ and $r_2 = 20\,mm$ are pressed together by a load $F = 1500\,N$ per unit length as visible in Figure 37. The initial separation of the contacting surfaces $\boldsymbol{g}$ is simply given by the difference between the circular cross-sections defining the topography of the cylinders:

$$\boldsymbol{g} = \left[\sqrt{(r_1^2 - \boldsymbol{x^2})} - r_1\right] - \left[\sqrt{(r_2^2 - \boldsymbol{x^2})} + r_2\right] \tag{3.97}$$

where $\boldsymbol{x}$ spans the region $[-2{,}2]mm$ with a mesh size $\Delta x = 0.004\,mm$ and the material properties are listed in Table 3.

Table 3: Material properties for cylinder-cylinder contact

	Cylinder 1	**Cylinder 2**
Young modulus $\boldsymbol{E}$ [MPa]	210000	210000
Poisson coefficent $\boldsymbol{\nu}$ [-]	0,3	0,3

The initial gap function $\boldsymbol{h} = h_0 + \boldsymbol{g}$ and the deformed one at equilibrium $\boldsymbol{h} = h_0 + \boldsymbol{g} + \boldsymbol{\delta}$ are visible in Figure 38 along with the pressure distribution, while the same pressure distribution is visible with the deformed profiles $\boldsymbol{h_1}$ and $\boldsymbol{h_2}$ in Figure 39. Then, the applied load per unit length F has been varied from $100\,N$ to $1500\,N$. The maximum pressure values and the estimated contact area from the proposed method, have been compared to Hertz theory [106] and the relative percentage error between those values has been computed as

$$\%err = \frac{v_{proposed} - v_{Hertz}}{v_{Hertz}} \cdot 100 \tag{3.98}$$

where $v_{proposed}$ and v_{Hertz} are the peak pressure or the estimated contact area obtained with the respective methods. The peak pressure values and those percentage relative errors are visible in Figure 40 and denote a good accuracy, with an error generally lower than 1%,

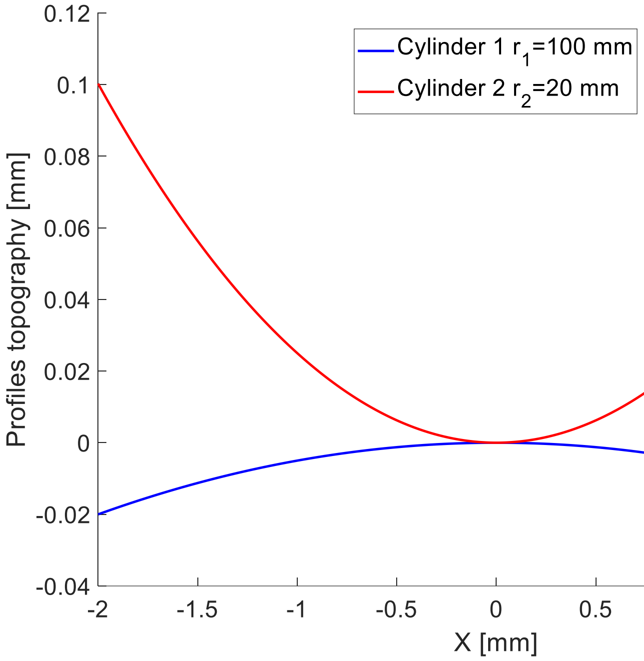

Figure 37: Cylinder topography close to the contact point

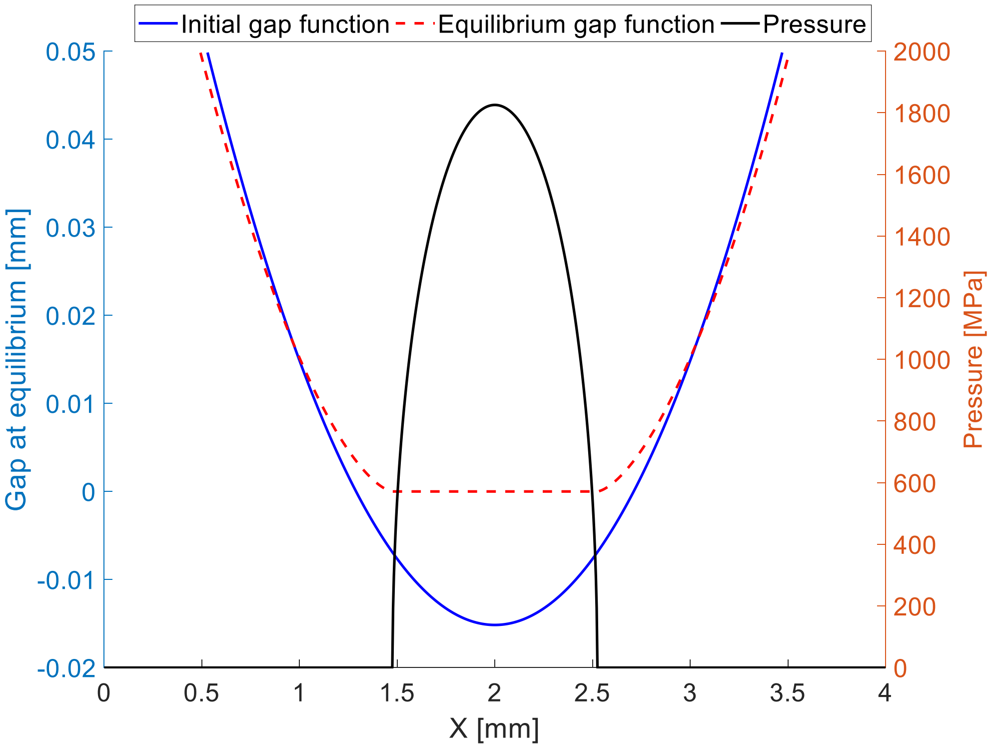

Figure 38: Rigid and deformed gap function and pressure distribution for cylinder-cylinder contact

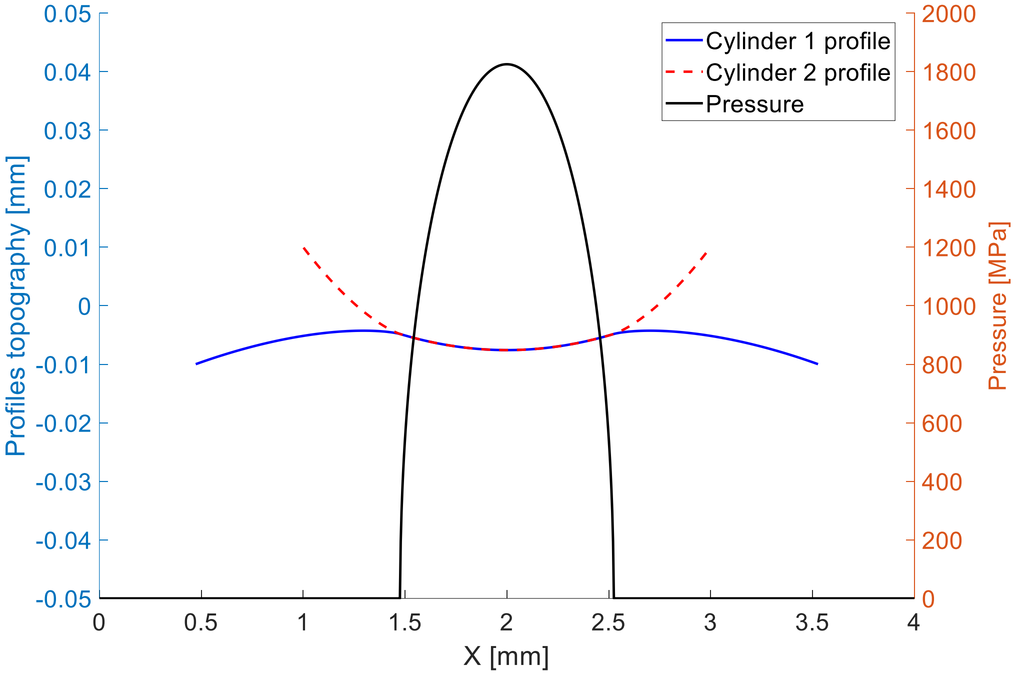

Figure 39: Deformed cylinders profiles and pressure distribution

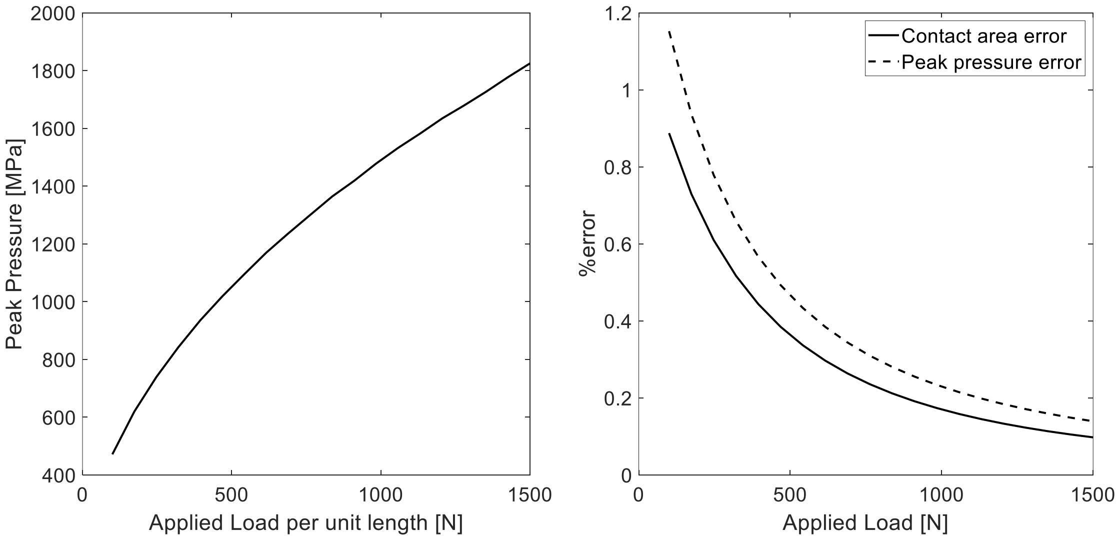

Figure 40: Peak pressure variation with increasing load (left), pressure and contact area relative percentage errors (right)

and a decreasing trend as the load increases since more contact points become part of the contact area. In such a simple example the estimation of the initial separation has been easy, but in order to apply the proposed method to gears with arbitrary profile modifications further steps are necessary. Since the equilibrium contact point is known trough the algorithm detailed in paragraph III.4, the mean tangent to both gear profiles is taken as the line where contact will happen. From this line normal lines are drawn and the intersection points, obtained with the line-to-line intersection method exposed in paragraph III.4, thus obtaining the initial separation as the normal distance between the intersection point and the mean common tangent at the equilibrium contact point. In the cylinder-cylinder contact

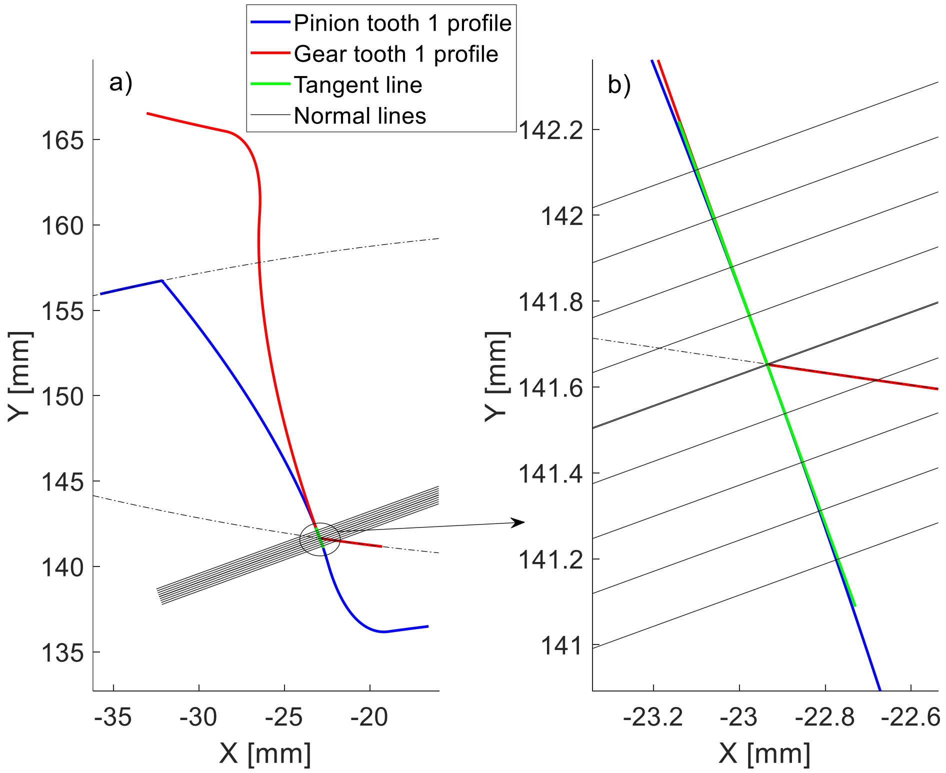

Figure 41: Initial profiles separation $\boldsymbol{g}$ estimation

the imposed rigid body indentation h_0 was intended as a vertical displacement of either cylinder towards the other. In the pinion-gear contact instead, in order to respect the meshing kinematics, a rotation is imposed as a rigid body rotation of the pinion towards the gear. Therefore, at each iteration it's needed to estimate again the initial separation $\boldsymbol{g_k}$

obtained through a tentative rigid body rotation $\theta_{0,k}$ for the k^{th} iteration computed in the same way as (3.90), hence

$$\theta_{0,k} = \theta_{0,k-1} + \frac{\theta_{0,k-1} - \theta_{0,k-2}}{f_{k-1} - f_{k-2}}(F - f_{k-1}) \tag{3.99}$$

In order to test the proposed method on gear applications where the non-Hertzian approach would show results that a Hertzian approach couldn't correctly analyze the contact is studied in the angular position when the tip corner of the gear comes in contact with the flank of the pinion as in Figure 41. The data of the gear pair considered is listed in Table 4. For a meaningful comparison only one teeth pair will be considered in contact in the position mentioned above and it will hence be applied with the full load $F = {}^{T}/_{r_b}$ in order to compare the pressure distribution and highlight the influence of the different profiles modifications. The positioning of the equilibrium contact point and hence of the contact line results from the iterative algorithm detailed in the previous paragraph. The deformed profiles and the pressure distribution of an unmodified gear pair is shown in Figure 42 and displays an

Table 4: Gear pair parameters

Parameter	Pinion	Gear
Number of teeth z [-]	28	28
Module m [mm]	3,175	3,175
Pressure angle α_P [°]	20	20
Face width b [mm]	6,35	6,35
Shaft radius r_s [mm]	20	20
Torque T [Nmm]	101686	
Young modulus E [MPa]	210000	210000
Poisson coefficent ν [-]	0,3	0,3

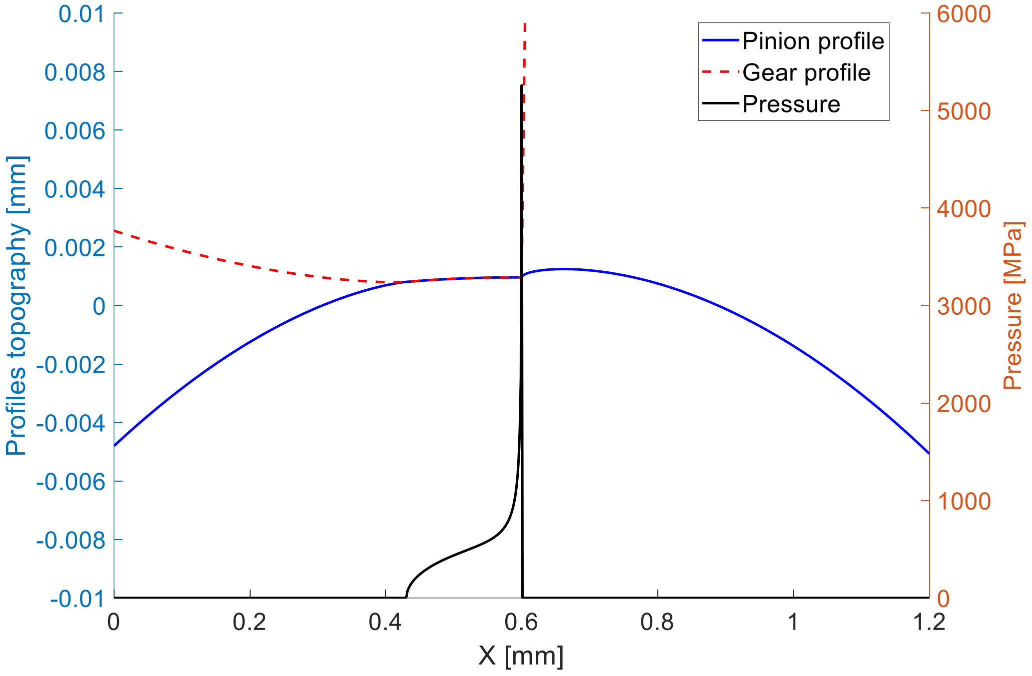

Figure 42: Gear tip corner contact without modifications

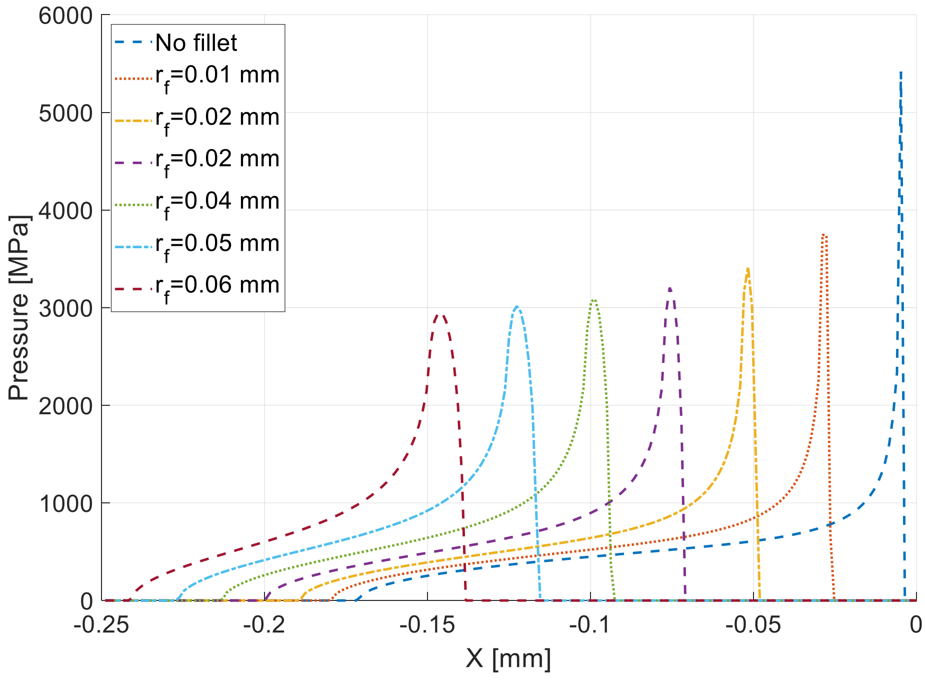

Figure 43: Effect of increasing tip fillet radius on tip corner contact

important pressure peak where the sharp corner of the driven gear contacts the flank of the pinion. Although the entity of the pressure peak is exaggerated by the fact that only a single teeth pair is considered taking the full load this is a better approach than considering the contact as Hertzian even in this case. In all upcoming graphs the 0 location of the x axis will be taken as the location of the corner contact point for an unmodified gear in order to also show the different location where contact happens. Indeed, in the industry particular care is taken to avoid this kind of interaction during meshing. Even if no special measure is taken a small tip fillet radius is present due to the machining process of the gears. The magnitude of the fillet tip radius r_f influences the maximum value of the pressure peak and also the shape of the pressure peak as shown in Figure 43, but this reduction is limited and increasing its value even further wouldn't decrease the overload by much. For this reason, and others as well such as minimizing the fluctuation of the STE and others, more elaborate tooth profiles modifications (TPM) are usually introduced during manufacturing. The TPM that can be studied in a 2D case are mainly the linear and parabolic tip relief modifications visible in

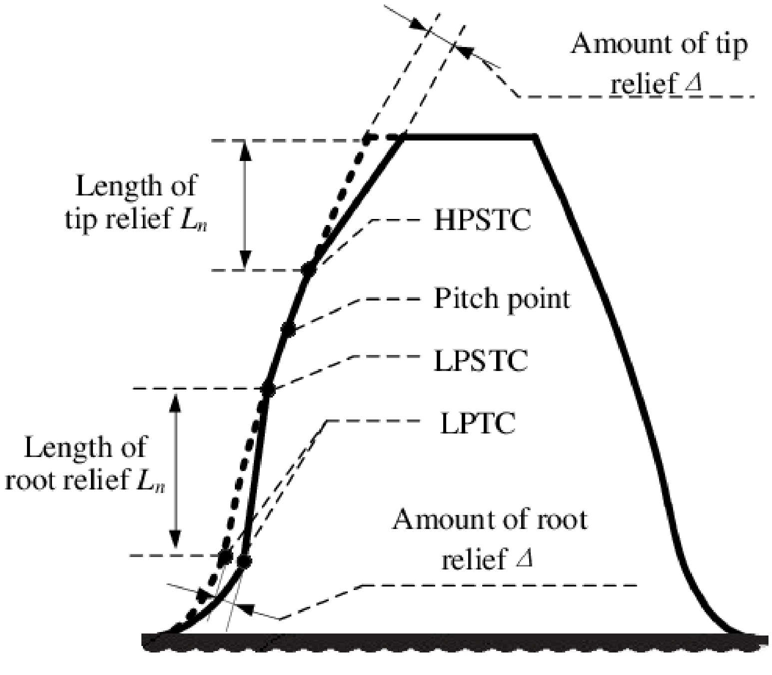

Figure 44: Tip relief nomenclature

Figure 44. For the linear tip relief, the modification is characterized by the length of the material to be removed l_t and by the maximum amount of material to be removed at the outer diameter Δ_t. As the name implies the amount of material removed decreases linearly from the maximum value Δ_t at the tip, to 0 after a length l_t. Similarly, but with a parabolic trend, the parabolic tip relief is characterized by the length of the material to be removed l_p and by the maximum amount of material to be removed at the outer diameter Δ_p. Various configurations will now be analyzed to highlight the effects of those modifications on the pressure distribution when tip corner contact occurs, first for the linear then for the parabolic tip relief. In Figure 45 the length of the material removed l_t is varied from 0.1 to $0.6\ mm$ with a constant $\Delta_t = 0.02\ mm$. It is evident that increasing the length reduces the maximum pressure experienced by the flank, but usually other considerations have to be taken into account since this increase would retard the approach of the profiles while anticipating the release condition thus increasing the single tooth contact region, which is not always desirable since it reduces the contact ratio. In Figure 46 the Δ_t is varied from 0.05 to $0.3\ mm$ with a constant $l_t = 0.4\ mm$. With those values as the material removed increases the

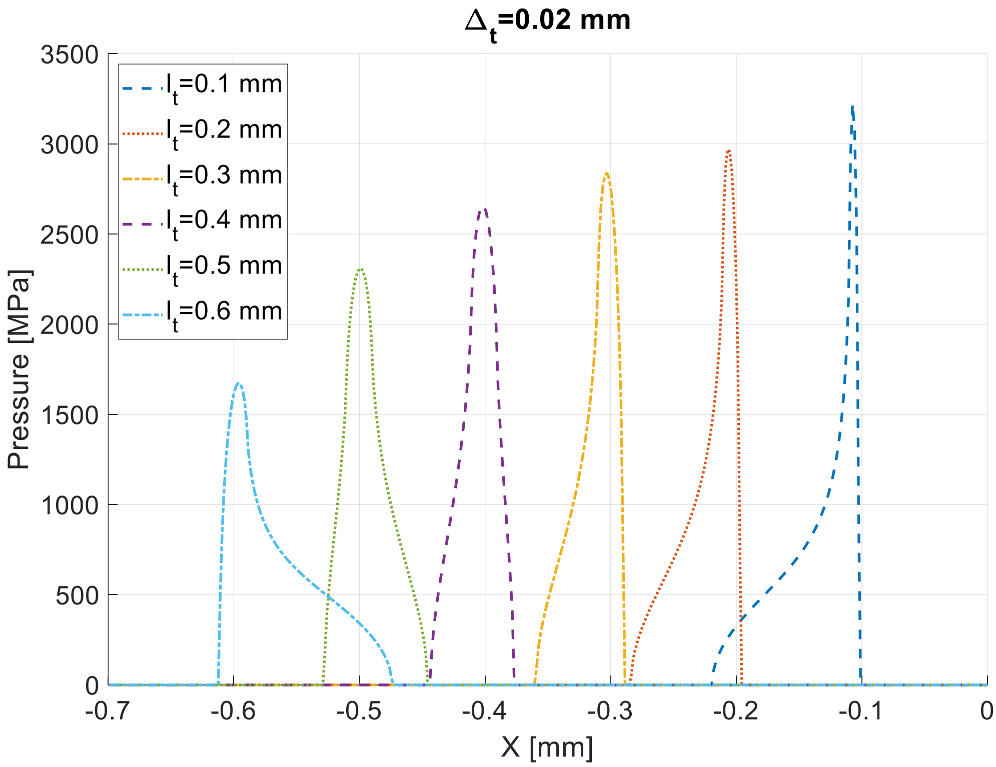

Figure 45: Effect of the increase in length l_t of linear tip relief

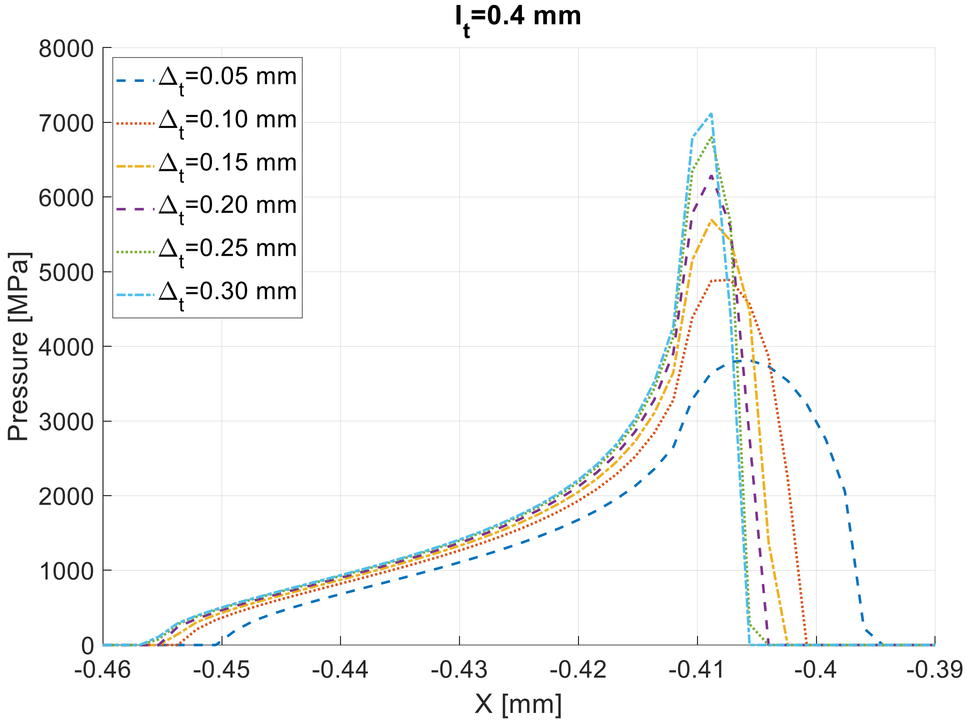

Figure 46: Effect of the increase in depth Δ_t *of linear tip relief*

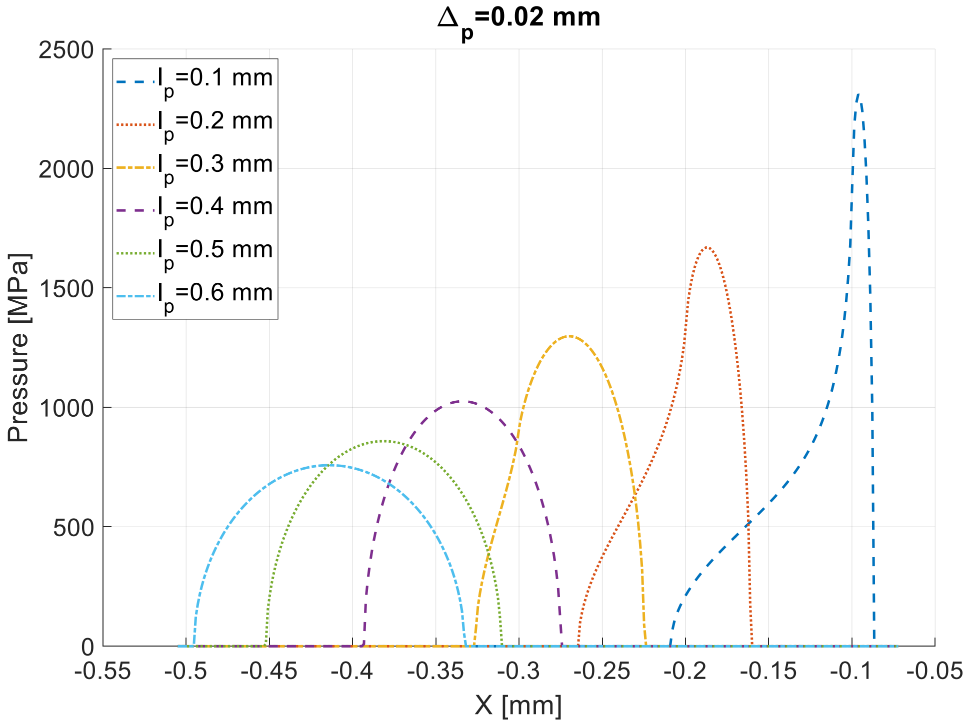

Figure 47: Effect of the increase in length l_p *of parabolic tip relief*

maximum pressure increases since a sharp corner is created because a discontinuity in the curvature of the profile is created and this affects the pressure distribution. Regarding the parabolic tip relief in Figure 47 the length of the material removed l_p is varied from 0.1 to $0.6\ mm$ with a constant $\Delta_p = 0.02\ mm$. It is evident that increasing the length reduces the maximum pressure experienced by the flank up to a point where the distribution is almost Hertz-like without any asymmetric pressure peak, but again considerations on the contact ratio must be taken into account. In Figure 48 the Δ_p is varied from 0.05 to $0.3\ mm$ with a constant $l_p = 0.4\ mm$. The parabolic distribution doesn't cause a discontinuity in the profile of the teeth flank, but however less material is left in the contact zone and therefore a pressure peak becomes progressively more noticeable as the amount of material removed is increased. In the tip corner contact condition, the non-Hertzian nature of this kind of contact is extremely evident, but when the corner is not involved anymore as the meshing process continues it becomes less important. However, this is approach is still more accurate since it considers the real curvature of the involute flank even considering arbitrary modifications and not just the osculating radius at the contact point with constant curvature as in classical analysis. More pressure distribution maps, with the real load distribution

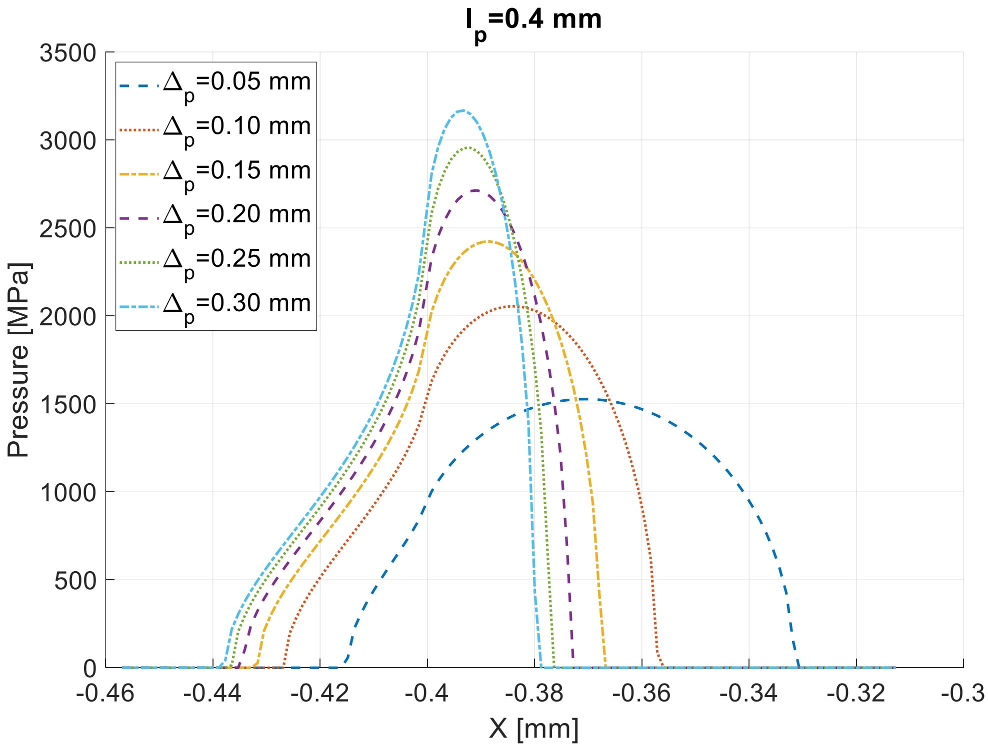

Figure 48: Effect of the increase in depth Δ_p of linear tip relief

among the teeth in contact will be shown in the next paragraph, and the pressure peaks as the teeth come and leave contact will still be evident in the real meshing conditions.

III.6 Results

In this section the results of the Semi Analytical (SA) approach, including the iterative process and the detailed contact analysis, will be shown. The final expression for the STE is finally

$$STE = \theta_g r_{b,g} - \theta_p r_{b,p} \tag{3.100}$$

where the subscript p indicates the pinion rotation, while g indicates the driven gear. The rotations θ_g and θ_p are measured at the point of maximum displacement in the contact area from the contact analysis, therefore including also the elastic deflection $\boldsymbol{\delta_p}$ and $\boldsymbol{\delta_g}$, and taken as the maximum value between the different teeth pairs in contact, therefore for LCRG

$$\begin{aligned} \theta_g &= \max\left(\theta_{g,1}, \theta_{g,2}\right) \\ \theta_p &= \max\left(\theta_{p,1}, \theta_{p,2}\right) \end{aligned} \tag{3.101}$$

and for HCRG

$$\begin{aligned} \theta_g &= \max\left(\theta_{g,1}, \theta_{g,2}, \theta_{g,3}\right) \\ \theta_p &= \max\left(\theta_{p,1}, \theta_{p,2}, \theta_{g,3}\right) \end{aligned} \tag{3.102}$$

The first comparison of the results from the proposed SA model is against a 2D plane elements FE model from Ansys. In Ansys model only three teeth have been modeled in order to reduce the computational costs since a very refined mesh has been adopted for the contacting flanks of the teeth, which have a mesh size of $0.1\ mm$ to have correct contact results, while the mesh is coarser elsewhere. Quadratic 8-node shell elements (PLANE183) have been used to discretize the geometry, while the deformable contact pair is described by pairs of frictionless contact-target elements (CONTA172-TARGE169) for 2D line contact. The geometrical and material properties are listed in Table 2. The inner diameter of the pinion

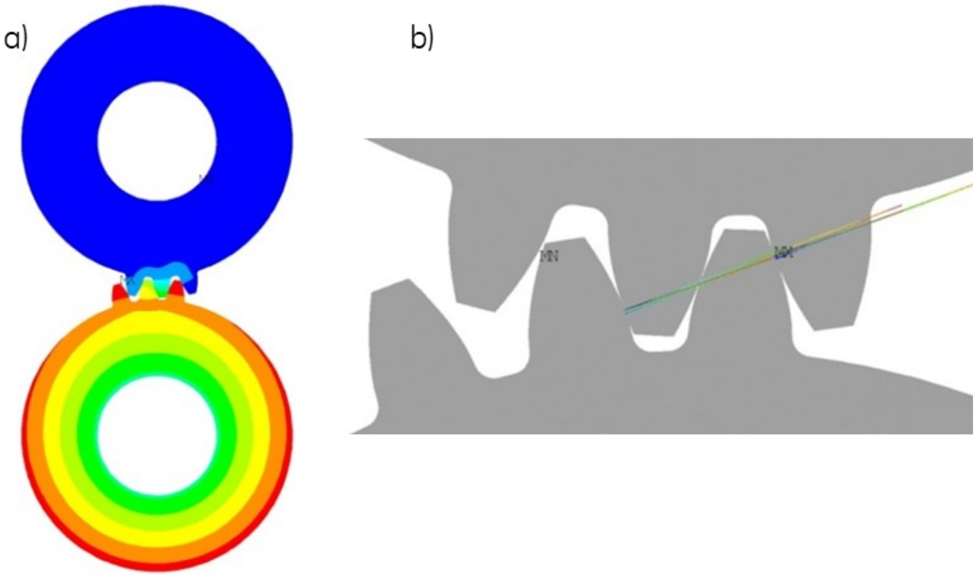

Figure 49: Details of Ansys model, displacements distribution (a) and contact pressures (b)

gear is connected through rigid body connection RBE2 elements to a central node where the torque is applied, and the STE is recorded. The inner diameter of the driven gear is constrained in the same way, but the central node is constrained against all displacements and rotations. The obtained results for one mesh cycle and the comparison against the current method are visible in Figure 50. The agreement between the two is good in terms of overall trend, while at the single contact a difference of $0.3e-4\ rad$ is present. Ansys results are not symmetric in the mesh cycle due to the lack of adjacent teeth and for the same reason the approach of the following tooth after single contact is slightly retarded with respect to the SA model. The second comparison that has been made has been against the results coming from the Dynamic Analysis of Spur Gear Transmissions (DANST) code from NASA [111]. The tested gears have parameters listed in Table 2 and have been analyzed for different levels of torque ranging from 100 to $900\ lb-in$ for one mesh cycle subdivided in 85 intermediate angular positions and the results are visible in Figure 51. The torque values correspond to a range $11.3-101.7\ Nm$. Again, the results compare really well except for an upward shift increasing with the torque applied which is constant throughout the meshing process and is probably caused by differences in the formulation employed to model the torsional displacement of the gear body. The two models agree particularly well in the determination of the reduction of the single contact portion of the engagement. In both comparisons no TPM was applied to the gears, but the effect to various levels of torque, ranging from 25.4 Nm

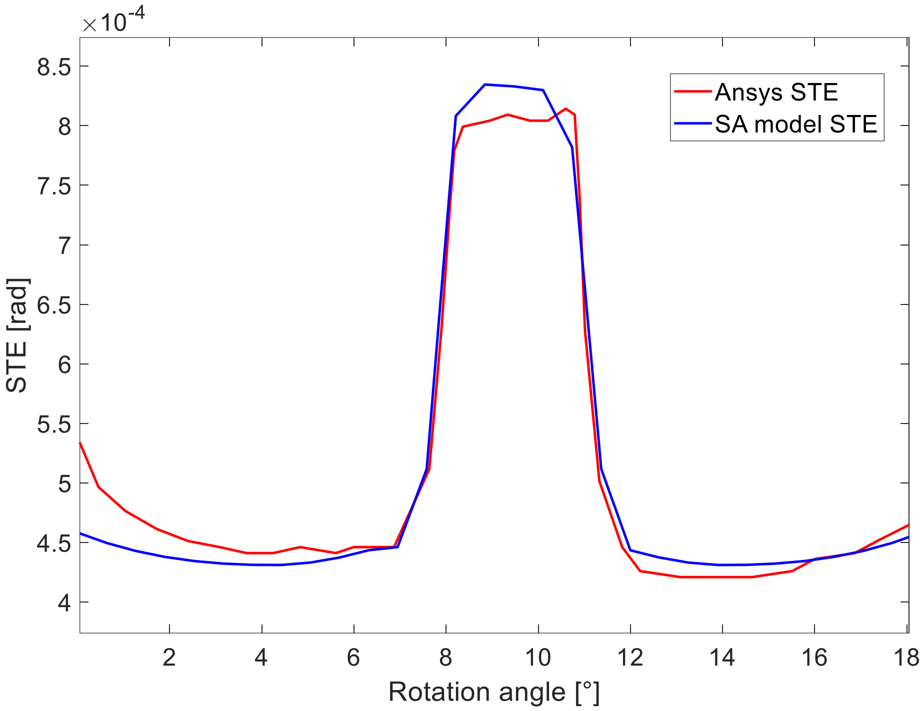

Figure 50: STE results from Ansys and Semi Analytical model

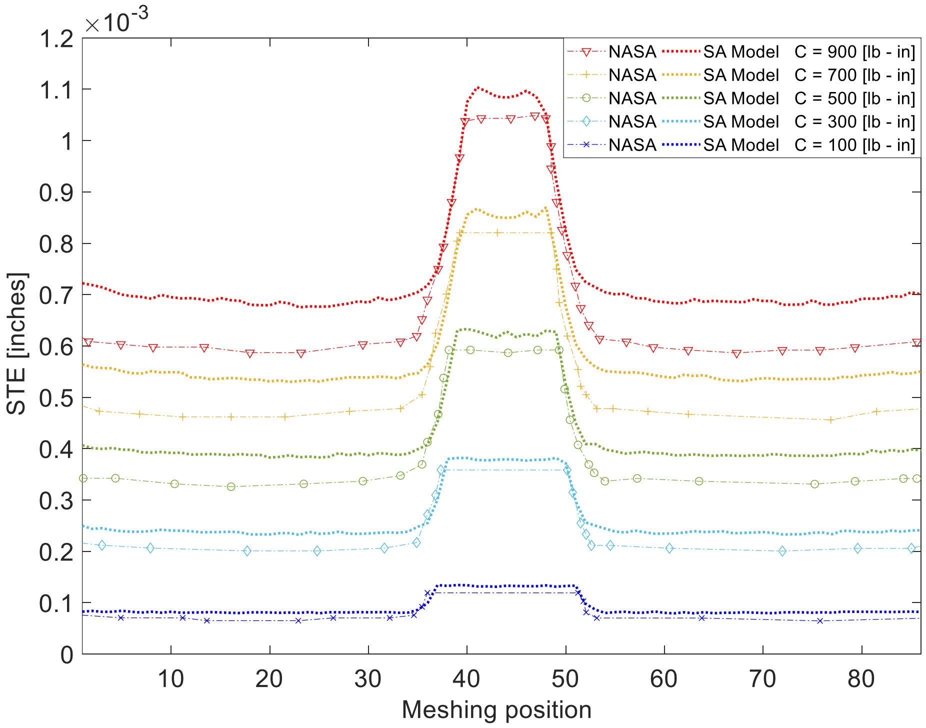

Figure 51: Comparison of NASA DANST results and SA model for several torques

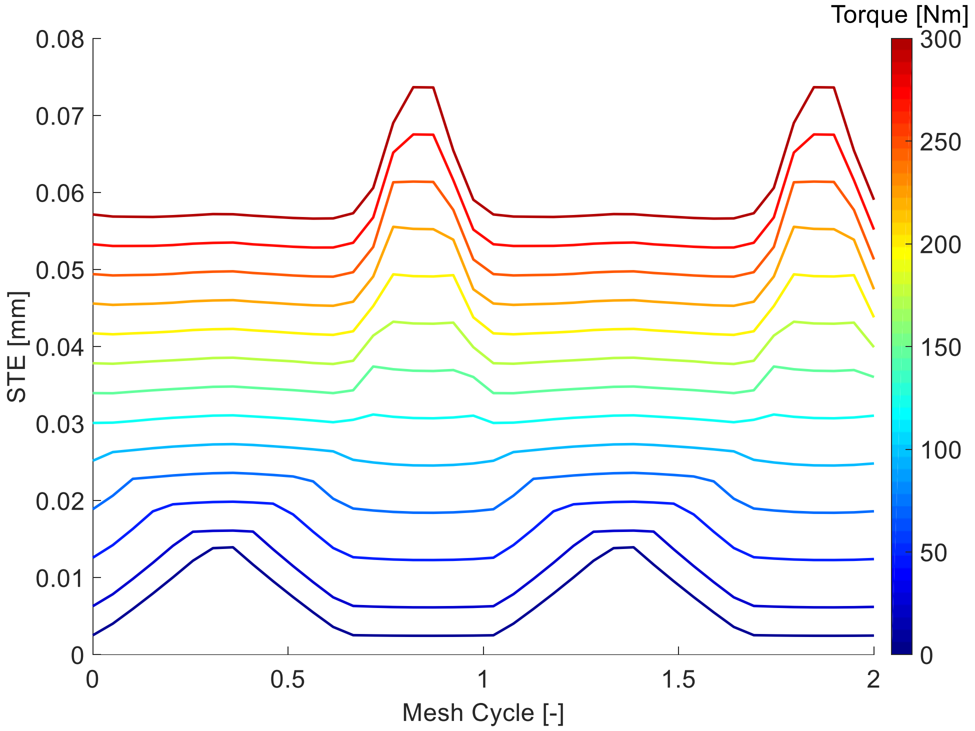

Figure 52: Effect of torque on gears with linear tip relief

to 305.1 Nm, for the same gears tested on the NASA code but this time with a linear tip relief ($\Delta_t = 0.0032\ mm, l_t\ = 0.96\ mm$) symmetric on both gears are analyzed in Figure 52 over two mesh cycles. As the torque increases also the mean value of the STE increases, but the region of single tooth contact strongly reduces, closely approaching the value of 2 for the highest level of torque. In Figure 53 a single STE for the same geometry under a torque of $101.7\ Nm$ is visible alongside with the load sharing coefficients for the different engaging teeth pairs. In this figure (Figure 53) and in the following ones the solid lines represents the load sharing coefficient for the main teeth pair C_1, while the dashed lines for the pair leaving contact C_0 and the dash-dot lines for the pair coming into contact C_2, as represented in Figure 29. The pressure distribution along the entire mesh process in these conditions is visible Figure 54 and displays the pressure peak as expected and discussed in the previous paragraph. The maximum pressure value is a lot lower than what visible in Figure 42 since in the present case the load acting at the beginning of contact is lower. However, this condition could still cause damage to the flank since the maximum pressure value at the beginning of contact is equal to $1088\ MPa$, which is larger than the maximum value in the single contact zone of the mesh cycle which is $763.3\ MPa$, and is usually the value for which gears are

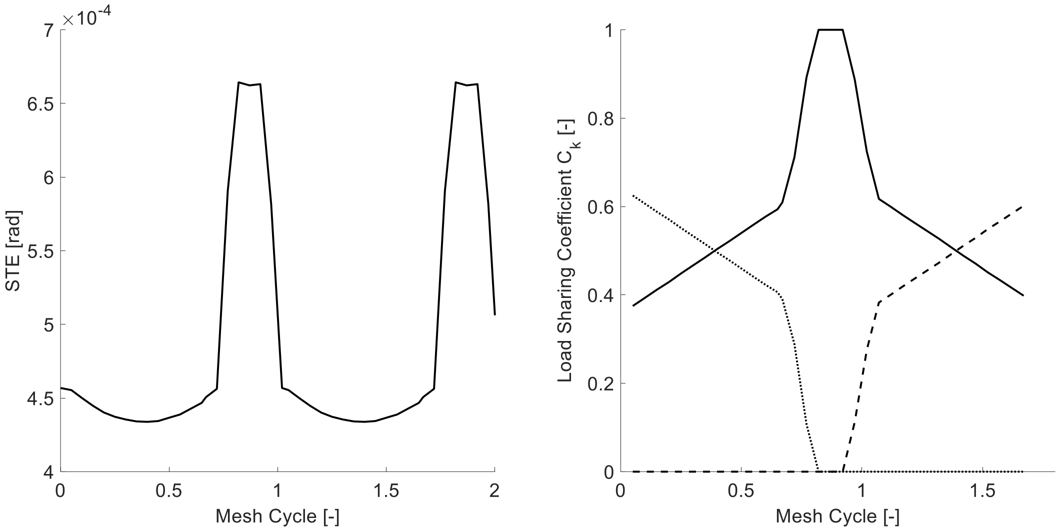

Figure 53: STE and load sharing coefficients without TPM

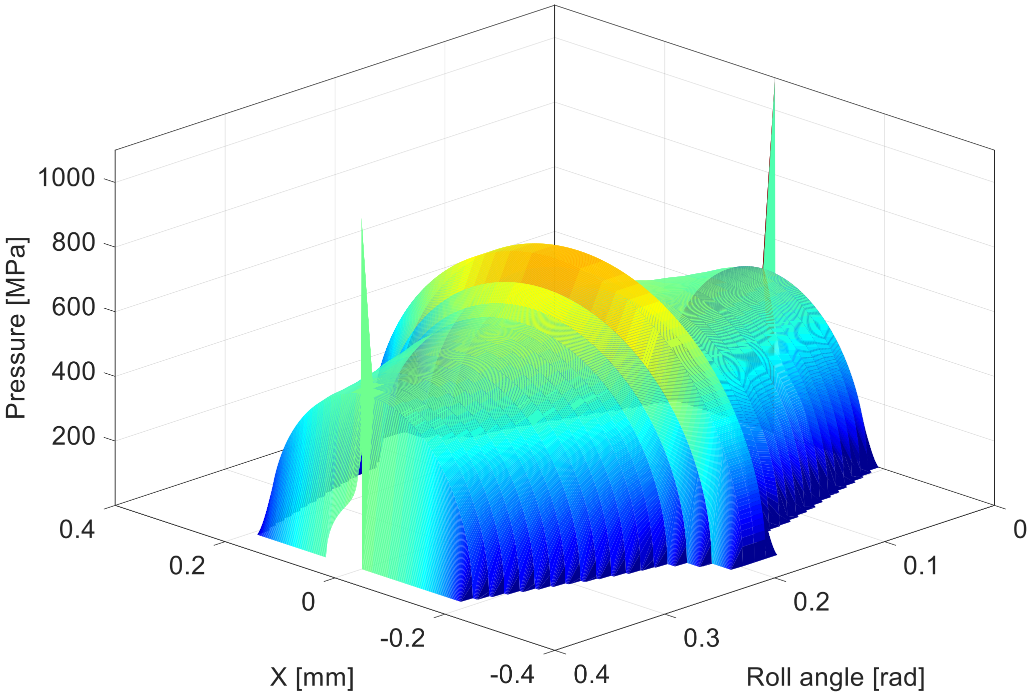

Figure 54: Pressure distribution along the entire mesh process without TPM

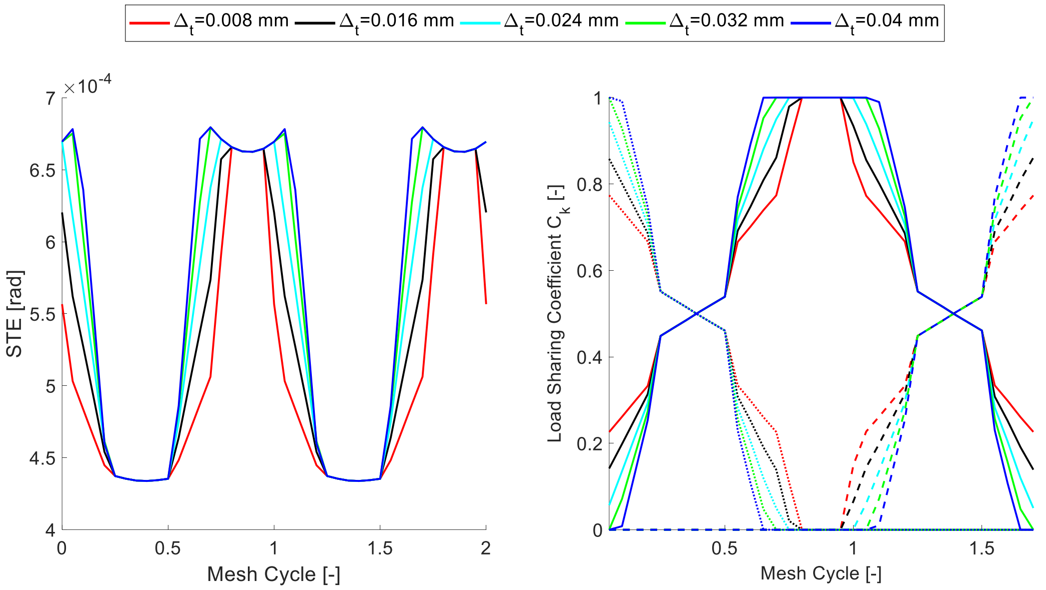

Figure 55: Effect of the variation of the amount of the material removed Δ_t in linear tip relief TPM $l_t = 0.96\ mm$

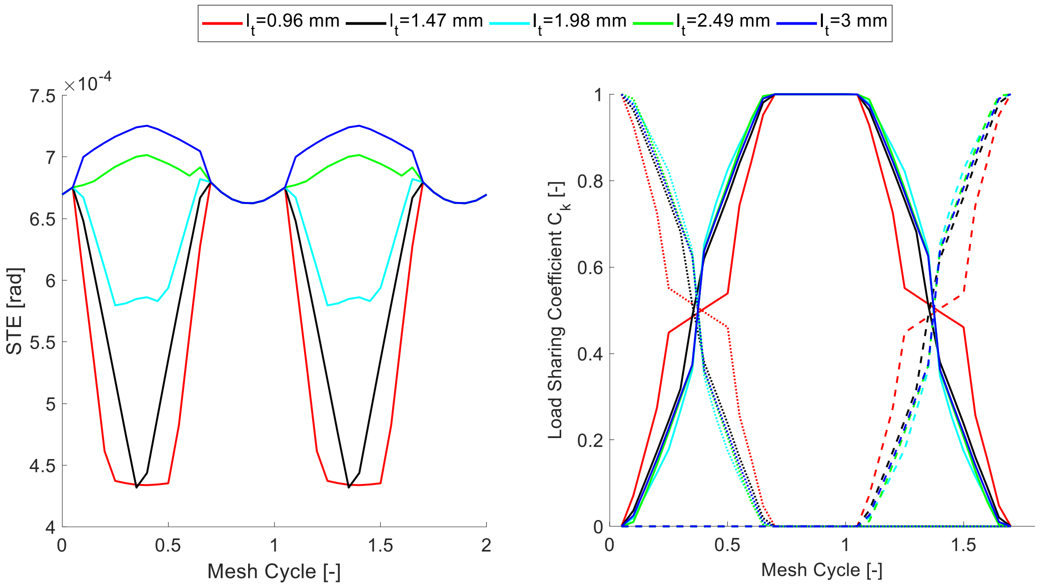

Figure 56: Effect of the variation of the length of the material removed l_t in linear tip relief TPM $\Delta_t = 0.032\ mm$

designed for. If not accounted for, this pressure peak could cause for example pitting on its surface and must hence be avoided. The effect of the linear tip relief is now analyzed. In Figure 55 the effect of the amount of material removed Δ_t is visible for a fixed length of $l_t = 0.96\ mm$.

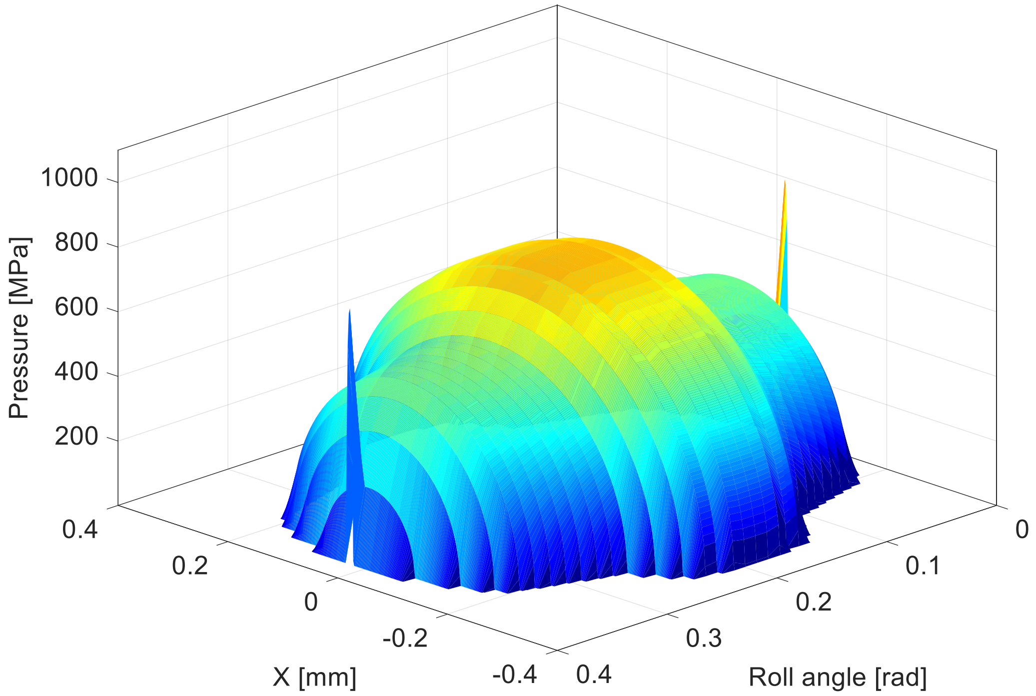

Figure 57: Pressure distribution along the entire mesh process with linear tip relief $l_t = 0.96\ mm\ \Delta_t = 0.032\ mm$

The values are varied from a minimum of $0.01\ mm$ up to $0.04\ mm$. The main effect is that, as the material removed increases, the length of the single contact zone increases since the teeth pair engage later and leave contact sooner than normal, effectively decreasing the expected contact ratio and leaving the peak to peak value of the STE unchanged. Also, the load sharing coefficient doesn't improve since the passage from double to single contact becomes even more abrupt as the material removed increases, while in the double contact zone the values remain unchanged. In Figure 56 the effect of the length of the linear tip relief is analyzed alongside with the changes it creates in the load sharing coefficients. The length of the material removed l_t is varied from $0.96\ mm$ up to $3\ mm$ and in this case some improvements on both the STE and the load sharing coefficients can be appreciated. Indeed, after a certain value the minimum value of the STE can be seen to increase thus effectively reducing its peak to peak value and at the same time smoothing the transition between the teeth since the fraction of the total load they experience changes without evident discontinuities. In Figure 57 the contact pressure on the flank during the mesh process can be observed for a linear tip relief TPM with $\mathrm{l_t} = 0.96\ \mathrm{mm}$ and $\Delta_\mathrm{t} = 0.032\ \mathrm{mm}$ and it can be

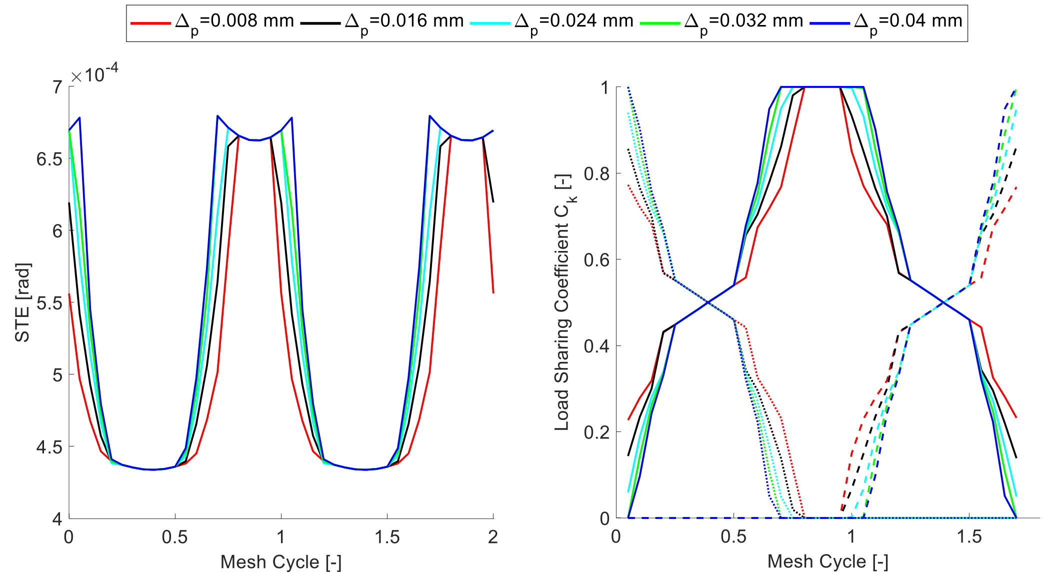

Figure 58: Effect of the variation of the amount of the material removed Δ_p *in linear tip relief TPM* $l_p = 0.96\ mm$

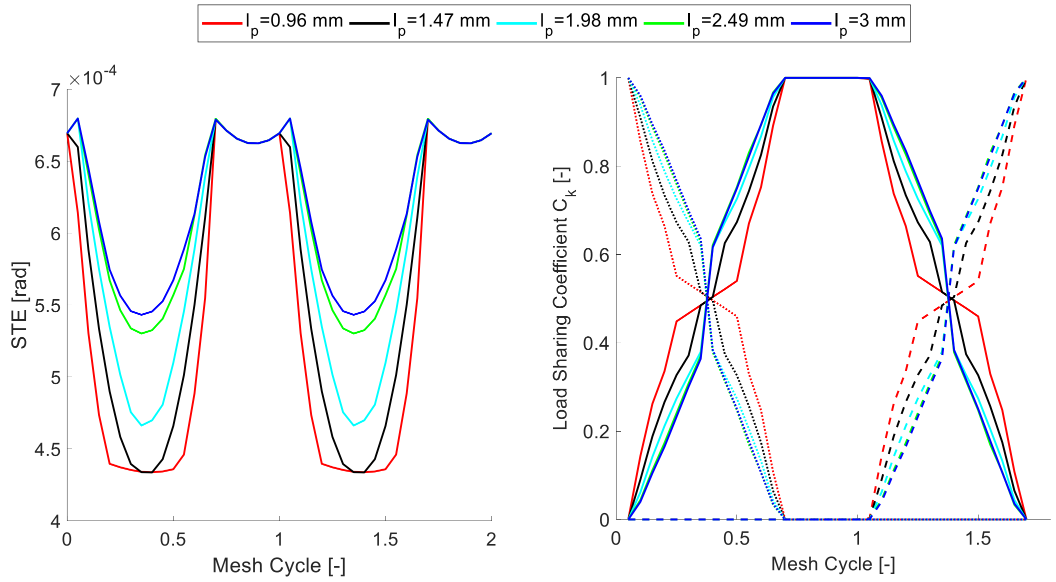

Figure 59: Effect of the variation of the length of the material removed l_p *in linear tip relief TPM* $\Delta_p = 0.032\ mm$

seen that thanks to this modification the pressure peak as the tooth comes into contact is reduced with respect to the unmodified case as in Figure 54. The peak value is equal to $793.1\ MPa$ which is still higher than the maximum pressure in the single contact zone of the mesh cycle but is less dangerous than the previous case, since it's only $29{,}8\ MPa$ higher than the design value. In Figure 58 the effect on the STE and the load sharing coefficients of the amount of material removed in a parabolic tip relief is visible. Its effects are similar to those of the linear tip relief since its only effect is to increase the fraction of the mesh cycle during which single contact occurs. The peak to peak value of the STE remains constant and the load sharing variation doesn't show evident beneficial effects. In Figure 59 the effect of the length of the parabolic tip relief is analyzed and in this case, similarly to what happens for the linear tip relief, some improvements can be seen. As the length of the material removed increase the minimum value of the STE increases and therefore the peak to peak ratio decreases. At the same time, the variation of the load sharing coefficients

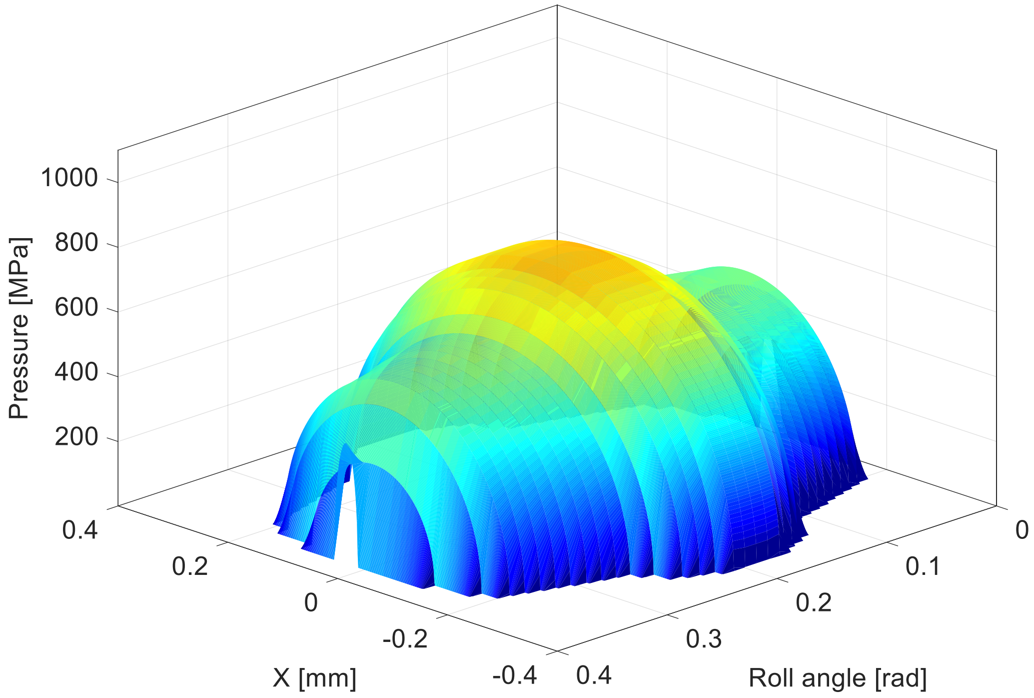

Figure 60: Pressure distribution along the entire mesh process with parabolic tip relief $l_p = 0.96\ mm\ \Delta_p = 0.032\ mm$

become smoother as the variation becomes more gradual. The effect of this modification is lower with respect to the linear tip relief and indeed for the same values of modification the reduction in the peak to peak value of the STE is lower. This is due to the different geometry of the two kind of modifications, since for the same values the volume effectively removed is higher for the linear tip relief, since the amount of material removed increases faster than with respect to the parabolic one. However, the pressure distribution along the entire mesh process for a gear modified with parabolic tip relief with $\mathrm{l_p} = 0.96\ \mathrm{mm}$ and $\Delta_\mathrm{p} = 0.032\ \mathrm{mm}$ can be seen in Figure 60 and this kind of modification is evidently more effective in reducing the pressure peak as the flanks of the gears come into contact. Indeed, the peak is almost completely eliminated ($370.4\ MPa$) and is just slightly higher than the pressure value when the tip corner contact effect disappears ($331.1\ MPa$), but still less than half of the design value in the single tooth contact portion of the mesh cycle and therefore poses no dangers to the integrity of the flank surface. More results and comparisons will be show in chapter V where the experimental test bench and the tests conducted on it will be discussed. The results given here are just examples of the capabilities of the proposed model, but it is clear that in order to achieve a good gear design those analyses alone are not enough. Indeed, a combinatory analysis taking into account the design loads and the possible combination of the macro (module, pressure angle, profile shift, etc.…) and micro (tip or root relief, kind of TPM, length and amount of material removed) have to be considered at the same time so as to create a response surface in which the effects of all parameters are linked and can therefore be used to estimate the better combination to improve the reliability, wear resistance, fatigue life or noise related issues depending on the objective or objectives of the analysis. This optimization approach, common in literature ([112], [113], [114]), is not in the scope of the current work but will be object of future research.

IV. 3D teeth contact analysis

IV.1 Introduction

In this chapter the extension to three dimensions of the previously presented model will be discussed. The needed modifications to the calculation of the gear's deflections will be shown first to include the effects of the eventual axial loads previously neglected allowing the analysis of helical gears or gears with arbitrary profile modifications along the facewidth. Then the updated procedure for the iterative contact point detection will be presented since the surface of the teeth will be considered as a 3D surface rather than a 2D line. Next, two approaches of frictionless rough contact models will be presented and applied against Hertz's theory and results available in literature in the 3D domain. The first model will be only applicable to equilateral triangles, while the second one is valid for any triangle shape. However, the calculations of the influence coefficients of the second model is more cumbersome and it offers only limited advantages since a representation of the contact plane is possible most of the time with equilateral triangles. Therefore, the second model will be only applied when needed. Finally results will be shown for both spur and helical gears in terms of STE and load sharing coefficients and the effects of profiles modifications will be discussed also in terms of pressure distributions along the flank.

IV.2 Operative deflections and iterative contact point detection

In order to take into account the gears as three dimensional bodies, which is necessary for helical gears, or for spur gears with profiles modifications over the facewidth rather than just uniform tip profile modifications, several changes are needed since in Cornell's models [21] only the planar behavior is considered. Indeed, in his model all deflections were computed in the direction of the application of the load for spur gears and as such it wouldn't be possible to include the effects of the helix angle and loads in the axial direction with just that approach. For simplicity and to keep the whole approach similar to the previously presented model, it was chosen to keep representing the teeth of the gears as clamped-free beams sectioned in thin slices as in Figure 16. Furthermore, the formulation of the root fillet influence on the displacements of the involute portion of the teeth will be dropped and the entire tooth, from the root to the tip radius, will be treated as a series of connected beam elements. To model each of the slices a Timoshenko beam element is computed as [115]

$$\boldsymbol{K_e} =$$

$$= \begin{bmatrix}
\frac{E_bA_b}{I_b} & 0 & 0 & 0 & 0 & 0 & -\frac{E_bA_b}{I_b} & 0 & 0 & 0 & 0 & 0 \\
0 & 12\frac{E_bI_{b,z}}{l_b^3}\chi_y & 0 & 0 & 0 & 6\frac{E_bI_{b,z}}{l_b^3}\chi_y & 0 & -12\frac{E_bI_{b,z}}{l_b^3}\chi_y & 0 & 0 & 0 & 6\frac{E_bI_{b,z}}{l_b^3}\chi_y \\
0 & 0 & 12\frac{E_bI_{b,y}}{l_b^3}\chi_z & 0 & -6\frac{E_bI_{b,y}}{l_b^3}\chi_z & 0 & 0 & 0 & -12\frac{E_bI_{b,y}}{l_b^3}\chi_z & 0 & -6\frac{E_bI_{b,y}}{l_b^3}\chi_z & 0 \\
0 & 0 & 0 & \frac{G_bJ_b}{l_b} & 0 & 0 & 0 & 0 & 0 & -\frac{G_bJ_b}{l_b} & 0 & 0 \\
0 & 0 & -6\frac{E_bI_{b,y}}{l_b^3}\chi_z & 0 & \frac{E_bI_{b,y}}{l_b^3}(3\chi_z+1) & 0 & 0 & 0 & 6\frac{E_bI_{b,y}}{l_b^3}\chi_z & 0 & \frac{E_bI_{b,y}}{l_b^3}(1-3\chi_z) & 0 \\
0 & 6\frac{E_bI_{b,z}}{l_b^3}\chi_y & 0 & 0 & 0 & \frac{E_bI_{b,z}}{l_b^3}(3\chi_y+1) & 0 & -6\frac{E_bI_{b,z}}{l_b^3}\chi_y & 0 & 0 & 0 & \frac{E_bI_{b,z}}{l_b^3}(1-3\chi_y) \\
-\frac{E_bA_b}{I_b} & 0 & 0 & 0 & 0 & 0 & \frac{E_bA_b}{I_b} & 0 & 0 & 0 & 0 & 0 \\
0 & -12\frac{E_bI_{b,z}}{l_b^3}\chi_y & 0 & 0 & 0 & -6\frac{E_bI_{b,z}}{l_b^3}\chi_y & 0 & 12\frac{E_bI_{b,z}}{l_b^3}\chi_y & 0 & 0 & 0 & -6\frac{E_bI_{b,z}}{l_b^3}\chi_y \\
0 & 0 & -12\frac{E_bI_{b,y}}{l_b^3}\chi_z & 0 & 6\frac{E_bI_{b,y}}{l_b^3}\chi_z & 0 & 0 & 0 & 12\frac{E_bI_{b,y}}{l_b^3}\chi_z & 0 & 6\frac{E_bI_{b,y}}{l_b^3}\chi_z & 0 \\
0 & 0 & 0 & -\frac{G_bJ_b}{l_b} & 0 & 0 & 0 & 0 & 0 & \frac{G_bJ_b}{l_b} & 0 & 0 \\
0 & 0 & -6\frac{E_bI_{b,y}}{l_b^3}\chi_z & 0 & \frac{E_bI_{b,y}}{l_b^3}(1-3\chi_z) & 0 & 0 & 0 & 6\frac{E_bI_{b,y}}{l_b^3}\chi_z & 0 & \frac{E_bI_{b,y}}{l_b^3}(3\chi_z+1) & 0 \\
0 & 6\frac{E_bI_{b,z}}{l_b^3}\chi_y & 0 & 0 & 0 & \frac{E_bI_{b,z}}{l_b^3}(1-3\chi_y) & 0 & -6\frac{E_bI_{b,z}}{l_b^3}\chi_y & 0 & 0 & 0 & \frac{E_bI_{b,z}}{l_b^3}(3\chi_y+1)
\end{bmatrix} \tag{4.1}$$

Where the thickness of each slice l_b is given by the distance between two consecutive points, s_i and s_{i+1}, along the X axis

$$l_b = X_{s_{i+1}} - X_{s_i} \tag{4.2}$$

The moment of inertia of the section in the Z direction is obtained as

$$I_{b,z} = \frac{4b}{3} \frac{\left(Y_{s_{i+1}} \cdot Y_{s_i}\right)^3}{Y_{s_{i+1}}^3 + Y_{s_i}^3} \tag{4.3}$$

while the one in the Y direction takes also into account the eventual presence of a helix angle β and hence is

$$I_{b,y} = \frac{1}{3}\left(\frac{b}{\cos(\beta)}\right)^3 Y_{s_i} \cos(\beta) \frac{Y_{s_{i+1}}}{Y_{s_{i+1}} + Y_{s_i}} \tag{4.4}$$

Lastly, the polar moment of inertia can be computed as

$$J_b = \frac{1}{3}\psi_b b h^3 \tag{4.5}$$

Where $\psi_b = 3\psi$ interpolating the data from Table 5 with $X_{s_{i+1}} - X_{s_i} \geq Y_{s_{i+1}} - Y_{s_i}$ using a piecewise cubic Hermite interpolating polynomial ("pchip") [116] [117].

Table 5: Data to obtain ψ_b

$\frac{\left(X_{s_{i+1}} - X_{s_i}\right)}{Y_{s_{i+1}} - Y_{s_i}}$	1	1.2	1.5	2	2.5	3	4	5	10	100
ψ_b	0.141	0.166	0.196	0.229	0.249	0.263	0.281	0.292	0.313	0.333

In Timoshenko beam theory shear correction factors in the Y and Z direction, χ_y and χ_z, are introduced to correctly take into account the shear effect which is not present in Euler-Bernoulli beam theory and those are computed for the Y direction as

$$\chi_y = \frac{12E_b I_{b,z}}{G_b l_b^2 \, {A_i}/{k_{b,y}}} \tag{4.6}$$

And for the Z direction

$$\chi_z = \frac{12E_b I_{b,y}}{G_b l_b^2 \, {A_i}/{k_{b,y}}} \tag{4.7}$$

Both χ_y and χ_z depend on shear correction factors $k_{b,y}$ and $k_{b,z}$ which depend of the Poisson's ratio of the material ν and for solid rectangular sections can be calculated as [118]

$$k_{b,y} = k_{b,z} = \frac{10(1+\nu)}{12+11\nu} \tag{4.8}$$

Once all elemental $\boldsymbol{K_e}$ are computed they are assembled into the global stiffness matrix $\boldsymbol{K}$ as per standard FEM procedures [119] and the rows and columns corresponding to the node at the base of the tooth are removed to represent the clamped constrain to be applied to obtain the correct representation. In this case the load and the corresponding force vector will be dependent on the location of the contact point which now lies in the 3D space. The points of the flank of each considered tooth are assembled to form a triangulated surface for both the pinion and the gear, as shown in Figure 61 for a single teeth pair and in Figure 62 for all teeth considered. The triangulation in Figure 61 refers to a gear pair with a helix angle $\beta = 30°$ and a facewidth $b = 10\ mm$, but the size of the triangles is actually much larger than what is used in the calculations, because otherwise it wouldn't be recognizable in the figure. In Figure 62 the triangles lines have been removed altogether for the same reason. In order to find the actual contact point at each iteration the deformed surfaces of the flanks of the pinion are rotated towards those of the driven gear and the resulting intersection points are found through the application of the Möller –Trumbore ray-triangle intersection algorithm [120] in which each triangle edge of each surface is treated as an infinitely long ray and an intersection is sought with the triangular faces of the opposite surface. If an intersection is found between the infinitely long ray and the surface of one of the triangles it is checked if it is a true intersection by checking if the location of the intersection point p_c lies between the endpoints of the considered edge (p_1, p_2) by

$$\|p_c - p_1\| + \|p_c - p_2\| = \|p_c - p_1\| \tag{4.9}$$

Usually this kind of ray tracing is computationally heavy and almost unusable without complex and specific hardware GPU acceleration, but its speed can be extremely improved by using an octree data structure [121] [122] to partition the triangles in which the groups of triangles are recursively subdivided in eight bins thus greatly reducing the computational effort by a huge amount and making it usable in an iterative process such as the one being

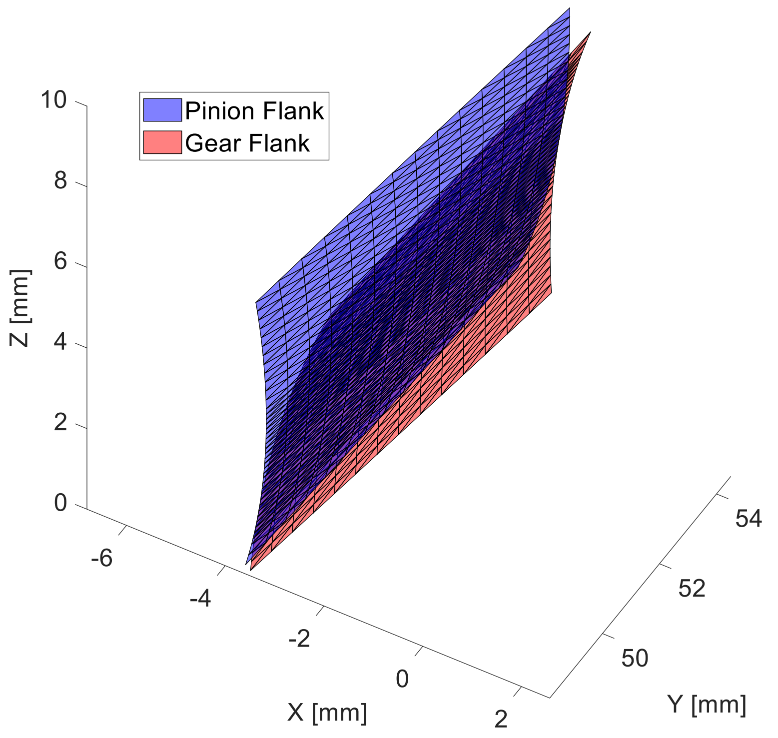

Figure 61: Pinion and gear flanks triangulated surfaces

presented without slowing it down. Once the coordinates of the contact point $\boldsymbol{O} = \{x_{cp}, y_{cp}, z_{cp}\}^T$ are known as visible in Figure 63 the normal vector to the contact point can be computed for each tooth pair from the closest point in the triangulation A, B, C and D visible in Figure 64. This is needed to compute the actual pressure and helix angle, μ_α and μ_β respectively, which will be in general different from the rigid counterparts α and β due to teeth deflections. Since all triangles considered ($\widehat{OAB}$, $\widehat{OBC}$, $\widehat{OCD}$, $\widehat{ODA}$) will have in general a different normal vector the average of them is found by constructing an orthogonal reference frame with origin in the contact point. The vector defining the local X axis is defined by

$$\boldsymbol{v_x} = \boldsymbol{u_j} - \boldsymbol{O} \tag{4.10}$$

where $\boldsymbol{u_j} = \{x_j, y_j, z_j\}$ and $j = A, B, C, D$ alternatively. An accessory vector is defined by

$$\boldsymbol{v_a} = \boldsymbol{u_k} - \boldsymbol{O} \tag{4.11}$$

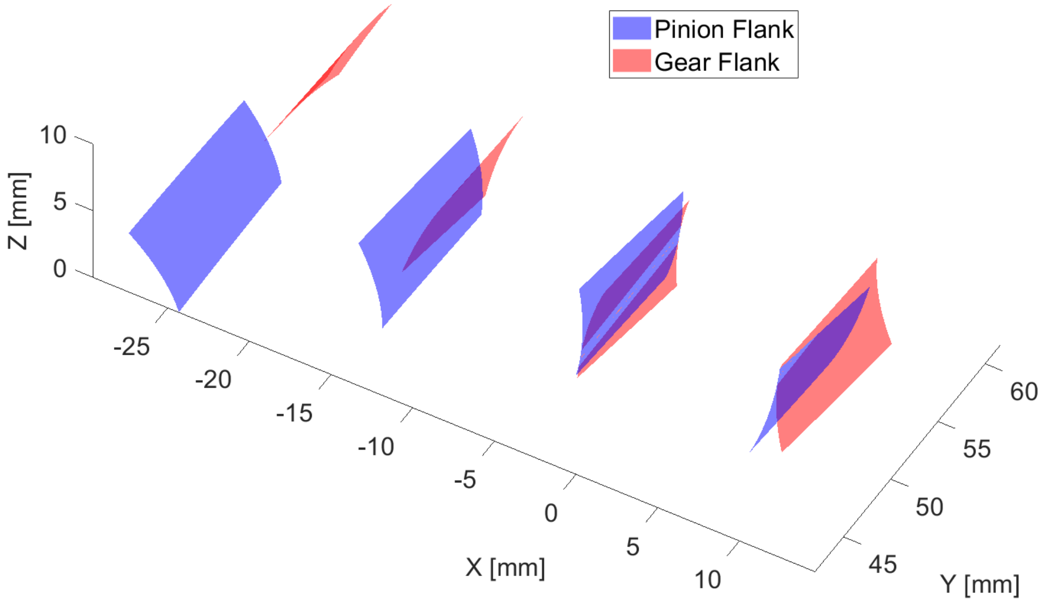

Figure 62: Surfaces of all considered flanks. Triangulations lines are removed for visualization purposes.

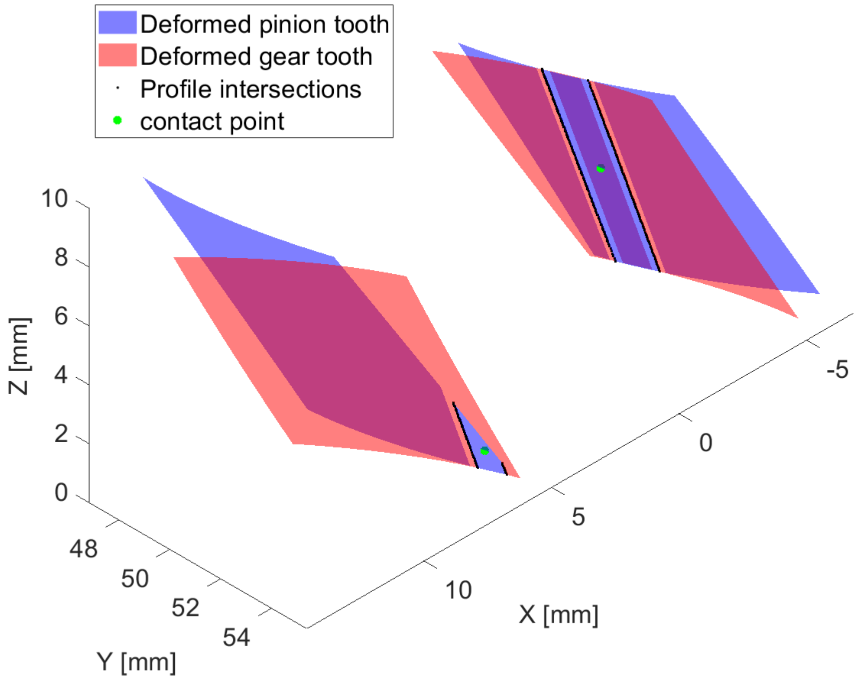

Figure 63: Intersections between the deformed triangulated profiles and new contact points

where $\boldsymbol{u_k} = \{x_k, y_k, z_k\}$ and $k = B, C, D, A$ alternatively. The vectors defining the Y and Z axis are then obtained as

$$\begin{aligned} \boldsymbol{v_y} &= \boldsymbol{v_z} \times \boldsymbol{v_x} \\ \boldsymbol{v_z} &= \boldsymbol{v_x} \times \boldsymbol{v_a} \end{aligned} \tag{4.12}$$

The versors are then obtained dividing the vectors with their norm

$$\boldsymbol{n_x} = \frac{\boldsymbol{v_x}}{\|\boldsymbol{v_x}\|} \quad \boldsymbol{n_y} = \frac{\boldsymbol{v_y}}{\|\boldsymbol{v_y}\|} \quad \boldsymbol{n_z} = \frac{\boldsymbol{v_z}}{\|\boldsymbol{v_z}\|} \tag{4.13}$$

Finally, the averaged versor normal to the surface in the contact point is simply obtained by

$$\boldsymbol{\bar{n}_z} = \{\bar{n}_{z,1}, \bar{n}_{z,2}, \bar{n}_{z,3}\} = \overline{\{\boldsymbol{n}_{\boldsymbol{z},\widehat{OAB}}, \boldsymbol{n}_{\boldsymbol{z},\widehat{OBC}}, \boldsymbol{n}_{\boldsymbol{z},\widehat{OCD}}, \boldsymbol{n}_{\boldsymbol{z},\widehat{ODA}},\}} \tag{4.14}$$

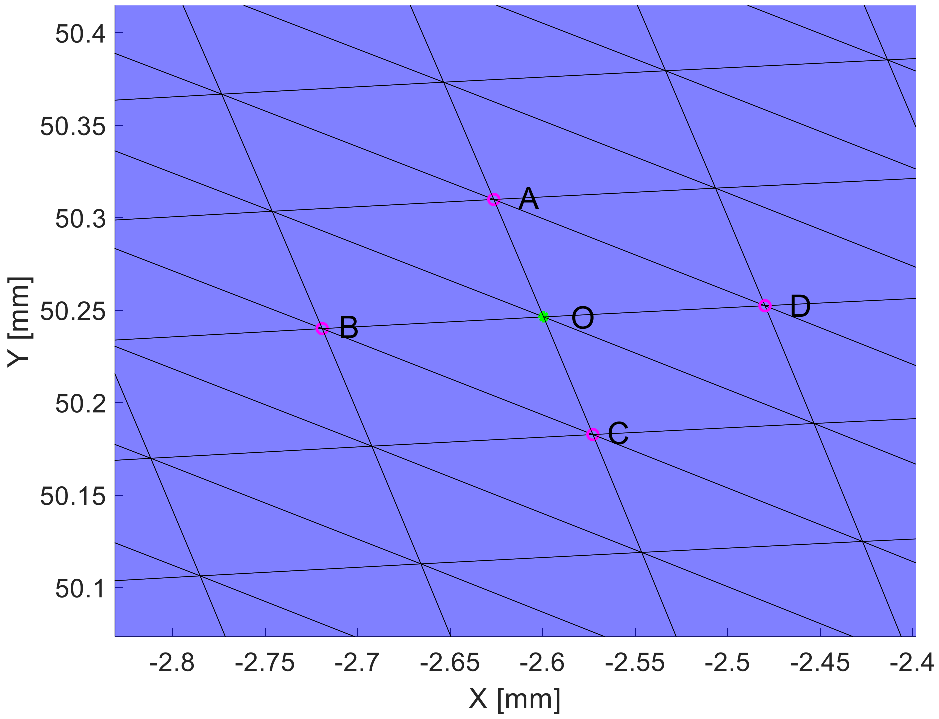

Figure 64: Points for the calculation of the normal vector to the contact point

From the components of the $\bar{\boldsymbol{n}}_{\boldsymbol{z}}$ versor the actual pressure angle μ_α and helix angle μ_β can be found by

$$\mu_\alpha = \tan^{-1}\left(\frac{\bar{n}_{z,2}}{\bar{n}_{z,1}}\right) \\ \mu_\beta = \tan^{-1}\left(\frac{\bar{n}_{z,3}}{\bar{n}_{z,1}}\right) \tag{4.15}$$

Using the obtained angles, the forcing terms to be applied to the Degrees Of Freedom (DOFs) pertaining the contact node can be obtained as

$$\boldsymbol{f_{cp}} = \begin{Bmatrix} f_x \\ f_y \\ f_z \\ m_x \\ m_y \\ m_z \end{Bmatrix} = \begin{Bmatrix} Fsin(\mu_\alpha) \\ Fcos(\mu_\alpha)\cos(\mu_\beta) \\ Fcos(\mu_\alpha)\sin(\mu_\beta) \\ Fcos(\mu_\alpha)\cos(\mu_\beta)\left(z_{cp} - b/2\right) \\ Fsin(\mu_\alpha)\left(z_{cp} - b/2\right) \\ 0 \end{Bmatrix} \tag{4.16}$$

which takes into account the fact that the teeth beam elements are considered at the mid-facewidth location ($b/2$) and that the location of the contact point can be offset from this location introducing the moment terms m_x and m_y in its components to include this effect. The term F is the magnitude of the force in the direction normal to the tooth profile

$$F = \frac{Tcos(\beta)}{r_b cos(\alpha)} C_k \tag{4.17}$$

Where C_k is the load sharing coefficient for the k^{th} teeth pair computed in the same way as detailed in chapter III. The complete force vector is obtained placing the terms of in their corresponding DOFs

$$\boldsymbol{f} = \left\{0\ 0\ 0\ \cdots \boldsymbol{f_{cp}}\ \cdots 0\ 0\ 0\right\}^{\boldsymbol{T}} \tag{4.18}$$

and finally, the displacements of each node of the beam are calculated from

$$\boldsymbol{\delta} = \boldsymbol{K^{-1}f} \tag{4.19}$$

in which the displacements and rotations of the j^{th} node in the beam

$$\boldsymbol{\delta_j} = \left\{\delta_x\ \delta_y\ \delta_z\ \vartheta_x\ \vartheta_y\ \vartheta_z\right\}^T \tag{4.20}$$

are then used to obtain the deflected 3D shape of the tooth profile for i^{th} node sharing the same X coordinate of the j^{th} node by

$$\boldsymbol{d_i} = \\ = \left[\begin{Bmatrix} x_{p,i} - \delta_x - \vartheta_y\left(z_{p,i} - b/2\right) \\ y_{p,i} - \delta_y + \vartheta_x\left(z_{p,i} - b/2\right) \\ z_{p,i} + \delta_z \end{Bmatrix} - \begin{Bmatrix} x_o \\ y_o \\ z_o \end{Bmatrix}\right]\begin{bmatrix} cos(\varphi_{b,i}+\theta) & -sin(\varphi_{b,i}+\theta) & 0 \\ sin(\varphi_{b,i}+\theta) & cos(\varphi_{b,i}+\theta) & 0 \\ 0 & 0 & 1 \end{bmatrix} + \begin{Bmatrix} x_o \\ y_o \\ z_o \end{Bmatrix} \tag{4.21}$$

Where $x_{p,i}$, $y_{p,i}$ and $z_{p,i}$ are the undeformed coordinates of the i^{th} of the flank profile and $\varphi_{b,i}$ is the rotation angle due to the deflection of the gear body calculated from y_A of eq. (3.36)

$$\varphi_{b,i} = tan^{-1}\left(\frac{y_A cos(\mu_\alpha)}{\sqrt{x_{p,i}^2 + y_{p,i}^2}cos(\alpha) - r_f}\right) \tag{4.22}$$

where r_f is the root radius of the gear and $\theta = \theta_A$ or $\theta = \theta_C$ due to the deflection of the adjacent teeth from eq. (3.44) or eq. (3.45) in which the subscript A or C depends on which teeth pair is being considered as visible in Figure 24. This process is repeated for each tooth pair considered, for both the pinion and the driven gear and thus all deformed profiles are obtained. The deformed profile of a teeth under load, with an helix angle $\beta = 30°$ and a facewidth $b = 10\ mm$, contacting almost at the tip edge is visible in Figure 65 in which the bending effect the effect of the body rotation and the influence of the adjacent teeth have been separated and increased by a factor of 1000 to make them clearly visible, while the flanks of the pinion and driven gear for two teeth pairs are visible in the initial and deformed configurations in Figure 66 scaled by the same factor. This iterative process is repeated until equilibrium is found as described by the algorithm in chapter III and when convergence is achieved a detailed 3D contact algorithm, which will be described next, is then employed to obtain the contact pressures and displacements which will contribute to the final calculation of the STE as already described.

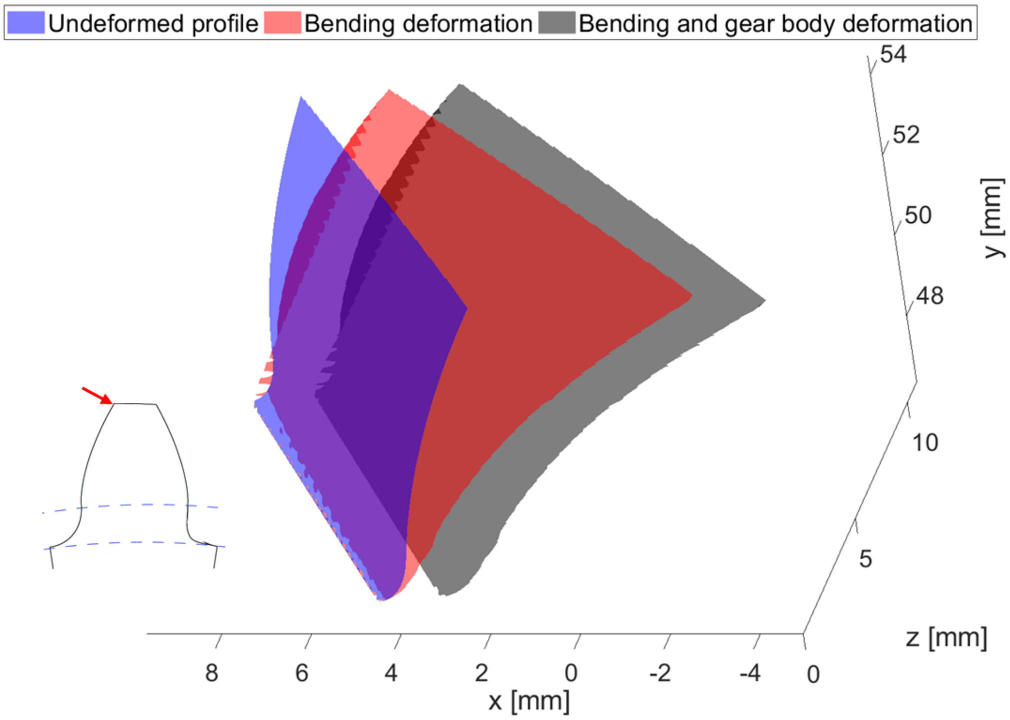

Figure 65: Deformed tooth profile under load. Deformations have been increased by a factor of 1000

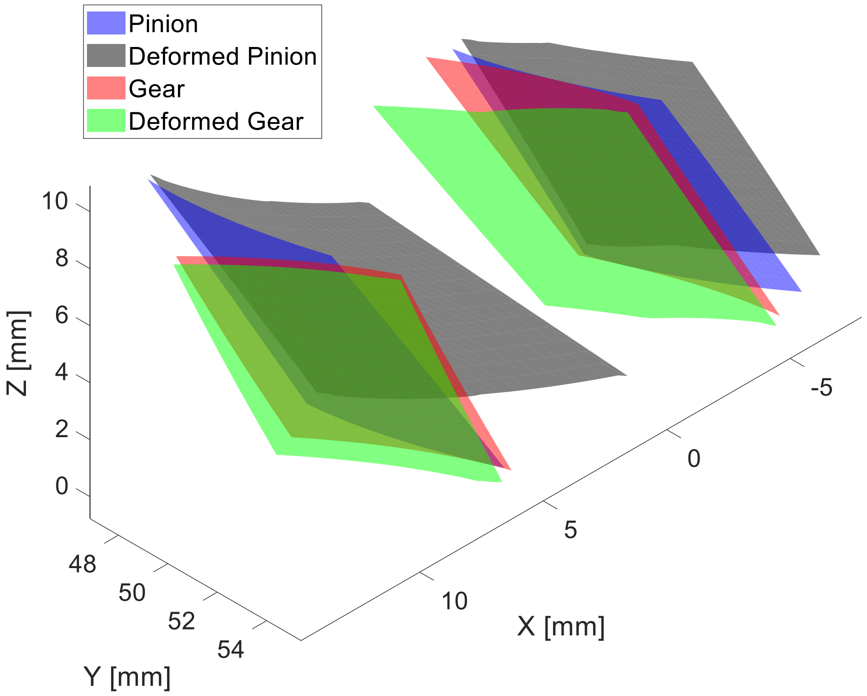

Figure 66: Deformed flanks of different teeth pairs. The deformations have been increased by a factor of 1000

IV.3 3D Non-Hertzian contact model

In this paragraph a 3D frictionless rough contact model will be presented. The basic formulation in terms of the Hertz-Signorini-Moreau problem is identical to what was discussed in III.5 and the same is valid for the iterative process to achieve the correct pressure distribution without traction (negative) pressures in any point of the computational domain. The differences lie in the fact that the contact line, discretized in uniform intervals, will be substituted by a contact plane, discretized through a triangular mesh, which obviously calls for a different formulation of the influence coefficients $\boldsymbol{C_{ij}}$ which will form the influence coefficients matrix $\boldsymbol{C}$. Another difference is that in the 2D case the pressure distribution was considered as piecewise constant, while in the present case a linear pressure distribution will be employed. Two different formulations will be discussed, and the main difference is the kind of triangles on which they can be applied as well as the computational effort and complexity to obtain the final influence coefficients matrices. However, over the same triangulation and with the same parameters they will be shown to yield very similar results among each other. The first formulation that will be introduced is the simplest one in terms of complexity but will be only applicable to regions triangulated using equilateral triangles and is based on the analytical formulations by Marmo *et al.* from [123] and [124]. Those formulations were based on surface integrals which could practically be solved only by symbolic computational toolboxes and hence were extremely computationally intensive. However, the same formulations were later specialized for direct numerical implementations by the same

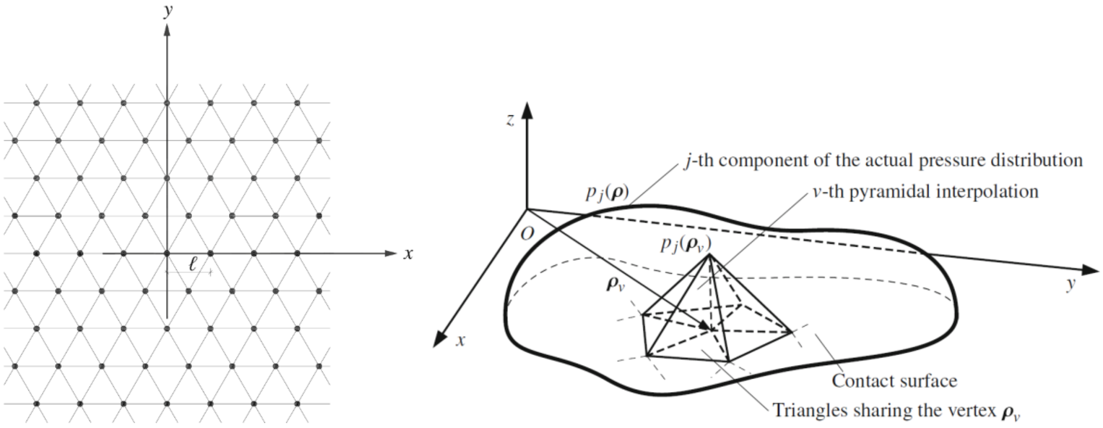

Figure 67: Equilateral triangular mesh and pyramidal pressures interpolation from [125]

researchers [125] over equilateral triangular domains whose edge length is equal to l and the pressure distribution is linearly interpolated over pyramidal domains as visible in Figure 67. Using this formulation, in order to obtain the influence coefficient matrix, it only needed to obtain the distance between each pair of i and j nodes of the domain as

$$r_{ij} = \sqrt{\left(x_i - x_j\right)^2 + \left(y_i - y_j\right)^2} \tag{4.23}$$

and then nondimensionalize it with respect to the edge length by

$$\rho_{ij} = \frac{r_{ij}}{l} \tag{4.24}$$

Then, using the nondimensional distance and the material shear modulus $G = {}^{E}\!/_{2(1+\nu)}$, the influence coefficients C_{ij} that form the $\boldsymbol{C}$ matrix are directly obtained from

$$C_{ij} = \begin{cases} \dfrac{1-v}{2\pi G}\dfrac{l}{2.854} \;\; if\ \rho_{ij} = 0 \\ \dfrac{1-v}{2\pi G}\dfrac{l}{1.159\rho_{ij} - 0.09} \;\; if\ \rho_{ij} \geq 1 \end{cases} \tag{4.25}$$

The second formulation that will be discussed is based on the closed-form solution of the contact problem proposed by Kalker and Van Randen [126] which was later fully derived and corrected by Boedo [127]. In this model a linearly varying normal pressure $p(\xi,\eta)$ is imposed on the half-space region as

$$p(\xi,\eta) = \frac{P_0\eta}{\gamma} \tag{4.26}$$

in which P_0 is the pressure in the apex $(0,\gamma)$ of the triangle in the local coordinate frame (ξ,η) with $\gamma > 0$ as visible in Figure 68. The displacement equation is then integrated, and a closed-form solution is obtained

$$I(a,b,c,t) = \frac{(a+bc)(t-c)[(a+bt)^2+(t-c)^2]^{1/2}}{4\pi(1+b)^2 abs(t-c)} + \frac{t^2-c^2}{4\pi}\operatorname{arcsinh}\left(\frac{a+bt}{t-c}\right) + \frac{(a+bc)(2c-ab+b^2c)}{4\pi(1+b^2)^{3/2}}\ln(A+B) \tag{4.27}$$

where

$$A = \frac{2b(a+bt)+2(t-c)}{(1+b^2)^{1/2}} \tag{4.28}$$

$$B = \frac{2(t-c)[(a+bt)^2+(t-c)^2]^{1/2}}{abs(t-c)} \tag{4.29}$$

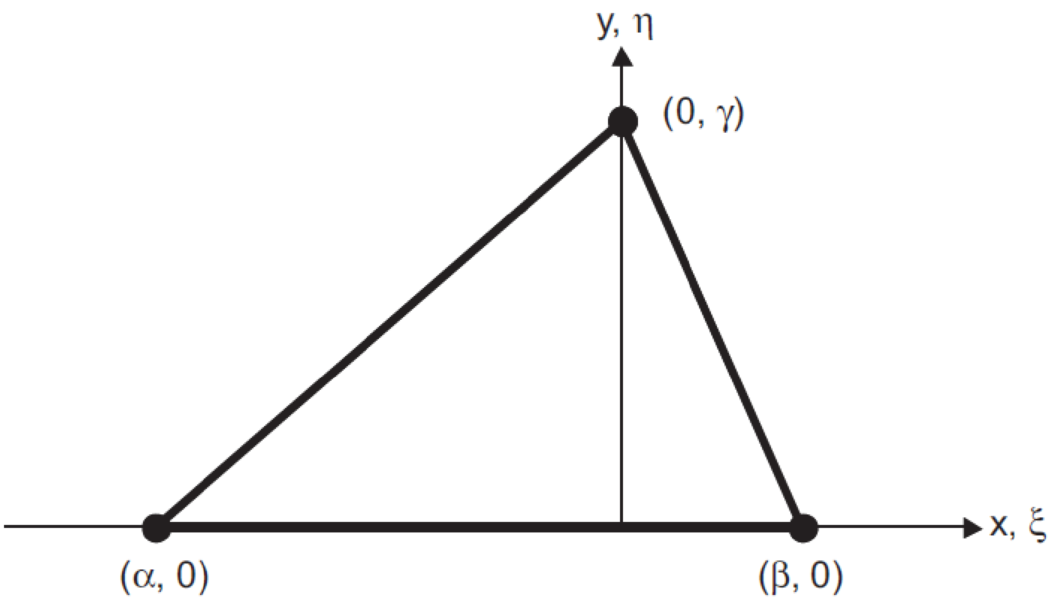

Figure 68: Local reference system for second contact formulation from [127]

The complete solution can then be written as:

- For $\bar{y} < 0$

$$\delta = I(\bar{\beta}-\bar{x},-\bar{\beta},\bar{y},1) - I(\bar{\beta}-\bar{x},-\bar{\beta},\bar{y},0) - I(\bar{\alpha}-\bar{x},-\bar{\alpha},\bar{y},1) + I(\bar{\alpha}-\bar{x},-\bar{\alpha},\bar{y},0) \tag{4.30}$$

- For $0 < \bar{y} < 1$

$$\begin{aligned}\delta = {} & I(\bar{\beta} - \bar{x}, -\bar{\beta}, \bar{y}, 0) - \lim_{t \to \bar{y}^-} I(\bar{\beta} - \bar{x}, -\bar{\beta}, \bar{y}, t) + I(\bar{\beta} - \bar{x}, -\bar{\beta}, \bar{y}, 0) \\ & - \lim_{t \to \bar{y}^+} I(\bar{\beta} - \bar{x}, -\bar{\beta}, \bar{y}, t) - I(\bar{\alpha} - \bar{x}, -\bar{\alpha}, \bar{y}, 0) \\ & + \lim_{t \to \bar{y}^-} I(\bar{\alpha} - \bar{x}, -\bar{\alpha}, \bar{y}, t) - I(\bar{\alpha} - \bar{x}, -\bar{\alpha}, \bar{y}, 1) \\ & + \lim_{t \to \bar{y}^+} I(\bar{\alpha} - \bar{x}, -\bar{\alpha}, \bar{y}, t)\end{aligned} \tag{4.31}$$

- For $\bar{y} > 1$

$$\begin{aligned}\delta = {} & I(\bar{\beta} - \bar{x}, -\bar{\beta}, \bar{y}, 0) - I(\bar{\beta} - \bar{x}, -\bar{\beta}, \bar{y}, 1) - I(\bar{\alpha} - \bar{x}, -\bar{\alpha}, \bar{y}, 0) \\ & + I(\bar{\alpha} - \bar{x}, -\bar{\alpha}, \bar{y}, 1)\end{aligned} \tag{4.32}$$

- For $\bar{y} = 0$

$$\begin{aligned}\delta = {} & I(\bar{\beta} - \bar{x}, -\bar{\beta}, 0,1) - \lim_{t \to 0^+} I(\bar{\beta} - \bar{x}, -\bar{\beta}, 0, t) - I(\bar{\alpha} - \bar{x}, -\bar{\alpha}, 0,1) \\ & + \lim_{t \to 0^+} I(\bar{\alpha} - \bar{x}, -\bar{\alpha}, 0, t)\end{aligned} \tag{4.33}$$

- For $\bar{y} = 1$

$$\begin{aligned}\delta = {} & I(\bar{\beta} - \bar{x}, -\bar{\beta}, 1,0) - \lim_{t \to 1^-} I(\bar{\beta} - \bar{x}, -\bar{\beta}, 1, t) + \lim_{t \to 1^-} I(\bar{\alpha} - \bar{x}, -\bar{\alpha}, 1, t) \\ & - I(\bar{\alpha} - \bar{x}, -\bar{\alpha}, 1,0)\end{aligned} \tag{4.34}$$

where $\bar{\alpha} = \alpha\backslash\gamma$, $\bar{\beta} = \beta\backslash\gamma$, $\bar{\alpha} = \alpha\backslash\gamma$, $\bar{x} = x\backslash\gamma$, $\bar{y} = y\backslash\gamma$, $\bar{\xi} = \xi\backslash\gamma$ and $\bar{\eta} = \eta\backslash\gamma$ are the nondimensional distances. The evaluation of the one-sided limits is needed since eq. (4.27) is undefined when $t = c$. Then the dimensional pressure-displacement coefficients are obtained as

$$w_{ij,k} = \delta \frac{1 - \nu}{G} \tag{4.35}$$

where the values of $w_{ij,k}$ with $k = 1, 2, 3$ for the entire triangulation need to be obtained three times, considering as the apex γ a different vertex of each triangle. Once this is done, the final influence coefficient is found by

$$C_{ij} = \sum_{j=1}^{n} w_{ij,k} \tag{4.36}$$

where n is the number of nodes in the triangulation and the summation is carried out by choosing the appropriate k in which node i is the vertex γ in the local coordinate frame. The two proposed models essentially give the same results when used on the same triangulation and therefore if not differently specified the coefficients from (4.25) will be used for the reasons mentioned earlier. The iterative solution process is the same as detailed in III.5. To validate the results obtained from the current approach a simple sphere to sphere contact is compared to the results from Hertz theory. The two contacting spheres have radii $R_1 = 100\ mm$ and $R_2 = 20\ mm$ respectively pressed together by a normal a load $F = 6500\ N$ on a $2 \times 2\ mm$ $(\boldsymbol{x} \times \boldsymbol{y})$ contact plane with triangles with a side length $l = 0.06\ mm$. The initial rigid body separation is simply obtained by

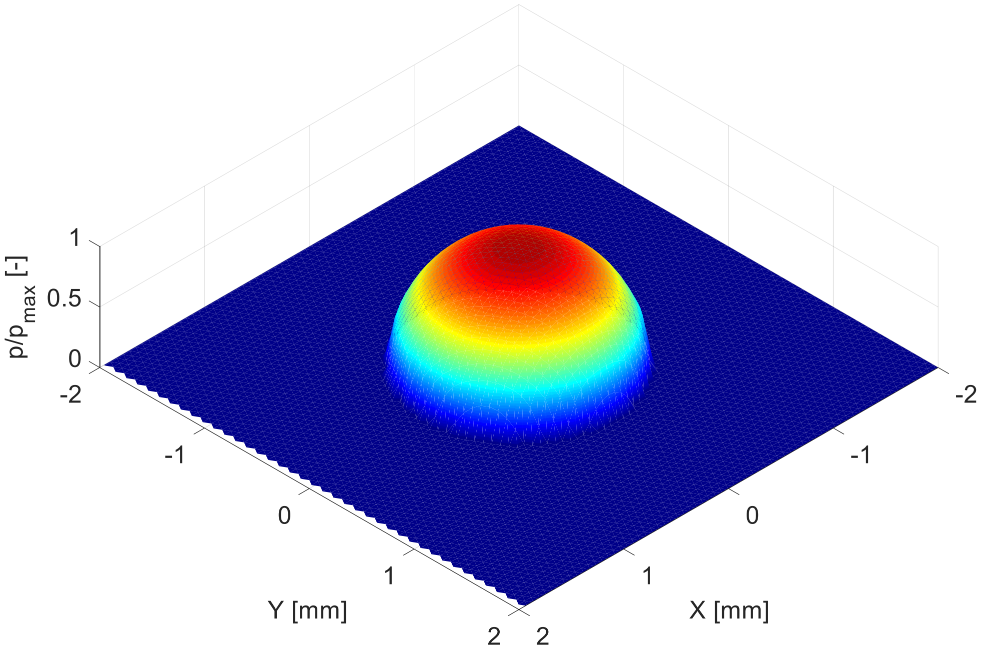

Figure 69: Pressure distribution p/p_{max} on the contact plane for the sphere-sphere contact

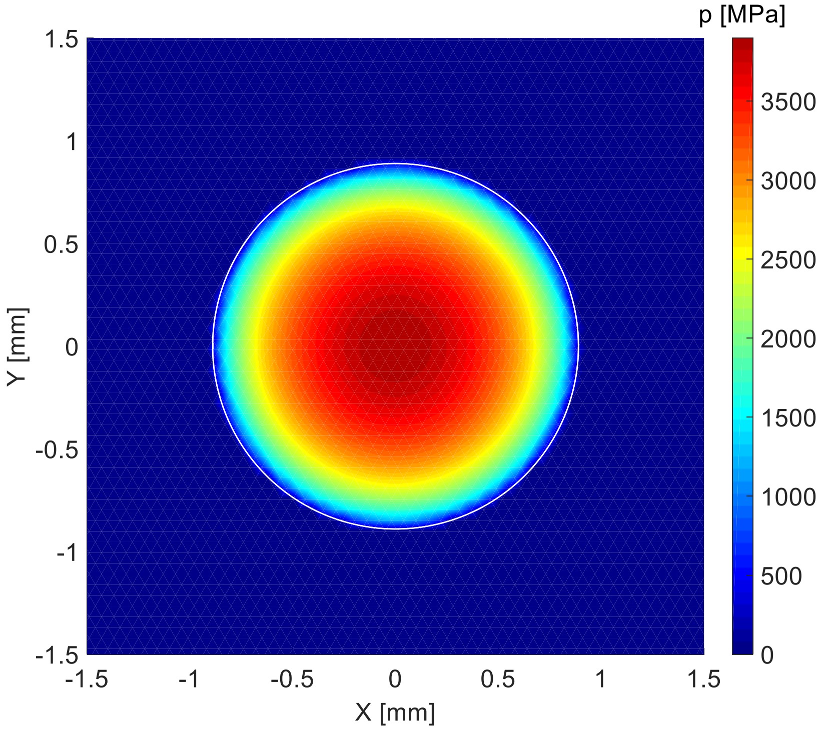

Figure 70: Pressure distribution for the sphere-sphere contact on the contact plane

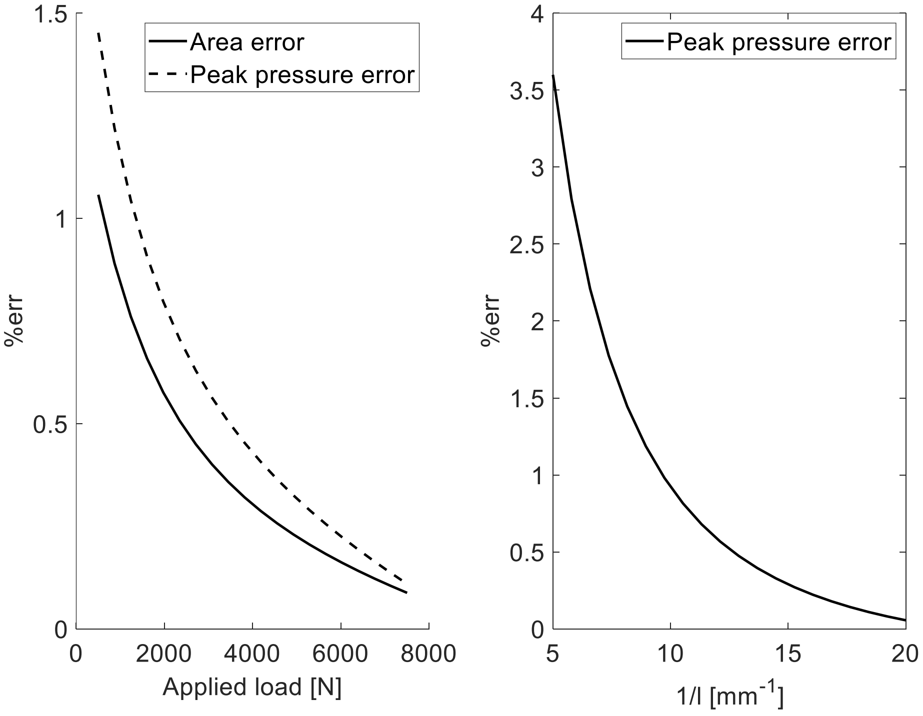

Figure 71: Sphere-sphere contact percent errors versus Hertz theory

$$\boldsymbol{g} = \left[\left(R_1^2 - \boldsymbol{x}^2 - \boldsymbol{y}^2\right)^{\frac{1}{2}} - R_1\right] - \left[\left(R_2^2 - \boldsymbol{x}^2 - \boldsymbol{y}^2\right)^{\frac{1}{2}} - R_2\right] \tag{4.37}$$

The distribution of the unit pressure $\mathrm{p}/\mathrm{p}_{\max}$ is visible in Figure 69 while in Figure 70 the same distribution is visible with the color bar defining the pressure values and the white line indicates the predicted solution from Hertz theory [106]. The visual comparison shows a very good agreement and a numerical comparison is shown in Figure 71 where the obtained values for a varying load between $500 \div 7500\, N$ show an error for both the maximum pressure and the contact area always lower than 1.5%. The influence of the mesh size is also visible in the same figure for the maximum load and shows a trend quickly approaching lower errors as the length of the triangles sides decreases. Next, and ellipsoid to ellipsoid contact is compared to the results from Hertz theory. The two contacting ellipsoids have major radii $R_1 = 100\, mm$ and $R_2 = 20\, mm$ and minor radii $r_1 = 40\, mm$ and $r_2 = 5\, mm$ respectively pressed together by a normal a load $F = 10500\, N$ on a $2 \times 2\, mm$ $(\boldsymbol{x} \times \boldsymbol{y})$ contact plane with triangles with a side length $l = 0.06\, mm$. The initial rigid body separation is simply obtained by

$$\boldsymbol{g} = \left[\frac{\boldsymbol{x}^2}{2R_1} + \frac{\boldsymbol{y}^2}{2r_1}\right] - \left[\frac{\boldsymbol{x}^2}{2R_2} + \frac{\boldsymbol{y}^2}{2r_2}\right] \tag{4.38}$$

The distribution of the unit pressure $\mathrm{p}/\mathrm{p}_{\max}$ is visible in Figure 72 while in Figure 73 the same distribution is visible with the color bar defining the pressure values and the white line indicates the predicted solution from Hertz theory [106]. The visual comparison shows a very good agreement and a numerical comparison is shown in Figure 74 where the obtained values for a varying load between $1000 \div 15000\, N$ show again an error for both the maximum pressure and the contact area always lower than 1.6%. The influence of the mesh size is also visible in the same figure for the maximum load and shows a trend quickly approaching lower errors as the length of the triangles sides decreases. In order to verify the non-Hertzian results a model of a crowned roller bearing contacting with a cylindrical inner race has been compared with the results from de Mul *et al.* [128] and the geometrical and material data can be seen in Figure 75 and the resulting cross-sections in the X and Y planes

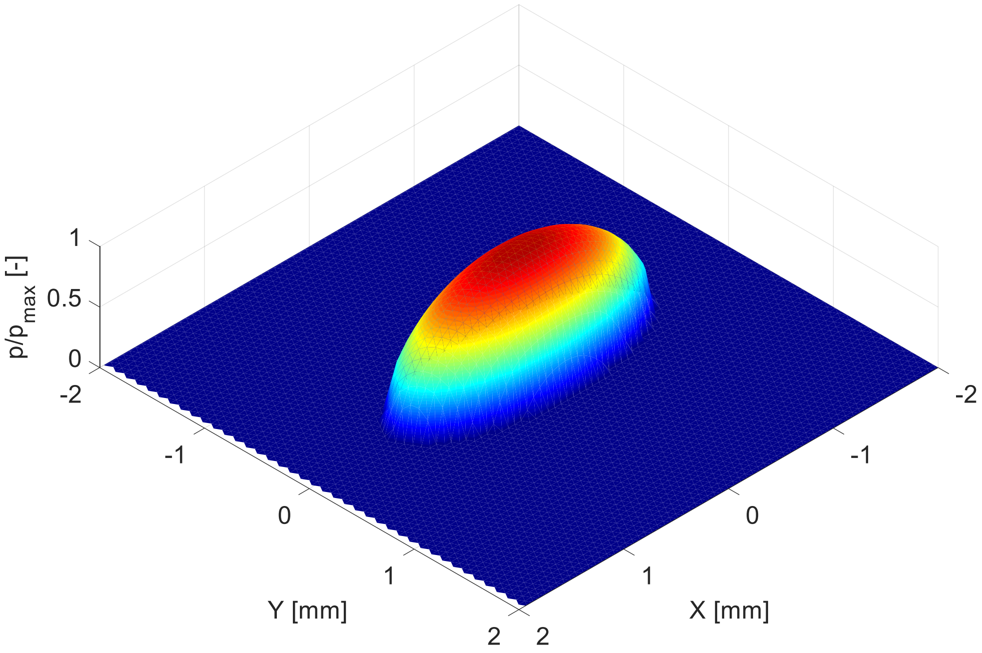

Figure 72: Pressure distribution p/p_{max} on the contact plane for the ellipsoid-ellipsoid contact

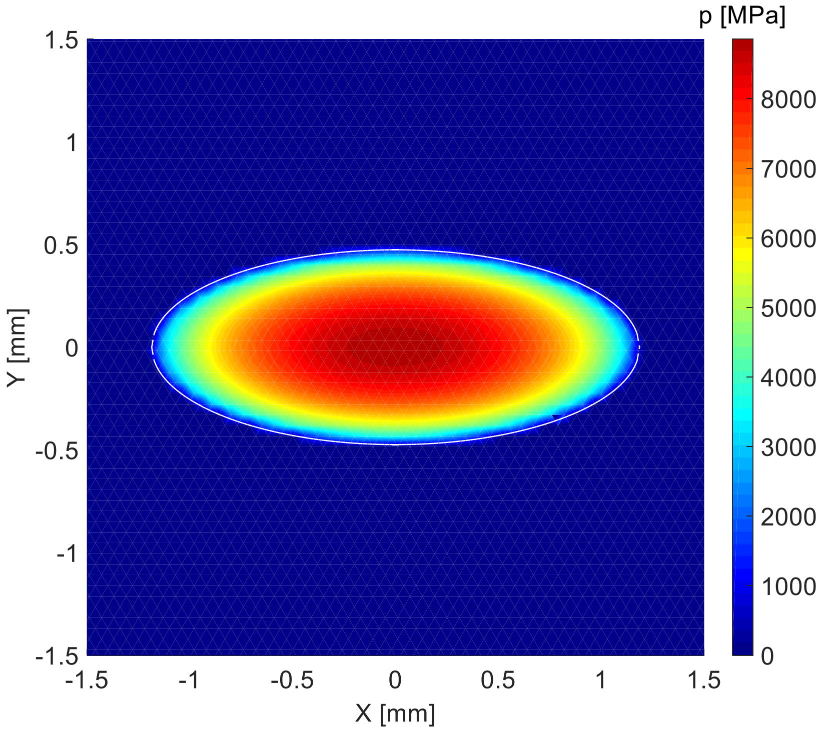

Figure 73: Pressure distribution for the ellipsoid-ellipsoid contact on the contact plane

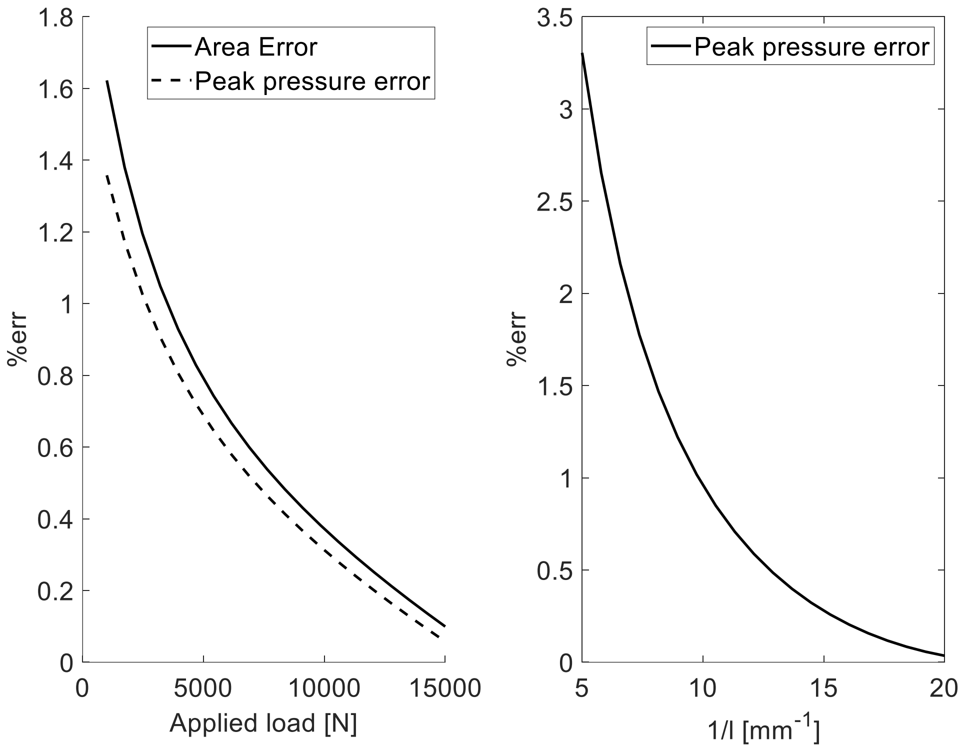

Figure 74: Ellipsoid-ellipsoid contact percent error versus Hertz theory

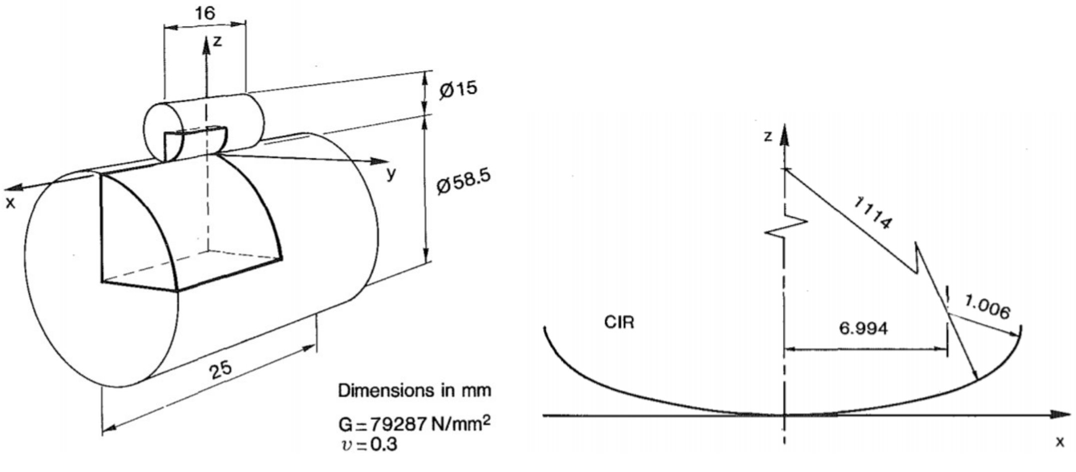

Figure 75: Crowned roller and disk geometrical and material properties

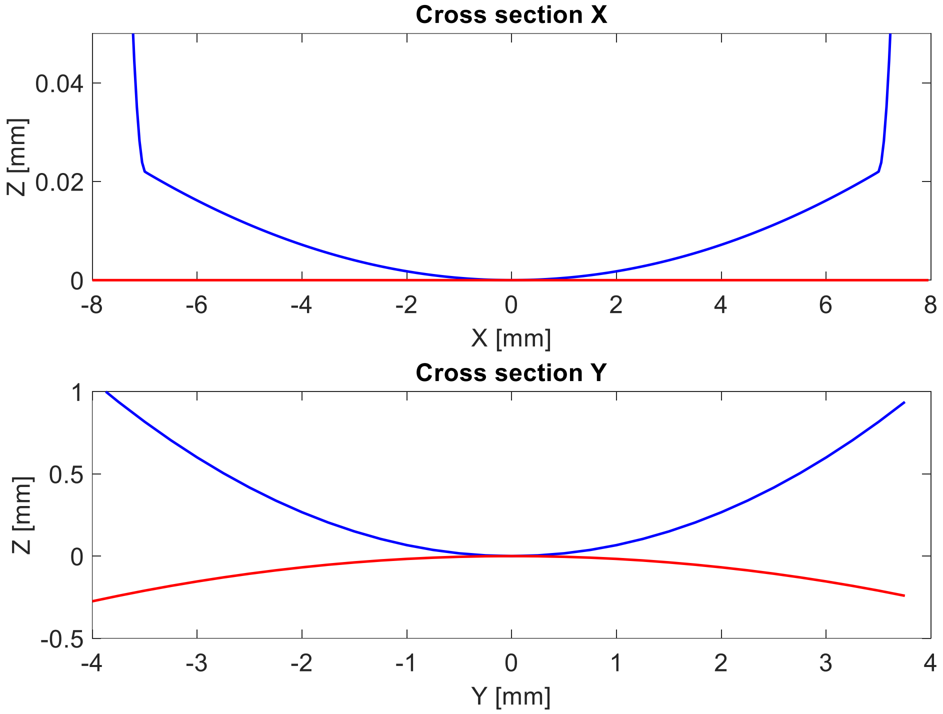

Figure 76: Profiles cross sections in X *and* Y *direction of the crowned roller and disk*

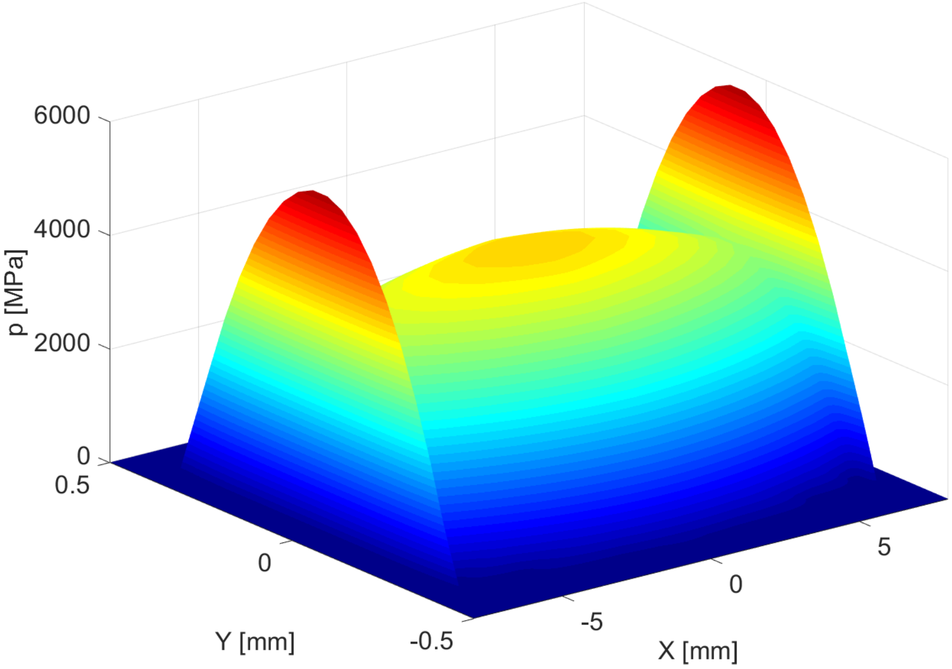

Figure 77: Pressure distribution on the contact plane for the crowned roller contact

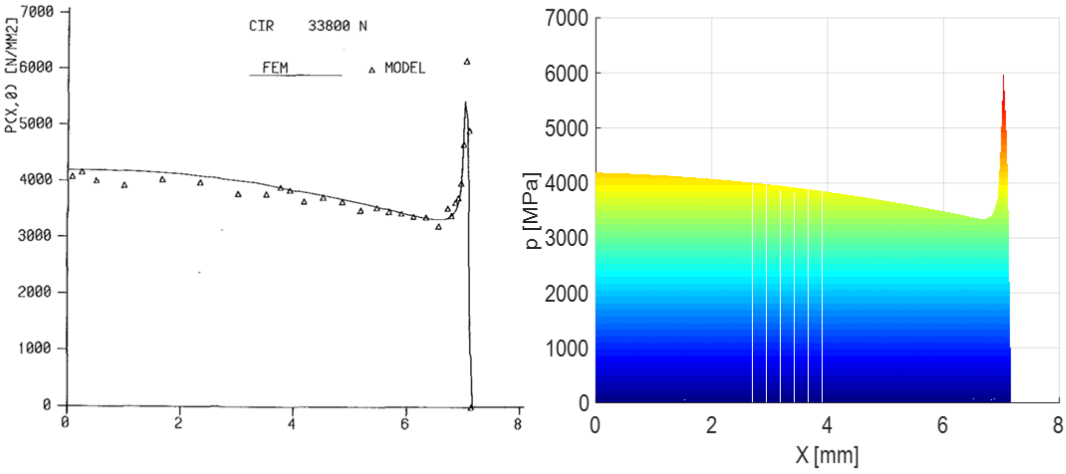

Figure 78: Pressure distribution along the X direction and comparison with results from [128]

in Figure 76. Due to the nature of the contact a mesh for the contact plane made with right triangles is chosen with equal sides of 0.02 mm and therefor the influence coefficient matrix $\boldsymbol{C}$ is formed using the approach from Boedo [127]. The resulting non-Hertzian pressure distribution resulting from the application of the current method can be seen in Figure 77 for a load $F = 33800\ N$ where two distinct pressure peaks can be distinguished on the contact plane, while the central part has a trend similar to the ellipsoid to ellipsoid contact seen earlier. The pressure variation along the X direction can be seen in Figure 78 along with the same results from [128] for the symmetric part of the contact. The pressure at $X = 0$ is close to $4000\ MPa$ in both cases and the trends are also very similar as well as the maximum

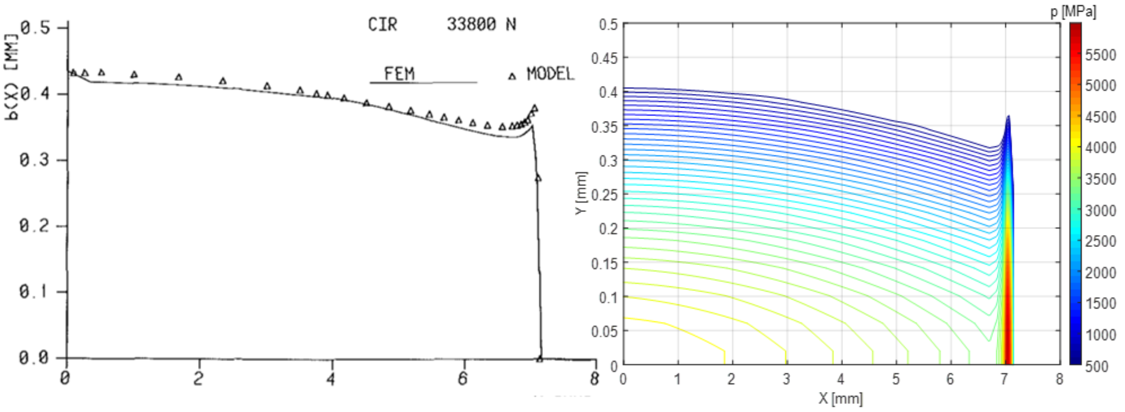

Figure 79:Pressure distribution along the XY plane and comparison with results from

pressure at the edge of contact, which for the case from literature is just slightly above $6000\ MPa$, while for the current model is $5987\ MPa$, thus they agree well with each other. A comparison of the view on the XY plane can be instead seen in Figure 79 where it can be appreciated also the agreement between the results since the maximum width at $X = 0$ is just above $0.4\ mm$ ($0.42\ mm$ for the current model) and also the width of the contact patch is around $7.2\ mm$ for the reference results and has the same value in the current case. The slight differences in the results are mainly due to different discretization since the exact value of the pressure and of the contact patch depends on this. Also, in [128] the contact plane is discretized using contact pressure rectangles, but the size of those elements is not given. In order to apply this method to the contact between gears a way to obtain the initial separation between the contacting profiles $\boldsymbol{g}$ is needed, since up to now the profiles were simple enough so that it could be found through simple analytical expressions. To do so, the equilibrium deformed contact point is used to compute a rotation matrix that will bring the profile normal to the XY contact plane. This rotation matrix for each of the contacting flanks is obtained from the versors from equations (4.10) through (4.14). The rotation matrix is then obtained as

$$\boldsymbol{R_\theta} = \begin{bmatrix} \boldsymbol{n_x} \\ \boldsymbol{n_y} \\ \boldsymbol{\bar{n}_z} \end{bmatrix} = \begin{bmatrix} n_{x,1} & n_{x,2} & n_{x,3} \\ n_{y,1} & n_{y,2} & n_{y,3} \\ \bar{n}_{z,1} & \bar{n}_{z,2} & \bar{n}_{z,3} \end{bmatrix} \tag{4.39}$$

and the new coordinates of each point of the flanks $\boldsymbol{u'_p} = \{x'_p, y'_p, z'_p\}^T$ in this position are then computed with

$$\begin{Bmatrix} x'_p \\ y'_p \\ z'_p \end{Bmatrix} = \boldsymbol{R_\theta} \left(\begin{Bmatrix} x_p \\ y_p \\ z_p \end{Bmatrix} - \begin{Bmatrix} x_{cp} \\ y_{cp} \\ z_{cp} \end{Bmatrix} \right) \tag{4.40}$$

where $\boldsymbol{u_p} = \{x_p, y_p, z_p\}^T$ are the coordinates of each of the point of the considered flank and $\boldsymbol{O} = \{x_{cp}, y_{cp}, z_{cp}\}^T$ are again the coordinates of the equilibrium contact point after deformation. Next, the rotated flanks are interpolated using polynomials of degree n in X and Y so that the final value of g can be directly obtained substituting the X and Y coordinates of the triangulation of the contact plane. The degree of the polynomial n is automatically chosen so as to minimize the difference between the original points and the interpolated values below a certain threshold which is usually set at $1e-6\ mm$, so that even the finest

TPM would be represented correctly, however those values are generally much lower as can be seen in Figure 80 for a gear with $\beta = 45°$ and a facewidth $b = 26\,mm$, in which for a computed $n = 9$ the errors Δ_z are in the order of $1e - 8\,mm$.

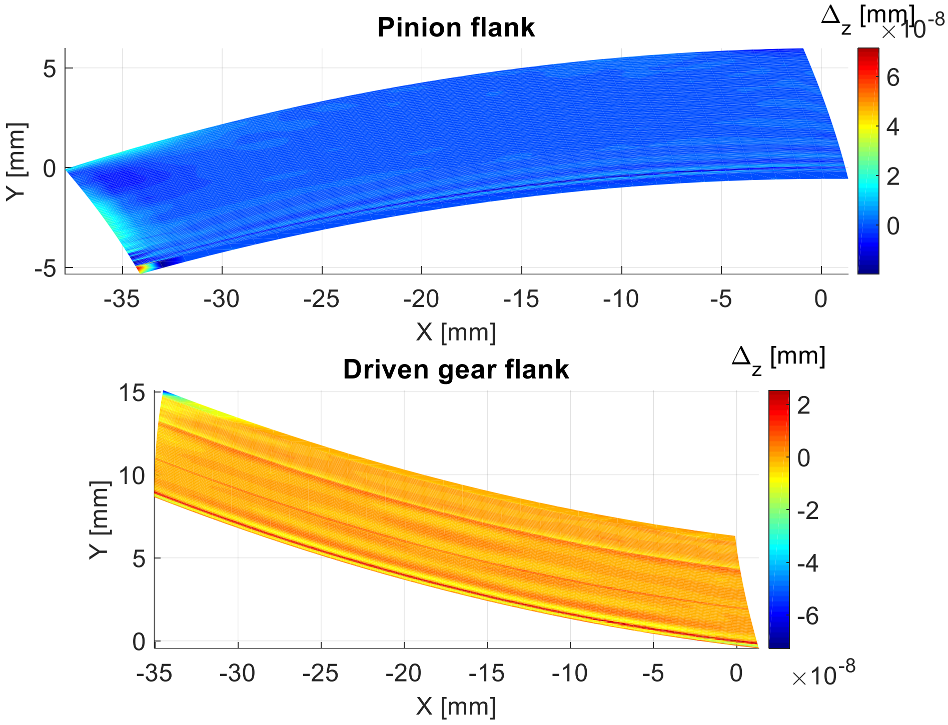

Figure 80: Example of interpolation errors of the flanks

In the next paragraph results will be shown for helical gears, but since the STE and load sharing coefficients have already been deeply discussed for spur gears in the previous chapter and since changing the approach from 2D to 3D doesn't affect the results, those will not be discussed however, contact results are of a different nature. The parameters of the gear pair analyzed here and in the upcoming paragraph are listed in Table 6, and the helix angle, if any, will be specified case by case. The pressure distribution on the flank of a spur gear ($\beta = 0°$) as experienced along its entire time in contact is visible in Figure 81, where no profile modification has been applied. As visible the single contact zone is distinguishable by its higher pressures, but again non-Hertzian pressure peaks are found at the tip of the tooth, and in this case also at its edges and those are further amplified at the corners of the flank where the tip and edges meet creating even higher pressure overloads. Again, those peaks

Table 6: Gear pair parameters

Parameter	Pinion	Gear
Number of teeth z [-]	28	28
Module m [mm]	3,175	3,175
Pressure angle α_P [°]	20	20
Face width b [mm]	16,35	16,35
Shaft radius r_s [mm]	20	20
Torque T [Nmm]	200000	
Young modulus E [MPa]	210000	210000
Poisson coefficent ν [-]	0,3	0,3

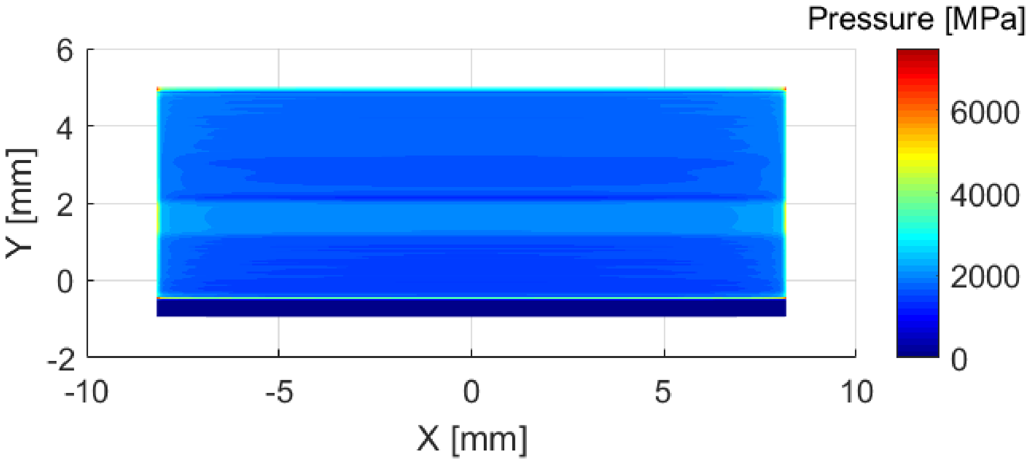

Figure 81: Flank pressure distribution without TPM

can be mitigated or removed altogether by modifying the profile of the flank introducing tooth profile modifications. Using the proposed 3D contact model is now possible to analyze also the effects of modifications made on the facewidth of the teeth, such as symmetric parabolic crowning, in which a certain amount of material Δ_c is removed in a parabolic trend starting from the mid width of the gear as visible in Figure 82. When a symmetric parabolic crowing of $\Delta_c = 0.0025\ mm$ is applied to the gear pair under analysis the resulting pressure distribution is then visible in Figure 83. The distinction between the single and double tooth contact is now even more visible and edge peaks are now absent, since when crowning is applied the contact between the flanks becomes similar to an ellipsoid-ellipsoid contact rather than a cylinder-cylinder contact as when the ideal involute is considered. However, pressure peaks at the tip and root of the tooth are still visible, which are generated when teeth enter and leave contact. To remove those peaks tip profile modifications can be manufactured along with crowning and the effects of a linear and a parabolic tip relief, can be appreciated in Figure 84 and Figure 85 respectively along with the same crowning seen

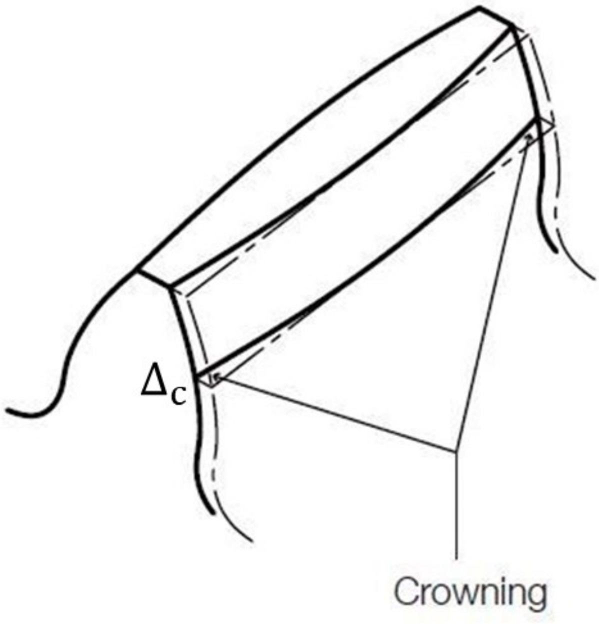

Figure 82: Crowning profile modification

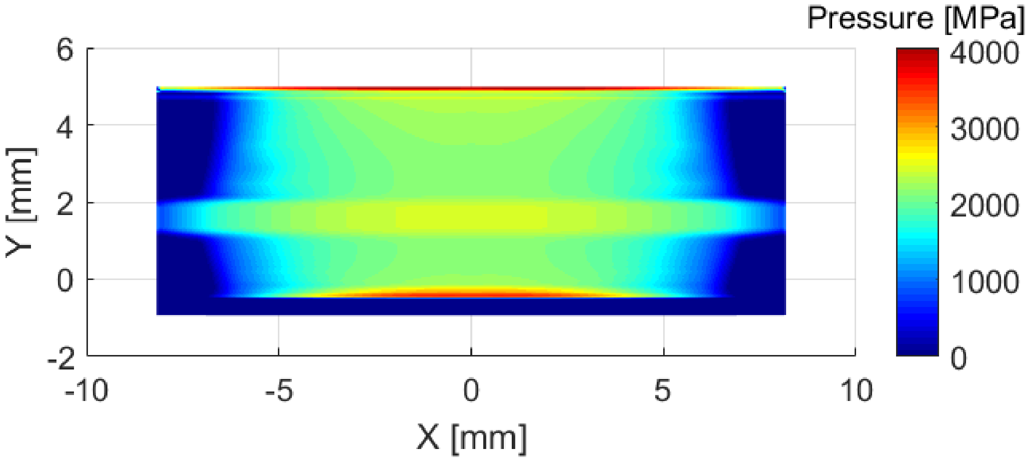

Figure 83: Flank pressure distribution with crowning $\Delta_c = 0.0025\ mm$

before. As a result of the application of said modifications to the flanks the single contact zone is larger due to the fact that teeth come into contact later and leave contact earlier confirming the reduction of the double tooth contact seen in the previous chapter. However, the pressure peaks at the tip and root of the flank are almost completely removed for the linear modification, and even lower for the parabolic one. The results are similar, but again in this case the reduction of the pressure overload is higher and smoother for the parabolic tip relief since no discontinuity and sharp edge is introduced on the flank

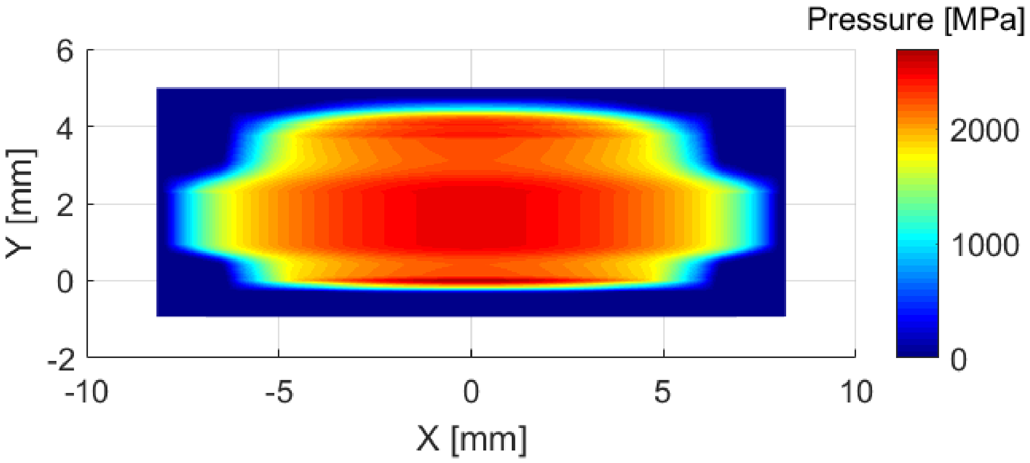

Figure 84: Flank pressure distribution with crowning $\Delta_c = 0.0025\ mm$ *and linear tip relief* $\Delta_t = 0.032\ mm, l_t = 0.96\ mm$

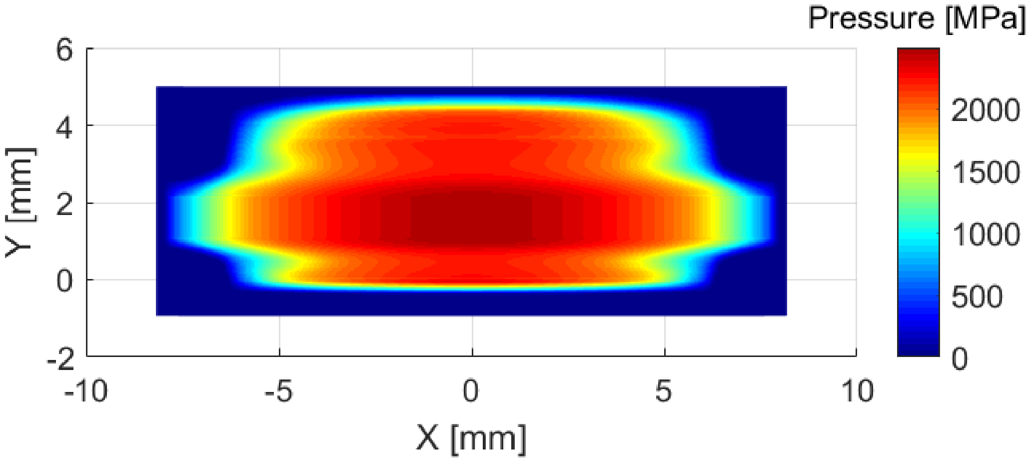

Figure 85: Flank pressure distribution with crowning $\Delta_c = 0.0025\ mm$ *and parabolic tip relief* $\Delta_p = 0.032\ mm, l_p = 0.96\ mm$

IV.4 Results

In this paragraph the proposed model is applied to the gear pair whose data is listed in Table 6 for various different helix angles and tooth profile modifications. The first comparison has been made to analyze the effect of the introduction of a helix angle which is probably the modification which impacts more the quasi static behavior and load sharing characteristics in a gear pair. In Figure 86 the helix angle β has been varied from $0°$ (spur gear) up to $45°$. The impact of this change is indeed evident and the single tooth contact region, which is noticeable for the spur gear, is almost completely eliminated already for $\beta = 7.5°$ and totally gone for $\beta = 15°$, which is expected since the helix angle increases the tooth contact ratio. Furthermore, as the helix angle increases the tooth becomes stiffer and both the mean and peak-to-peak ratio of the STE are reduced. In Figure 87 the torque applied on a gear pair with $\beta = 22.5°$ and linear tip relief ($l_t = 0.96\ mm, \Delta_t = 0.032\ mm$) is varied from 0.1 to 3 times its nominal value. As the torque increases both the mean and peak-to-peak ratio of the STE tend to increase, reaching a maximum for around 300 Nm of torque, but after that it reduces as the contact ratio increases. The pressure distribution on the flank of a gear pair with $\beta = 45°$ and no TPM is visible in Figure 88. Said distribution is dominated by the pressure peaks, especially on the edges of the gear and not much can be said of the distribution in the middle

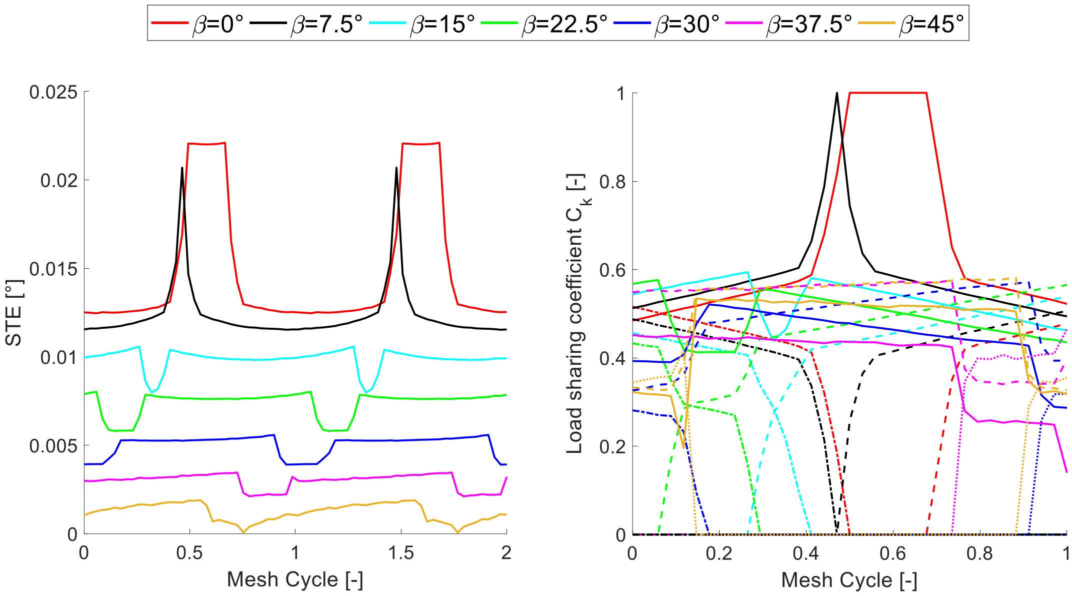

Figure 86: Effect of helix angle on the STE and load sharing coefficient C_k

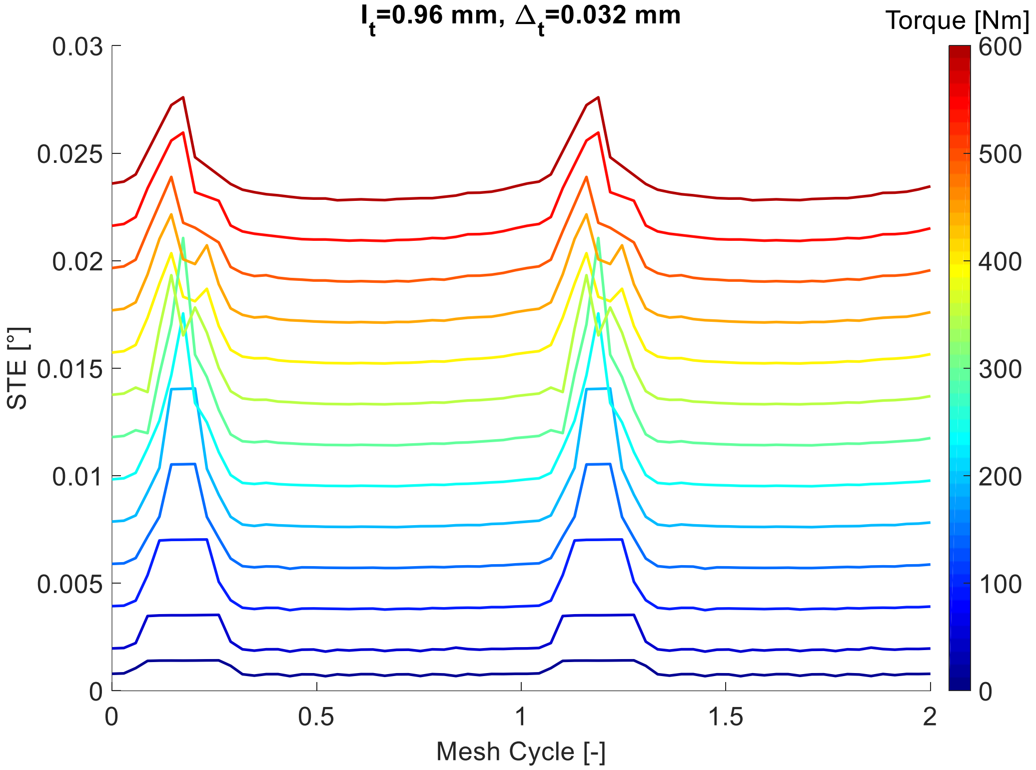

Figure 87: Effect of torque on the STE with $\beta = 22.5°$ *and linear tip relief*

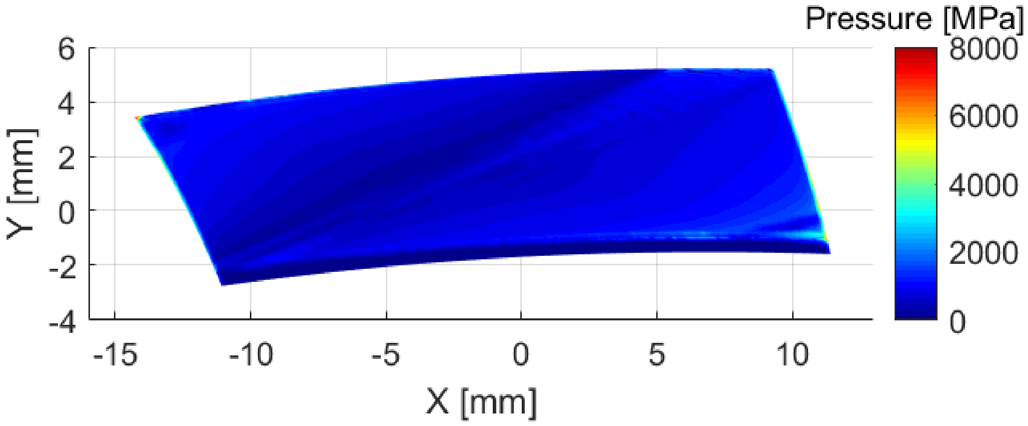

Figure 88: Flank pressure distribution for $\beta = 45°$ *without TPM*

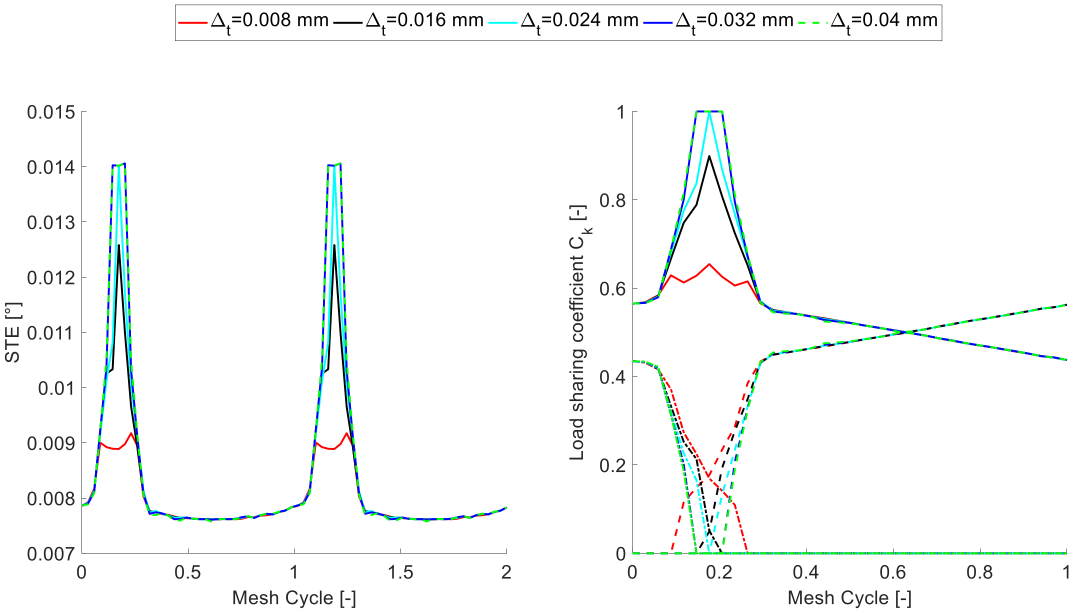

Figure 89: Effect of linear tip relief amount of material removed on the STE and load sharing C_k coefficient for $\beta = 22.5°$ with $l_t = 0.96\ mm$

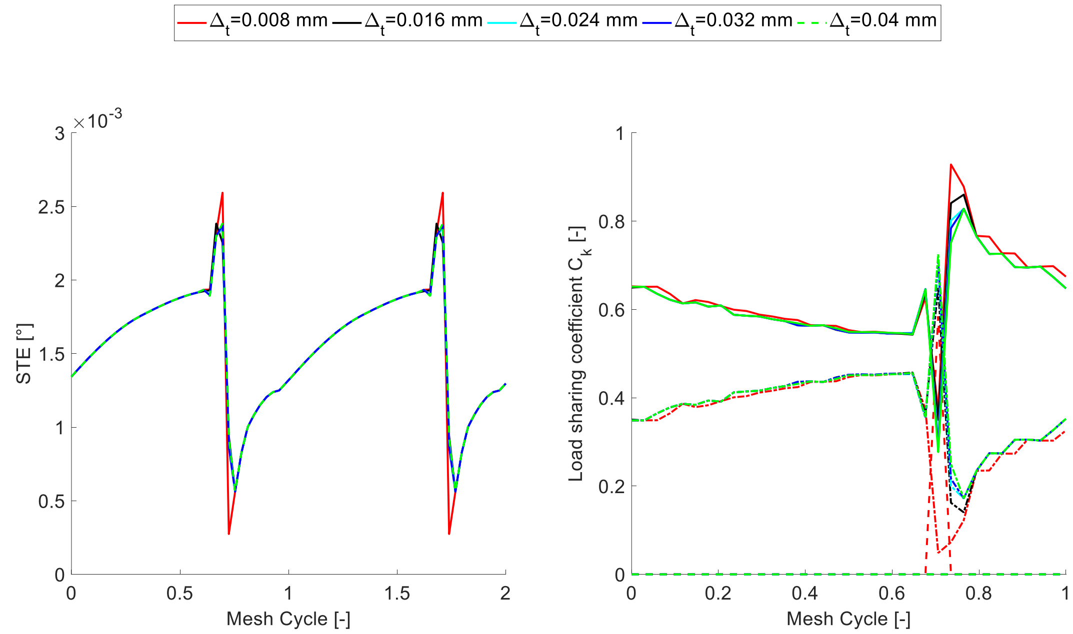

Figure 90: Effect of linear tip relief amount of material removed on the STE and load sharing C_k coefficient for $\beta = 45°$ with $l_t = 0.96\ mm$

of the flank. The peaks are especially accentuated at the bottom-right and top-left corners since those are the regions where the teeth first engage and leave contact at the end of their contact cycle. Next the effect of the combination of a helix angle and linear tip relief is

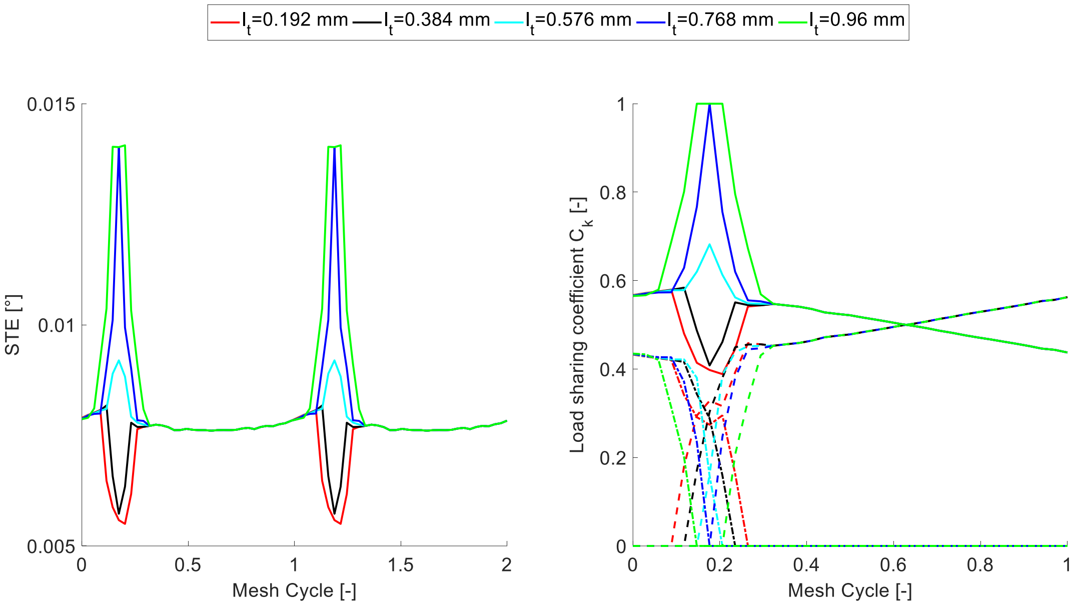

Figure 91: Effect of linear tip relief length of modification on the STE and load sharing C_k coefficient for $\beta = 22.5°$ with $\Delta_t = 0.032\ mm$

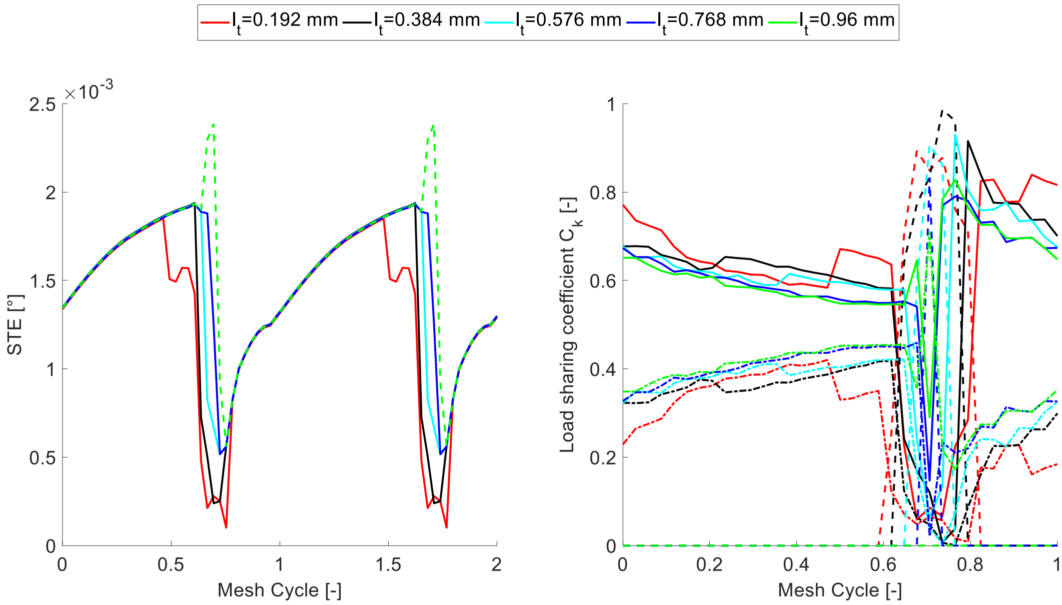

Figure 92: Effect of linear tip relief length of modification on the STE and load sharing C_k coefficient for $\beta = 45°$ with $\Delta_t = 0.032\ mm$

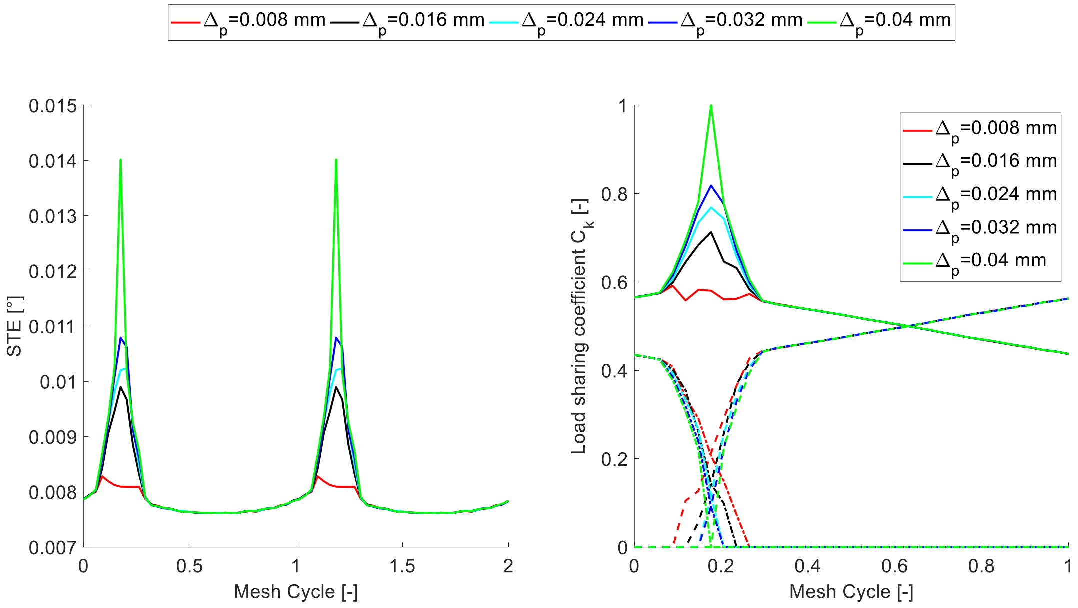

Figure 93: Effect of parabolic tip relief amount of material removed on the STE and load sharing C_k coefficient for $\beta = 22.5°$ with $l_p = 0.96\ mm$

analyzed. In Figure 89 the amount of material removed is varied for a fixed length of modification $l_t = 0.96\ mm$ and $\beta = 22.5°$. As the amount of material removed increases the triple tooth contact region gets narrower and then vanishes thus increasing the peak-to-peak value of the STE and lowering the contact ratio, while the same analysis for $\beta = 45°$ visible in Figure 90 shows much less variation as the amount of material removed increases. Similar trends are obtained when the length of the modification is varied for a fixed $\Delta_t = 0.032\ mm$ as visible in Figure 91 and Figure 92 for $\beta = 22.5°$ and $\beta = 45°$ respectively. In this case however the influence of this modification parameter is noticeable even for the maximum helix angle since the triple contact region displays a significant reduction as the length of the modification increases. The same analyses are then conducted for the parabolic tip relief starting from increasing the amount of material removed for a fixed length of modification $l_p = 0.96\ mm$ as visible in Figure 93 for $\beta = 22.5°$ and for $\beta = 45°$ in Figure 94. The trend is again similar to the linear profile modification and for the lower helix angle the reduction of the triple tooth contact region and its consequent increase of the peak-to-peak value of the STE is noticeable, but less than before since the total amount of material removed is lower due to its parabolic nature, while its impact on the higher helix angle is still very low. Similarly, the length of the modification is varied for a fixed $\Delta_p = 0.032\ mm$ as visible in Figure 95 and Figure 96 for $\beta = 22.5°$ and for $\beta = 45°$ respectively. The effects are similar to before, and

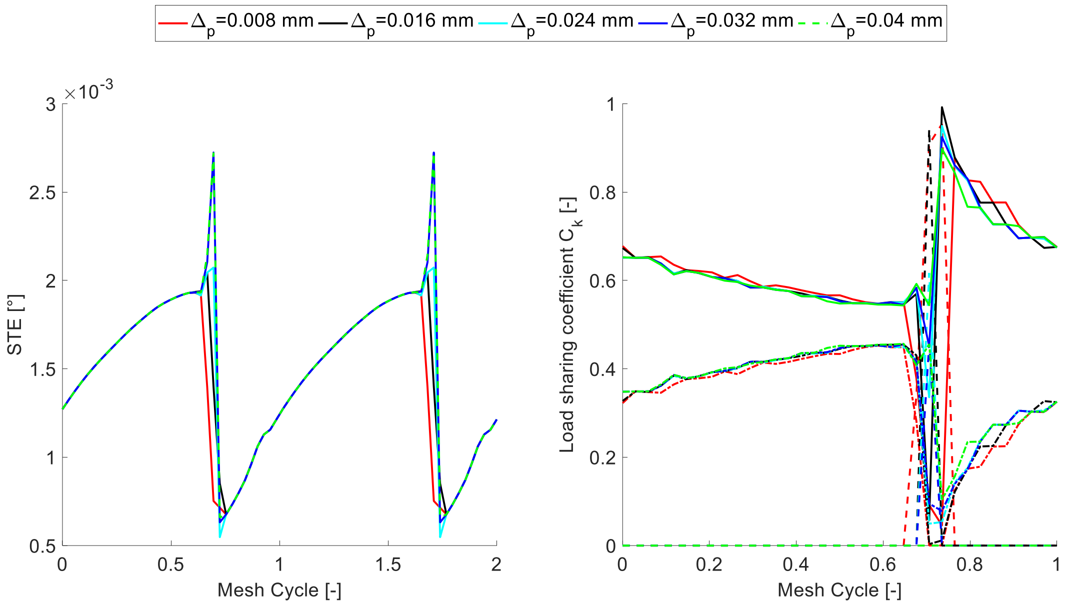

Figure 94: Effect of parabolic tip relief amount of material removed on the STE and load sharing C_k coefficient for $\beta = 45°$ with $l_p = 0.96\ mm$

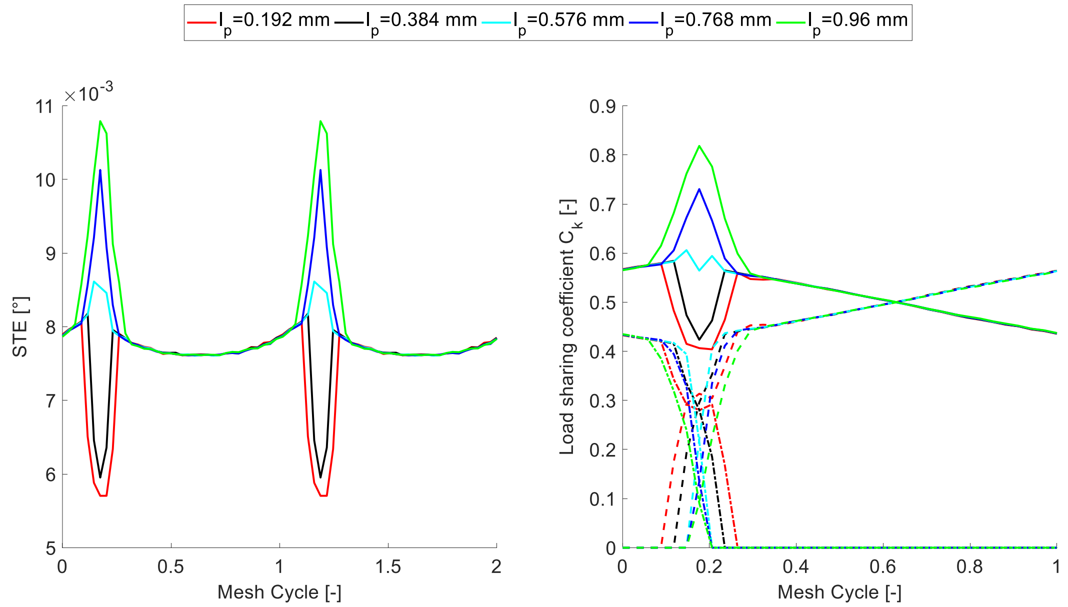

Figure 95: Effect of parabolic tip relief length of modification on the STE and load sharing C_k coefficient for $\beta = 22.5°$ with $\Delta_p = 0.032\ mm$

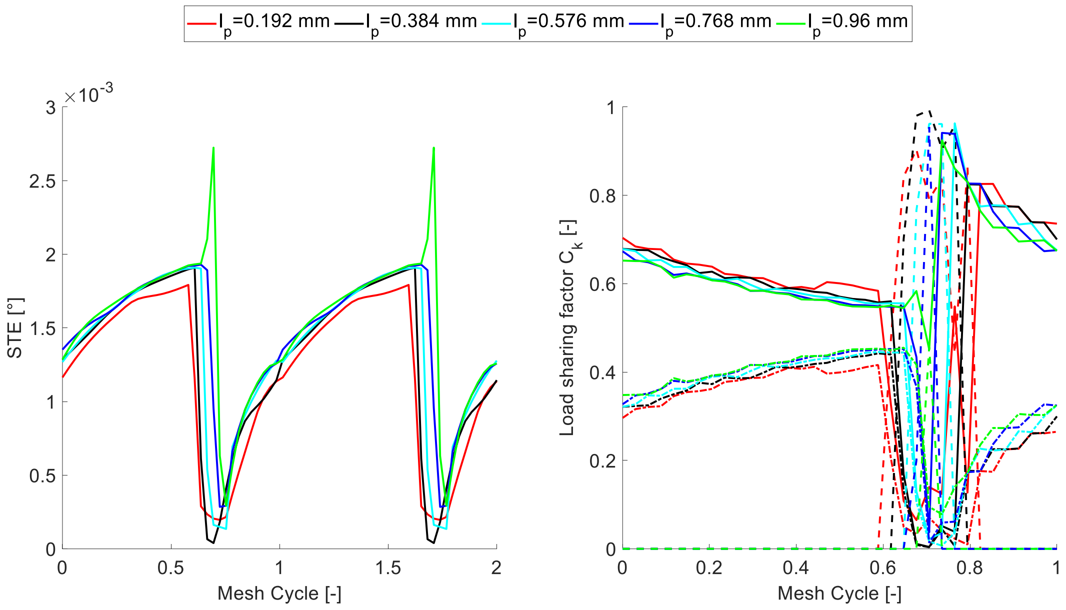

Figure 96: Effect of parabolic tip relief length of modification on the STE and load sharing C_k *coefficient for* $\beta = 45°$ *with* $\Delta_p = 0.032\ mm$

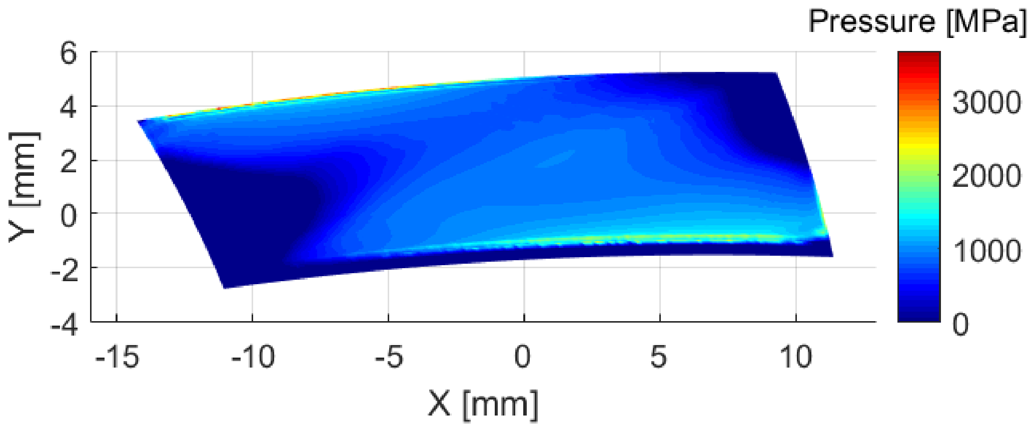

Figure 97: Flank pressure distribution with crowning $\Delta_c = 0.025\ mm$

also the sensitivity of the maximum helix angle is again higher to the modification of this parameter. While the crowning doesn't influence much the STE, its effect can be appreciated when considering the pressure distribution on the flank as visible in Figure 97. Evidently the pressure peaks at the edges are almost completely removed, greatly lowering the maximum pressure, while the peaks at the tip and root of the flank are still present and an evident pressure drop and reduction in the contact area is noticeable during the triple contact region of the engagement. The combination of crowning with linear and parabolic tip relief can be

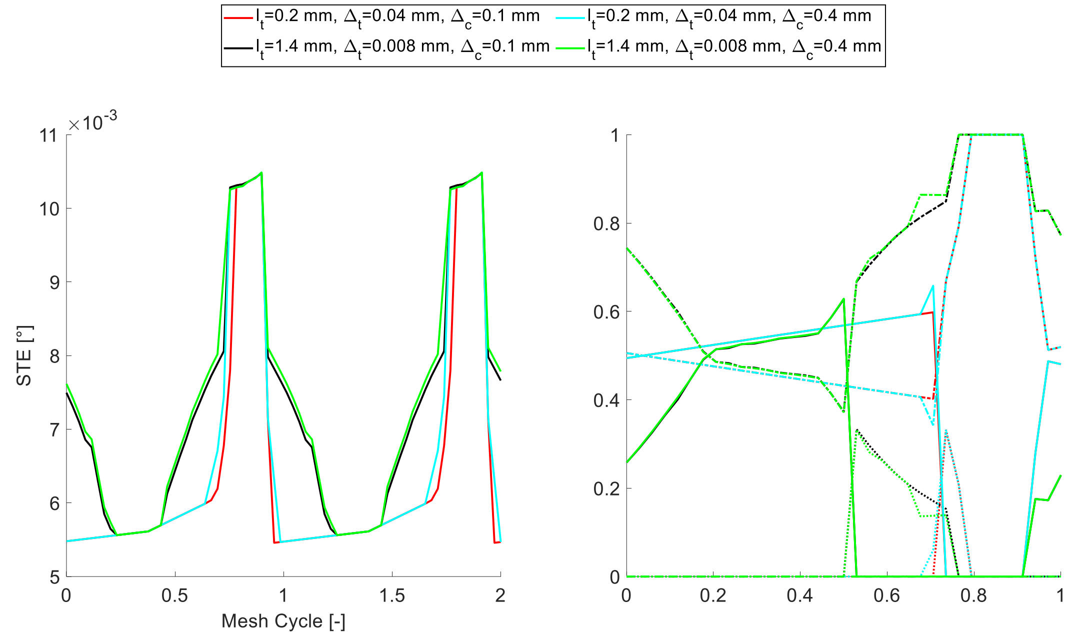

Figure 98: Effect of combinations of crowning and linear tip relief modifications on the STE and load sharing C_k coefficient for $\beta = 22.5°$

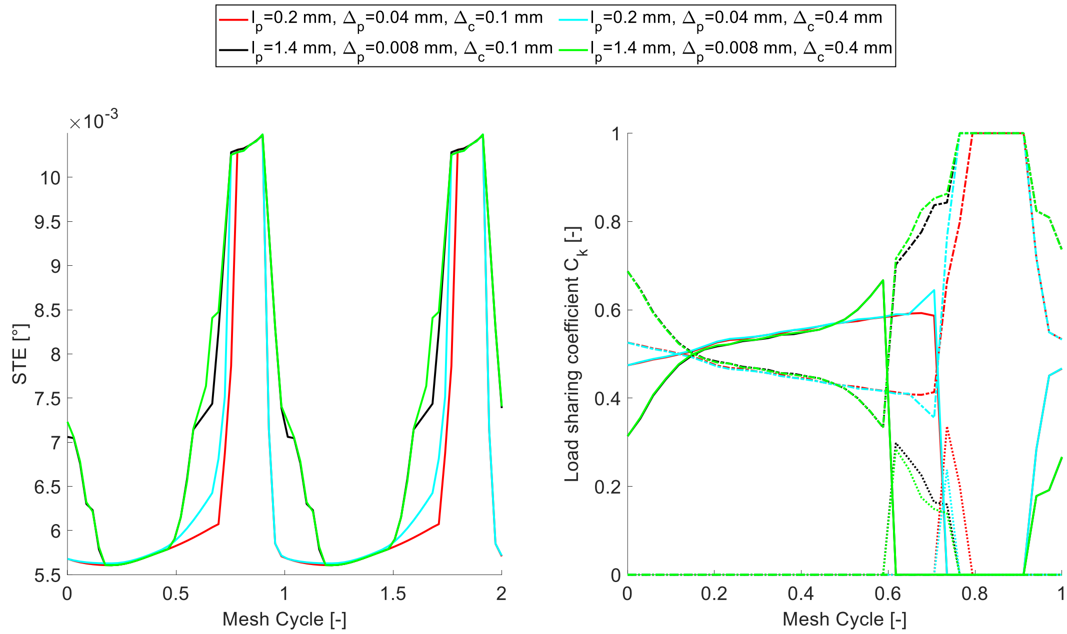

Figure 99: Effect of combinations of crowning and parabolic tip relief modifications on the STE and load sharing C_k coefficient for $\beta = 22.5°$

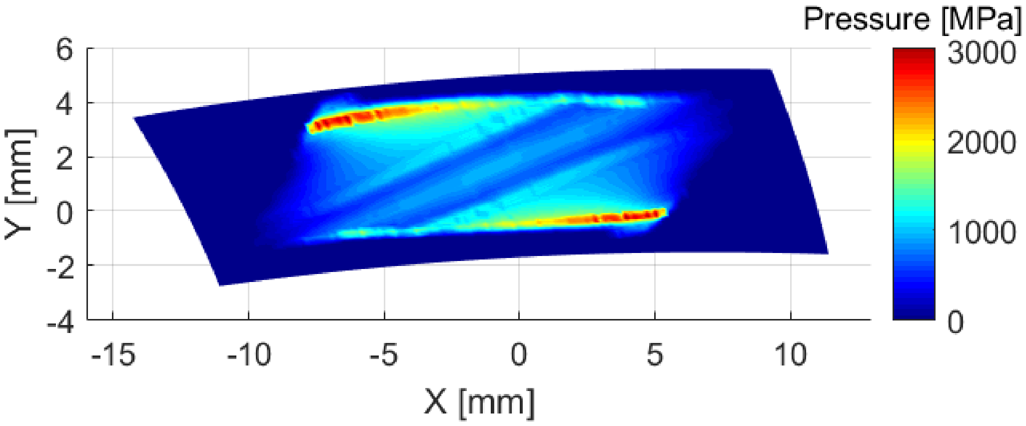

Figure 100: Flank pressure distribution with crowning $\Delta_c = 0.025\ mm$ *and linear tip relief* $\Delta_t = 0.032\ mm, l_t = 0.96\ mm$

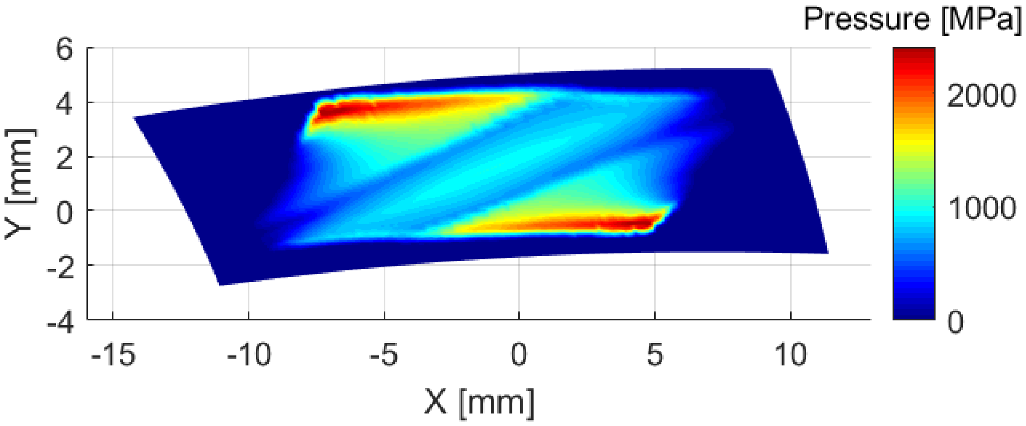

Figure 101: Flank pressure distribution with crowning $\Delta_c = 0.025\ mm$ *and parabolic tip relief* $\Delta_p = 0.032\ mm, l_p = 0.96\ mm$

appreciated in Figure 98 and Figure 99 respectively for $\beta = 22.5°$ where it can be seen that the amount of crowning does not influence too much the STE or the load sharing coefficients. The combination of the effects of crowning and tip relief modifications on the flank pressure distribution is visible in Figure 100 for linear tip relief and in Figure 101 for parabolic tip relief. The cumulative effect of those profile modifications effectively removes the pressure peaks at the tip, root, and edges of the flank, greatly lowering the maximum pressure and confining the contact zone entirely inside the flank for this level of torque considered. Considering the linear tip modification case, the pressure still rises in the zone where the discontinuity from the ideal crowned involute is machined. For the parabolic modification case, the removal rate of the material is lower going from the start of the modification towards the tip and also no discontinuity is introduced allowing the contact zone to extend further up towards the tip and also down towards the root of the flank thus lowering even more the maximum pressure experienced by the flank during its engagement.

V. Experimental test bench

V.1 Introduction

In this chapter a test bench for measuring the Static Transmission Error of two mating gears is presented and a comparison with the results obtained with the previously presented methods will be presented. The test bench illustrated here is designed to evaluate the actual STE of two gears under load in quasi-static conditions. In particular, this testbed can be divided in two macro elements: the first one is the mechanism composed by weights and pulleys that generates a driving and a braking torque up to $500\ Nm$. The second element is composed by two structures called "supports": one fixed to the floor and the other movable in order to be as much as possible flexible to set tests for every kind of gears (spur, helical, bevel, hypoid, etc.). Above these two supports the kinematic chain (shafts, bearings, gears), the torque-meter to measure the instantaneous torque and two high precision angular encoders to detect angular differences up to $10^{-6}\ rad$ are mounted. In literature, the most common existing typologies of test benches for these kinds of applications are:

- Open loop
- Power recirculation

One example of open-loop single-stage test bench developed by Baud and Velex [129] whose operating scheme is shown in Figure 102. This typology is more flexible, but the power supplied by the motor is completely dissipated and therefore the motor and the braking component need to be constantly powered, limiting the maximum power in most applications. This type of test bench is suggested if different kinds and dimensions of gears have to be tested and the power involved is limited. Those researchers used this testbed to find a relationship between the dynamic transmission error (DTE) and the dynamic factor that represents the overload at different spin speed. For the experimental measurement they mounted a set of strain gauges placed at the root of the teeth of the pinion and across the face width of the driven gear. Instead, the power recirculation test bench has higher performance because it permits a substantial recovery from the output torque of the tested

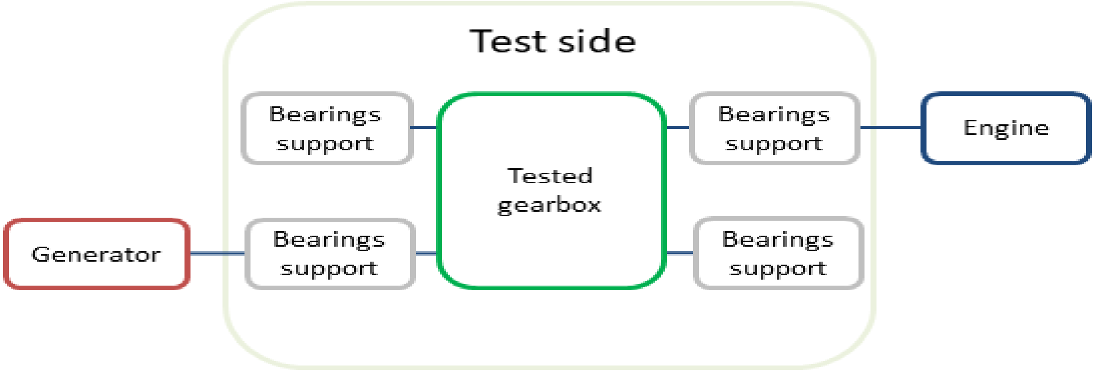

Figure 102: Open loop test bench typical layout

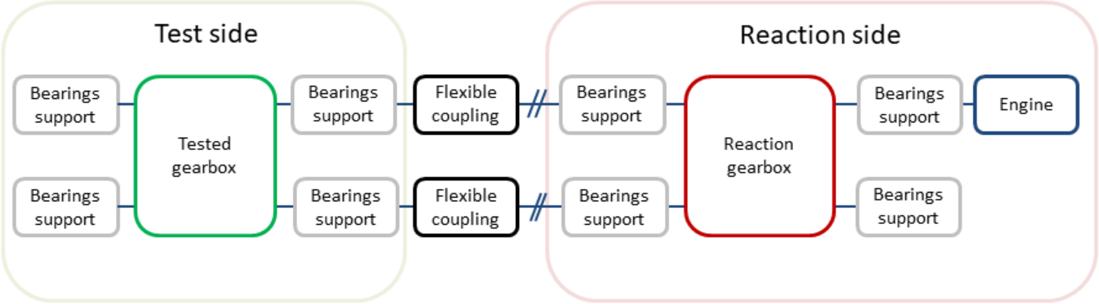

Figure 103: Closed loop power recirculation test bench typical layout

gears, through the use of a secondary gears coupling called reaction pair. The input power is lower than the previous test bench, however, if a different dimension gear pair has to be analyzed, both test and reaction pairs must be designed again. Anyway, the secondary gearbox must be designed in order to resist much longer than any tested gearbox. Figure 103 shows a typical layout involved in a power recirculation test bench. Both Benatar *et al.* [130] and Palermo *et al.* [131] used a set of two rotary encoders to measure the actual angular position of the two different shafts, from which they derived the Transmission Error. The first research group assembled two incremental encoders *Heidenhain RON 287* with $\pm 2.5''$ accuracy and 18000 lines per revolution, whereas the second one mounted two incremental encoders *Heidenhain RON 285C* with $\pm 5''$ accuracy and 18000 lines count per revolution. The aim of the test bench described here is to measure the quasi-static transmission error of a couple of gears and to overcome some limits of both the above-mentioned typologies. On one hand, it has the flexibility of an open-loop testbed without energy dissipation, indeed the torque transmission is provided by a system of moving masses and pulleys. On the other hand, it is useful to analyze every typology of gears with a particular setup that will be described in the next paragraphs.

V.2 Test bench description

Figure 104 shows the whole experimental setup that can be summarized into five main groups of components:

- Structural parts
- Transmission of loads
- Measurement system
- Security system

The structural parts are those that sustain the transmission of the motion and the measurement system, ensuring simultaneously high stiffness and high flexibility in terms of the layout of gears coupling guaranteeing a wide range of testable gears. The transmission of the motion provides an input torque and a braking torque trough the same substructure. The measurement system reads with high precision the information about the deformations involved. Since the masses of the components are consistent, and the risk of harm is high, a security system set the rules for safe setup and test.

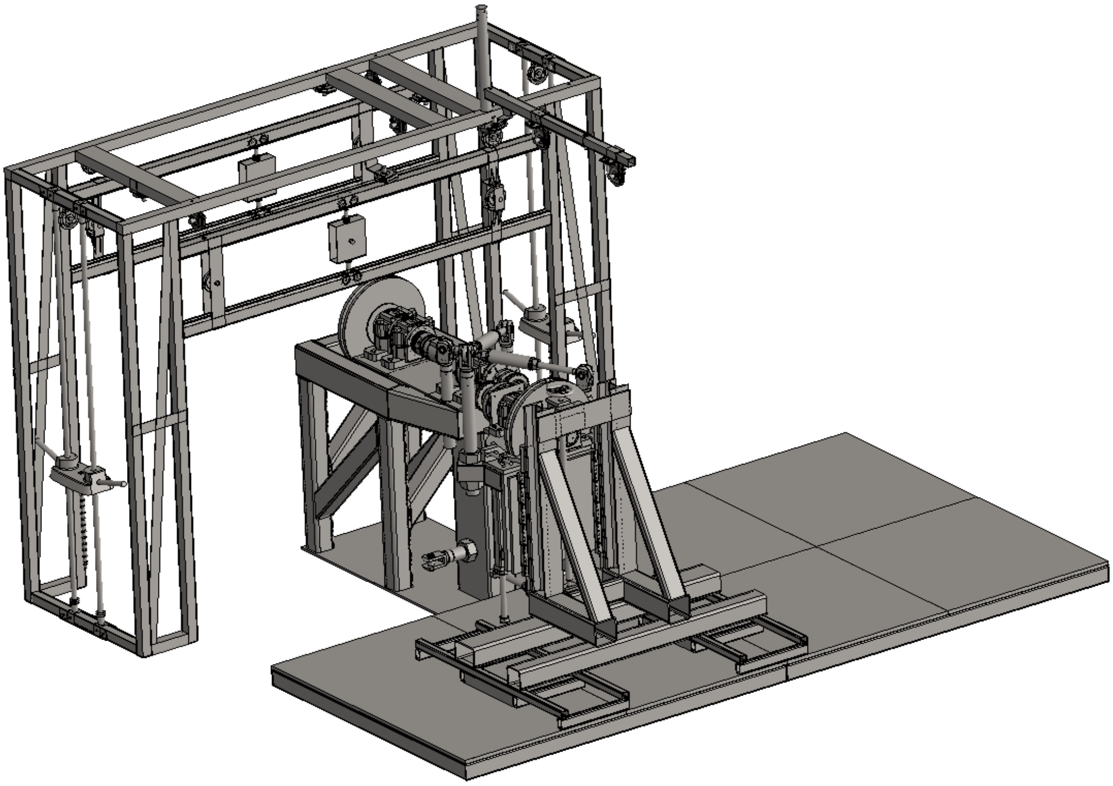

Figure 104: Test bench assembly including all components

V.2.1 Structural parts

The structural parts comprehend five main sub-components:

- Weights support
- Fixed support
- Movable support
- Tie rods
- Fixed platform

In the first one, two sets of "gym" weights are placed at the right and left side of the support. Respectively the right weights are used for the input torque, the left ones for the braking torque and vice versa. The weights are transferred by a series of pulleys to the fixed and movable supports. In particular, the upper part of the support has an *Einhell* hoist lever arm that can transfer the braking/driving torque from the weight support to the braking/driving shaft on the movable support. This arm can be easily adapted to the position of the movable support through a rotation and through two movable brackets. The fixed support is composed by rigid metal profiles on which the input shaft group is located. Furthermore, it is doweled to the ground through a 10 mm steel plate. The movable support, on which the output shaft group is located, can be shifted for the setup over the metallic fixed platform. Once the setup is finished, firstly the tie rods have to be mounted to connect directly the fixed and the movable supports, in order to close the forces loop. Finally, the movable support has to be fixed to the platform through two *SPD* electro-permanent chucks that apply each $100\ kN$ in the vertical direction and can resist up to $20\ kN$ in the tangential direction which are visible in Figure 105. The movable support is the main component of the whole testbed. Once the test gears are mounted on the two shafts, the movable support has to be regulated to ensure the correct engagement. Firstly, the macro-dimensional shifts have to be done

Figure 105: SPD electro-permanent chuck to clamp the movable support

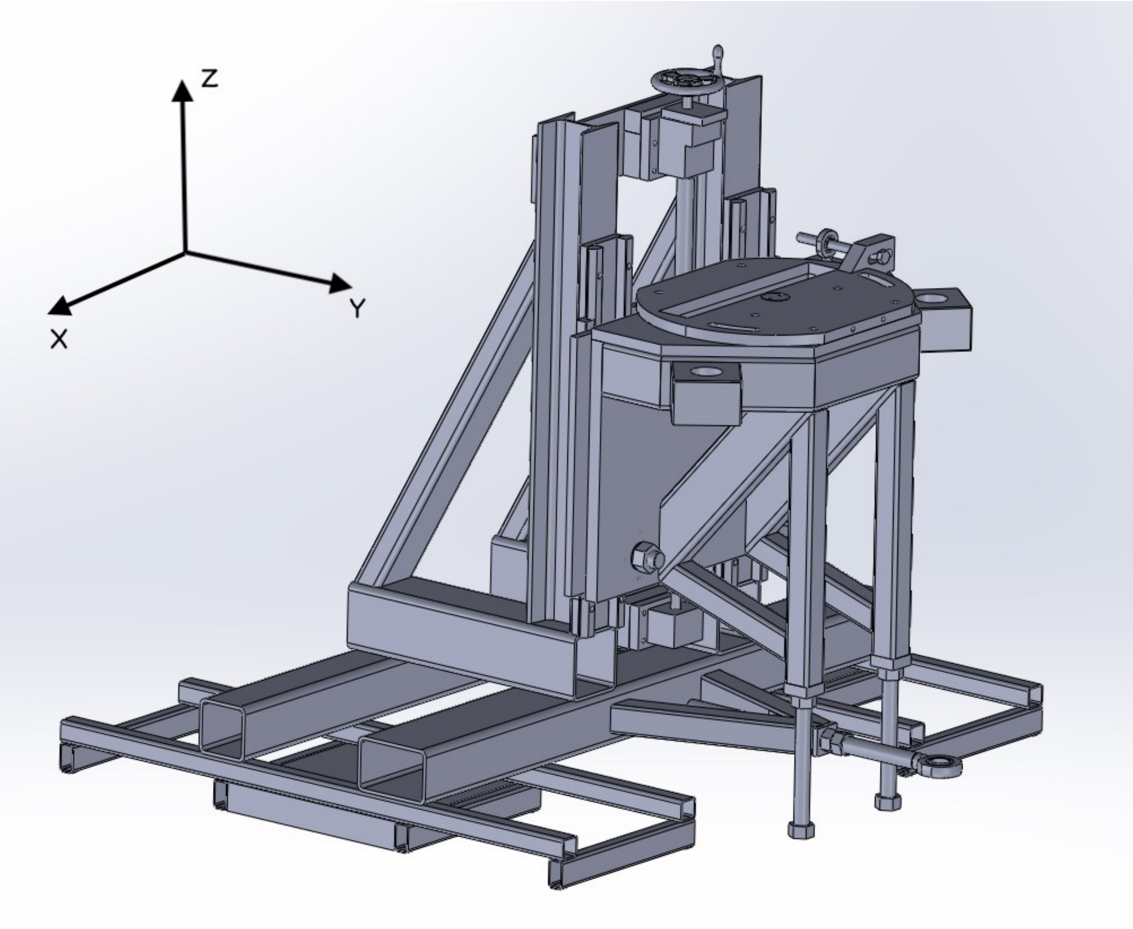

Figure 106: Movable support for macro and micro position adjustments and its reference frame

through a transpallet to approach the driven gear to the driving one at the initial position of the engagement. In Figure 106 the reference frame is established: axis Z along the vertical direction, axis Y along the approaching direction, axis X along the horizontal direction. Since the movable support can be moved around the fixed one, it allows different types of couplings. For instance, if the two shafts are both parallel to the axis Y, cylindrical gear couples can be tested. If the movable shaft lays on axis X, perpendicular or skewed with respect to the fixed one, bevel and spiral bevel gears can be tested. In such a way, all possible gears configuration can be tested, by varying that angle. Afterwards, once the macro-adjustment is done, the movable support is provided with different mechanisms to ensure micro-adjustment in order to achieve correct contact between the tested gears or even to introduce intentional misalignments and measure their effects. The permitted micro-adjustments are linear motion along Y and Z, rotational motion around X and Z. The output

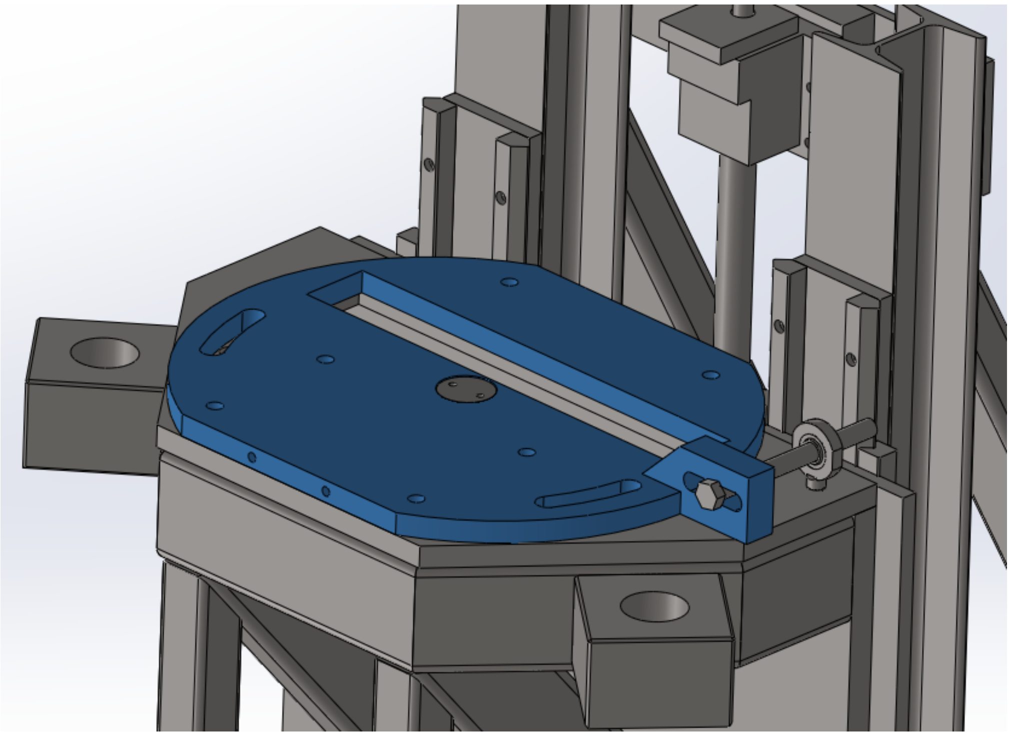

Figure 107: Detail of the plate in the movable support which allows for rotational adjustments around the Z axis

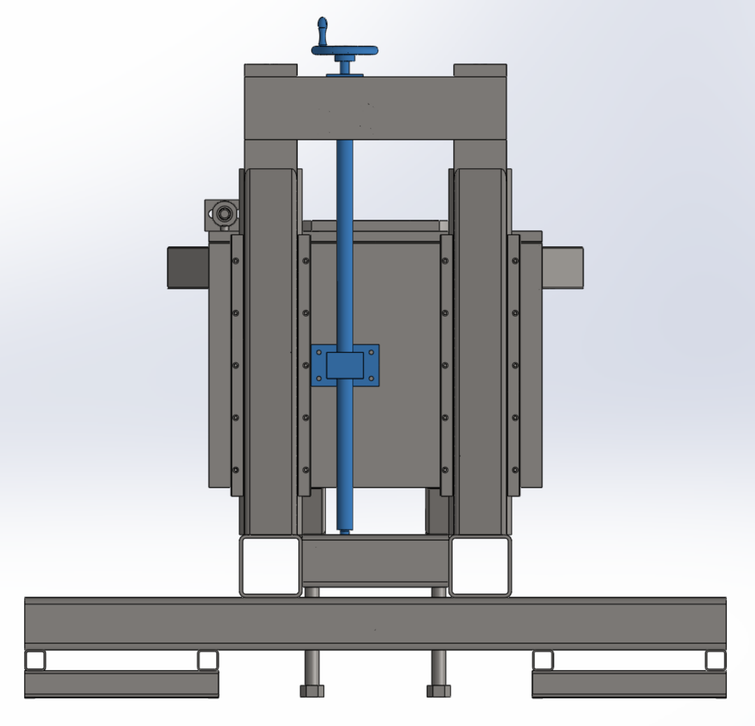

Figure 108: Detail of the backside of the movable support highlighting the trapezoidal screw allowing the vertical adjustments in the Z direction

shaft is mounted on a rotatable platform, shown in Figure 107. This platform can rotate through an adjusting screw with very fine threads around axis Z. This regulation can be used to remove angular misalignment or to see the effect of an imposed misalignment of this kind on the STE. The backside of the support in Figure 108 shows the mechanism that allows the vertical adjustment along the axis Z: a *Bimeccanica s.r.l.* trapezoidal threaded spindle mechanism controlled through a handwheel allows the vertical motion of the gears. Thisregulation can be used to see the effect of a higher center distance of the shafts on the contact ratio and therefore on the STE. Furthermore, there are four threaded screws positioned at the vertices of a rectangle of a vertical plate, with the axis along Y: in particular, depending on which screws and on if they are tightened or loosened, it is possible to obtain fine adjustments along Y or induce a small rotation around axis X.

V.2.2 Transmission of loads

The transmission of the motion transmits the torque from the weights support to the tested gears, respectively the input torque to the gear on the fixed support and the braking torque to the gear on the movable support and vice versa. This transmission is guaranteed by the following sub-groups of components:

- Pulleys and brackets
- Shafts

Once the macro and the micro-adjustments are done, the weights dedicated to the input torque have to be lifted before the test through a hoist, whereas the braking weights have to lay at the bottom. When the test is run, the input torque weights descend while the braking weights start to ascend generating opposing torques in the test gears. Since the measurement has to be done in quasi-static conditions, during the setup of the machine it is necessary to choose the correct amount of weights and the discrepancy between the two sides that, overcoming the internal friction of the system, guarantees a continuous motion at low spin velocity of the gears. The two groups possess a total amount of $125\ kg$ each one, discretely selectable from $5\ kg$ to $125\ kg$. To control the discrepancy needed or to add other weights the system provides two further appendices which can be loaded for a total of $20\ kg$.

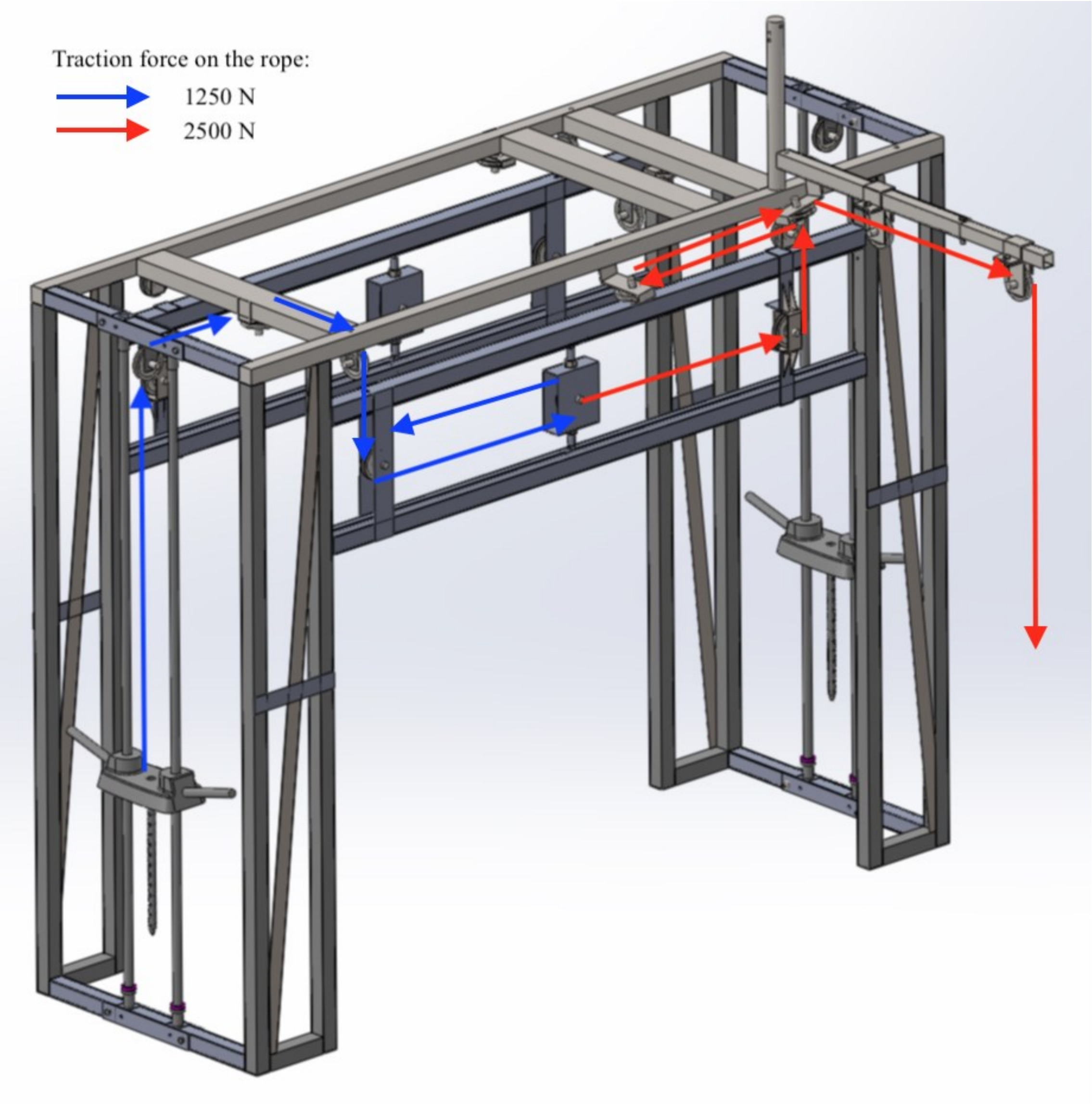

Figure 109: Pulleys setup and path of the forces for the braking weights

The total height of the support is $2\ m$, whereas the average distance run by the weights is about $1.3\ m$. The load generated by the weights is transmitted by means of a $5\ mm$ diameter steel rope that passes through a series of $110\ mm$ diameter pulleys. The path of the forces for the braking torque run through the ropes is represented in figure 9, in the case in which the load of $125 kg$ is lifted. Both paths for the input and the brake are divided identically into two parts, depending on the amount of the force that stresses the rope. Firstly, due to the gravity the force is about $1250\ N$. The force is then doubled by means of a guide pulley that moves horizontally on the weight support: this means that with the maximum weights it is possible to apply a tangential force of $2500N$ at the shafts. At the extremities of the shafts on the fixed and movable supports, two identical pulleys are fixed: their diameter is $400\ mm$. A maximum input torque of $500\ Nm$ is therefore guaranteed. All the pulleys installed on the weights support are made of steel and integrate a ball bearing designed in accordance with *EN10204* standard. The pulleys on the two shafts are manufactured by *Poggi Trasmissioni Meccaniche S.p.A.*, with minor pitch diameter designed according to *ISO R 419* and *DIN 2211*. These pulleys are designed for being coupled with the shaft through a tapered adapter sleeve: due to construction requirements of the testbed, both internal housings have been processed to have a shaft-hub connection through key.

V.2.3 Measurement system

The measurement system is composed by all the items that are used to measure the STE and to monitor the parameters involved during the analysis. In particular, the STE depends strictly on the level of torque, therefore it is necessary to detect the instantaneous trend of the exchanged torque. For this reason, a torque meter has been interposed between the two shafts on the fixed support, through two *R+W BKM 100* model couplings by *R+W Italia s.r.l.* The torque meter is a *T22/500Nm* from *HBM GmbH* that only detects the torque value without any retroactive feedback on the weights, up to $500\ Nm$. Figure 110 shows these components. The two *Heidenhain RCN8580* encoders shown in Figure 111 have been mounted: they are absolute angle encoders of $1''$ accuracy with measuring standard *DIADUR* circular scale with absolute and incremental track of 32768 lines per revolution, which are hence much more accurate than the ones commonly used in literature as discussed in the introduction. The STE is measured by means of the difference of the angular position between the input and the output gears as measured by the encoders. The main difference with the other test benches is the connection between the encoders and the rest of the system. Indeed, in the previous test benches the encoders are fixed at the free-ends of the shafts near the gears and therefore the Transmission Error (TE) is detected from the torsional deformation of the shafts. Whereas, here the STE is measured directly on the gears through the decoupling mechanical joint shown in Figure 112. The decoupling joint is commonly known as quill drive in literature and has been extensively used in the past especially in the railways industry. This mechanism is made of two collars, the one on the left is connected to the rotational part of the encoder, whereas the right one to the gear test article. Between the two collars, a series of elements are used to unite cinematically the two parts: an example of these items' assembly is shown

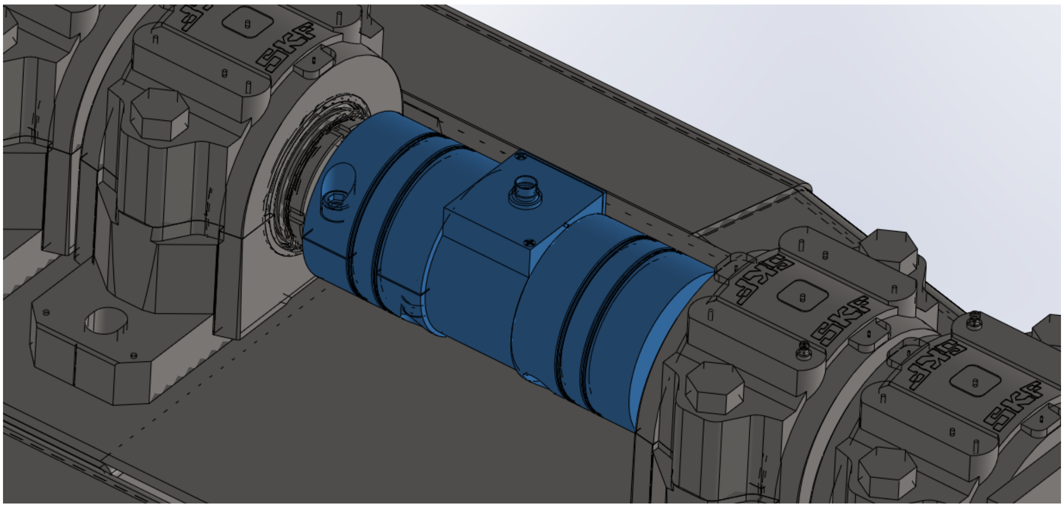

Figure 110: Detail of the torque sensor and the flexible couplings

Figure 111: Heidenhein RCN 8580 Encoder

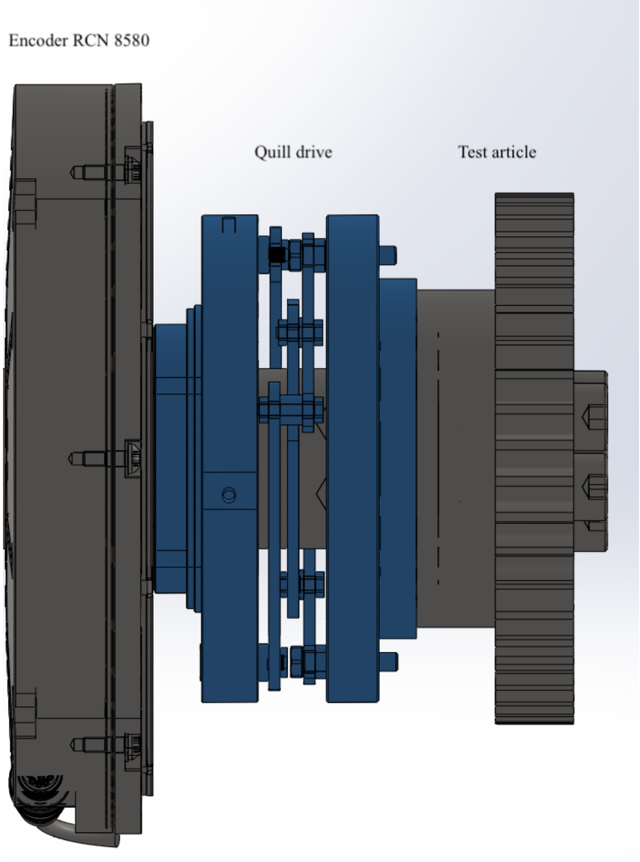

Figure 112: Detail of the quill drive mechanism as designed for the test bench

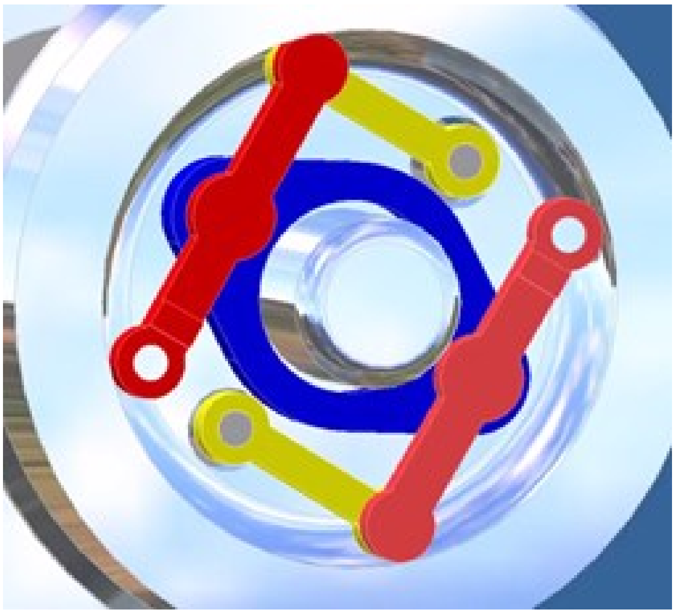

Figure 113: Detail of the quill drive mechanism

in Figure 113. The stationary part of the encoder is fixed on a vertical plate, the shaft passes through them with a significant tolerance and is axially fixed to the test article through five screws. In this way, the deformations coming from the gear are decoupled: the torsional one, that is the one of interest for the STE evaluation, is transferred from the collar on the right to the left one and therefore is read by the encoder; whereas the others, in the radial and axial directions due to the respective loads acting on the test gears, are absorbed by the elements between the two collars. Thus, essentially this kind of joint is employed to decouple the tangential deformation from the other ones, ensuring that the encoder reads the correct deformation and is unloaded if its inner reacting torque due to internal friction is neglected.

V.2.4 Security system

The test bench does not require a certification in accordance with machinery directive *2006/42/CE*, however it has to respond to the essential requirements of security according to the law. Therefore, it is necessary to provide appropriate safety systems not to expose people to any kind of danger. Consequently, a perimetral safety grate surrounds the whole test bench and an access door with an interlocked retention system is provided, as shown in Figure 114. The latter is connected with a pressure air system that blocks the weights and unblocks the electro-permanent chucks of the movable support when the entrance door is open, in order to avoid accidental movements of the weights. The test can be run only when the operator stays outside the tested area, outside safety grate. The test bench as assembled in the laboratory of Politecnico di Torino is visible in Figure 115.

Figure 114: Safety grating and control panel of the test bench

Figure 115: Test bench as assembled in the laboratory

V.3 Results

The gear pair tested is visible in Figure 116 and the main parameters of the two identical gears are listed in Table 7. Those are scraps of production provided by *Licat s.r.l.* for free and as such they haven't undergone the process of case hardening as expected by design requirements and more importantly they haven't undergone the final processes to finish the engaging flanks and thus still have machining allowances which strongly impact their

Table 7: Test gear pair parameters

Gear Parameters	Dimensions
Module m	$3\ mm$
Profile shift x	$-1.11\ mm$
Number of teeth Z	46
Pressure angle α	$20°$
Face width b	$20\ mm$
Material Ovako 255G	**Value**
Chemical composition	18NiCrMo14-6
E	$210\ GPa$
ν	0.3

Figure 116: Test gear pair

engaging. The reason why those gears were scrapped during production is that during the manufacturing operation, right after the teeth were roughed, an important run-out error was found, which at that point was impossible to correct, and were therefore discarded. In order to at least mitigate this defect, the initial meshing position of the gears was chosen to line-up the angular positions in which the gear on the fixed support has the maximum (positive) run-out error with the one in which the gear on the movable support has the minimum (negative) run-out error so that during the engagement the two effects partially compensate each other. Completely removing this error has not been possible as will be visible later since the average error for both gears is in the order of $\pm 0.6\ mm$. Furthermore, the gears have suffered significant damages due to poor handling and storing as visible in Figure 117, where important scores and signs of oxidation are visible. By design those gears were not meant to engage with each other and indeed both have a negative profile shifting, rather than a symmetric one, or some other combination which would result in an approximate equality in bending strength factors or in an approximate equality of ratios of specific sliding or slide/roll ratio. Despite those circumstances some preliminary tests have been performed which, while not useful for the experimental validation of the proposed approaches earlier presented, have highlighted some needed changes that are currently in production to solve slight unforeseen design flaws. The first step was to verify the repeatability of the measurements despite the aforementioned issues. The gears have been made to mesh together by slowly turning the pulley of the movable support at a rather constant speed and applying the bare

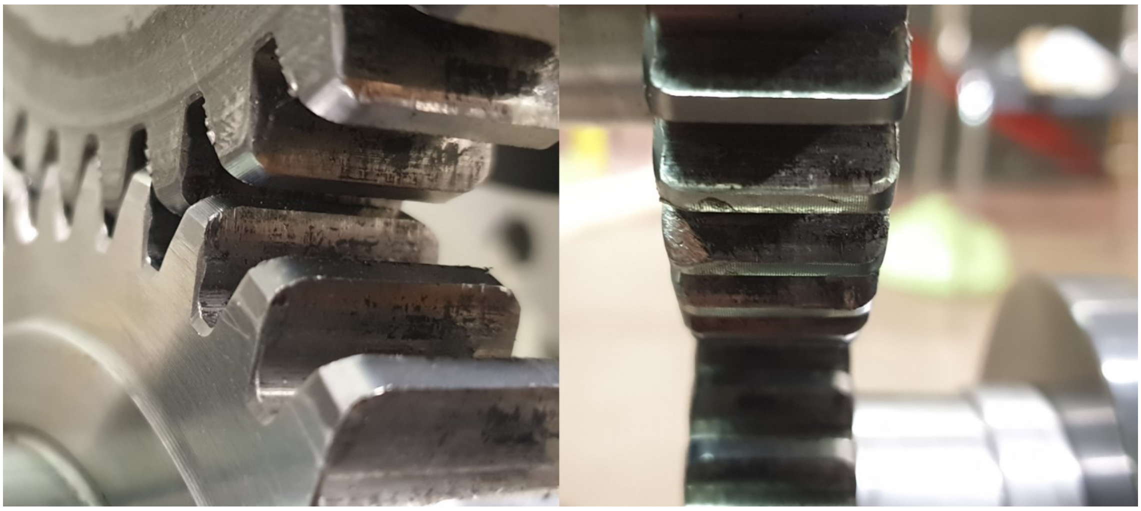

Figure 117: Examples of the damages on the flanks

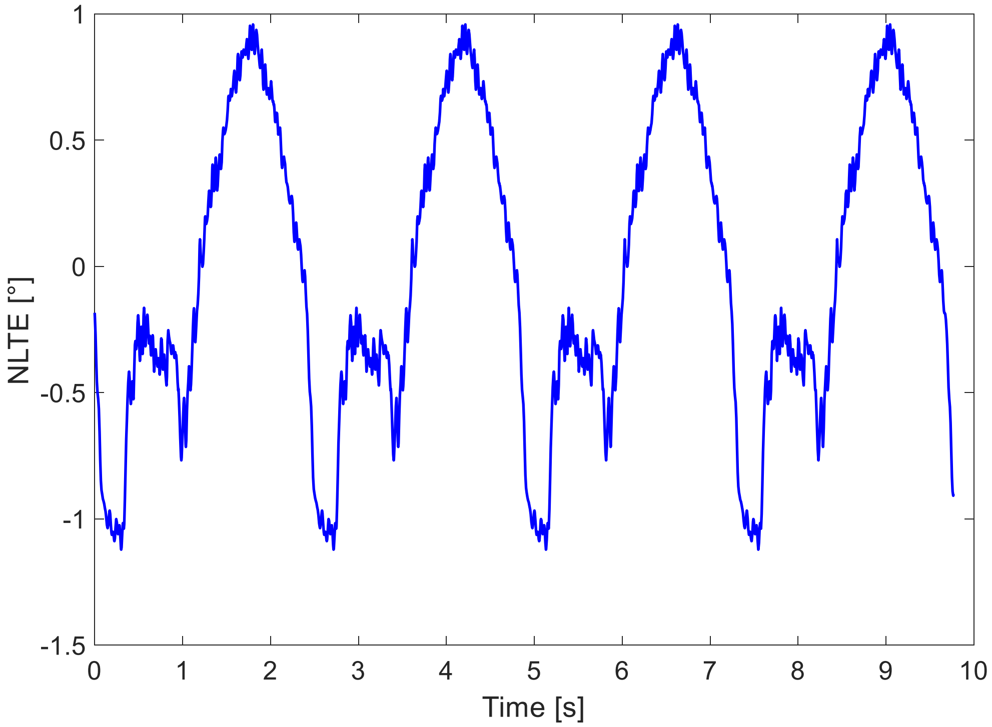

Figure 118: No Load Transmission Error

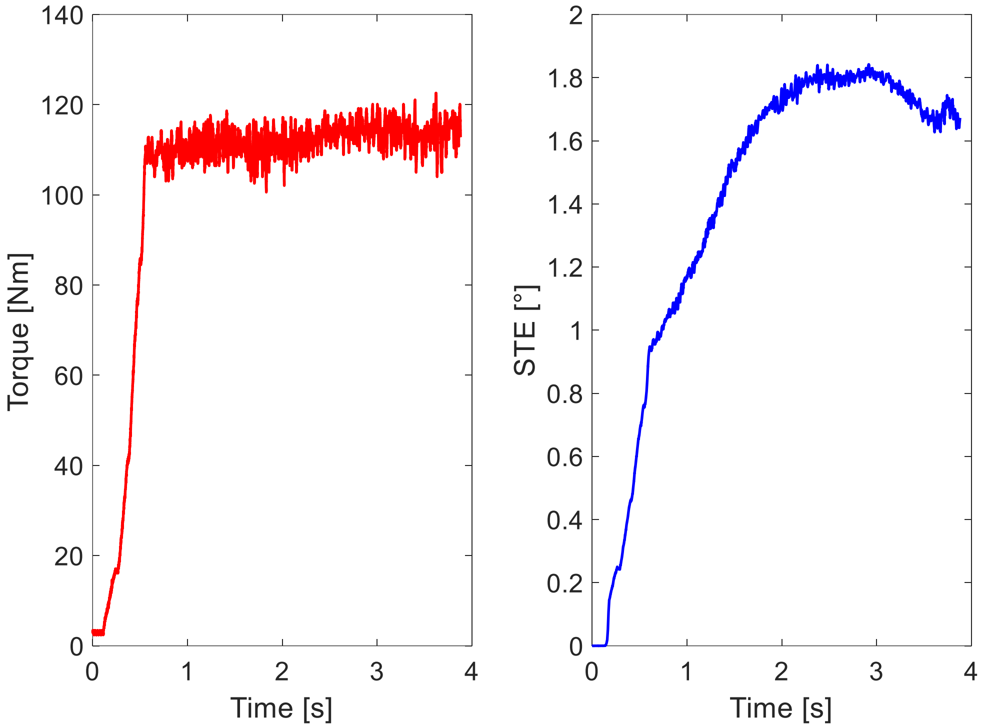

Figure 119: Test results at $110\ Nm$

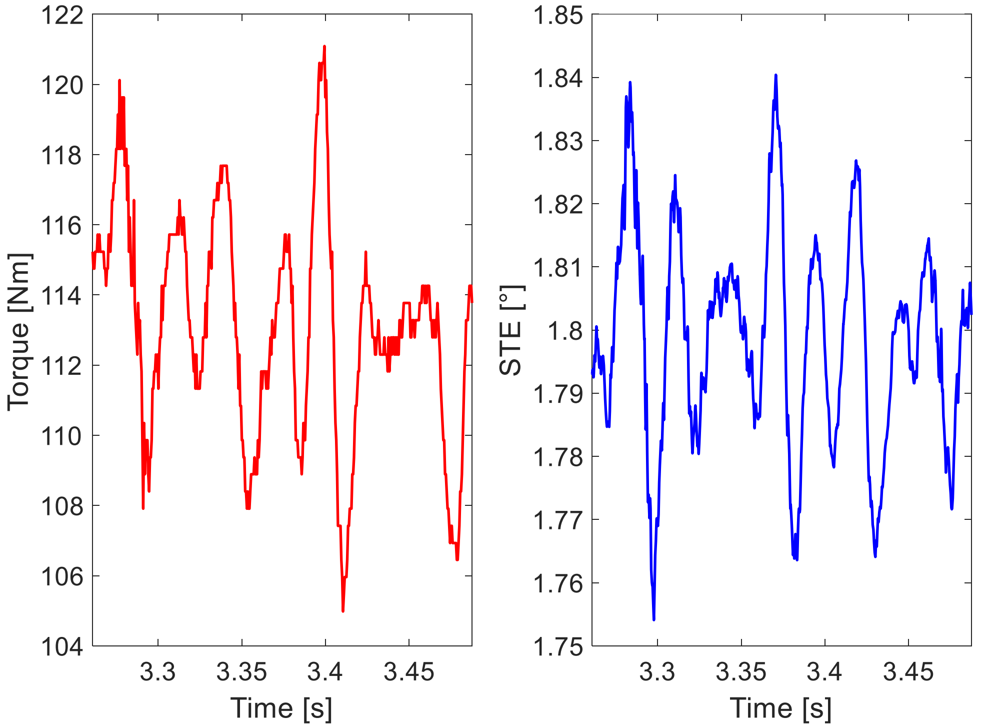

Figure 120: Detail of the test results at $110\ Nm$

minimum load so as to measure the NLTE which is shown in Figure 118. The acquired signal is extremely repeatable and shows the huge impact that the run-out error has during the rotation of the gears which causes oscillations of about $\pm1°$. Nevertheless, tests have been also performed at different torque levels for example the results at 110 Nm are shown in Figure 119 where the acquired signals of both the torque meter and encoders are shown with a load difference between the sides small enough just to overcome internal frictions. The end of the signal acquisition is determined by the termination of the descent of the weights which stops the rotation of the gears but keeps them under load. Aside for the impact on the measured STE of the run-out error also the torque is oscillating which makes a correlation of the experimental data with the computed values even harder. Indeed, there is a strong correlation with the fluctuation of the torque and the measured values as is visible in Figure 120 where the torque is seen varying up to $15\ Nm$, considerably impacting the results, which are made even worse by the damages on the flanks. The cause of the torque oscillation has been found in the alternating pivoting motion occurring in the load weight packs as they descend or ascend. The weight packs are commercially available and are sold together with the $20\ mm$ round steel guides set $250mm$ apart from each other. The guides and the weights are connected only through a pair of short ($20\ mm$) plastic bushings placed on the first weight ingot as visible in Figure 121. Since the bushings are very compliant and the holes have not been precisely manufactured, when the weights descend one of the two bushings is pressed harder than the other against its guide rod, generating friction, while the other descends more and then finds itself hardly pressed against the guide, freeing the other one which then descends more than its counterpart. This process repeats itself up until the weights have completed their descent and cause the oscillations in the torque seen before. This has been verified firstly by inspecting the bushings, which appear already damaged even tough very few tests have been performed at relatively low loads, but also by increasing the difference in weights as much as possible thus increasing their descent speed. The results of this test are visible in Figure 122 in which severe torque fluctuations are evident and indeed, during the quick descent of the weights the guide rods were seen to be severely oscillating from side to side due to this alternating pivoting motion in the compliant bushings. To remove this issue a solution is being manufactured. The plastic bushings will be substituted with much stiffer and longer linear bearings with ball recirculation housed in a support in which they will be placed in holes precisely manufactured $250\ mm$ from each other. This should remove the pivoting effect since the guides and the linear bearings will be at the correct

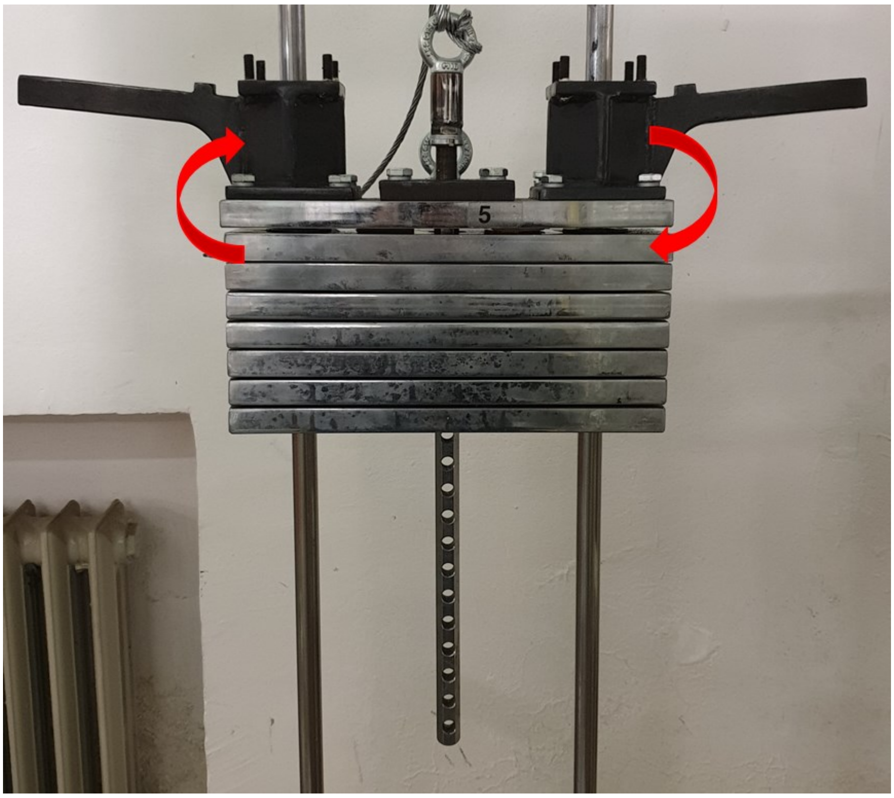

Figure 121: Oscillation of the weight pack causing torque fluctuations

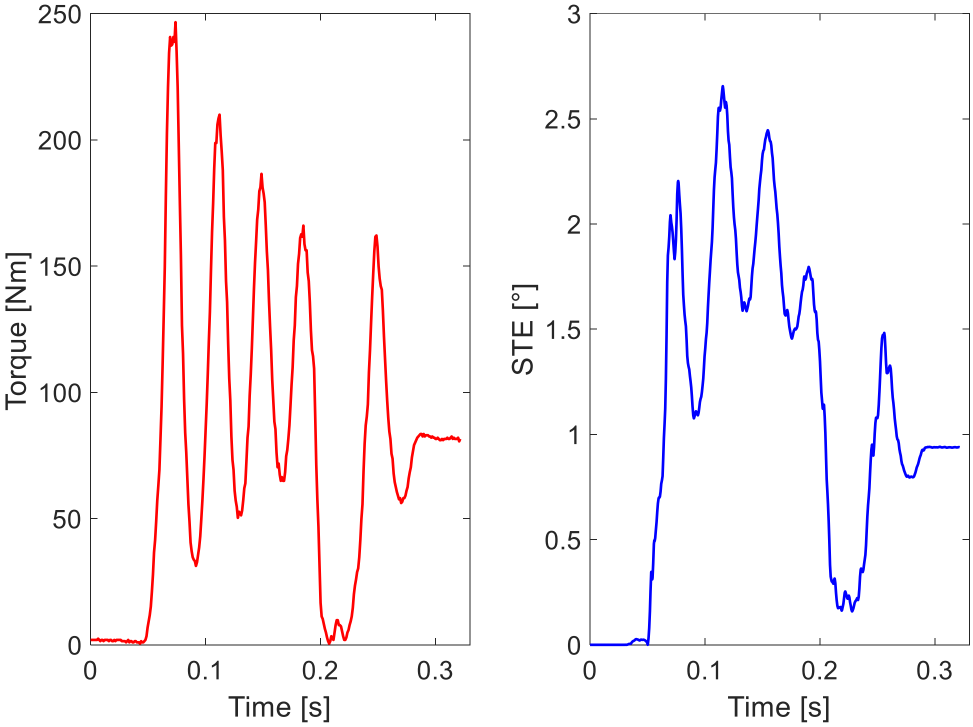

Figure 122: Test results at $80\ \mathrm{Nm}$ *with increased weight difference*

distance and will also be much stiffer, thus smoothly guiding the weights. As evident the results here presented are not suitable for any kind of experimental comparison, but they will be updated as soon as the new parts are manufactured and precision gears, with allowable tolerances, will be available. Unfortunately, due to the emergency and lockdown due to the COVID-19 pandemic the laboratory was not accessible for any kind of test. Furthermore the manufacturers of the needed parts to improve the behavior of the test bench and remove the defects described above have severely limited their operation, focusing entirely to the production of parts needed by the agribusiness industry, causing severe delays in the procurement and production of components. At the time of writing the suppliers have not fixed an estimated date of shipping for the upgrades and due to the time constraints for imposed by the university it is not known if further results will be available before the final dissertation.

VI. Compliant gear dynamics

VI.1 Introduction

In this chapter a scheme to compute the dynamic response in the time domain for a gear using a set of Reduced Order Models (ROM) will be described. In order to get the most accurate response possible a FE representation of the gear will be used, and therefore the formulation of the employed element, an 8-node solid brick, will be described first. Next, the algorithm used to obtain the dynamic behavior of the considered gear will be detailed which will use a Newmark scheme using a constant angular difference between two successive time instants, rather than a constant time step as common in literature. Then, the proposed algorithm will be applied to a gear with flexible teeth, but a rigid web and several results will be shown, including the effect of the gyroscopic effect on its dynamics. Finally, the same approach will be applied to a gear with a thin compliant web and again several results will be shown, including the effect of the introduction of the stress stiffening phenomenon and that of different profile modifications.

VI.2 FE formulation

In order to simulate the dynamic response of a compliant gear, a FE model is required, and the implemented formulation will be described here. The element chosen is an isoparametric 8-node brick element, also known as Hexa8, whose global reference frame (X, Y, Z) and the local one (ξ, η, ζ) in which the nodes coordinates assume the values of ± 1 is visible in Figure 123 [132] [133]. For a generic element the coordinates in the local reference frame (x, y, z) are obtained from the coordinates of the nodes in the global reference (x_i, y_i, z_i) frame as

$$
\begin{aligned}
x &= \sum_{i=1}^{8} n_i(\xi, \eta, \zeta) x_i \\
y &= \sum_{i=1}^{8} n_i(\xi, \eta, \zeta) y_i \\
z &= \sum_{i=1}^{8} n_i(\xi, \eta, \zeta) z_i
\end{aligned}
\tag{6.1}
$$

Where the shape functions n_i are defined as

$$
\begin{aligned}
n_1 &= \tfrac{1}{8}(1-\xi)(1-\eta)(1-\zeta) \quad n_2 = \tfrac{1}{8}(1+\xi)(1-\eta)(1-\zeta) \\
n_3 &= \tfrac{1}{8}(1+\xi)(1+\eta)(1-\zeta) \quad n_4 = \tfrac{1}{8}(1-\xi)(1+\eta)(1-\zeta) \\
n_5 &= \tfrac{1}{8}(1-\xi)(1-\eta)(1+\zeta) \quad n_6 = \tfrac{1}{8}(1+\xi)(1-\eta)(1+\zeta) \\
n_7 &= \tfrac{1}{8}(1+\xi)(1+\eta)(1+\zeta) \quad n_8 = \tfrac{1}{8}(1-\xi)(1+\eta)(1+\zeta)
\end{aligned}
\tag{6.2}
$$

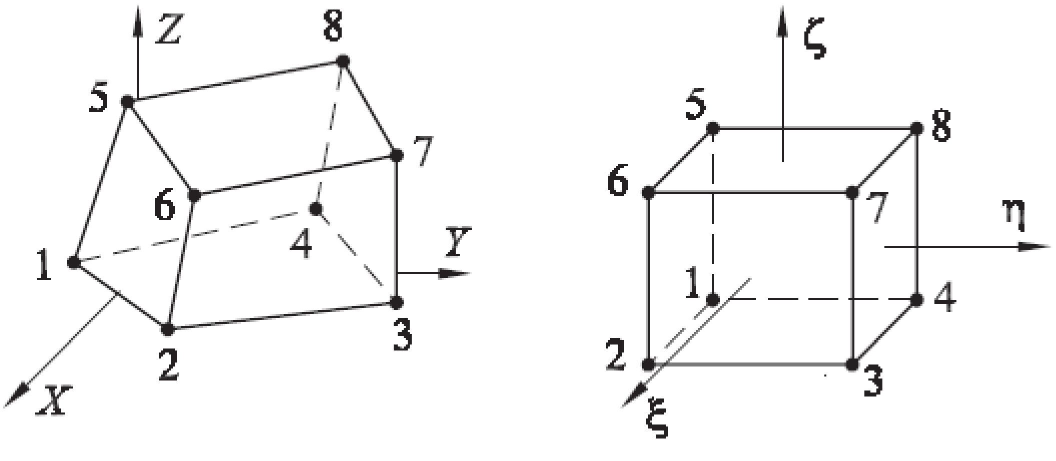

Figure 123: Global (X, Y, Z) and local (ξ, η, ζ) reference frames [132]

The derivatives of the shape functions with respect to the natural reference frame are then

$$
\begin{aligned}
&\frac{\partial n_1}{\partial \xi} = -\tfrac{1}{8}(1-\eta)(1-\zeta) && \frac{\partial n_1}{\partial \eta} = -\tfrac{1}{8}(1-\xi)(1-\zeta) && \frac{\partial n_1}{\partial \zeta} = -\tfrac{1}{8}(1-\xi)(1-\eta)\\
&\frac{\partial n_2}{\partial \xi} = \tfrac{1}{8}(1-\eta)(1-\zeta) && \frac{\partial n_2}{\partial \eta} = -\tfrac{1}{8}(1+\xi)(1-\zeta) && \frac{\partial n_2}{\partial \zeta} = -\tfrac{1}{8}(1+\xi)(1-\eta)\\
&\frac{\partial n_3}{\partial \xi} = \tfrac{1}{8}(1+\eta)(1-\zeta) && \frac{\partial n_3}{\partial \eta} = \tfrac{1}{8}(1+\xi)(1-\zeta) && \frac{\partial n_3}{\partial \zeta} = -\tfrac{1}{8}(1+\xi)(1+\eta)\\
&\frac{\partial n_4}{\partial \xi} = -\tfrac{1}{8}(1+\eta)(1-\zeta) && \frac{\partial n_4}{\partial \eta} = \tfrac{1}{8}(1-\xi)(1-\zeta) && \frac{\partial n_4}{\partial \zeta} = -\tfrac{1}{8}(1-\xi)(1+\eta)\\
&\frac{\partial n_5}{\partial \xi} = -\tfrac{1}{8}(1-\eta)(1+\zeta) && \frac{\partial n_5}{\partial \eta} = -\tfrac{1}{8}(1-\xi)(1+\zeta) && \frac{\partial n_5}{\partial \zeta} = \tfrac{1}{8}(1-\xi)(1-\eta)\\
&\frac{\partial n_6}{\partial \xi} = \tfrac{1}{8}(1-\eta)(1+\zeta) && \frac{\partial n_6}{\partial \eta} = -\tfrac{1}{8}(1+\xi)(1+\zeta) && \frac{\partial n_6}{\partial \zeta} = \tfrac{1}{8}(1+\xi)(1-\eta)\\
&\frac{\partial n_7}{\partial \xi} = \tfrac{1}{8}(1+\eta)(1+\zeta) && \frac{\partial n_7}{\partial \eta} = \tfrac{1}{8}(1+\xi)(1+\zeta) && \frac{\partial n_7}{\partial \zeta} = \tfrac{1}{8}(1+\xi)(1+\eta)\\
&\frac{\partial n_8}{\partial \xi} = -\tfrac{1}{8}(1+\eta)(1+\zeta) && \frac{\partial n_8}{\partial \eta} = \tfrac{1}{8}(1-\xi)(1+\zeta) && \frac{\partial n_8}{\partial \zeta} = \tfrac{1}{8}(1-\xi)(1+\eta)
\end{aligned}
\tag{6.3}
$$

The displacements in the global reference frame are transformed to the local one in the same way, as

$$
\begin{aligned}
u &= \sum_{i=1}^{8} n_i(\xi,\eta,\zeta)u_i\\
v &= \sum_{i=1}^{8} n_i(\xi,\eta,\zeta)v_i\\
w &= \sum_{i=1}^{8} n_i(\xi,\eta,\zeta)w_i
\end{aligned}
\tag{6.4}
$$

where u_i, v_i, w_i are the displacements of the nodes with respect to the undeformed configuration (x_i, y_i, z_i). The stiffness matrix $\boldsymbol{K_e}$ of each element can be obtained by integrating over its volume the energy of deformation as

$$\boldsymbol{K_e} = \int_V \boldsymbol{B^T D B}\, dV \tag{6.5}$$

where $\boldsymbol{B}$ is the strain-displacement relationship matrix

$$\boldsymbol{B} =$$

$$= \begin{bmatrix}
\frac{\partial n_1}{\partial x} & \cdots & \frac{\partial n_i}{\partial x} & \cdots & \frac{\partial n_8}{\partial x} & & & & & & & & & & \\
& & & & & \frac{\partial n_1}{\partial y} & \cdots & \frac{\partial n_i}{\partial y} & \cdots & \frac{\partial n_8}{\partial y} & & & & & \\
& & & & & & & & & & \frac{\partial n_1}{\partial z} & \cdots & \frac{\partial n_i}{\partial z} & \cdots & \frac{\partial n_8}{\partial z} \\
& & & & & \frac{\partial n_1}{\partial y} & \cdots & \frac{\partial n_i}{\partial y} & \cdots & \frac{\partial n_8}{\partial y} & \frac{\partial n_1}{\partial z} & \cdots & \frac{\partial n_i}{\partial z} & \cdots & \frac{\partial n_8}{\partial z} \\
\frac{\partial n_1}{\partial x} & \cdots & \frac{\partial n_i}{\partial x} & \cdots & \frac{\partial n_8}{\partial x} & & & & & & \frac{\partial n_1}{\partial z} & \cdots & \frac{\partial n_i}{\partial z} & \cdots & \frac{\partial n_8}{\partial z} \\
\frac{\partial n_1}{\partial x} & \cdots & \frac{\partial n_i}{\partial x} & \cdots & \frac{\partial n_8}{\partial x} & \frac{\partial n_1}{\partial y} & \cdots & \frac{\partial n_i}{\partial y} & \cdots & \frac{\partial n_8}{\partial y} & & & & &
\end{bmatrix} \tag{6.6}$$

and $\boldsymbol{D}$ is the matrix defining the elastic properties of the material

$$\boldsymbol{D} = \frac{E}{(1+\nu)(1-\nu)} \begin{bmatrix}
1-\nu & \nu & \nu & & & \\
\nu & 1-\nu & \nu & & & \\
\nu & \nu & 1-\nu & & & \\
& & & \frac{1-2\nu}{2} & & \\
& & & & \frac{1-2\nu}{2} & \\
& & & & & \frac{1-2\nu}{2}
\end{bmatrix} \tag{6.7}$$

while V is the volume of the element. In the previous formulas and in the following ones empty places in the matrices denote zeroes. In the strain-displacement matrix $\boldsymbol{B}$ the derivatives of the shape functions with respect to the global reference frame are present and those can be obtained trough

$$\begin{Bmatrix} \dfrac{\partial n_i}{\partial \xi} \\ \dfrac{\partial n_i}{\partial \eta} \\ \dfrac{\partial n_i}{\partial \zeta} \end{Bmatrix} = \boldsymbol{J} \begin{Bmatrix} \dfrac{\partial n_i}{\partial x} \\ \dfrac{\partial n_i}{\partial y} \\ \dfrac{\partial n_i}{\partial z} \end{Bmatrix} \tag{6.8}$$

where $\boldsymbol{J}$ is the Jacobian of the coordinate transformation

$$\boldsymbol{J} = \begin{bmatrix} \dfrac{\partial x}{\partial \xi} & \dfrac{\partial y}{\partial \xi} & \dfrac{\partial z}{\partial \xi} \\ \dfrac{\partial x}{\partial \eta} & \dfrac{\partial y}{\partial \eta} & \dfrac{\partial z}{\partial \eta} \\ \dfrac{\partial x}{\partial \zeta} & \dfrac{\partial y}{\partial \zeta} & \dfrac{\partial z}{\partial \zeta} \end{bmatrix} \tag{6.9}$$

And the components are obtained as:

$$\frac{\partial x}{\partial \xi} = \sum_{i=1}^{8} \frac{\partial n_i}{\partial \xi} x_i, \qquad \frac{\partial y}{\partial \xi} = \sum_{i=1}^{8} \frac{\partial n_i}{\partial \xi} y, \dots \tag{6.10}$$

And similarly, for the other components. Finally, the partial derivatives of the shape functions needed to form the $\boldsymbol{B}$ matrix are obtained as

$$\begin{Bmatrix} \dfrac{\partial n_i}{\partial x} \\ \dfrac{\partial n_i}{\partial y} \\ \dfrac{\partial n_i}{\partial z} \end{Bmatrix} = \boldsymbol{J^{-1}} \begin{Bmatrix} \dfrac{\partial n_i}{\partial \xi} \\ \dfrac{\partial n_i}{\partial \eta} \\ \dfrac{\partial n_i}{\partial \zeta} \end{Bmatrix} \tag{6.11}$$

Therefore, in the natural coordinates frame the infinitesimal volume for integration can hence be expressed as $dV = \det(\boldsymbol{J})\, d\xi d\eta d\zeta$ and therefore the integral in becomes

$$\boldsymbol{K_e} = \int_{-1}^{1} \int_{-1}^{1} \int_{-1}^{1} \boldsymbol{B^T D B} \det(\boldsymbol{J})\, d\xi d\eta d\zeta \tag{6.12}$$

In order to evaluate this integral a numerical integration scheme is employed and for this kind of element a 2x2x2 Gauss scheme is used, in which each integration point has unit weight and coordinates [134]

$$\begin{aligned} &I{:}\left(-\frac{\sqrt{3}}{3},-\frac{\sqrt{3}}{3},-\frac{\sqrt{3}}{3}\right), \qquad && II{:}\left(\frac{\sqrt{3}}{3},-\frac{\sqrt{3}}{3},-\frac{\sqrt{3}}{3}\right) \\ &III{:}\left(\frac{\sqrt{3}}{3},\frac{\sqrt{3}}{3},-\frac{\sqrt{3}}{3}\right), && IV{:}\left(-\frac{\sqrt{3}}{3},\frac{\sqrt{3}}{3},-\frac{\sqrt{3}}{3}\right) \\ &V{:}\left(-\frac{\sqrt{3}}{3},-\frac{\sqrt{3}}{3},\frac{\sqrt{3}}{3}\right), && VI{:}\left(\frac{\sqrt{3}}{3},-\frac{\sqrt{3}}{3},\frac{\sqrt{3}}{3}\right) \\ &VII{:}\left(\frac{\sqrt{3}}{3},\frac{\sqrt{3}}{3},\frac{\sqrt{3}}{3}\right), && VIII{:}\left(-\frac{\sqrt{3}}{3},\frac{\sqrt{3}}{3},\frac{\sqrt{3}}{3}\right) \end{aligned} \tag{6.13}$$

As visible in Figure 124. However, this simple implementation suffers from shear and volumetric locking which lead to an overestimation of the element stiffness matrix. In order to relieve this phenomenon for isotropic materials the material tensor $\boldsymbol{D}$ from eq. (6.7) is split into its two subcomponents

$$\begin{aligned} \boldsymbol{D_{11}} &= \frac{E}{(1+\nu)(1-\nu)}\begin{bmatrix} 1-\nu & \nu & \nu \\ \nu & 1-\nu & \nu \\ \nu & \nu & 1-\nu \end{bmatrix} \\ \boldsymbol{D_{22}} &= \frac{E}{(1+\nu)(1-\nu)}\begin{bmatrix} \frac{1-2\nu}{2} & & \\ & \frac{1-2\nu}{2} & \\ & & \frac{1-2\nu}{2} \end{bmatrix} \end{aligned} \tag{6.14}$$

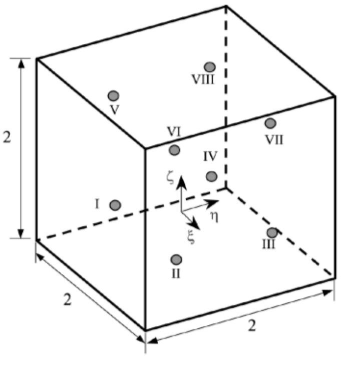

Figure 124: 2x2x2 Gauss integration points location

As well as the strain-displacement matrix $\boldsymbol{B}$

$$
\begin{gathered}
\boldsymbol{B_1} = \begin{bmatrix}
\frac{\partial n_1}{\partial x} & \cdots & \frac{\partial n_i}{\partial x} & \cdots & \frac{\partial n_8}{\partial x} & & & & & & & & & & \\
& & & & & \frac{\partial n_1}{\partial y} & \cdots & \frac{\partial n_i}{\partial y} & \cdots & \frac{\partial n_8}{\partial y} & & & & & \\
& & & & & & & & & & \frac{\partial n_1}{\partial y} & \cdots & \frac{\partial n_i}{\partial y} & \cdots & \frac{\partial n_8}{\partial y}
\end{bmatrix} \\
\boldsymbol{B_2} = \begin{bmatrix}
& & & & & \frac{\partial n_1}{\partial y} & \cdots & \frac{\partial n_i}{\partial y} & \cdots & \frac{\partial n_8}{\partial y} & \frac{\partial n_1}{\partial z} & \cdots & \frac{\partial n_i}{\partial z} & \cdots & \frac{\partial n_8}{\partial z} \\
\frac{\partial n_1}{\partial x} & \cdots & \frac{\partial n_i}{\partial x} & \cdots & \frac{\partial n_8}{\partial x} & & & & & & \frac{\partial n_1}{\partial z} & \cdots & \frac{\partial n_i}{\partial z} & \cdots & \frac{\partial n_8}{\partial z} \\
\frac{\partial n_1}{\partial x} & \cdots & \frac{\partial n_i}{\partial x} & \cdots & \frac{\partial n_8}{\partial x} & \frac{\partial n_1}{\partial y} & \cdots & \frac{\partial n_i}{\partial y} & \cdots & \frac{\partial n_8}{\partial y} & & & & &
\end{bmatrix}
\end{gathered}
\tag{6.15}
$$

Then the integral for the stiffness matrix is also split as

$$
\boldsymbol{K_e} = \int_V \boldsymbol{B^T D B}\, dV = \int_V \boldsymbol{B_1^T D_{11} B_1}\, dV + \int_V \boldsymbol{B_2^T D_{22} B_2}\, dV \tag{6.16}
$$

This technique is called selective underintegration since it separates the integration of the normal strains from the shear ones. Indeed, the stiffness portion due to the normal strains is integrated using the same 2x2x2 Gauss scheme presented earlier, while the shear terms are integrated using only one point in the center of the element with a weight of 8. The obtained matrix is then less stiff and does not suffer from shear or volumetric locking. However, another problem is introduced since spurious zero strain energy modes arise. Those are elastic deformation modes in which the deformation strain energy is zero and hence could be assimilated to rigid body modes, but those are not rigid and hence are unphysical and must be eliminated to obtain the correct results. For the 8-node brick there are 3 of these modes which are visible in Figure 125.

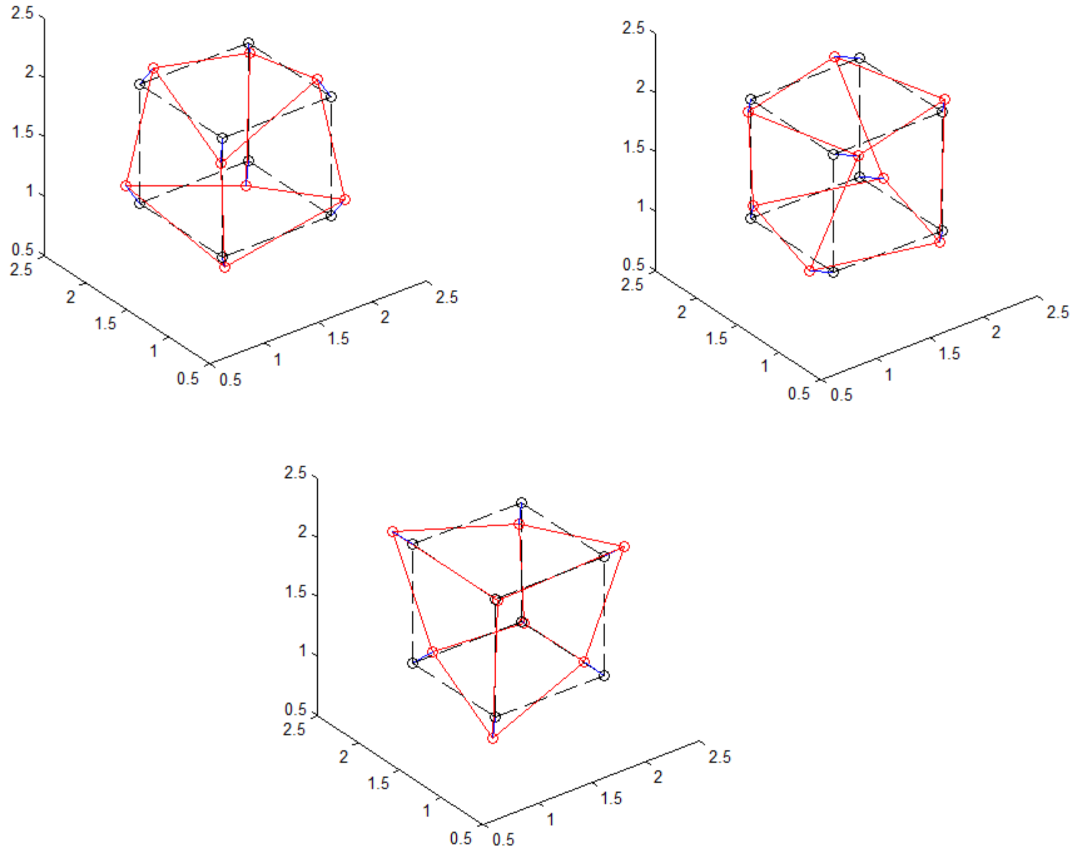

Figure 125: Spurious zero strain energy modes for the 8-node brick

In order to avoid these spurious modes several techniques have been studied in literature. The simplest one consists in computing the selectively reduced matrix for each element as is, and then applying a corrective stiffness matrix to remove a posteriori the spurious modes. The procedure is as follows:

1- Compute the selectively reduced stiffness matrix $\boldsymbol{K_e}$

2- Compute the eigenvalues and eigenvectors ω_s , $\boldsymbol{\phi_s}$

3- Obtain the nodal forces for each eigenvector $\boldsymbol{\phi_{s,0}}$ whose eigenvalue is 0

$$f_n = \boldsymbol{K_e \phi_{s,0}}$$

4- Finally, the corrective stiffness term is obtained as

$$\boldsymbol{K_c} = \boldsymbol{F_0 \Phi_s^{-1}}$$

where $\boldsymbol{\Phi}_{\boldsymbol{s}}$ is the matrix of the eigenvectors $\boldsymbol{\phi}_{\boldsymbol{s}}$ and $\boldsymbol{F}_{\boldsymbol{0}}$ is a matrix of zeros in which the nodal forces are inserted in the corresponding columns of the spurious eigenvectors $\boldsymbol{\phi}_{\boldsymbol{s},\boldsymbol{0}}$ as they are sorted in $\boldsymbol{\Phi}_{\boldsymbol{s}}$. While this method is effective, it is extremely computationally heavy since it requires the solution of an eigenproblem for each element of the FE model. Jacquotte and Oden proposed a procedure applicable to the final assembled matrix [135] [136] in which the orthogonality of the solution is imposed with respect to the spurious modes identified and as such those hidden mechanisms can never be excited. Another approach which allows the a priori elimination has been presented in [137]. The procedure is similar to the a posteriori method, but the spurious modes eigenvectors are assumed to be known and constant and therefore the corrective stiffness can be computed only once and applied to all elements, but this is applicable only in uniform meshes. The solution implemented in the current model is based on the work of MacNeal [119] in which instead of using only the central node for underintegration one virtual node is used for each face. Those nodes, whose location is shown in Figure 126 are virtual since the actual values to be used in the calculation are actually obtained averaging the values obtained in the neighboring Gauss points, weighted by their Jacobian in order for the elements to pass the patch test.

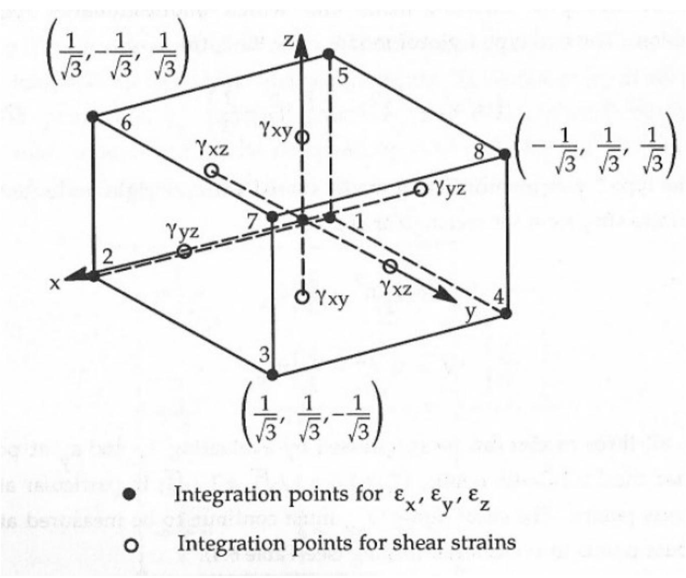

Figure 126: Selective underintegration scheme used in the current model, from [119]

Even with these precautions the formulation still suffers from volumetric locking. In order to solve this remaining problem some authors, like Wilson [138] and Taylor [139], proposed to introduce additional shape functions, known as "bubble functions", and therefore also increasing the number of DOFs. Again, this approach is slow and complex, but MacNeal proposed a solution by introducing instead of additional shape functions an Enhanced Assumed Strain (EAS) field which extends the $\boldsymbol{B_1}$ matrix as

$$\boldsymbol{B_1'} = [\boldsymbol{B_1}\ \boldsymbol{B_a}] \tag{6.17}$$

Where the additional EAS field is defined as

$$\boldsymbol{B_a} = \frac{1}{det(\boldsymbol{J})}\begin{bmatrix} \xi & 0 & 0 & \xi\eta & 0 & \xi\zeta \\ 0 & \eta & 0 & \xi\eta & \eta\zeta & 0 \\ 0 & 0 & \zeta & 0 & \eta\zeta & \xi\zeta \end{bmatrix} \tag{6.18}$$

In which again the factor $1/\det(\boldsymbol{J})$ is needed to satisfy the patch test. The combination of this EAS approach with the selective reduced integration solves all locking problems and doesn't introduce spurious modes, however it is only applicable is the strains are aligned to global (X, Y, Z) reference frame. Therefore, a transformation is needed to pass from the strains in the deformed reference frame $\overline{\varepsilon_x}, \overline{\varepsilon_y}, \overline{\varepsilon_z}, \overline{\gamma_{xy}}, \overline{\gamma_{xz}}, \overline{\gamma_{yz}}$ to the corresponding ones aligned to the local one. For this purpose, three angles are defined as visible in Figure 127:

- α: angle between Y and $\bar{y}$
- δ: angle between Z and $\bar{z}$
- ϑ: angle between the X axis and the projection of $\bar{z}$ on the XY plane

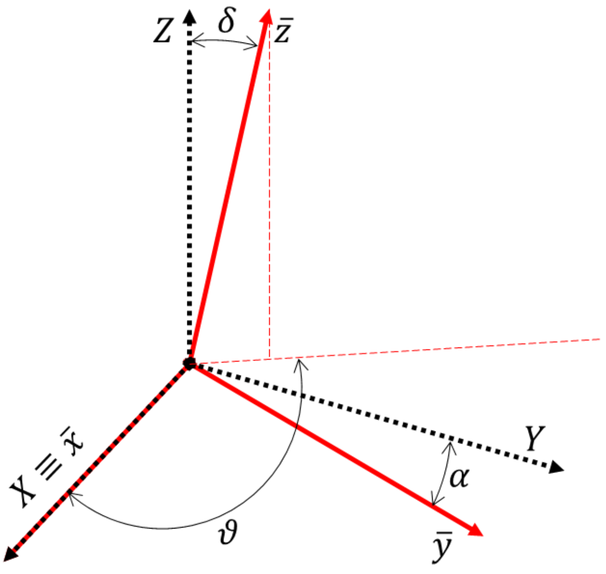

Figure 127: Definition of the angles to obtain the aligned strains

The versors $\bar{\boldsymbol{\imath}}, \bar{\boldsymbol{\jmath}}, \bar{\boldsymbol{k}}$ of the distorted reference frame expressed in the correct one are:

$$\begin{aligned} \bar{\boldsymbol{\imath}} &= (1, 0, 0) \\ \bar{\boldsymbol{\jmath}} &= (\sin\alpha\,, \cos\alpha\,, 0) \\ \bar{\boldsymbol{k}} &= (\cos\vartheta\,, \sin\vartheta\,, \cos\delta\,) \end{aligned} \tag{6.19}$$

The position of a point $\boldsymbol{p}$ can then be described with the versors $\bar{\boldsymbol{\imath}}, \bar{\boldsymbol{\jmath}}, \bar{\boldsymbol{k}}$ in the distorted reference frame

$$\boldsymbol{p} = \bar{x}\bar{\boldsymbol{\imath}} + \bar{y}\bar{\boldsymbol{\jmath}} + \bar{z}\bar{\boldsymbol{k}} \tag{6.20}$$

And its coordinates in the global reference frame are then

$$\begin{aligned} x &= \bar{x} + \bar{y}\sin\alpha + \bar{z}\cos\vartheta\sin\delta \\ y &= \bar{y}\cos\alpha + \bar{z}\sin\vartheta\sin\delta \\ z &= \bar{z}\cos\delta \end{aligned} \tag{6.21}$$

Thus, writing the transformation matrix and inverting it, the rotation matrix from the global reference frame to the distorted one can be obtained as

$$\begin{Bmatrix} \bar{x} \\ \bar{y} \\ \bar{z} \end{Bmatrix} = \begin{bmatrix} 1 & tan(\alpha) & -\sec(\alpha) tan(\delta) cos(t + a) \\ 0 & sec(\alpha) & -sec(\alpha) tan(d) sin(t) \\ 0 & 0 & sec(\delta) \end{bmatrix} \begin{Bmatrix} x \\ y \\ z \end{Bmatrix} \tag{6.22}$$

In order to obtain the correct deformation matrix, the integrand $\boldsymbol{B^T D B}$ will have to be multiplied not only for the Jacobian of the transformation from global to natural coordinates, but also for the Jacobian of the transformation from the global cartesian to the distorted one, which is obtained by

$$\boldsymbol{J_d} = \begin{bmatrix} \frac{\partial x}{\partial \bar{x}} & \frac{\partial y}{\partial \bar{x}} & \frac{\partial z}{\partial \bar{x}} \\ \frac{\partial x}{\partial \bar{y}} & \frac{\partial y}{\partial \bar{y}} & \frac{\partial z}{\partial \bar{y}} \\ \frac{\partial x}{\partial \bar{z}} & \frac{\partial y}{\partial \bar{z}} & \frac{\partial z}{\partial \bar{z}} \end{bmatrix} \rightarrow \boldsymbol{J_d} = \begin{bmatrix} 1 & 0 & 0 \\ \sin\alpha & \cos\alpha & 0 \\ \cos\vartheta\sin\delta & \sin\vartheta\sin\delta & \cos\delta \end{bmatrix} \tag{6.23}$$

Which yields

$$\det(\boldsymbol{J_d}) = \cos\alpha\cos\delta \tag{6.24}$$

The displacements instead follow a projective rule and therefore to obtain the components of a displacement vector $\boldsymbol{s}\{u, v, w\}$ in the distorted reference frame from the global one a simple scalar product between the distorted versors and the displacement vector as

$$\begin{gathered}\bar{u} = u \\ \bar{v} = u\sin\alpha + v\cos\alpha \\ \bar{w} = u\cos\vartheta\sin\delta + v\sin\vartheta\sin\delta + w\cos\delta\end{gathered} \tag{6.25}$$

Or, in matrix form

$$\begin{Bmatrix}\bar{u} \\ \bar{v} \\ \bar{w}\end{Bmatrix} = \begin{bmatrix}1 & 0 & 0 \\ sin(\alpha) & cos(\alpha) & 0 \\ sin(\delta)cos(\vartheta) & sin(\delta)sin(\vartheta) & cos(\delta)\end{bmatrix}\begin{Bmatrix}u \\ v \\ w\end{Bmatrix} \tag{6.26}$$

Under the small displacements, small strains hypothesis the strains are usually written as

$$\begin{gathered}\varepsilon_x = \frac{\partial u}{\partial x}, \qquad \varepsilon_y = \frac{\partial v}{\partial y}, \qquad \varepsilon_z = \frac{\partial w}{\partial z} \\ \\ \gamma_{xy} = \frac{\partial u}{\partial y} + \frac{\partial v}{\partial x}, \qquad \gamma_{yz} = \frac{\partial v}{\partial z} + \frac{\partial w}{\partial y}, \qquad \gamma_{xz} = \frac{\partial u}{\partial z} + \frac{\partial w}{\partial x}\end{gathered} \tag{6.27}$$

but with respect to the distorted reference frame the partial derivatives of the displacements are

$$\begin{gathered}\frac{\partial\bar{u}}{\partial\bar{x}} = \frac{\partial u}{\partial x}\frac{\partial x}{\partial\bar{x}} + \frac{\partial u}{\partial y}\frac{\partial y}{\partial\bar{x}} + \frac{\partial u}{\partial z}\frac{\partial z}{\partial\bar{x}} \\ \\ \frac{\partial\bar{v}}{\partial\bar{y}} = \left(\frac{\partial u}{\partial x}\frac{\partial x}{\partial\bar{y}} + \frac{\partial u}{\partial y}\frac{\partial y}{\partial\bar{y}} + \frac{\partial u}{\partial z}\frac{\partial z}{\partial\bar{y}}\right)\sin\alpha + \left(\frac{\partial v}{\partial x}\frac{\partial x}{\partial\bar{y}} + \frac{\partial v}{\partial y}\frac{\partial y}{\partial\bar{y}} + \frac{\partial v}{\partial z}\frac{\partial z}{\partial\bar{y}}\right)\cos\alpha \\ \\ \frac{\partial w}{\partial z} = \left(\frac{\partial u}{\partial x}\frac{\partial x}{\partial\bar{z}} + \frac{\partial u}{\partial y}\frac{\partial y}{\partial\bar{z}} + \frac{\partial u}{\partial z}\frac{\partial z}{\partial\bar{z}}\right)\cos\vartheta\sin\delta + \left(\frac{\partial v}{\partial x}\frac{\partial x}{\partial\bar{z}} + \frac{\partial v}{\partial y}\frac{\partial y}{\partial\bar{z}} + \frac{\partial v}{\partial z}\frac{\partial z}{\partial\bar{z}}\right)\sin\vartheta\sin\delta \\ + \left(\frac{\partial w}{\partial x}\frac{\partial x}{\partial\bar{z}} + \frac{\partial w}{\partial y}\frac{\partial y}{\partial\bar{z}} + \frac{\partial w}{\partial z}\frac{\partial z}{\partial\bar{z}}\right)\cos\delta\end{gathered} \tag{6.28}$$

And similarly, for the omitted components of the partial derivatives needed. For computer implementation the whole transformation for the strains can be summed up by a matrix-vector product

$$\begin{Bmatrix} \overline{\varepsilon_x} \\ \overline{\varepsilon_y} \\ \overline{\varepsilon_z} \\ \overline{\gamma_{xy}} \\ \overline{\gamma_{yz}} \\ \overline{\gamma_{xz}} \end{Bmatrix} = \boldsymbol{L} \begin{Bmatrix} \varepsilon_x \\ \varepsilon_y \\ \varepsilon_z \\ \gamma_{xy} \\ \gamma_{yz} \\ \gamma_{xz} \end{Bmatrix} \tag{6.29}$$

Where $\boldsymbol{L}$ is the transformation matrix

$$\boldsymbol{L} = \\ = \begin{bmatrix} 1 & 0 & 0 & 0 & 0 & 0 \\ sin^2(\alpha) & cos^2(\alpha) & 0 & cos(\alpha)sin(\alpha) & 0 & 0 \\ sin^2(\delta)cos^2(\alpha) & sin^2(\delta)sin^2(\alpha) & cos^2(\delta) & sin^2(\delta)cos(\vartheta)sin(\vartheta) & sin(\delta)cos(\delta)sin(\vartheta) & sin(\delta)cos(\delta)cos(\vartheta) \\ 2sin(\alpha) & 0 & 0 & cos(\alpha) & 0 & 0 \\ 2sin(\alpha)sin(\delta)cos(\vartheta) & 2cos(\alpha)sin(\delta)cos(\vartheta) & 0 & sin(\delta)cos(\vartheta-\alpha) & cos(\alpha)cos(\delta) & sin(\alpha)cos(\delta) \\ 2sin(\delta)cos(\vartheta) & 0 & 0 & sin(\delta)sin(\vartheta) & 0 & cos(\delta) \end{bmatrix} \tag{6.30}$$

In the global cartesian reference frame the strains are usually obtained by

$$\boldsymbol{\varepsilon} = \boldsymbol{Bs} \tag{6.31}$$

And similarly, in the distorted one

$$\overline{\boldsymbol{\varepsilon}} = \overline{\boldsymbol{B}}\overline{\boldsymbol{s}} \tag{6.32}$$

To transform the displacement vector from the global to the distorted frame, the following transformation matrix can be defined

$$\boldsymbol{T_r} = \begin{bmatrix} 1 & 0 & 0 & & & & \\ \sin\alpha & \cos\alpha & 0 & & & & \\ \cos\vartheta\sin\delta & \sin\vartheta\sin\delta & \cos\delta & & & & \\ & & & 1 & 0 & 0 & \\ & & & \sin\alpha & \cos\alpha & 0 & \\ & & & \cos\vartheta\sin\delta & \sin\vartheta\sin\delta & \cos\delta & \\ & & & & & & \dots \end{bmatrix} \tag{6.33}$$

So that

$$\bar{\boldsymbol{s}} = \boldsymbol{T_r s} \tag{6.34}$$

Similarly, for the strains

$$\bar{\boldsymbol{\varepsilon}} = \boldsymbol{Ls} \tag{6.35}$$

Therefore

$$\boldsymbol{\varepsilon} = \boldsymbol{L^{-1}\bar{B}T_r s} \tag{6.36}$$

Where $\bar{\boldsymbol{B}}$ is the strain-displacement relationship matrix obtained in the distorted reference frame using the selective reduced integration and the EAS field, which can then be written with respect to the global one by

$$\boldsymbol{B} = \boldsymbol{L^{-1}\bar{B}T_r} \tag{6.37}$$

Substituting in (6.5) the following is obtained

$$\widetilde{\boldsymbol{K}}_{\boldsymbol{e}} = \int_V \left(\boldsymbol{L^{-1}\bar{B}T_r}\right)^{\boldsymbol{T}} \boldsymbol{D}\left(\boldsymbol{L^{-1}\bar{B}T_r}\right) dV \tag{6.38}$$

Also including the Jacobians of the successive transformation the final matrix formulation is expressed by

$$\widetilde{\boldsymbol{K}}_{\boldsymbol{e}} = \int_{-1}^{1}\int_{-1}^{1}\int_{-1}^{1} \left(\boldsymbol{L^{-1}\bar{B}T_r}\right)^{\boldsymbol{T}} \boldsymbol{D}\left(\boldsymbol{L^{-1}\bar{B}T_r}\right) \det(\boldsymbol{J}) \det(\boldsymbol{J_d}) d\xi d\eta d\zeta \tag{6.39}$$

However, due to the introduction of the additional EAS field $\widetilde{\boldsymbol{K}}_{\boldsymbol{e}}$ has 6 more additional DOFs which need to be eliminated since they do not correspond to any physical DOF. Including the selectively underintegrated matrix $\overline{\boldsymbol{B}'_2}$ and the EAS, matrix $\bar{\boldsymbol{B}}$ is partitioned as follows

$$\bar{\boldsymbol{B}} = \begin{bmatrix} \bar{\boldsymbol{B}}_{\boldsymbol{1}} & \bar{\boldsymbol{B}}_{\boldsymbol{a}} \\ \overline{\boldsymbol{B}'_{\boldsymbol{2}}} & \boldsymbol{0} \end{bmatrix} \tag{6.40}$$

Therefore, $\widetilde{\boldsymbol{K}}_{\boldsymbol{e}}$ is partitioned as

$$\widetilde{\boldsymbol{K}}_{\boldsymbol{e}} = \begin{bmatrix} \boldsymbol{K}_{\boldsymbol{iso,iso}} & \boldsymbol{K}_{\boldsymbol{iso,a}} \\ \boldsymbol{K}_{\boldsymbol{a,iso}} & \boldsymbol{K}_{\boldsymbol{a,a}} \end{bmatrix} \tag{6.41}$$

Where $\boldsymbol{K}_{\boldsymbol{iso,iso}}$ represents the isoparametric part of the matrix, $\boldsymbol{K}_{\boldsymbol{a,a}}$ the part due to the EAS field and $\boldsymbol{K}_{\boldsymbol{iso,a}} = \boldsymbol{K}_{\boldsymbol{a,iso}}^{\boldsymbol{T}}$ the connecting portions. The final matrix $\boldsymbol{K}_{\boldsymbol{e}}$ can be obtained by static condensation [140] as

$$\boldsymbol{K}_{\boldsymbol{e}} = \boldsymbol{K}_{\boldsymbol{iso,iso}} - \boldsymbol{K}_{\boldsymbol{iso,a}} \boldsymbol{K}_{\boldsymbol{a,a}}^{-\boldsymbol{1}} \boldsymbol{K}_{\boldsymbol{iso,a}}^{\boldsymbol{T}} \tag{6.42}$$

For a dynamic analysis also the inertial properties are needed, which are expressed by the mass matrix

$$\boldsymbol{M}_{\boldsymbol{e}} = \rho \int_V \boldsymbol{n}^{\boldsymbol{T}} \boldsymbol{n} \, dV \tag{6.43}$$

Where n is a matrix containing all shape functions

$$\boldsymbol{n} = \begin{bmatrix} n_1 & \dots & n_i & \cdots & n_8 & & & & & & & & & & \\ & & & & & n_1 & \dots & n_i & \cdots & n_8 & & & & & \\ & & & & & & & & & & n_1 & \dots & n_i & \cdots & n_8 \end{bmatrix} \tag{6.44}$$

The volume integral can be again expressed as

$$\boldsymbol{M}_{\boldsymbol{e}} = \rho \int_{-1}^{1} \int_{-1}^{1} \int_{-1}^{1} \boldsymbol{n}^{\boldsymbol{T}} \boldsymbol{n} \det(\boldsymbol{J}) \, d\xi d\eta d\zeta \tag{6.45}$$

Which is again numerically evaluated on a 2x2x2 Gauss grid. For the purposes of this work further matrices will be needed, and they will be defined later when the effect considered will be introduced in the algorithm.

VI.3 Algorithm description

In this paragraph the iterative algorithm to obtain the time domain response of gears including most possible flexibilities will be detailed. In order to achieve the desired results a consistent pre-processing phase is needed. The first step is obtaining the mesh discretization as nodes and elements to be input to generate the required mass and stiffness matrices. This is done in a parametric way by separating the half-tooth region in its involute, fillet and web portions as visible in Figure 128 similarly to [141], [103] or [142] and others. The number of nodes in each region can be controlled almost independently, except for the number of nodes in the thickness direction of the half tooth, which must be constant throughout the three regions to give continuity to the mesh. Through various parameters combinations different element sizes and densities can be obtained as visible in Figure 129. Next, a selection of the nodes on the entire inner radius region of the web is selected to be connected through a rigid joint connection to a central node. To do this, 6 rows and columns are added to the obtained matrices

$$\boldsymbol{K_f} = \begin{bmatrix} \boldsymbol{K} & \boldsymbol{0_{n,6}} \\ \boldsymbol{0_{6,n}} & \boldsymbol{0_{6,6}} \end{bmatrix}, \boldsymbol{M_f} = \begin{bmatrix} \boldsymbol{M} & \boldsymbol{0_{n,6}} \\ \boldsymbol{0_{6,n}} & \boldsymbol{0_{6,6}} \end{bmatrix} \tag{6.46}$$

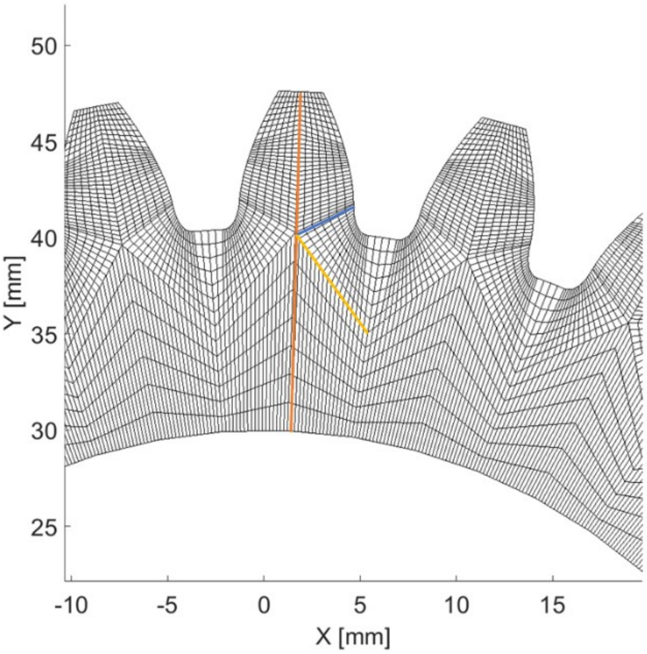

Figure 128: Parametric mesh generation and subdivision areas of the teeth

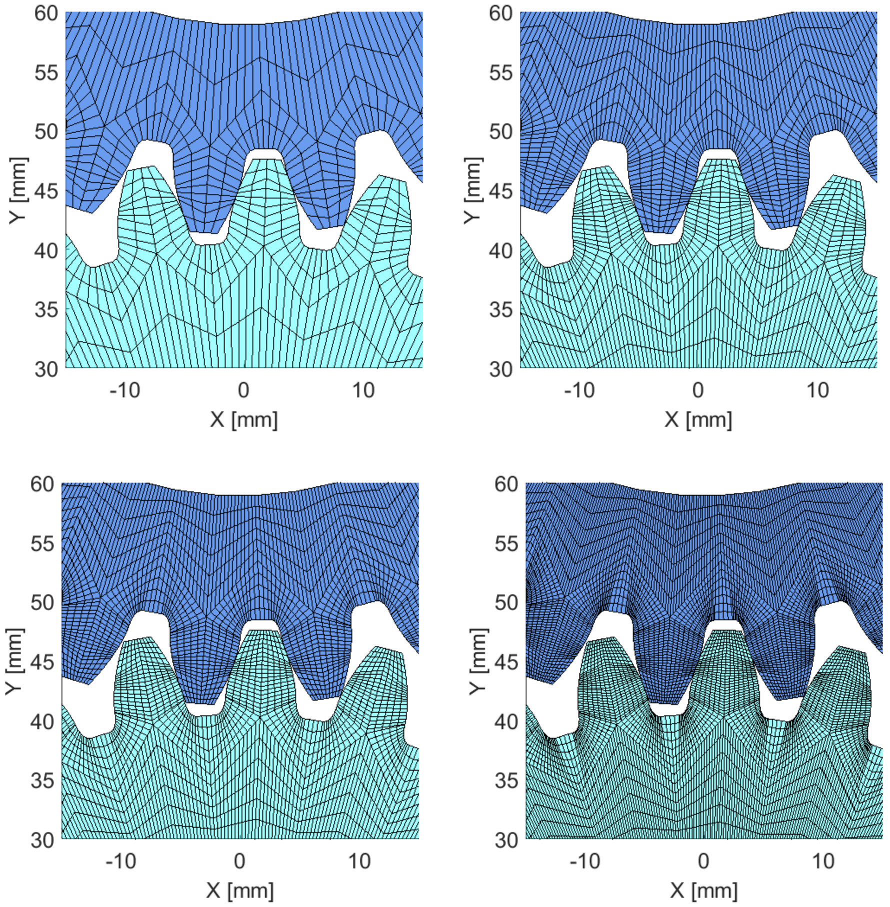

Figure 129: Parametric gear FE meshes with varying element sizes

to leave space for an additional virtual node in the center of rotation of the gear, which will be the master node of this rigid joint connection, while the nodes on the inner radius will be the slaves, all connected to the same central master node. For each master-slave pair the rigid joint transformation matrix is computed as [143]

$$\begin{Bmatrix} \boldsymbol{u_m} \\ \boldsymbol{u_s} \end{Bmatrix} = \boldsymbol{T_{rj}} \boldsymbol{u_m} = \begin{bmatrix} 1 & & \\ & 1 & \\ & & 1 \\ 0 & -\Delta z & +\Delta y \\ +\Delta z & 0 & -\Delta x \\ -\Delta y & +\Delta x & 0 \end{bmatrix} \boldsymbol{u_m} \tag{6.47}$$

where $\boldsymbol{u_m}$ indicates the master node DOFs, while $\boldsymbol{u_s}$ the slave ones. Δx, Δy and Δz are the distances between the h^{th} slave node and the master central node. For each h^{th} slave node considered a $\boldsymbol{T}_{\boldsymbol{rj,h}}$ transformation matrix is hence computed and assembled into the entire transformation matrix

$$\boldsymbol{T}_{\boldsymbol{RJ}} = \begin{bmatrix} \boldsymbol{I} & \boldsymbol{0} \\ \boldsymbol{0} & \boldsymbol{T}_{\boldsymbol{rj},1} \\ \vdots & \vdots \\ & \boldsymbol{T}_{\boldsymbol{rj,h}} \end{bmatrix} \tag{6.48}$$

where $\boldsymbol{I}$ is an identity matrix of suitable dimension. The DOFs of matrices $\boldsymbol{K}_{\boldsymbol{f}}$ and $\boldsymbol{M}_{\boldsymbol{f}}$ are sorted placing first all DOFs that are not interested in this transformation ($\boldsymbol{u}_{\boldsymbol{all}}$), then the DOFs of the virtual node created which will be the master node ($\boldsymbol{u}_{\boldsymbol{t}}$) and lastly the h slave nodes in the same order as their transformation matrix has been placed in $\boldsymbol{T}_{\boldsymbol{RJ}}$. The matrices with the embedded rigid joint connection towards the central node are then simply obtained by

$$\boldsymbol{K}_{\boldsymbol{j}} = \boldsymbol{T}_{\boldsymbol{RJ}}^{\boldsymbol{T}} \boldsymbol{K}_{\boldsymbol{f}} \boldsymbol{T}_{\boldsymbol{RJ}}\, , \boldsymbol{M}_{\boldsymbol{j}} = \boldsymbol{T}_{\boldsymbol{RJ}}^{\boldsymbol{T}} \boldsymbol{M}_{\boldsymbol{f}} \boldsymbol{T}_{\boldsymbol{RJ}} \tag{6.49}$$

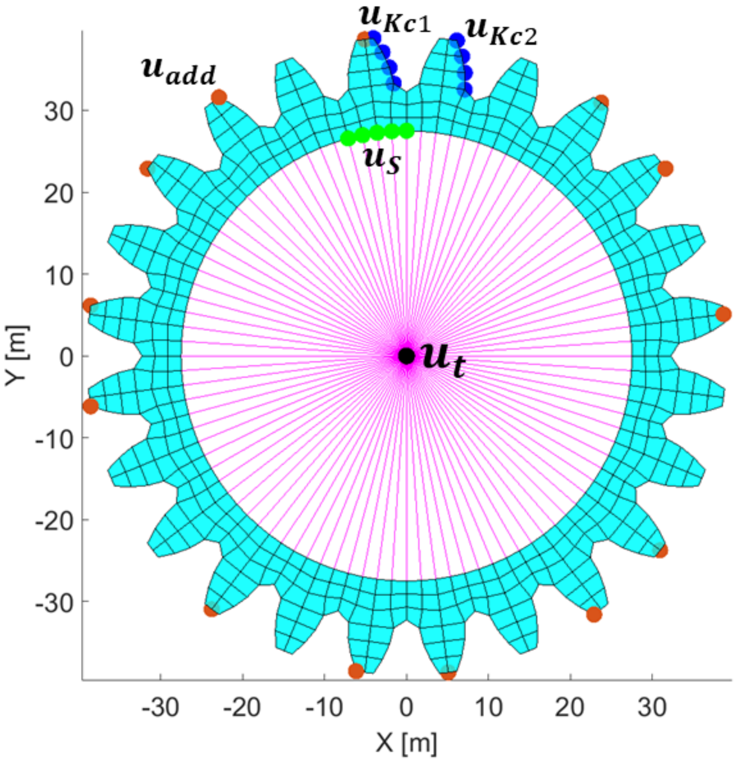

Figure 130: Master nodes locations. Blue dots: Contact mesh stiffnesses. Green dots: Sensor nodes. Orange dots: Additional nodes. Black dot: Rigid joint master node, torque application and DTE readout

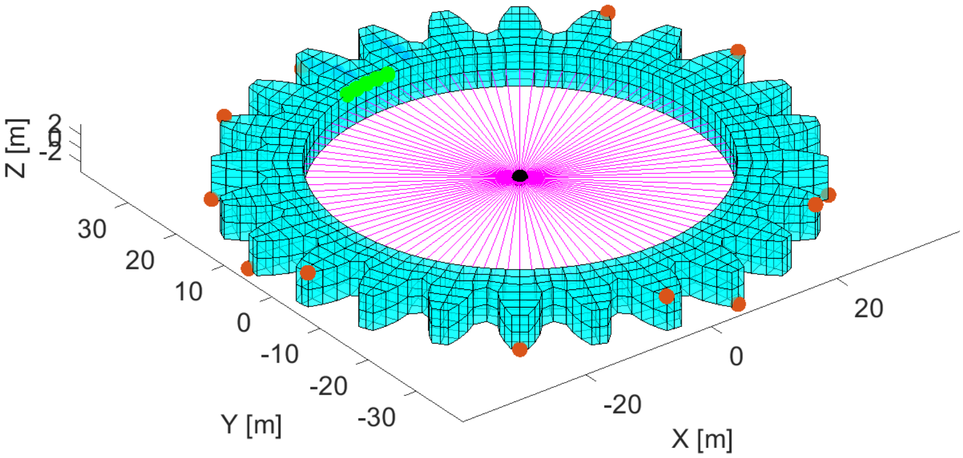

Figure 131: Detailed view of the additional nodes (orange dots) computed using MoGeSeC

The virtual node thus created, which connects all inner radius points selected to itself, will have three translational DOFs as well as three rotational DOFs. All those additional DOFs will be constrained, by deleting the appropriate rows and columns of the matrices, except for the rotational DOF around the Z axis, where the torque T to the gear will be applied and the DTE will be read. As stated in the introduction of the chapter, the proposed scheme will employ a ROM in order to decrease the matrices sizes and reduce the otherwise impossibly long computational times. The idea is to exploit the periodic nature of the meshing action to obtain a ROM containing only the necessary DOFs to represent the interaction and the cyclical excitation that is typical of gears. The geometrical properties of a gear are also cyclically symmetric with a period angle $\theta = 360/Z$ and so can be considered the properties of FE model. For example a force can be applied to any node on the flank of one teeth and results obtained, but if the same properly rotated force is applied to the homologous node on following or previous flank the results will be the same, except for a delay angle equal to $\pm\theta$. In the proposed approach this cyclic repletion will be exploited by reducing as much as possible the number of DOFs of the ROM by considering only a limited number of loaded or observed nodes to one sector spanning the angle θ, while the typical travelling excitation wave will be created by expanding, sorting and reducing the obtained displacements, velocities and accelerations in the time domain each time the angle θ has been spanned. The master nodes, and their related DOFs are visible in Figure 130, and their meaning is as follows:

- Sensor nodes $\boldsymbol{u_S}$ (green dots): The dynamic displacements of these nodes will be used to read and analyze the dynamic response of the gear in the radial and axial directions, simulating the behavior of a proximity sensor in an experimental test. For this reason, a number of them is needed, enough to span the angle θ. How a single displacement is obtained from all those nodes will be detailed later.
- Contact mesh stiffness nodes $\boldsymbol{u_{Kc1}}, \boldsymbol{u_{Kc2}}$ (blue dots): The source of excitation of the whole system will be the periodic variation of the location of the connection point of the contact stiffness and also its intensity. All nodes pertaining to the flank at a determined axial coordinate are selected and two teeth are needed to model LCRG, while three or more would be needed to model HCRG.
- Additional nodes $\boldsymbol{u_{add}}$ (orange dots): Those nodes are selected thanks to a Modal-Geometrical Selection Criterion (MoGeSeC) [144] in order to select the nodes where the most modal content is located as visible in Figure 131 to improve the accuracy of the ROM. These are not strictly needed since they won't play any part in the calculations and could be avoided in order to further reduce the matrices dimensions, at a cost in accuracy.
- Central node $\boldsymbol{u_t}$ (black dot): This node is the master node of the rigid joint connection, linking the selected nodes on the inner radius to itself as describe earlier. The torque will be applied on the rotational DOF left unconstrained and its displacement will be taken as the output DTE from the time domain response, imitating the readout of an angular encoder.

Hence, the final vector of the master DOFs is assembled as

$$\boldsymbol{u_m} = \left\{\boldsymbol{u_S^T}\ \boldsymbol{u_{Kc1}^T} \boldsymbol{u_{Kc2}^T}\ \boldsymbol{u_{add}^T}\ \boldsymbol{u_t^T}\ \right\}^{\boldsymbol{T}} \tag{6.50}$$

In order to use always the same set of master DOFs and to describe the meshing process a set of matrices, each rotated of a small angle $\Delta\theta = \theta/N$, is first obtained, where N is the number subdivisions of the mesh cycle chosen as visible in Figure 132. This will imply that the angular distance covered between each time step will be $\Delta\theta$ and hence the interval Δt between the successive time instants will vary with the speed. Given a starting rotational velocity Ω_s and a final one Ω_f the constant angular acceleration is simply obtained by

$$\dot{\Omega} = \frac{\Omega_f - \Omega_s}{t} \tag{6.51}$$

where t is the total time in which the speed sweep will happen. The instantaneous rotational velocity Ω_i at a generic time instant t_i is obtained by

$$\Omega_i = \Omega_{i-1} + \dot{\Omega}(t_i - t_{i-1}) \tag{6.52}$$

where

$$t_i = t_{i-1} + \frac{\Omega_{i-1} + \sqrt{\Omega_{i-1}^2 + 2\Delta\theta\dot{\Omega}}}{\dot{\Omega}} \tag{6.53}$$

The matrices at each angular position in the mesh cycle are obtained by matrix rotation, in which the nodal rotation matrix for a generic node is

$$\boldsymbol{R}_{\mathbf{\Delta\theta,i}} = \begin{bmatrix} \cos\,(\Delta\theta \cdot (\mathrm{z}-1)) & sin(\Delta\theta \cdot (\mathrm{z}-1)) & 0 \\ -sin(\Delta\theta \cdot (\mathrm{z}-1)) & \cos\,(\Delta\theta \cdot (\mathrm{z}-1)) & 0 \\ 0 & 0 & 1 \end{bmatrix} \tag{6.54}$$

where $z = 1,2,..,N$, which are then assembled on the diagonal of the full rotation matrix $\boldsymbol{R}_{\mathbf{\Delta\theta,z}}$ of suitable dimension to perform matrix rotation as

$$\boldsymbol{K_z} = \boldsymbol{R}^{\boldsymbol{T}}_{\mathbf{\Delta\theta,z}}\boldsymbol{K_j}\boldsymbol{R}_{\mathbf{\Delta\theta,z}}, \boldsymbol{M_z} = \boldsymbol{R}^{\boldsymbol{T}}_{\mathbf{\Delta\theta,z}}\boldsymbol{M_j}\boldsymbol{R}_{\mathbf{\Delta\theta,z}} \tag{6.55}$$

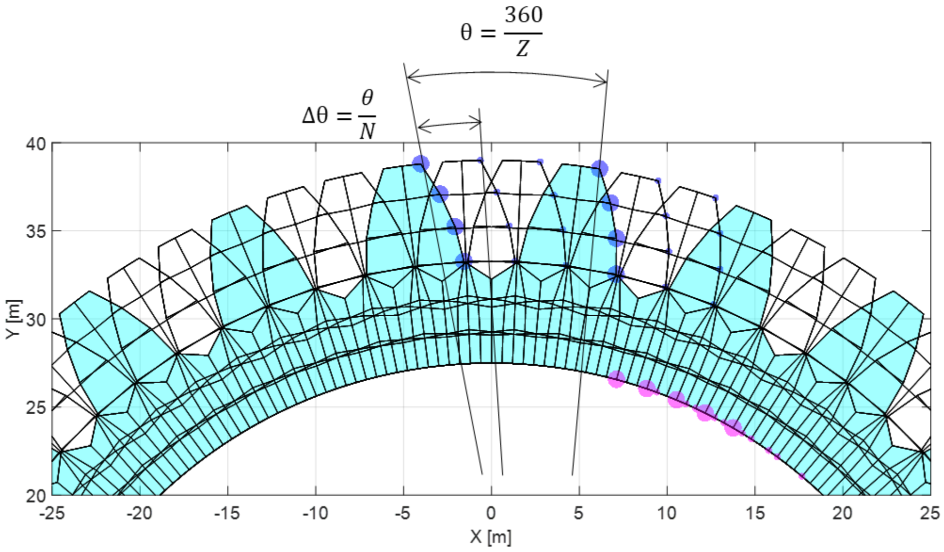

Figure 132: Incremental rotation of the gear

For each of those matrices a Craig-Bampton (CB) [145] Component Mode Synthesis (CMS) is obtained, first by partitioning the matrices separating the masters and slaves DOFs as

$$\begin{bmatrix} \boldsymbol{M_{mm}} & \boldsymbol{M_{ms}} \\ \boldsymbol{M_{sm}} & \boldsymbol{M_{ss}} \end{bmatrix} \begin{Bmatrix} \boldsymbol{\ddot{u}_m} \\ \boldsymbol{\ddot{u}_s} \end{Bmatrix} + \begin{bmatrix} \boldsymbol{K_{mm}} & \boldsymbol{K_{sm}} \\ \boldsymbol{K_{sm}} & \boldsymbol{K_{ss}} \end{bmatrix} \begin{Bmatrix} \boldsymbol{u_m} \\ \boldsymbol{u_s} \end{Bmatrix} = \begin{Bmatrix} \boldsymbol{f_m} \\ \boldsymbol{f_s} \end{Bmatrix} \tag{6.56}$$

The transformation matrix of the CB-CMS $\boldsymbol{T_{cb}}$ is obtained by

$$\begin{Bmatrix} \boldsymbol{u_m} \\ \boldsymbol{u_s} \end{Bmatrix} = \boldsymbol{T_{cb,z}} \begin{Bmatrix} \boldsymbol{u_m} \\ \boldsymbol{q_m} \end{Bmatrix} = \begin{bmatrix} \boldsymbol{I} & \boldsymbol{0} \\ \boldsymbol{\Psi_c} & \boldsymbol{\Phi_l} \end{bmatrix} \begin{Bmatrix} \boldsymbol{u_m} \\ \boldsymbol{q_m} \end{Bmatrix} \tag{6.57}$$

where $\boldsymbol{\Psi_c}$ is the static part of the reduction

$$\boldsymbol{\Psi_c} = -\boldsymbol{K_{ss}^{-1}} \boldsymbol{K_{sm}} \tag{6.58}$$

And $\boldsymbol{\Phi_l}$ is the matrix of eigenvectors $\boldsymbol{\phi_i}$ obtained by modal analysis on the equivalent matrices where the master DOFs are constrained, i.e. by keeping only the rows and columns pertaining to the slave DOFs $\boldsymbol{u_s}$

$$\boldsymbol{\Phi_l} = [\boldsymbol{\varphi_1} \quad \cdots \quad \boldsymbol{\phi_i} \quad \cdots \quad \boldsymbol{\phi_{nm}}] \tag{6.59}$$

The CB-CMS mass matrix for the z^{th} angular position is then obtained as

$$\boldsymbol{M_z^r} = \boldsymbol{T_{cb,z}^T} \boldsymbol{M_z} \boldsymbol{T_{cb,z}} \tag{6.60}$$

and similarly, for the z^{th} stiffness matrix

$$\boldsymbol{K_z^r} = \boldsymbol{T_{cb,z}^T} \boldsymbol{K_z} \, \boldsymbol{T_{cb,z}} \tag{6.61}$$

Alternatively, for faster computation, the reduced matrices can be obtained by calculating separately their components, namely for the mass matrix

$$\boldsymbol{M_z^r} = \begin{bmatrix} \boldsymbol{M_{mm}} + \boldsymbol{\Psi_c^T} \boldsymbol{M_{ss}} \boldsymbol{\Psi_c} & \boldsymbol{\Psi_c^T} \boldsymbol{M_{ss}} \boldsymbol{\Phi_l} \\ [\boldsymbol{\Psi_c^T} \boldsymbol{M_{ss}} \boldsymbol{\Phi_l}]^{\boldsymbol{T}} & \boldsymbol{I} \end{bmatrix} \tag{6.62}$$

and for the stiffness matrix

$$\boldsymbol{K}_{\boldsymbol{z}}^{\boldsymbol{r}} = \begin{bmatrix} \boldsymbol{K}_{\boldsymbol{mm}} + \boldsymbol{K}_{\boldsymbol{ms}}\boldsymbol{\Psi}_{\boldsymbol{c}} & \boldsymbol{0} \\ \boldsymbol{0} & \boldsymbol{\omega}_{\boldsymbol{l}} \end{bmatrix} \tag{6.63}$$

Where $\boldsymbol{\omega}_{\boldsymbol{l}}$ are the corresponding eigenvalues to the eigenvectors $\boldsymbol{\Phi}_{\boldsymbol{l}}$. The damping model chosen is proportional Rayleigh damping of the form

$$\boldsymbol{C}_{\boldsymbol{z}} = \alpha_c \boldsymbol{M}_{\boldsymbol{z}} + \beta_c \boldsymbol{K}_{\boldsymbol{z}} \tag{6.64}$$

Where the values of α_c and β_c will be detailed later, while the reduced matrix is again obtained as

$$\boldsymbol{C}_{\boldsymbol{z}}^{\boldsymbol{r}} = \boldsymbol{T}_{\boldsymbol{cb,z}}^{\boldsymbol{T}} \boldsymbol{C}_{\boldsymbol{z}}\, \boldsymbol{T}_{\boldsymbol{cb,z}} \tag{6.65}$$

All $\boldsymbol{K}_{\boldsymbol{z}}^{\boldsymbol{r}}, \boldsymbol{C}_{\boldsymbol{z}}^{\boldsymbol{r}}, \boldsymbol{M}_{\boldsymbol{z}}^{\boldsymbol{r}}$ matrices are obviously saved to be used in the integration scheme, while all others are discarded, except for the following ones:

- The rotation matrix of the angle Δθ

$$\boldsymbol{R}_{\boldsymbol{\Delta\theta}} = \begin{bmatrix} \begin{bmatrix} \cos(\Delta\theta) & sin(\Delta\theta) & 0 \\ -sin(\Delta\theta) & \cos(\Delta\theta) & 0 \\ 0 & 0 & 1 \end{bmatrix} & & \\ & \ddots & \\ & & \begin{bmatrix} \cos(\Delta\theta) & sin(\Delta\theta) & 0 \\ -sin(\Delta\theta) & \cos(\Delta\theta) & 0 \\ 0 & 0 & 1 \end{bmatrix} \end{bmatrix} \tag{6.66}$$

- The matrix that will be used to expand the displacements, velocities, and accelerations once $z = N$

$$\boldsymbol{T}_{\boldsymbol{cb,N}} \tag{6.67}$$

- The reduction matrix that will be used to reduce the displacements, velocities, and accelerations to begin the new mesh cycle for $z = 1$

$$\boldsymbol{T}_{\boldsymbol{r,1}} = (\boldsymbol{T}_{\boldsymbol{cb,1}}^{\boldsymbol{T}} \boldsymbol{T}_{\boldsymbol{cb,1}}) \boldsymbol{T}_{\boldsymbol{cb,1}}^{\boldsymbol{T}} \tag{6.68}$$

whose use will be apparent next. This preprocessing phase is computationally heavy, but it can be done only once if the macro-geometrical parameters of the considered gear do not change. Once this phase is completed, the iterative integration scheme can proceed, which is based on the Newmark [146] scheme with constant acceleration. The constants used are

$$\alpha_{NM} = \frac{1}{4}, \delta_{NM} = \frac{1}{2} \tag{6.69}$$

In the Newmark integration scheme, regrouping the terms of the equation of motion to be solved the following expression is obtained for the i^{th} time step, which corresponds to the z^{th} angular position

$$\ddot{\boldsymbol{u}}^{*}{}_{\boldsymbol{i}} = \boldsymbol{S}_{\boldsymbol{i}} \boldsymbol{\delta r}_{\boldsymbol{i}} \tag{6.70}$$

where

$$\boldsymbol{S}_{\boldsymbol{i}} = \boldsymbol{M}_{\boldsymbol{z},\boldsymbol{i}}^{\boldsymbol{r}} + \Delta t_i \boldsymbol{C}_{\boldsymbol{z},\boldsymbol{i}}^{\boldsymbol{r}} + \Delta t_i^2 \alpha_{NM} \left(\boldsymbol{K}_{\boldsymbol{z},\boldsymbol{i}}^{\boldsymbol{r}} + \boldsymbol{K}_{\boldsymbol{c},\boldsymbol{i}}^{\boldsymbol{r}} \right) \tag{6.71}$$

Where the time interval Δt_i changes from step to step. The residual vector $\boldsymbol{\delta r}_{\boldsymbol{i}}$ is obtained from the following matrices

$$\begin{gathered}
\boldsymbol{D}_{\boldsymbol{i}} = -\left(\boldsymbol{K}_{\boldsymbol{z},\boldsymbol{i}}^{\boldsymbol{r}} + \boldsymbol{K}_{\boldsymbol{c},\boldsymbol{i}}^{\boldsymbol{r}} \right) \\
\boldsymbol{V}_{\boldsymbol{i}} = -\boldsymbol{C}_{\boldsymbol{z},\boldsymbol{i}}^{\boldsymbol{r}} - \Delta t_i \left(\boldsymbol{K}_{\boldsymbol{z},\boldsymbol{i}}^{\boldsymbol{r}} + \boldsymbol{K}_{\boldsymbol{c},\boldsymbol{i}}^{\boldsymbol{r}} \right) \\
\boldsymbol{A}_{\boldsymbol{i}} = -\boldsymbol{C}_{\boldsymbol{z},\boldsymbol{i}}^{\boldsymbol{r}} (1 - \delta_{NM}) \Delta t_i - \left(\boldsymbol{K}_{\boldsymbol{z},\boldsymbol{i}}^{\boldsymbol{r}} + \boldsymbol{K}_{\boldsymbol{c},\boldsymbol{i}}^{\boldsymbol{r}} \right) \left(\frac{1}{2} - \alpha_{NM} \right) \Delta t_i^2
\end{gathered} \tag{6.72}$$

which are then assembled as

$$\delta \boldsymbol{r}_{\boldsymbol{i}} = \boldsymbol{f} + \boldsymbol{D}_{\boldsymbol{i}} \boldsymbol{u}_{\boldsymbol{i-1}} + \boldsymbol{V}_{\boldsymbol{i}} \dot{\boldsymbol{u}}_{\boldsymbol{i-1}} + \boldsymbol{A}_{\boldsymbol{i}} \ddot{\boldsymbol{u}}_{\boldsymbol{i-1}} \tag{6.73}$$

Where $\boldsymbol{u}_{\boldsymbol{i-1}}$, $\dot{\boldsymbol{u}}_{\boldsymbol{i-1}}$, $\ddot{\boldsymbol{u}}_{\boldsymbol{i-1}}$ are respectively the displacements, velocities, and accelerations vectors at the previous time step. The external force vector $\boldsymbol{f}$ will be considered constant throughout the entirety of simulation and its only non-null value will be the torque T applied to the only free DOF of the central master node of the rigid joint connection. The acceleration at the current time step is then computed as

$$\ddot{\boldsymbol{u}}^{*}{}_{\boldsymbol{i}} = \boldsymbol{S}_{\boldsymbol{i}}^{-\boldsymbol{1}} \delta \boldsymbol{r}_{\boldsymbol{i}} \tag{6.74}$$

Using this acceleration vector and the displacements, velocities, and accelerations of the previous step the new ones can then be computed, namely for the velocities

$$\dot{\boldsymbol{u}}^{*}{}_{\boldsymbol{i}} = \dot{\boldsymbol{u}}_{\boldsymbol{i-1}} + (1 - \delta_{NM} M)\ddot{\boldsymbol{u}}_{\boldsymbol{i-1}} + \delta_{NM} \ddot{\boldsymbol{u}}^{*}{}_{\boldsymbol{i}} \Delta t_i \tag{6.75}$$

And for the displacements

$$\boldsymbol{u}^{*}{}_{\boldsymbol{i}} = \boldsymbol{u}_{\boldsymbol{i-1}} + \Delta t_i \dot{\boldsymbol{u}}_{\boldsymbol{i-1}} + \Delta t_i^2 \left(\frac{1}{2} - \alpha_{NM}\right) \ddot{\boldsymbol{u}}_{\boldsymbol{i-1}} + \alpha_{NM} \ddot{\boldsymbol{u}}^{*}{}_{\boldsymbol{i}} \Delta t_i^2 \tag{6.76}$$

The displacements, velocities and accelerations $\boldsymbol{u}^{*}{}_{\boldsymbol{i}},\ \dot{\boldsymbol{u}}^{*}{}_{\boldsymbol{i}}, \ddot{\boldsymbol{u}}^{*}{}_{\boldsymbol{i}}$ thus obtained are marked by the apex $*$ since they have been obtained with the z^{th} rotated matrices along the mesh cycle, but for the next time step the $(z+1)^{th}$ matrices will have to be used. Since the only difference between the two sets of matrices is a rigid rotation of Δθ, the same rotation will be applied to the current results to obtain a suitable set of inputs for the next time step as

$$\boldsymbol{u}_{\boldsymbol{i}} = \boldsymbol{R}_{\boldsymbol{\Delta\theta}} \boldsymbol{u}^{*}{}_{\boldsymbol{i}} \, , \dot{\boldsymbol{u}}_{\boldsymbol{i}} = \boldsymbol{R}_{\boldsymbol{\Delta\theta}} \dot{\boldsymbol{u}}^{*}{}_{\boldsymbol{i}} \, , \ddot{\boldsymbol{u}}_{\boldsymbol{i}} = \boldsymbol{R}_{\boldsymbol{\Delta\theta}} \ddot{\boldsymbol{u}}^{*}{}_{\boldsymbol{i}} \tag{6.77}$$

This iterative time advancement can continue for each z^{th} angular position of the mesh cycle, until $z = N$ when special measures have to be taken since the cycle has to be reset to its initial condition, while keeping the travelling wave of excitation continuous. To do so, the displacements, velocities and accelerations obtained for the i^{th} time step where $z = N$ are first expanded to obtain again the values for all DOFs of the full FE model. This is done by employing the saved $\boldsymbol{T}_{\boldsymbol{cb,N}}$ as

$$\boldsymbol{u}_{\boldsymbol{i,F}} = \begin{Bmatrix} \boldsymbol{u}_{\boldsymbol{m}} \\ \boldsymbol{u}_{\boldsymbol{s}} \end{Bmatrix} = \boldsymbol{T}_{\boldsymbol{cb,N}} \boldsymbol{u}_{\boldsymbol{i}} \, , \dot{\boldsymbol{u}}_{\boldsymbol{i,F}} = \begin{Bmatrix} \dot{\boldsymbol{u}}_{\boldsymbol{m}} \\ \dot{\boldsymbol{u}}_{\boldsymbol{s}} \end{Bmatrix} = \boldsymbol{T}_{\boldsymbol{cb,N}} \dot{\boldsymbol{u}}_{\boldsymbol{i}} \, , \ddot{\boldsymbol{u}}_{\boldsymbol{i,F}} = \begin{Bmatrix} \ddot{\boldsymbol{u}}_{\boldsymbol{m}} \\ \ddot{\boldsymbol{u}}_{\boldsymbol{s}} \end{Bmatrix} = \boldsymbol{T}_{\boldsymbol{cb,N}} \ddot{\boldsymbol{u}}_{\boldsymbol{i}} \tag{6.78}$$

where the subscript F indicates that they represent the full FE model. Then the obtained vectors are sorted so that for the next mesh cycle the master DOFs selected will be the ones geometrically corresponding to ones of the last cycle, but with an angular difference of $\theta = 360/Z$, meaning that that the homologous nodes currently selected will be taken on the next tooth, following the sense of rotation. Thus, the same geometrical points will be chosen, but advanced of one tooth and then the new set of displacements, velocities, and accelerations, sorted in this new configuration, is reduced using the reduction matrix for $z = 1$

$$\begin{aligned} \boldsymbol{u}_{i,F} &= \boldsymbol{T}_{r,1}\boldsymbol{u}'_{i,f} = \boldsymbol{T}_{r,1}\begin{Bmatrix} \boldsymbol{u}'_m \\ \boldsymbol{u}'_s \end{Bmatrix} \\ \dot{\boldsymbol{u}}_{i,F} &= \boldsymbol{T}_{r,1}\dot{\boldsymbol{u}}'_{i,f} = \boldsymbol{T}_{r,1}\begin{Bmatrix} \dot{\boldsymbol{u}}'_m \\ \dot{\boldsymbol{u}}'_s \end{Bmatrix} \\ \ddot{\boldsymbol{u}}_{i,F} &= \boldsymbol{T}_{r,1}\ddot{\boldsymbol{u}}'_{i,f} = \boldsymbol{T}_{r,1}\begin{Bmatrix} \ddot{\boldsymbol{u}}'_m \\ \ddot{\boldsymbol{u}}'_s \end{Bmatrix} \end{aligned} \tag{6.79}$$

Where $\begin{Bmatrix} \boldsymbol{u}'_m \\ \boldsymbol{u}'_s \end{Bmatrix}, \begin{Bmatrix} \dot{\boldsymbol{u}}'_m \\ \dot{\boldsymbol{u}}'_s \end{Bmatrix}, \begin{Bmatrix} \ddot{\boldsymbol{u}}'_m \\ \ddot{\boldsymbol{u}}'_s \end{Bmatrix}$ are the newly sorted sets of masters and slaves DOFs. In this way the cycle can begin again with $z = 1$ and the $(i+1)^{th}$ time step can be computed, while this process is repeated each time that $z = N$ resetting then the counter to $z = 1$ until the completion of all required time steps. As stated, the external force vector $\boldsymbol{f}$ will be considered constant throughout the entire simulation, but the excitation of the dynamic system comes from the time-varying and moving contact mesh stiffness $\boldsymbol{K}^r_{c,i}$which acts upon the DOFs $\boldsymbol{u}_{Kc1}$ and $\boldsymbol{u}_{Kc2}$ of the two teeth pairs considered as in Figure 130 in the reduced matrices. The time-varying contact mesh stiffness is simulated by a grounded spring whose matrix form is

$$\boldsymbol{K}_{cm} = c_n k_{p,i} \begin{bmatrix} cos(\alpha) & 0 & 0 \\ 0 & sin(\alpha) & 0 \\ 0 & 0 & 0 \end{bmatrix} \tag{6.80}$$

in which $k_{p,i}$ is the instantaneous value of the mesh contact stiffness at time i for tooth pair p and c_n is a weight coefficient which changes from 0 to 1 and is different for each node considered, and α is the pressure angle. At the z^{th} angular position the location of the contact point is known trough one of the proposed models from Chapters III or IV and its location is compared to the coordinates of the n^{th} selected node on the flank for the reduced systems: if the location of the contact point coincides with one of the selected nodes then the corresponding coefficient is set to one and all others are set to zero, while if the contact point lies between two nodes the coefficient linearly varies similarly to 1D shape functions as

$$c_{n-1} = \frac{x_n - x}{x_n - x_{n-1}}\,, c_n = \frac{x_{n-1} - x}{x_n - x_{n-1}} \tag{6.81}$$

where x_n is the pseudo coordinate of the node on the flank as seen on a line, and this verifies $\sum_{n=1}^{mn} c_n = 1$ for every angular position considered, where mn is the number of mesh nodes selected on the flank to which the DOFs $\boldsymbol{u_{Kc1}}$ or $\boldsymbol{u_{Kc2}}$ correspond. Therefore, to simulate both the time variation of the value of the contact stiffness due to the meshing interaction and the motion of said stiffness along the flank as it varies during the mesh cycle, for every i^{th} time instant the matrices are assembled placing the grounded springs on the DOFs related for each of the considered nodes on the flank, so for the first tooth pair the matrices are placed on the DOFs of $\boldsymbol{u_{Kc1}}$

$$\boldsymbol{K^r_{1,i}} = \\ = \begin{bmatrix} \ddots & & & \\ & c_1 k_{1,i} \begin{bmatrix} cos(\alpha) & 0 & 0 \\ 0 & sin(\alpha) & 0 \\ 0 & 0 & 0 \end{bmatrix} & & \\ & & \ddots & \\ & & & c_{mn} k_{1,i} \begin{bmatrix} cos(\alpha) & 0 & 0 \\ 0 & sin(\alpha) & 0 \\ 0 & 0 & 0 \end{bmatrix} \\ & & & & \ddots \end{bmatrix} \tag{6.82}$$

And for the second one

$$\boldsymbol{K^r_{2,i}} = \\ = \begin{bmatrix} \ddots & & & \\ & c_1 k_{2,i} \begin{bmatrix} cos(\alpha) & 0 & 0 \\ 0 & sin(\alpha) & 0 \\ 0 & 0 & 0 \end{bmatrix} & & \\ & & \ddots & \\ & & & c_{mn} k_{2,i} \begin{bmatrix} cos(\alpha) & 0 & 0 \\ 0 & sin(\alpha) & 0 \\ 0 & 0 & 0 \end{bmatrix} \\ & & & & \ddots \end{bmatrix} \tag{6.83}$$

A visualization of the motion of the contact mesh stiffness and its variation in a mesh cycle using this method is visible in Figure 133. Clearly this approach can be easily extended for

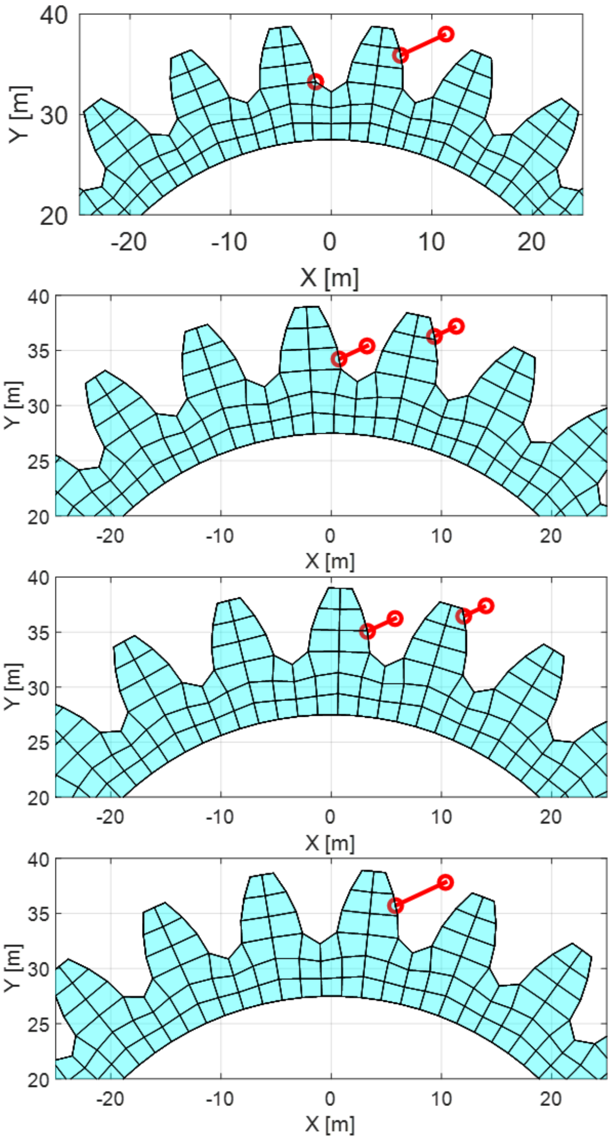

Figure 133: Position and magnitude variation of the contact mesh stiffness on the teeth flanks. The length of the red line indicates the module of the contact mesh stiffness applied.

gears with contact ratio greater than 2 with minimal modifications in the process. A similar approach is used to simulate the readout of a proximity sensor on the edge of the rim where the nodes corresponding to the DOFs $\boldsymbol{u_S}$ of the selected sensor nodes. Since a proximity sensor is fixed at a predetermined angular position the response must be read at the same location for every time step and angular position during rotation. To do so the displacements $\{u_S, v_S, w_S\}^T$ of each of the s selected sensor nodes is used to compute the displacements at a fixed point by

$$u_i = \sum_{n=1}^{s} c_s u_s \,, v_i = \sum_{n=1}^{s} c_s v_s \,, w_i = \sum_{n=1}^{s} c_s w_s, \tag{6.84}$$

where c_s are weights computed in a similar way of c_n only in this case the angular distance between the wanted read angle Ψ and the instantaneous position of the s^{th} sensor node is considered to assign the weight to each of the obtained displacements from the sensor nodes. Similarly, using the weights c_n and the displacements of the nodes where the contact mesh stiffness is applied the dynamic mesh deflection can be obtained along the direction of application of the load for each loaded tooth. This dynamic mesh deflection is obtained at each time step for each considered tooth and is positive if the grounded spring simulating the contact mesh stiffness is compressed, while negative if it's working in traction. If such situation occurs, for the next time step the instantaneous value of the contact mesh stiffness $k_{p,i}$ is set to 0 thus simulating a partial or total contact loss in the mating teeth, depending on how many teeth have a negative dynamic mesh deflection. In the next paragraphs the proposed model will be applied to a gear first with a rigid web and later to one with a compliant one. Further effects will be introduced along the way and the effect of several parameters will be investigated. However, as will be shown, due to the combination of geometry, parameters and loads no contact loss has been detected in any of the proposed tests. To summarize the proposed model aims to simulate the dynamic response of a single gear through a series of reductions and expansions of the degrees of freedom depending on the geometrical position at the considered timestep. The model is loaded by an external constant torque T applied on the central master node while the time-varying grounded springs $k_{p,1}$ and $k_{p,2}$ which act as sinks for the input energy, while the outputs are the displacements, velocities and accelerations of the set of sensor nodes $\boldsymbol{u_S}$, as well as the displacement of the central master node for the DTE. The schematization of this model is visible in Figure 134 where the same color scheme of Figure 130 is applied to differentiate the different sets of master nodes.

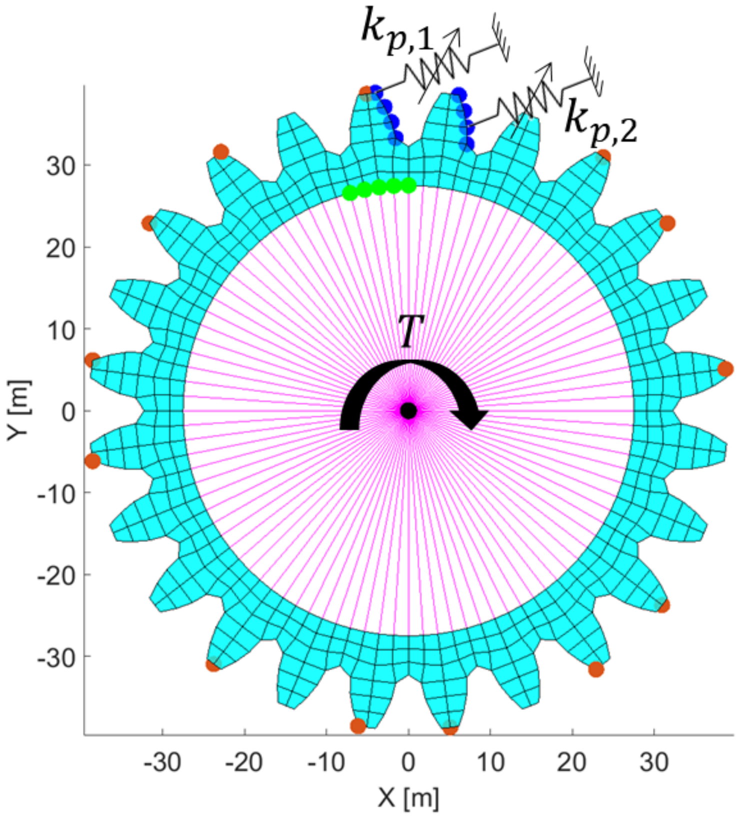

Figure 134: Schematization of the proposed dynamic model

VI.4 Rigid web results

As a first step the dynamic behavior of a gear with flexible teeth and rim, but with a rigid web will be analyzed. The main parameters are listed in Table 8 and the resulting 3D FE model is visible in Figure 135 where also the 81 master DOFs are indicated which together with 201 additional modes $\boldsymbol{\Phi}_{\boldsymbol{l}}$ contribute to the total matrices dimension of 285 total DOFs. In this paragraph and in the following one, unless otherwise specified, the constants that define the damping matrix α_c and β_c have been set to:

$$\begin{gathered} \alpha_c = 1 \\ \beta_c = 1e-7 \end{gathered} \tag{6.85}$$

which are on the low end of the values usually employed in literature for this kind of damping model. Using the full matrices and the eigenvalues and eigenvectors are obtained, classified by their mode shape, and compared to the ones from Nastran and the results up to $9kHz$ are listed in Table 9 from which an extremely close agreement between the proposed implementation and the commercial software can be appreciated. The 1D mode shape has a higher frequency than the 2D one since an additional stiffness, simulating a supporting shaft, has been added to the DOFs pertaining the central node for stability reasons. A selection of the mode shapes is visible in Figure 136. Although no other gear is currently considered, in order to estimate the contact mesh stiffness $k_{p,i}$ for tooth pairs 1 and 2, the gear is taken to be meshing with an identical one and the resulting contact mesh stiffness

Table 8: Gear and material data

Gear Parameters	Dimensions
Module m	$3\ mm$
Profile shift x	$0\ mm$
Number of teeth Z	24
Pressure angle α	$20°$
Face width b	$20\ mm$
Material - PEEK	Value
E	$5.7\ GPa$
ρ	$1320\ kg/m^3$
ν	0.38
Torque T	$30\ Nm$

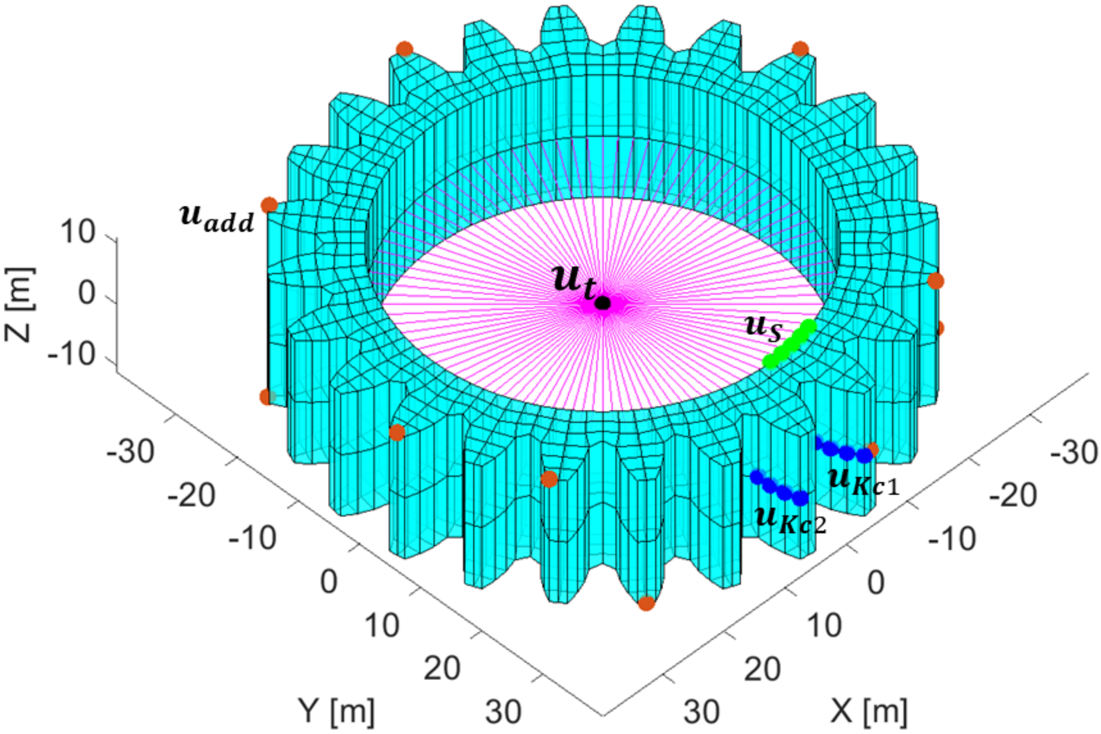

Figure 135: Rigid web gear FE discretization and master DOFs

over one mesh cycle is visible in Figure 137. Applying this periodic variation with the constant torque T under quasi-static conditions yields the displacements in the radial, tangential and axial directions as presented in Figure 138. The expected Campbell diagram in the stationary reference frame is visible in Figure 139 for the considered velocity range $100 \div 1260 \frac{rad}{s}$ in which even though no rotor dynamic effect has been introduced yet, the mode shapes still diverge in the forward and backward whirling travelling waves except for the axial and torsional modes which remain constant as expected. In order to quantify the excitation source usually a Fast Fourier Transform (FFT) of the STE is computed which in this case is visible in the upper portion of Figure 141 and the main harmonics are those corresponding to Excitation Orders (EO or Engine Orders) which are multiples of the number of teeth Z. However, in this case the STE is the result of the application of the time-varying contact mesh stiffness under constant torque and hence in order to analyze this excitation source the FFT of the contact mesh stiffness as experienced by a single teeth during an entire gear rotation is visible in the lower portion of the same figure. Under this situation the load is comparable to one as seen in a rotating reference frame, in which an axis is fixed to the gear and rotates with it with the same angular velocity. Therefore, considering the harmonic n it has a pulsation equal to

$$\omega_{b/f} = \omega \pm n \cdot \Omega = \Omega \cdot (z \pm n) = \Omega \cdot EO_{b/f} \tag{6.86}$$

Table 9: Mode frequencies and comparison with Nastran for the rigid web gear

Mode N°	Mode type	Freq. [Hz]	%err w.r.t Nastran [-]
1	2D	3028,59	3,58e-6
2	2D	3028,63	9,47e-6
3	1D	3255,84	2,07e-6
4	1D	3255,90	3,04e-6
5	Axial\0D	3685,46	3,54e-7
6	3D	4258,26	4,21e-6
7	3D	4258,74	3,03e-6
8	Torsional	6168,31	5,22e-7
9	4D	6367,57	3,77e-6
10	4D	6367,91	4,11e-6
11	5D	8779,44	3,09e-6
12	5D	8780,13	3,41e-6

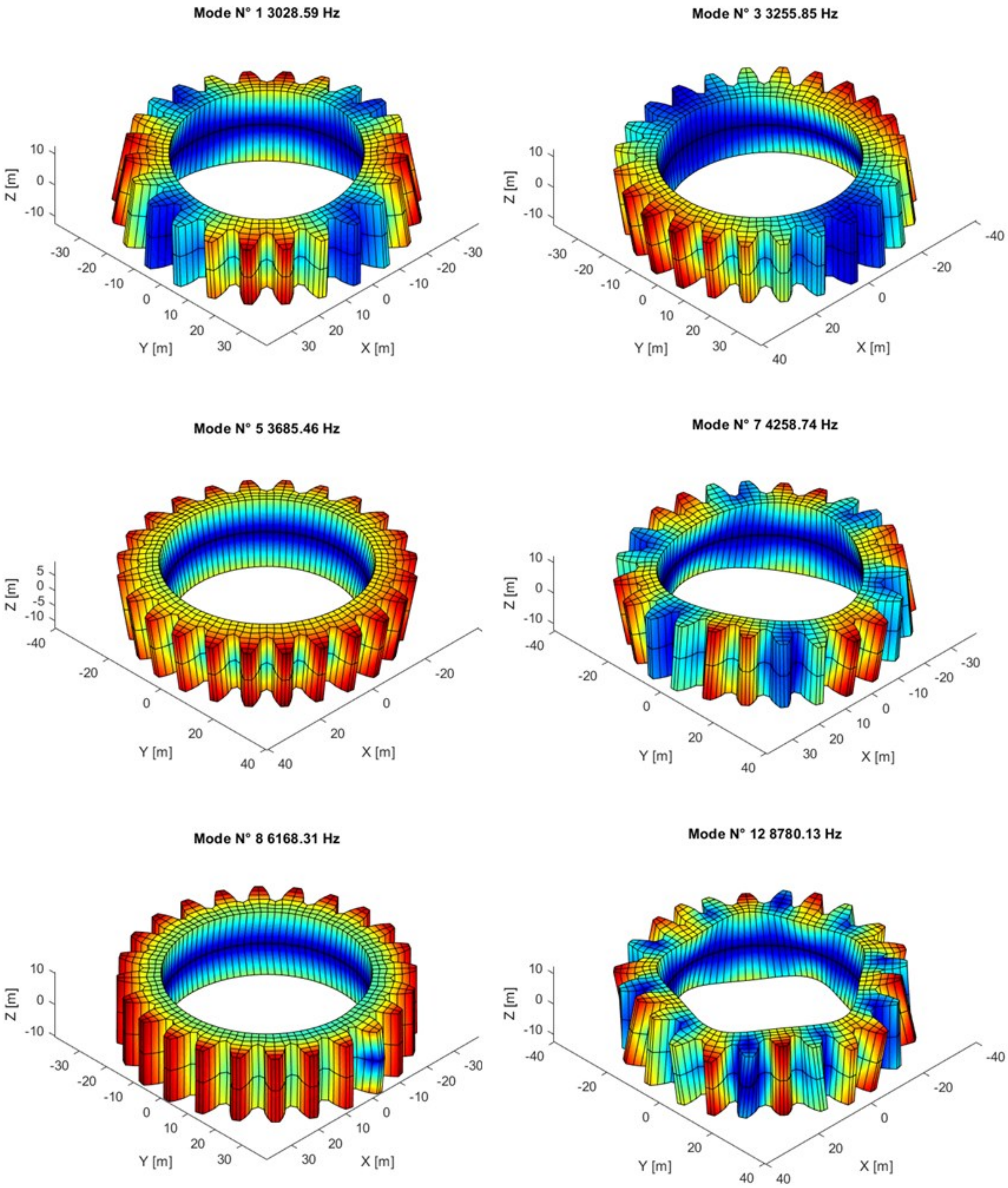

Mode N° 1 3028.59 Hz

Mode N° 3 3255.85 Hz

Mode N° 5 3685.46 Hz

Mode N° 7 4258.74 Hz

Mode N° 8 6168.31 Hz

Mode N° 12 8780.13 Hz

Figure 136: Mode shapes and frequencies - Rigid web

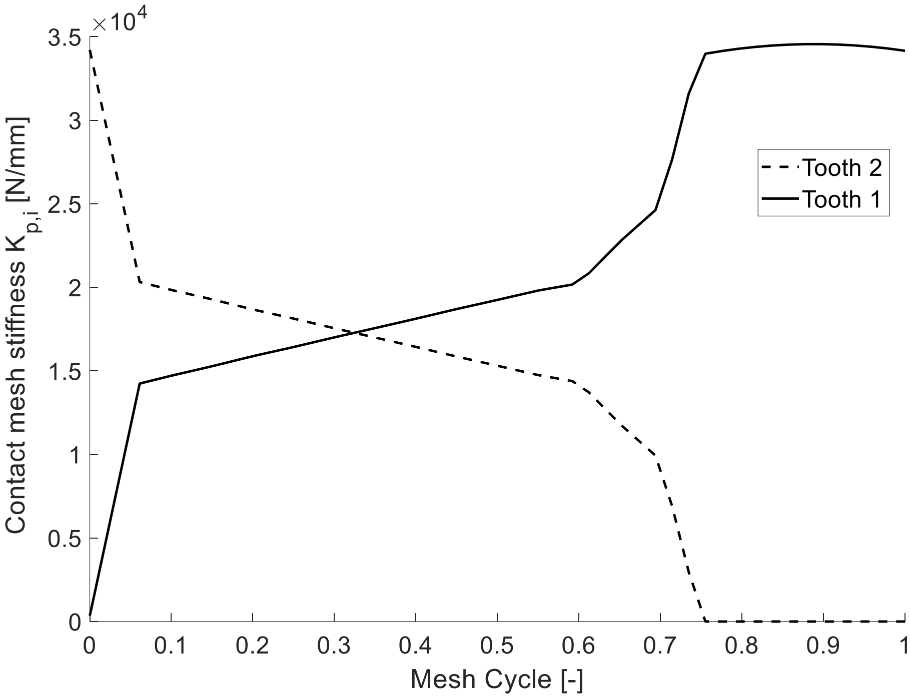

Figure 137: Evolution of the contact mesh stiffness $k_{p,i}$ over one mesh cycle

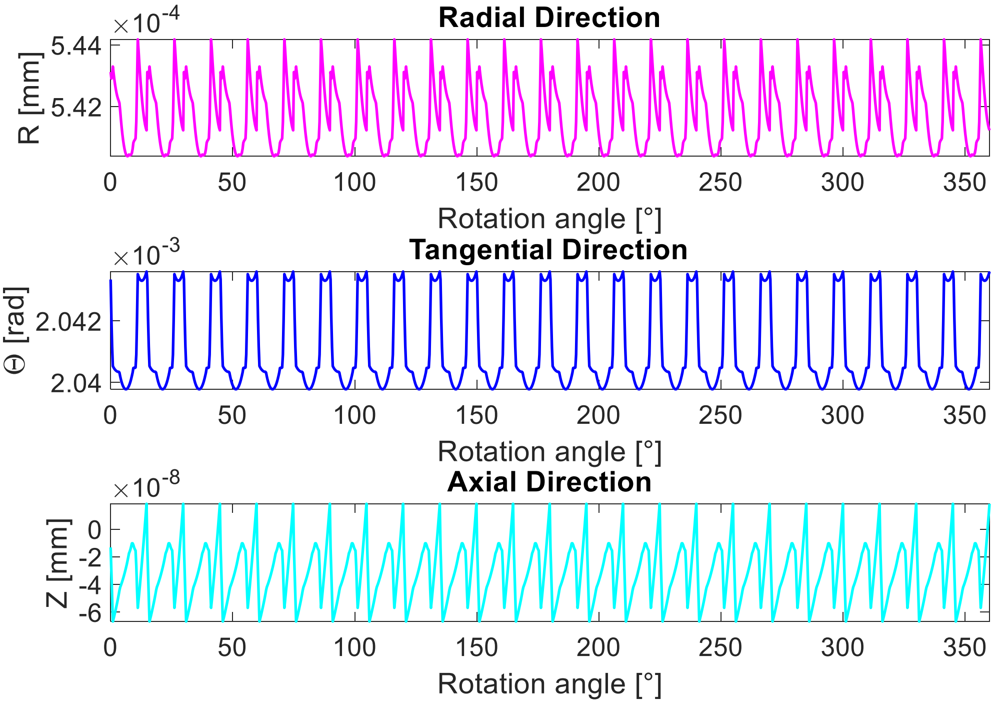

Figure 138: Displacements as experienced by the sensor under quasi-static conditions

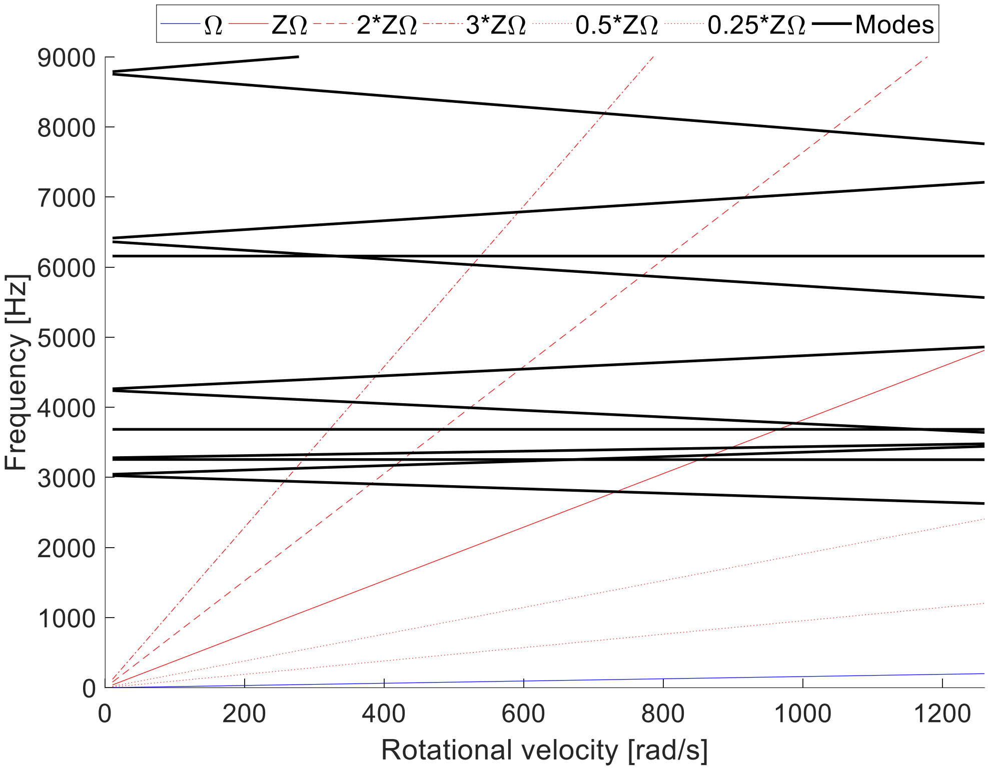

Figure 139: Campbell diagram

in which the subscripts b and f differentiate between the backward and forward whirling waves respectively and $\omega = Z \cdot \Omega$, thus the relevant EOs are

$$\begin{cases} EO_b = z + n \\ EO_f = z - n \end{cases} \tag{6.87}$$

In order to apply the model detailed in the previous paragraph the subdivision of the mesh cycle has been set to $N = 50$ and given the considered velocity range this yields a maximum time step equal to $\Delta t_{max} = 1.67e-5\ s$ at the beginning of the sweep, while the minimum value is $\Delta t_{min} = 2.62e-6\ s$ at the end of it. The variation of the instantaneous time step Δt_i and rotational velocity Ω as a function of time are visible in Figure 140 and those values for the continuous speed sweep will be used for all simulations of both rigid and compliant gears for consistency. The resulting dynamic displacements, as read by the different sensors, in the radial, tangential and axial direction are visible in Figure 142, while the dynamic mesh deflection is visible in Figure 143, and as stated earlier does not display any contact loss during the engagement. This mesh deflection accounts only for the dynamic compression experienced by the contact mesh stiffnesses $k_{p,i}$. These results are hence taken at non constant time intervals and therefore in order to obtain a spectrogram of the signal they are resampled at a constant time interval equal to $1 \cdot 10^{-6}\ s$. The resampled time response is then subdivided in segments composed of 524288 values, 90% overlap ratio, no windowing and the spectrogram is then obtained as visible in Figure 144 for the radial direction. The overlap of this spectrogram with the expected Campbell diagram and the spectrograms of the dynamic displacements in the tangential and axial direction are visible in Appendix A. The first phenomenon that will be introduced next is the gyroscopic effect. According to [147] the velocity vector components of a point vibrating and rotating around an axis with a rotational speed Ω can be defined by:

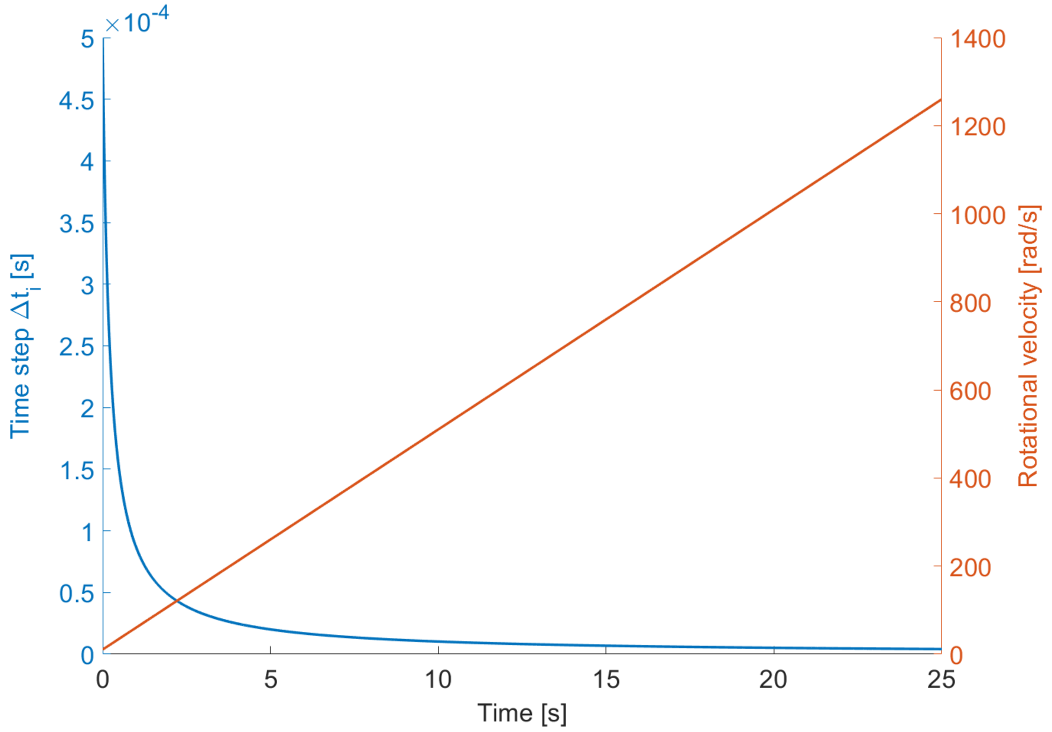

Figure 140: Variation of the instantaneous time step Δt_i *and rotational velocity* Ω *as a function of time*

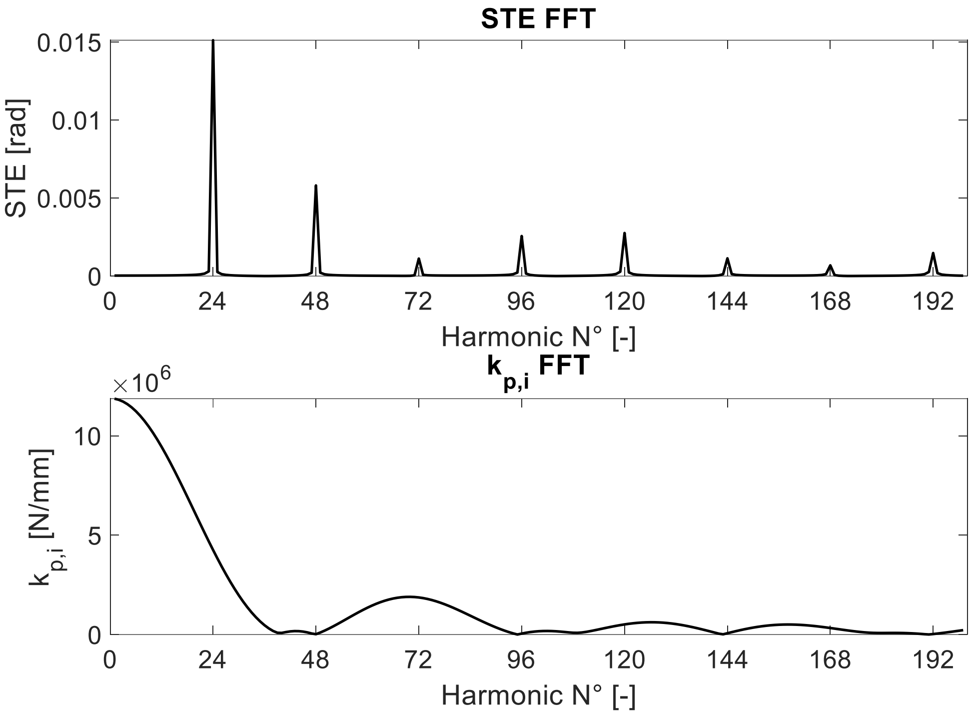

Figure 141: FFT of the excitation sources

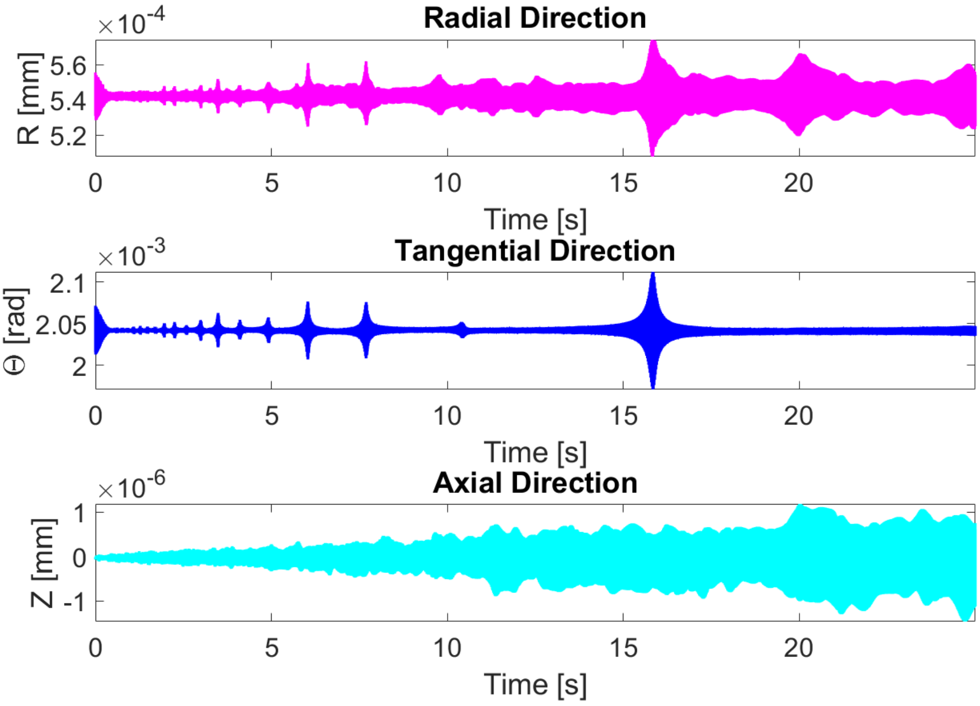

Figure 142: Dynamic displacements as experienced by the sensor nodes

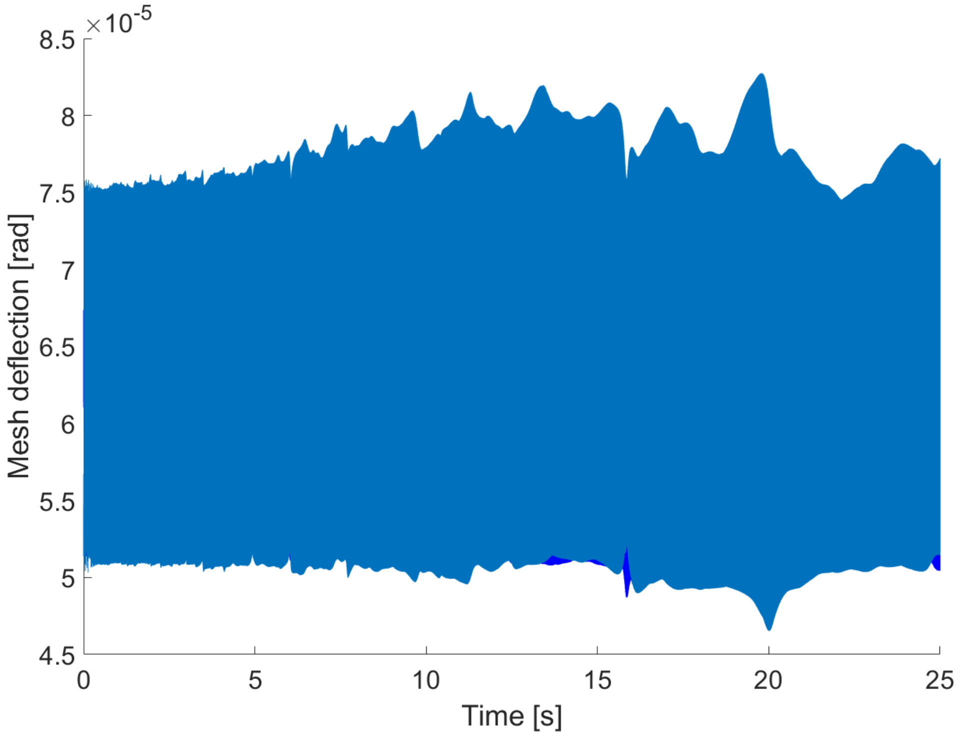

Figure 143: Dynamic mesh deflection

$$\begin{aligned} v_{x,i} &= \dot{u}_i cos\Omega t + \dot{v}_i sin\Omega t + \left(\dot{\theta}_i \varphi_i - \Omega\right)(-x_i sin\Omega t + y_i cos\Omega t) + (\dot{\theta}_i cos\Omega t \\ &\qquad - \dot{\varphi}_i sin\Omega t)\left(w_i + x_i \theta_i - y_i \varphi_i\right) \\ v_{y,i} &= -\dot{u}_i sin\Omega t + \dot{v}_i cos\Omega t + \left(\Omega - \dot{\theta}_i \varphi_i\right)(x_i sin\Omega t + y_i cos\Omega t) - (\dot{\theta}_i cos\Omega t \\ &\qquad - \dot{\varphi}_i sin\Omega t)\left(w_i + x_i \theta_i - y_i \varphi_i\right) \\ v_{z,i} &= \dot{w}_i + x_i \dot{\theta}_i - y_i \dot{\varphi}_i \end{aligned} \tag{6.88}$$

where

$$\theta_i = \frac{\partial u_i}{\partial z} \ \varphi_i = \frac{\partial v_i}{\partial z} \tag{6.89}$$

Hence, its kinetic energy due to gyroscopic effects can be written as

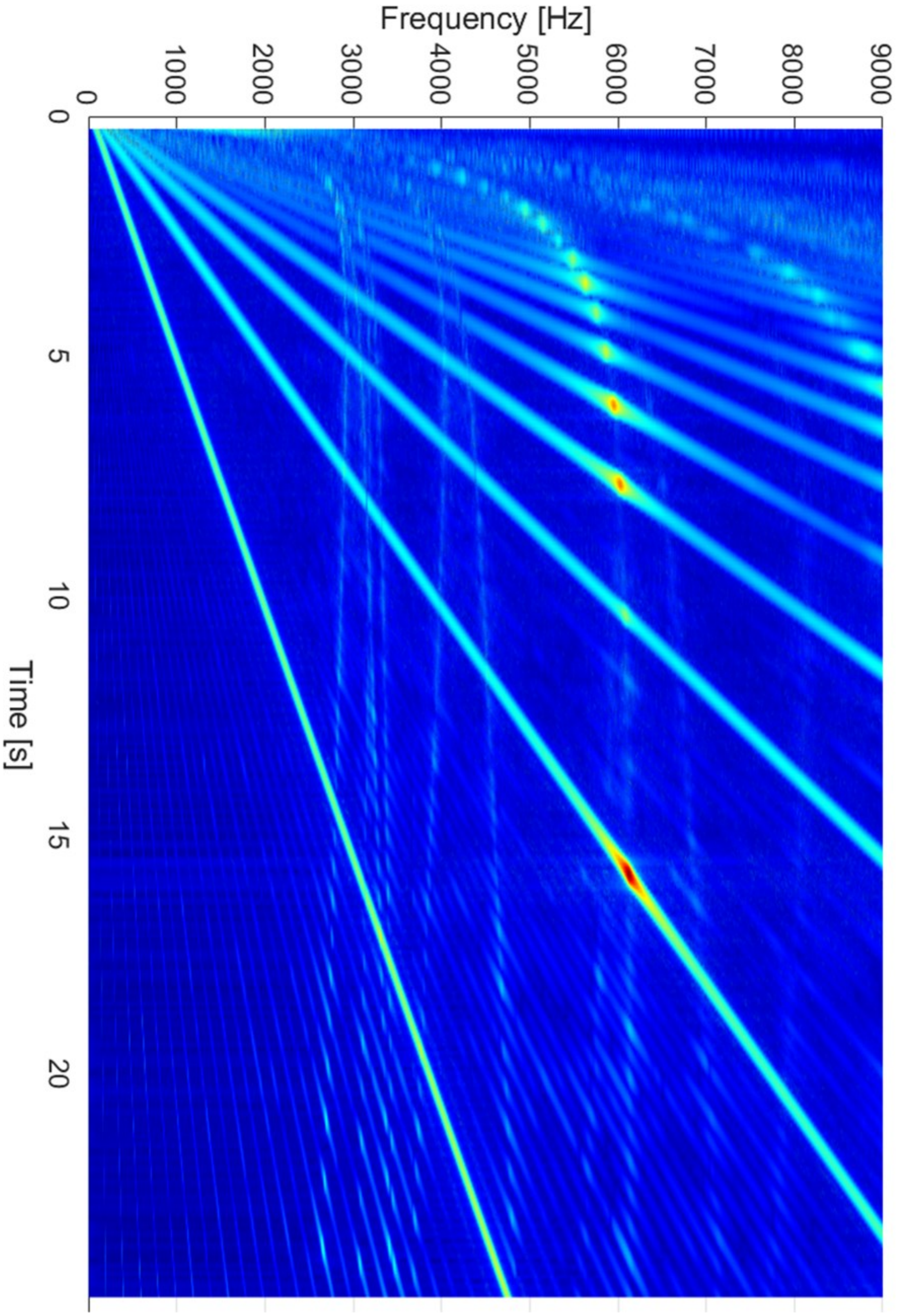

Figure 144: Spectrogram of the radial dynamic displacements

$$T_g = -\Omega \int_V \left(\left(\dot{\theta}_i \varphi_i + \theta_i \dot{\varphi}_i \right) x_i^2 + x_i y_i \left(\dot{\theta}_i \theta_i + \dot{\varphi}_i \varphi_i \right) + w_i \left(\dot{\theta}_i y_i + \dot{\varphi}_i x_i \right) \right) dV \tag{6.90}$$

However, the only components of the above expression which contribute to the inertia forces are

$$T_g = -\Omega \int_V w_i \left(\dot{\theta}_i y_i + \dot{\varphi}_i x_i \right) dV \tag{6.91}$$

Which can be discretized on the DOFs of the element $\boldsymbol{q_e}$ as

$$T_g = \Omega \boldsymbol{q_e^t G_e q_e} \tag{6.92}$$

Finally, integrating the above expression and employing the shape functions previously defined, the portion of the elemental gyroscopic matrix $\boldsymbol{G_e}$ connecting the DOFs of nodes i and j can be written as

$$\boldsymbol{G_e}(i,j) = \rho \begin{bmatrix} 0 & 0 & \int_{v_k} \left(\frac{\partial N_i}{\partial z} N_j x_{i,j} \right) dv_k \\ 0 & 0 & -\int_{v_k} \left(\frac{\partial N_i}{\partial z} N_j y_{i,j} \right) dv_k \\ -\int_{v_k} \left(\frac{\partial N_i}{\partial z} N_j x_{i,j} \right) dv_k & \int_{v_k} \left(\frac{\partial N_i}{\partial z} N_j y_{i,j} \right) dv_k & 0 \end{bmatrix} \tag{6.93}$$

in which the anti-symmetric nature of the gyroscopic matrix can be appreciated. Naturally, the assembled gyroscopic matrix of the structure G is then treated in the same way as the mass and stiffness ones and must then be included the iterative Newmark scheme for this effect to be taken into account. Matrix $\boldsymbol{S_i}$ is then formed as

$$\boldsymbol{S_i} = \boldsymbol{M_{z,i}^r} + \Delta t_i (\boldsymbol{C_{z,i}^r} + \Omega_i \boldsymbol{G_{z,i}^r}) + \Delta t_i^2 \alpha_{NM} \left(\boldsymbol{K_{z,i}^r} + \boldsymbol{K_{c,i}^r} \right) \tag{6.94}$$

and the residual vector $\boldsymbol{\delta r_i}$ is obtained from the following updated matrices

$$\boldsymbol{D_i} = -\left(\boldsymbol{K}^{\boldsymbol{r}}_{\boldsymbol{z,i}} + \boldsymbol{K}^{\boldsymbol{r}}_{\boldsymbol{c,i}}\right)$$

$$\boldsymbol{V_i} = -\boldsymbol{C}^{\boldsymbol{r}}_{\boldsymbol{z,i}} - \Omega_i \boldsymbol{G}^{\boldsymbol{r}}_{\boldsymbol{z,i}} - \Delta t_i\left(\boldsymbol{K}^{\boldsymbol{r}}_{\boldsymbol{z,i}} + \boldsymbol{K}^{\boldsymbol{r}}_{\boldsymbol{c,i}}\right) \tag{6.95}$$

$$\boldsymbol{A_i} = -(\boldsymbol{C}^{\boldsymbol{r}}_{\boldsymbol{z,i}} + \Omega_i \boldsymbol{G}^{\boldsymbol{r}}_{\boldsymbol{z,i}})(1 - \delta_{NM})\Delta t_i - \left(\boldsymbol{K}^{\boldsymbol{r}}_{\boldsymbol{z,i}} + \boldsymbol{K}^{\boldsymbol{r}}_{\boldsymbol{c,i}}\right)\left(\frac{1}{2} - \alpha_{NM}\right)\Delta t_i^2$$

while the rest of the process remains unchanged. The expected Campbell diagram with this introduction is visible in Figure 145, while the comparison with and without this effect can be seen in Figure 146. The impact of this introduction is not too great since the radius of the considered gear is small, but still it's non negligible especially for the mode shapes with the lowest number of nodal diameters. Similarly, to what has been done before the spectrogram of the dynamic response of this case can be appreciated in Figure 147 for the radial direction While the results for the tangential and axial direction are visible in Appendix A, as well as the superposition of the radial spectrogram with the modal Campbell diagram. For testing purposes, the damping coefficients have been doubled and set to

$$\begin{gathered} \alpha'_c = 2 \\ \beta'_c = 2e - 7 \end{gathered} \tag{6.96}$$

In order to compare the amplitude of the responses with the original and doubled damping the excitation orders Z and $2Z$ are extracted from the spectrograms of the dynamic responses and compared in Figure 148 and Figure 149. The amplitudes of the response on the EO Z are rather small compared to the ones from the EO $2Z$ especially in the radial and tangential direction, while the axial response is similar. This is mainly because the rigid web considered in this case stiffens the system too much. Regarding the change in the amplitudes when the damping is doubled on the order Z this change is visible but becomes evident especially on the EO $2Z$ where the amplitude is almost halved in the radial and tangential directions. Next an increase of 1.5 times of the torque applied to the system is considered. Under this new load the contact mesh stiffness changes and this variation is visible in Figure 150 for one mesh cycle, while the variation of the quasi static displacements can be appreciated in Figure 151. To compare the harmonic content of both the newly obtained STE and contact mesh stiffness variation their FFT has been again analyzed in the stationary

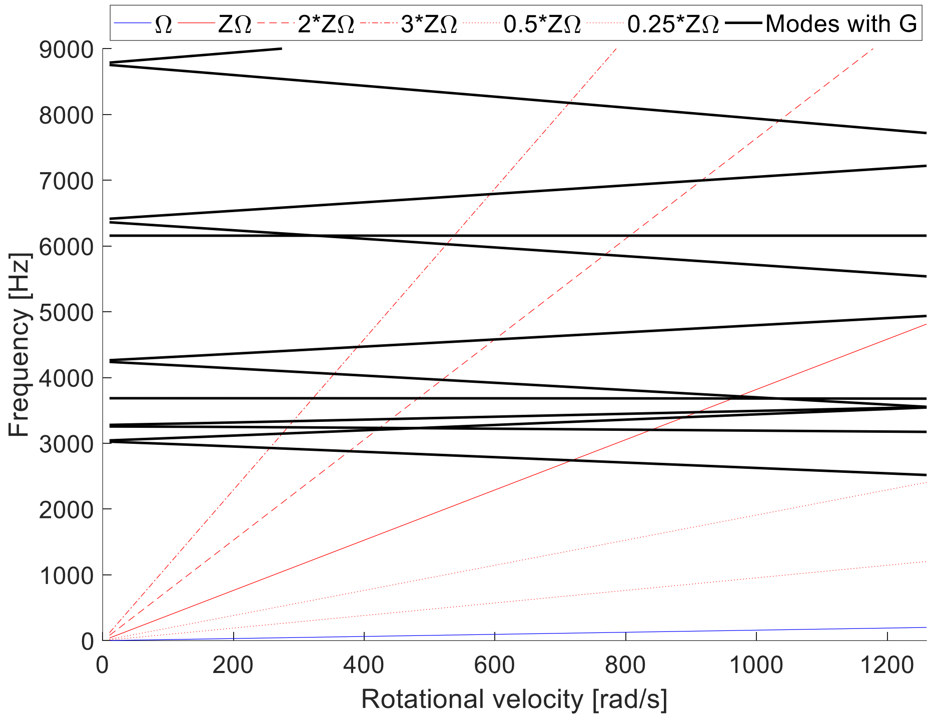

Figure 145: Campbell diagram with gyroscopic effect

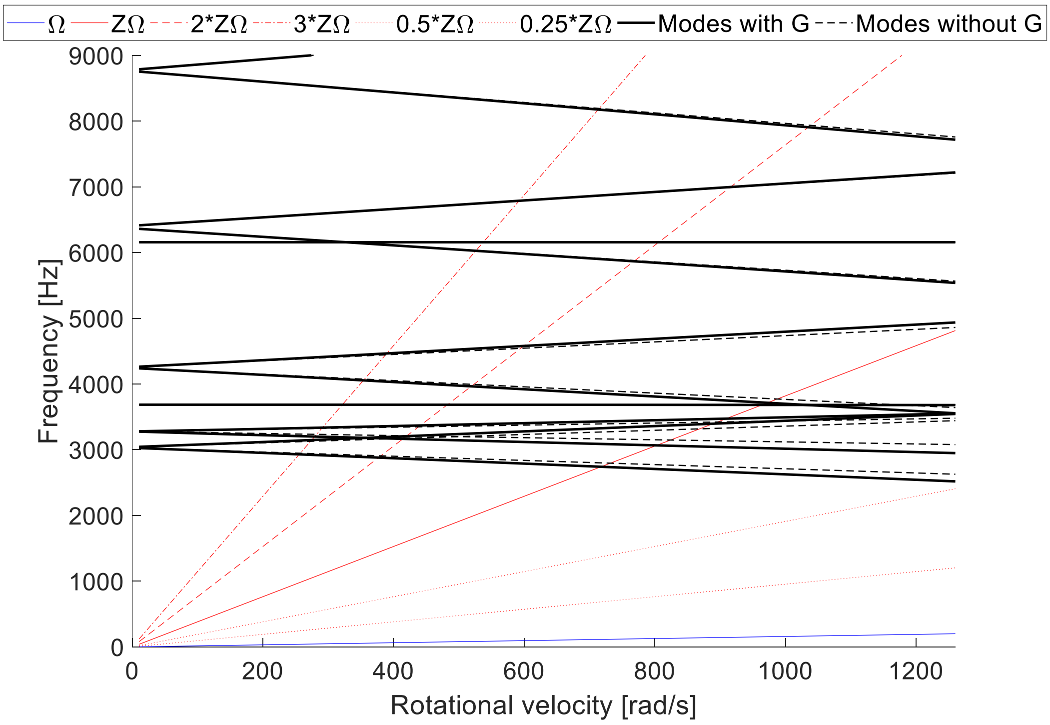

Figure 146: Comparison of the Campbell diagram with and without gyroscopic effect

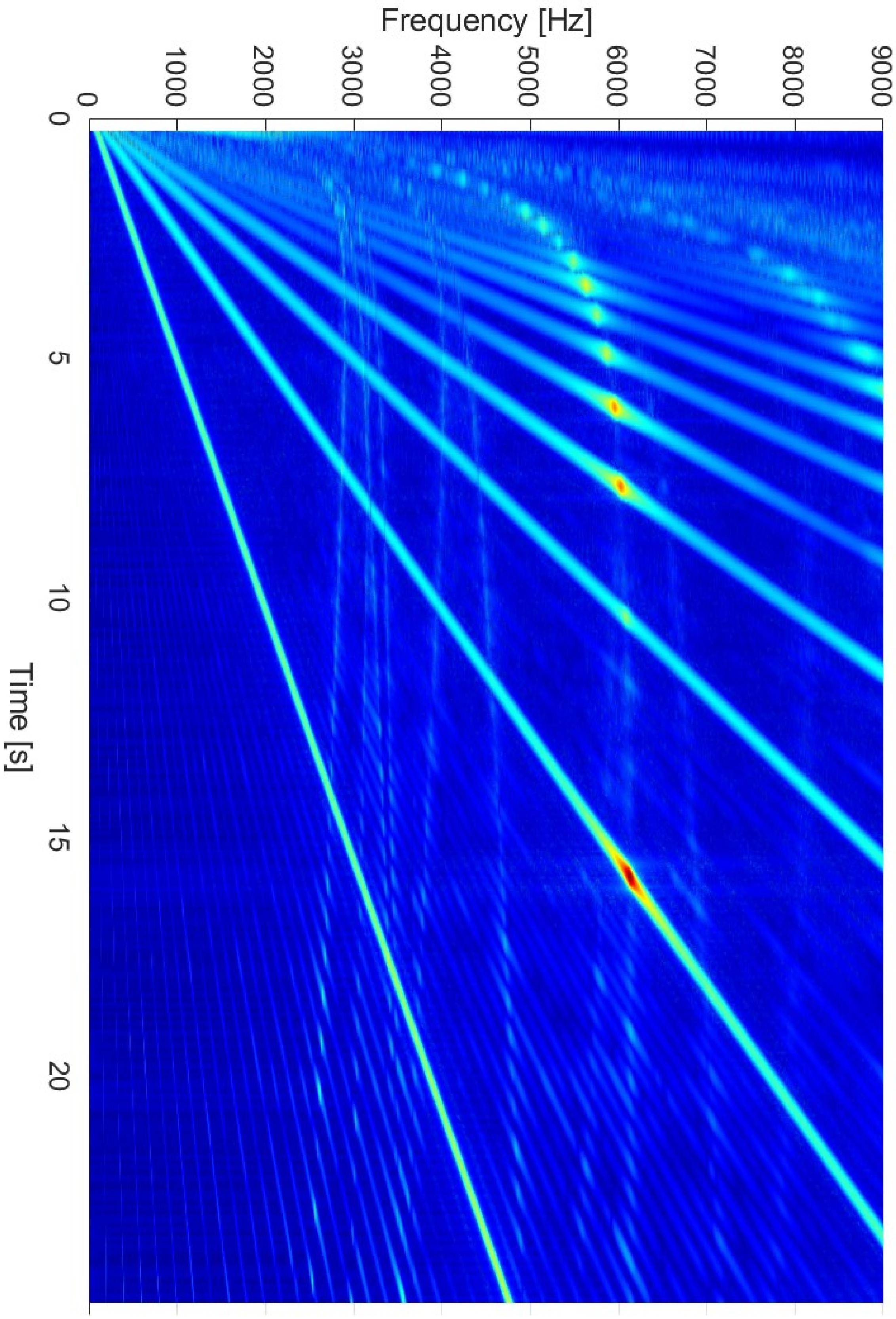

Figure 147: Spectrogram of the dynamic displacements in the radial direction with gyroscopic effect

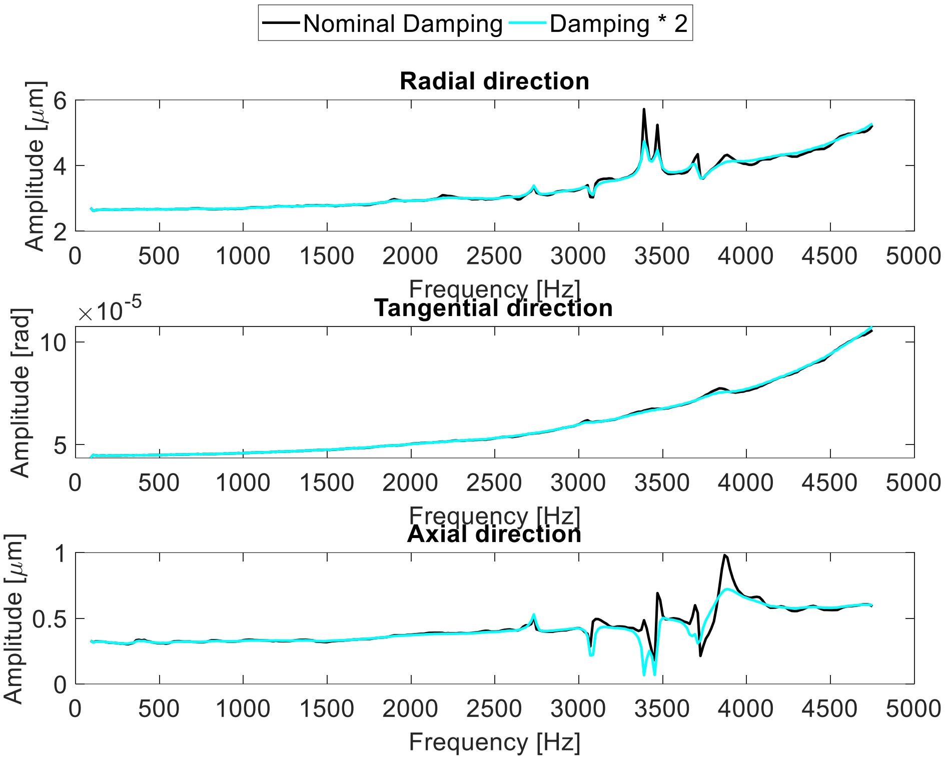

Figure 148: Effect of damping on the order $Z\Omega$

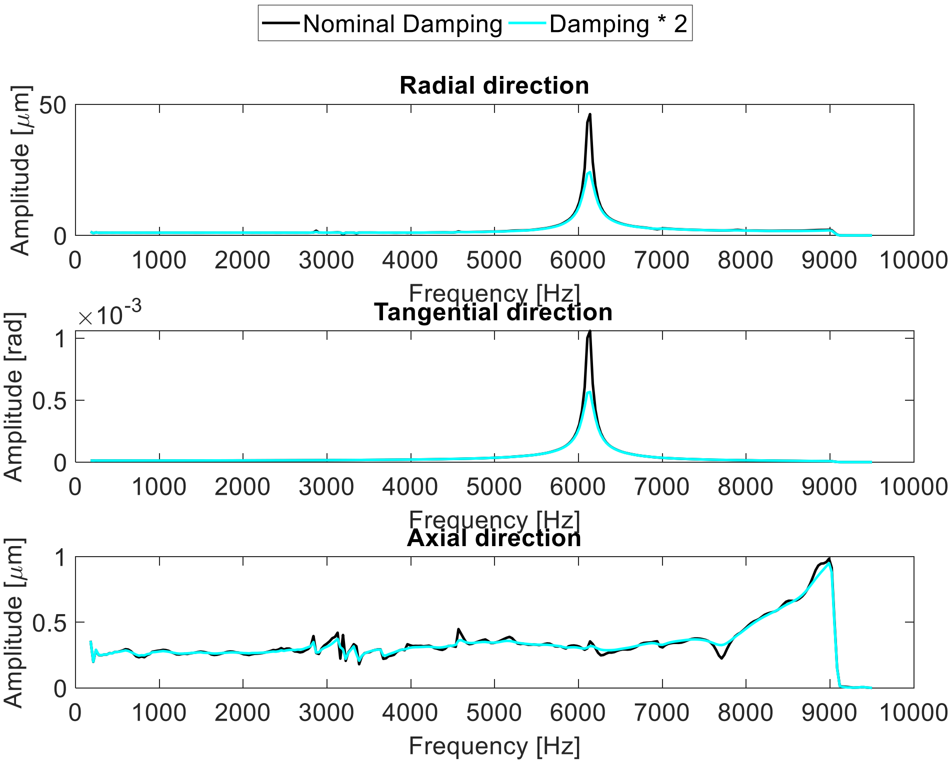

Figure 149: Effect of damping on the order $2Z\Omega$

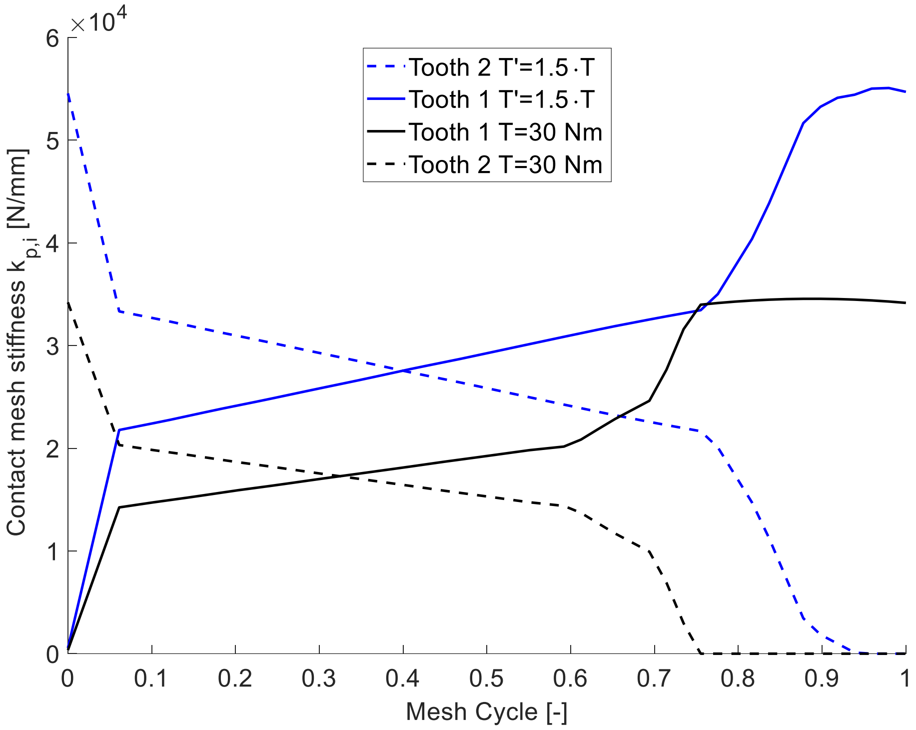

Figure 150: Variation of the contact mesh stiffness over one mesh cycle under nominal (black $30\ Nm$) torque and 1.5 times (blue $45\ Nm$) the nominal torque

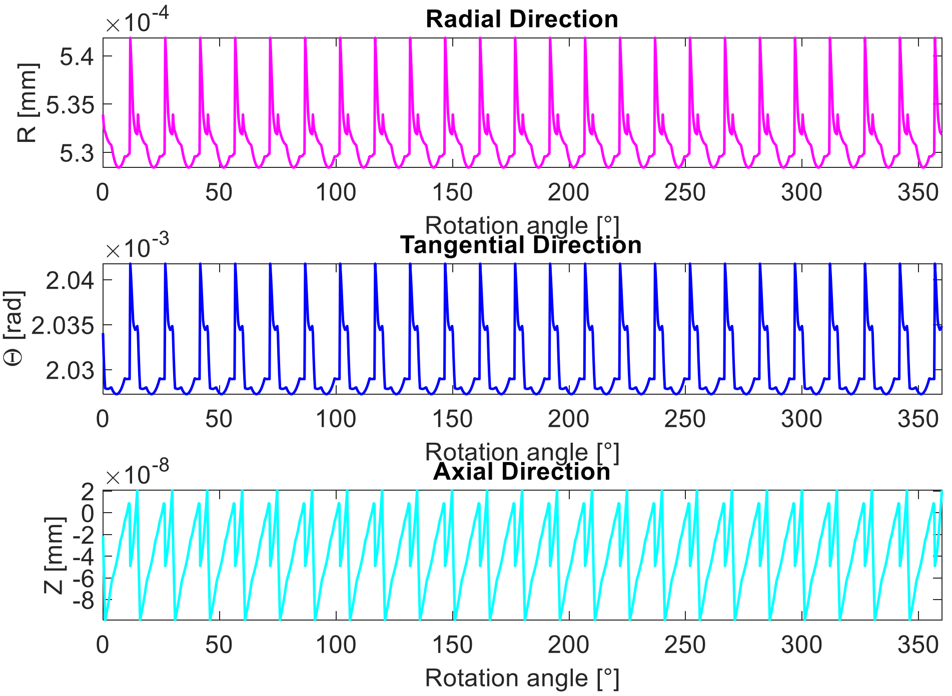

Figure 151: Quasi-static displacements under 1.5 times the nominal torque

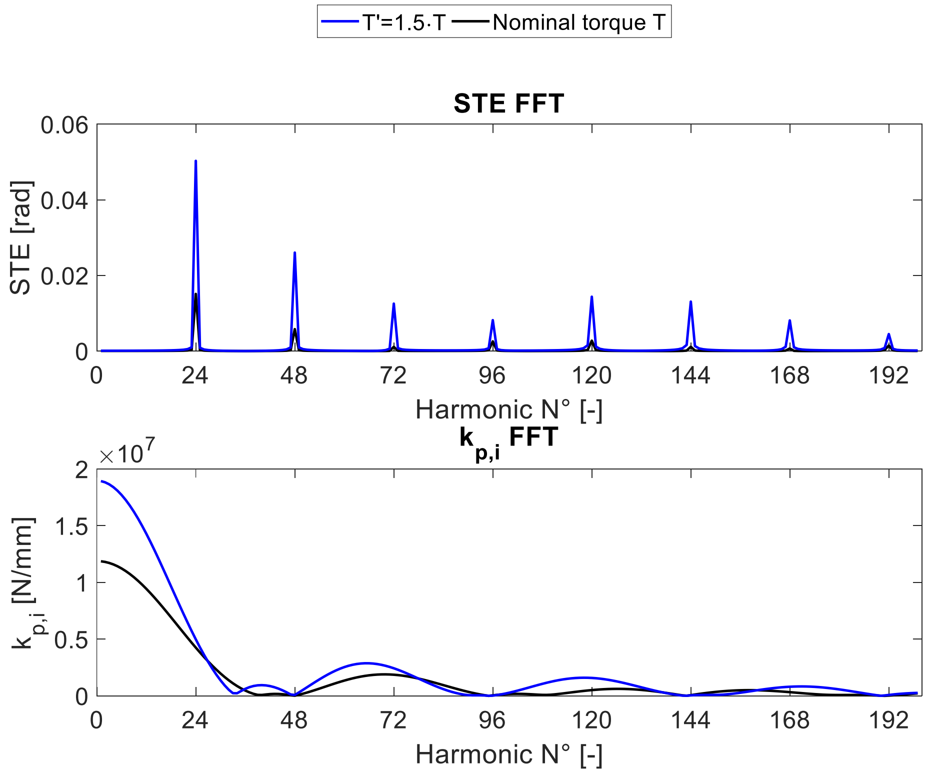

Figure 152: FFT of the excitation sources under nominal torque and 1.5 times the nominal torque

reference frame for the STE and in the rotating one for the $k_{p,i}$. Since the variation of the contact mesh stiffness is determined by a nonlinear approach also its change with the increased load is, which reflects on both the STE and the different FFT. The amplitude of the responses is compared for the EO Z and $2Z$ in Figure 153 and Figure 154 respectively. In those figures the obtained response for the nominal torque with nominal contact mesh stiffness is compared with the ones with increased torque and tis related $k_{p,i}$, but also the response where the contact mesh stiffness is kept unchanged while the load is increased is presented. Evidently the increase in the torque plays a role in augmenting the vibration levels resulting from the model, but the main effect is visible when also the contact mesh stiffness assumes its real value and the amplitudes are evidently much higher for all direction considered.

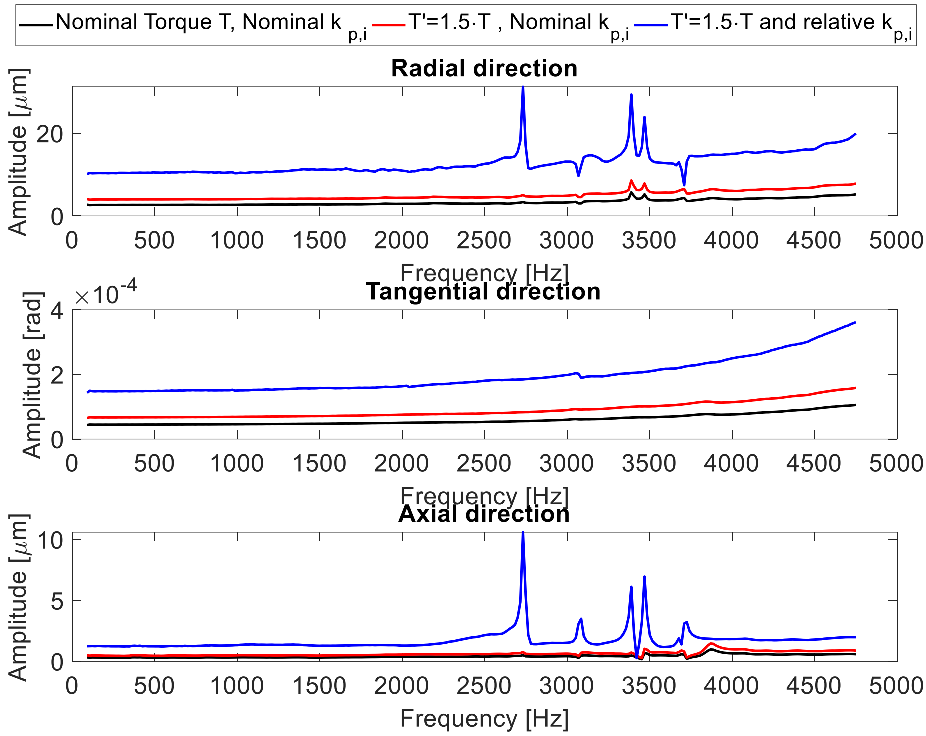

Figure 153: Effect of torque and variation of the contact mesh stiffness under nominal and 1.5 times the nominal torque on the order $Z\Omega$

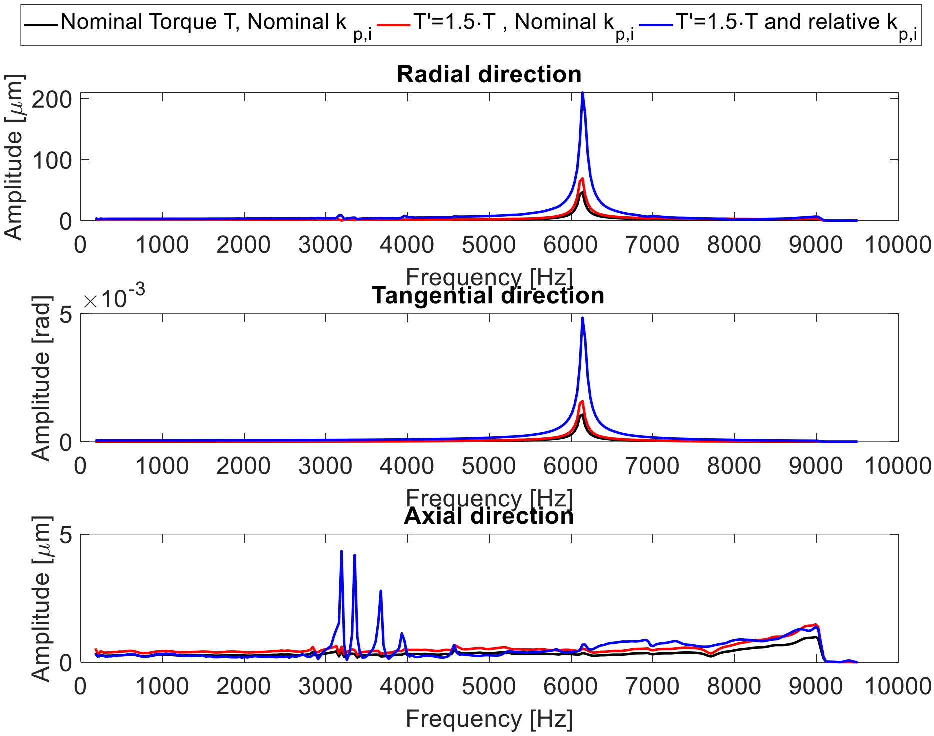

Figure 154: Effect of torque and variation of the contact mesh stiffness under nominal and 1.5 times the nominal torque on the order $2Z\Omega$

VI.5 Compliant web results

In this paragraph the dynamic behavior of a gear with the same main parameters as in the previous one (listed in Table 8) will be analyzed but with the introduction of a very thin flexible web with a thickness of $1.66\ mm$. The geometry and its FE discretization are visible in Figure 155 were also the master DOFs are marked. In this case, to keep the resultant of the application of the contact mesh stiffnesses centered, two rows of nodes have been selected for the interested teeth, and therefore its value will be split in half and applied to the correct nodes. For this reason, the total number of master DOFs rises to 309 since the number of additional modes of matrix $\mathbf{\Phi}_{\boldsymbol{l}}$ has been kept equal to 201 as in the previous case. The frequencies and type of the mode shapes in the $9\ kHz$ range are listed in Table 10 in which again the comparison with Nastran is extremely close, with negligible frequency differences and in Figure 156 are visible some of those mode shapes. Also the load and damping coefficients have been kept constant from the previous example and the variation of the contact mesh stiffness $k_{p,i}$ for a mesh cycle is shown in Figure 157, while the displacements experienced by the sensor nodes in quasi static condition obtained under constant torque and with the variation of said stiffness can be seen in Figure 158 and they are quite different from the ones obtained with the rigid web due to the introduction of this additional compliance. The modal Campbell diagram in the velocity range from 100 to $1260\,\frac{rad}{s}$ is visible in Figure 159 in which the gyroscopic effect is included, but again due to the small dimensions of the considered gear doesn't show a meaningful impact. The FFT of the variation of the STE in the stationary frame as well as the one of the contact mesh stiffness variation in the rotating one are displayed in Figure 160. Under these conditions, with a subdivision of the mesh cycle has been set to $N = 50$ and given the considered velocity range this yields a maximum time step equal to $\Delta t_{max} = 1.67e - 5\ s$ at the beginning of the sweep, while the minimum value is $\Delta t_{min} = 2.62e - 6\ s$ at the end of it. The resulting dynamic displacements, as read by the different sensors, in the radial, tangential and axial direction are visible in Figure 161 which show marked oscillations at different rotational speeds which were not present in the rigid web case. This reflects also on the dynamic variation of the mesh deflection, visible in Figure 162, but also in this case no contact loss is registered since the values are positive for the entire time history and a detail of this dynamic displacement at

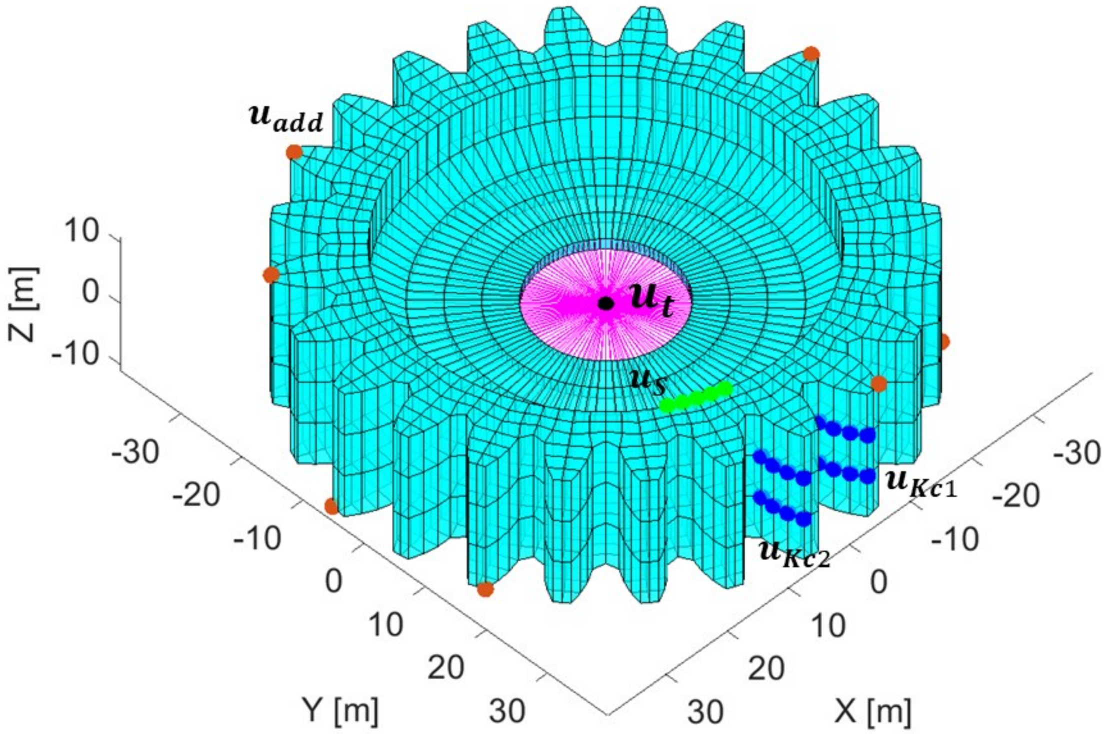

Figure 155: Compliant web gear FE discretization and master DOFs

Table 10: Mode frequencies and comparison with Nastran for the compliant web gear

Mode N°	Mode type	Freq. [Hz]	%err w.r.t Nastran [-]
1	1D	360,25	8,74e-6
2	1D	360,38	1,27e-6
3	Axial	670,30	1.01e-7
4	Torsional	1650,48	3,04e-7
5	2D	2140,61	5,97e-6
6	2D	2140,99	3,07e-6
7	Trasl.	3853,64	4,58e-6

8	Trasl.	3854,89	5,97e-6
9	3D	5390,86	1,03e-6
10	3D	5391,54	1,23e-6
11	2D ip	5860,06	2,24e-6
12	2D ip	5860,84	2,35e-6
13	0D+1C	6564,92	1,22e-6
14	1D+1C	7376,63	1,21e-6
15	1D+1C	7377,59	8,41e-7
16	3D ip	8014,45	2,24e-6
17	3D ip	8015,49	9,21e-7
18	4D	8935,77	2,77e-6
19	4D	8936,96	1,94e-6

the highest resonance occurring at $17.234\,s$ is shown in Figure 163 which displays a dominant sinusoidal nature. From the dynamic displacements the spectrogram of the response is again obtained after resampling at a constant time interval equal to $1e-6\,s$. The resampled time response is then subdivided in segments composed of 524288 values, 90% overlap ratio, no windowing and the resulting spectrogram from the axial displacements is visible in Figure 167, while the superposition of this spectrogram and the modal Campbell diagram can be consulted in Appendix B as well as the spectrograms in the radial and tangential direction. In order to fully take into consideration the flexibility of the web another effect must be taken into consideration which is the differential stiffness or stress stiffening effect. The name of this effect comes from the fact that the stresses caused by a deformation under load are used as inputs to generate an additional load dependent stiffness matrix obtained under linear hypotheses and the used in the dynamic integration scheme. The approach here implemented is based again on Nastran implementation [148] and its derivation starts by including in the definition of the potential energy also the effects of the initial stresses provoked by external loads w_p, which yields

$$w_p = \frac{1}{2}\int_V \left[w_x^2\left(\sigma_y+\sigma_z\right)+w_y^2(\sigma_x+\sigma_z)+w_z^2\left(\sigma_x+\sigma_y\right)-2w_xw_y\tau_{xy}-2w_yw_z\tau_{yz} - 2w_zw_x\tau_{xz}\right]dV \tag{6.97}$$

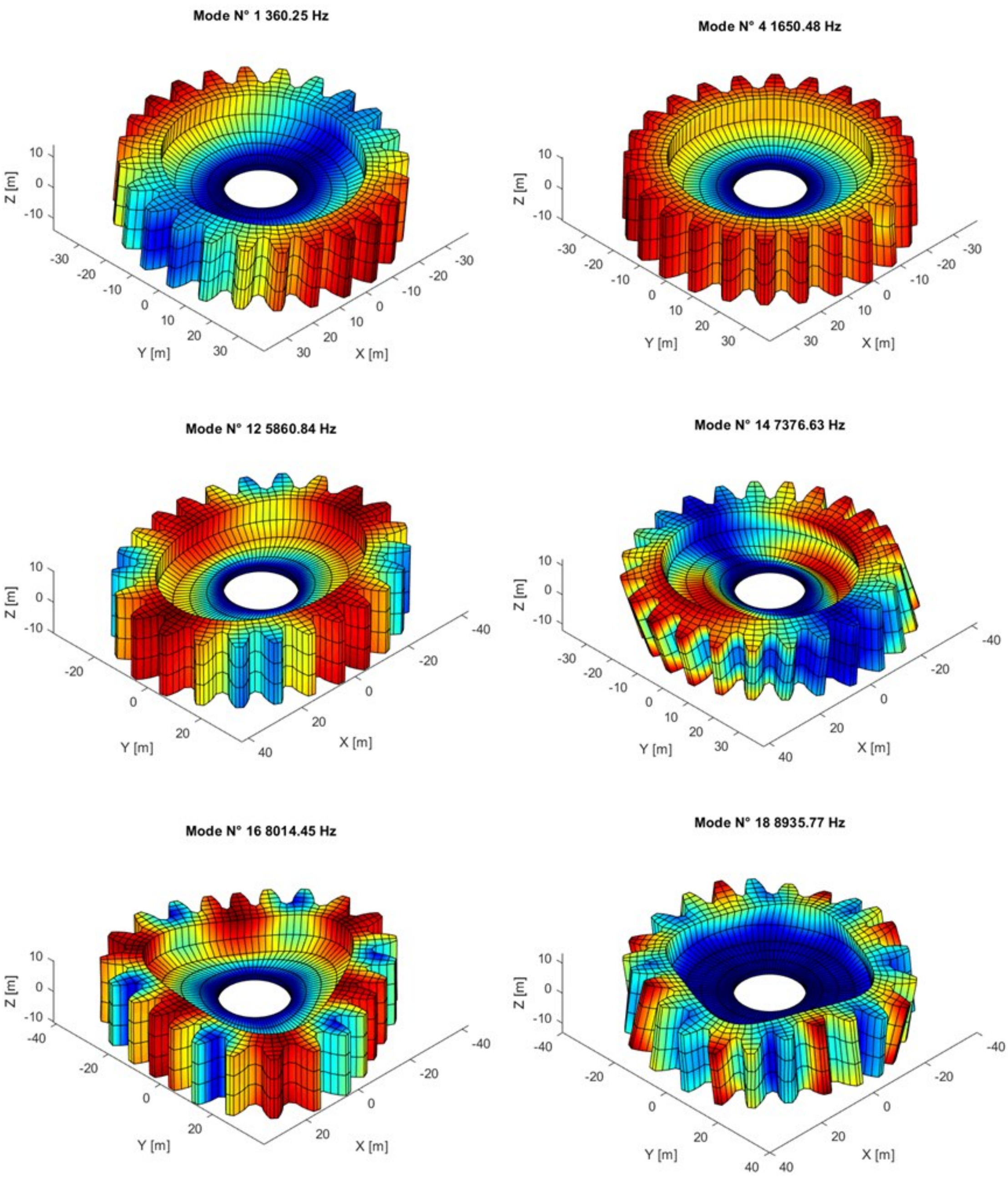

Figure 156: Example mode shapes of the compliant gear

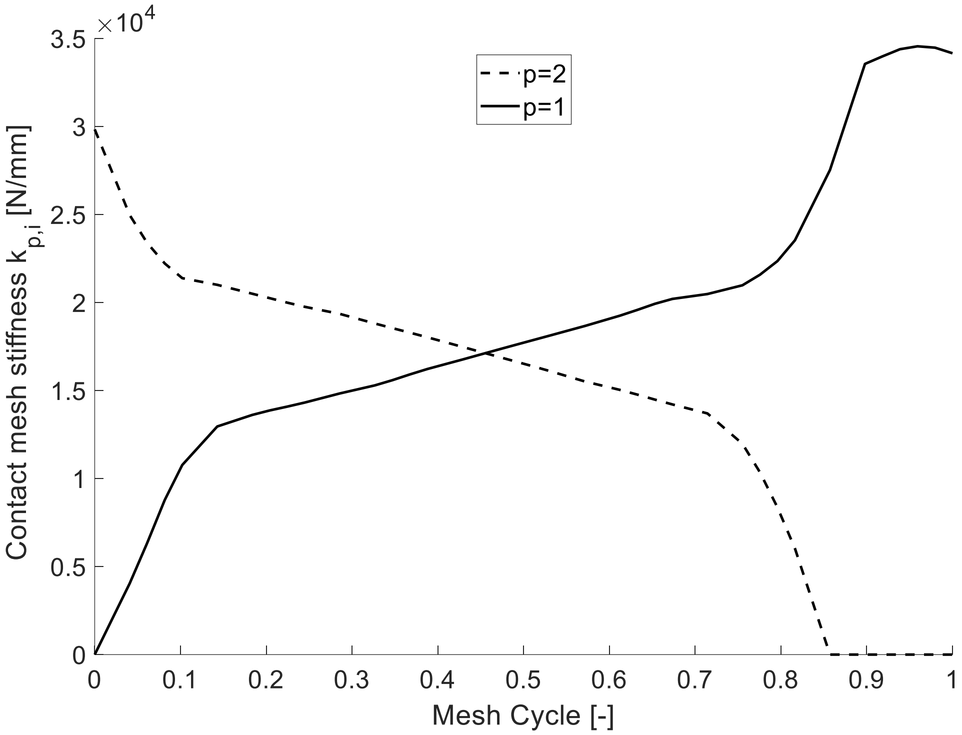

Figure 157: Contact mesh stiffness variation over one mesh cycle

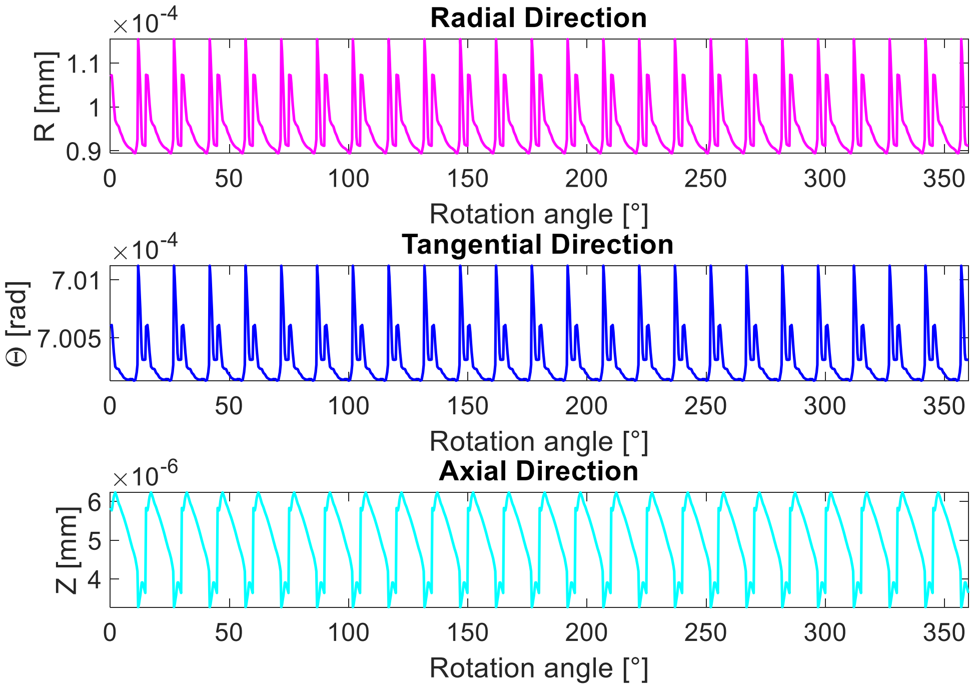

Figure 158: Displacements as experienced by the sensor under quasi-static conditions

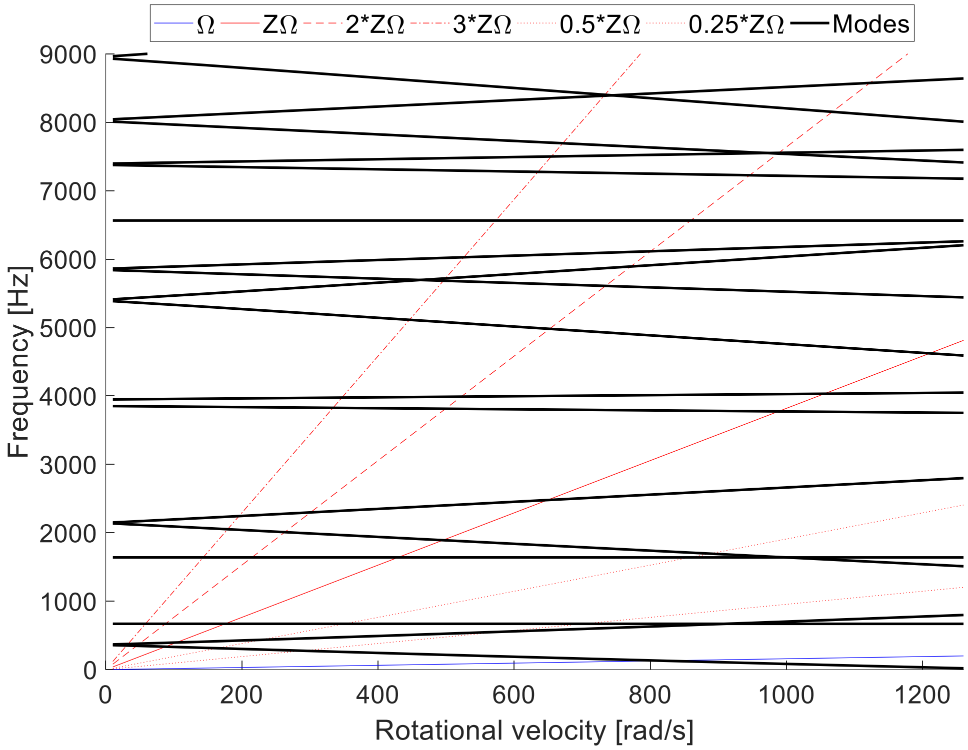

Figure 159: Campbell diagram with gyroscopic effect

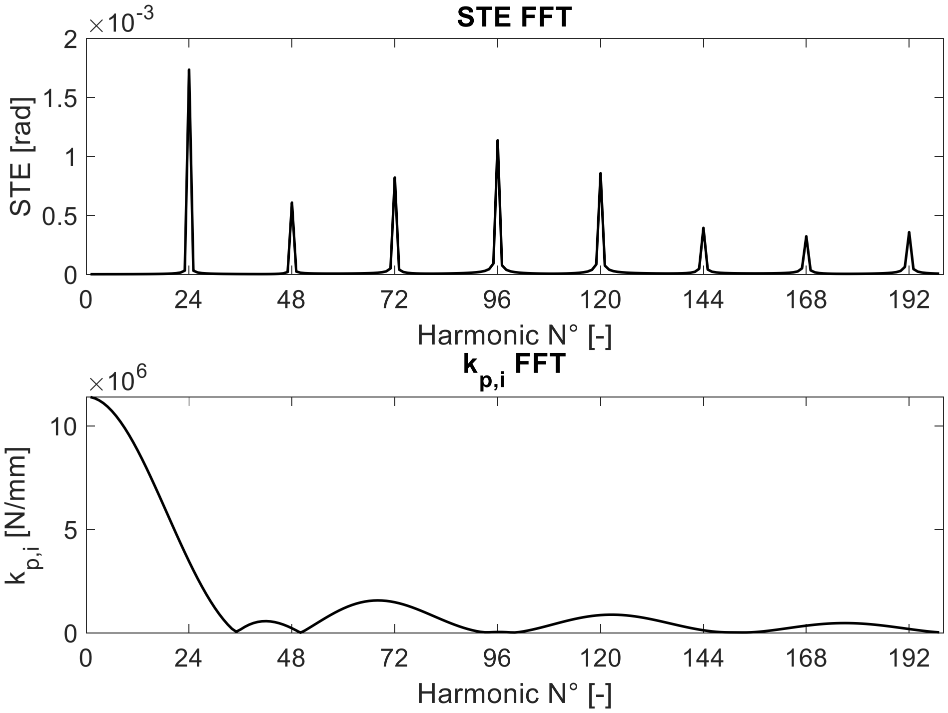

Figure 160: FFT of the excitation sources

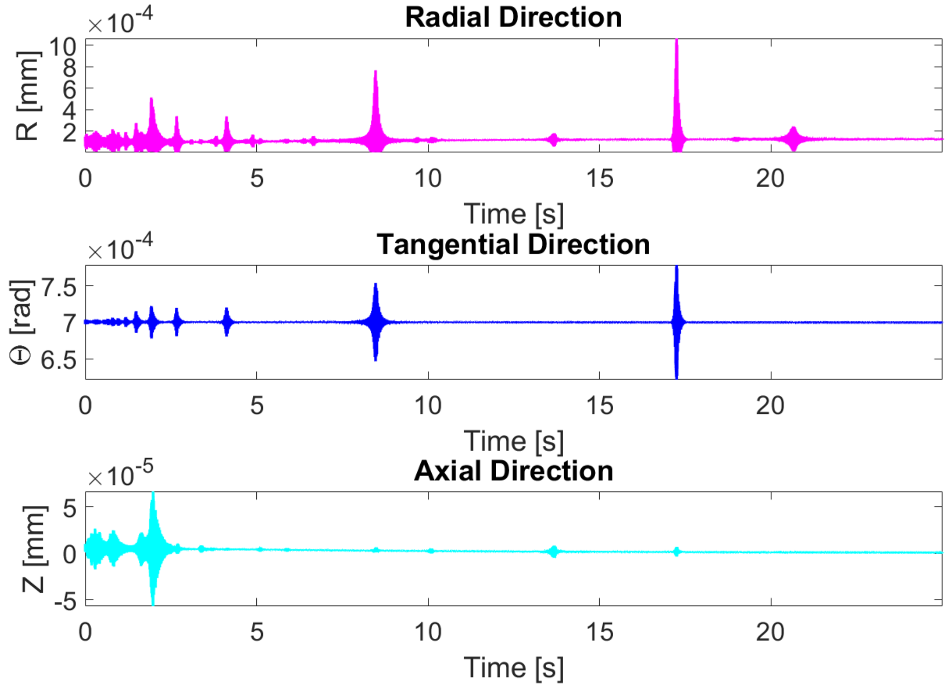

Figure 161: Dynamic displacements as experienced by the sensor nodes

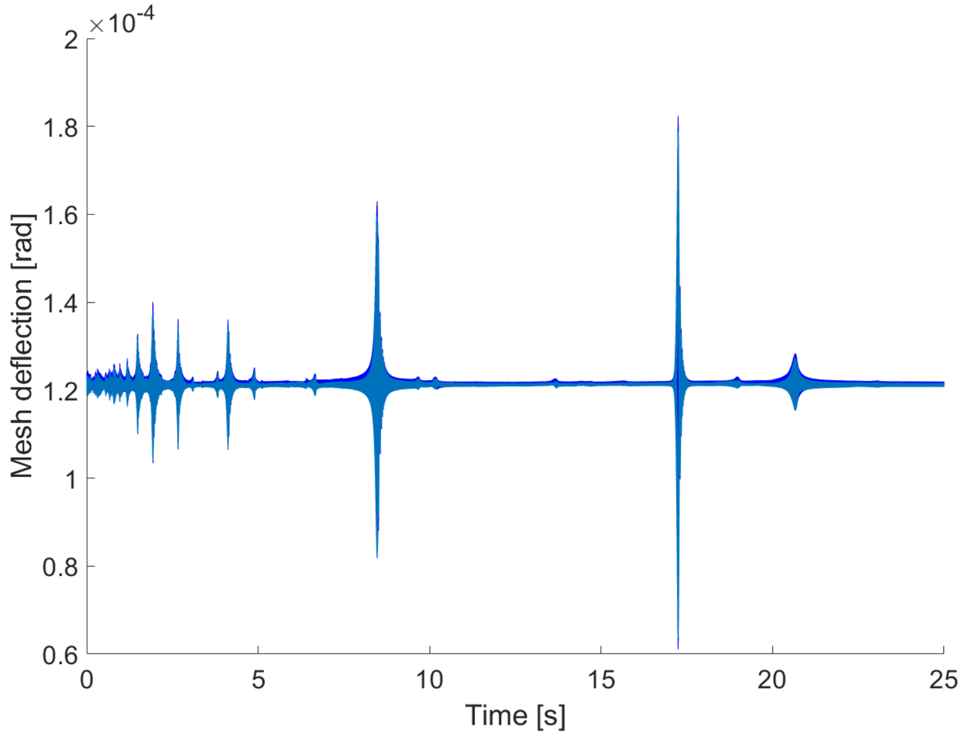

Figure 162: Dynamic mesh deflection

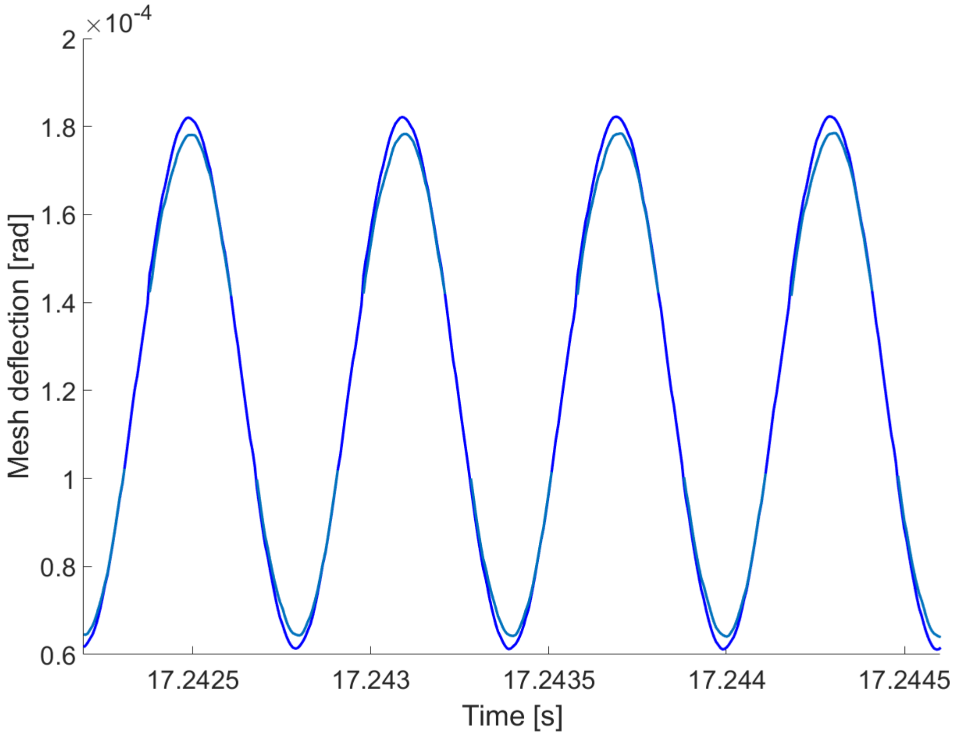

Figure 163: Detail of the dynamic mesh deflection

Where V is the volume of the element, the normal and shear stresses $\sigma_x, \sigma_y, \sigma_z, \tau_{xy}, \tau_{xz}, \tau_{yz}$are recovered from a stress recovery procedure by using equation (6.36) to first get the strains and then getting the stress components using the matrix defining the elastic properties of the material (6.7), while the rotations w_x, w_y, w_z are obtained by

$$\begin{aligned} w_x &= \frac{1}{2}\left(\frac{\partial w}{\partial y} - \frac{\partial v}{\partial z}\right) \\ w_y &= \frac{1}{2}\left(\frac{\partial u}{\partial z} - \frac{\partial w}{\partial x}\right) \\ w_x &= \frac{1}{2}\left(\frac{\partial v}{\partial x} - \frac{\partial u}{\partial y}\right) \end{aligned} \tag{6.98}$$

where u, v, w are the nodal displacements. In matrix form this can be written as

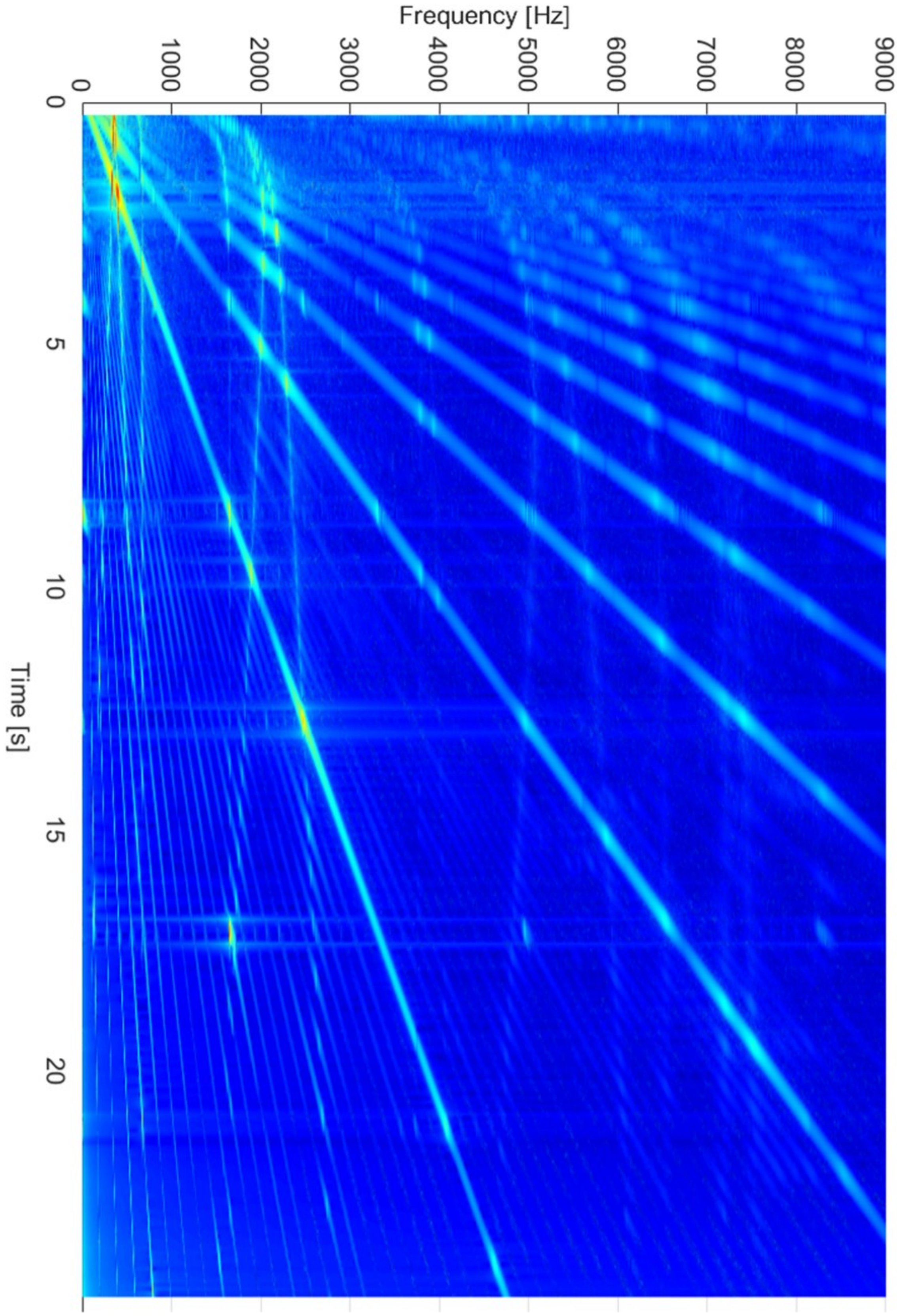

Figure 164: Spectrogram of the dynamic response in the axial direction

$$\begin{Bmatrix} w_x \\ w_y \\ w_z \end{Bmatrix} = [\boldsymbol{C_1}\,\boldsymbol{C_2}\,\cdots\boldsymbol{C_8}] \begin{Bmatrix} u_1 \\ v_1 \\ w_1 \\ u_2 \\ v_2 \\ w_2 \\ \vdots \\ u_8 \\ v_8 \\ w_8 \end{Bmatrix} = \boldsymbol{\overline{C}u_e} \tag{6.99}$$

where $\boldsymbol{\overline{C}}$ is formed by the sub matrices $\boldsymbol{C_i}$ containing the shape function derivatives

$$\boldsymbol{C_i} = \begin{bmatrix} 0 & -\frac{\partial N_i}{\partial z} & \frac{\partial N_i}{\partial y} \\ \frac{\partial N_i}{\partial z} & 0 & -\frac{\partial N_i}{\partial x} \\ -\frac{\partial N_i}{\partial y} & \frac{\partial N_i}{\partial x} & 0 \end{bmatrix} \tag{6.100}$$

for $i = 1,2,..,8$. The elemental stress stiffness matrix $\boldsymbol{K_{ss,e}}$ is obtained after Gauss point integration scheme from

$$\boldsymbol{K_{ss,e}} = \int_{V_e} \boldsymbol{\overline{C}^T K_{ww} \overline{C}} dV_e \tag{6.101}$$

Where the matrix containing the stresses $\boldsymbol{K_{ww}}$ is written as

$$\boldsymbol{K_{ww}} = \begin{bmatrix} \sigma_y + \sigma_z & -\tau_{xy} & -\tau_{xz} \\ -\tau_{xy} & \sigma_x + \sigma_z & -\tau_{yz} \\ -\tau_{xz} & -\tau_{yz} & \sigma_x + \sigma_y \end{bmatrix} \tag{6.102}$$

In the current case the stresses considered are caused by the elastic displacements due to the inertial effect of the rotational velocity applied to the gear. This load is dependent with Ω^2 but the displacements are obtained linearly and therefore this procedure is performed only once at the reference rotational velocity of $1\frac{rad}{s}$ thus forming the assembled system stress stiffening matrix $\boldsymbol{K_{ss}}$ which is then treated in the same manner as the other matrices to obtain the N reduced matrices $\boldsymbol{K}^{r}_{ss,i}$. This effect is hence introduced by modifying the assembly of matrix $\boldsymbol{S_i}$ which is then formed as

$$\boldsymbol{S_i} = \boldsymbol{M}^{r}_{z,i} + \Delta t_i(\boldsymbol{C}^{r}_{z,i} + \Omega_i \boldsymbol{G}^{r}_{z,i}) + \Delta t_i^2 \alpha_{NM}\left(\boldsymbol{K}^{r}_{z,i} + \boldsymbol{K}^{r}_{c,i} + \Omega_i^2 \boldsymbol{K}^{r}_{ss,i}\right) \tag{6.103}$$

and the residual vector $\boldsymbol{\delta r_i}$ is obtained from the following updated matrices

$$\boldsymbol{D_i} = -\left(\boldsymbol{K}^{r}_{z,i} + \boldsymbol{K}^{r}_{c,i} + \Omega_i^2 \boldsymbol{K}^{r}_{ss,i}\right)$$

$$\boldsymbol{V_i} = -\boldsymbol{C}^{r}_{z,i} - \Omega_i \boldsymbol{G}^{r}_{z,i} - \Delta t_i\left(\boldsymbol{K}^{r}_{z,i} + \boldsymbol{K}^{r}_{c,i} + \Omega_i^2 \boldsymbol{K}^{r}_{ss,i}\right) \tag{6.104}$$

$$\boldsymbol{A_i} = -(\boldsymbol{C}^{r}_{z,i} + \Omega_i \boldsymbol{G}^{r}_{z,i})(1 - \delta_{NM})\Delta t_i - \left(\boldsymbol{K}^{r}_{z,i} + \boldsymbol{K}^{r}_{c,i} + \Omega_i^2 \boldsymbol{K}^{r}_{ss,i}\right)\left(\frac{1}{2} - \alpha_{NM}\right)\Delta t_i^2$$

while the rest of the scheme remains unchanged. The Campbell diagram over the rotational speed range obtained with this effect included is visible in Figure 165 and its effect on the modal frequencies is highlighted by the comparison in Figure 166 where the values with and without the stress stiffening are compared. Due to the particularly thin geometry of the web in the current case the stress field is non negligible leading to noticeable deviations as the rotational speed increases which are mostly constant for all mode shapes with radial or axial components. The spectrogram of the time domain response in the axial direction is shown in Figure 167 and the overlap of this spectrogram with the modal Campbell diagram can be found in Appendix B as well as the spectrograms of the dynamic responses in the radial and tangential direction. The extraction of the response orders Z and $2Z$ can be seen in Figure 168 and Figure 169 respectively in which the frequency shift can be appreciated, while the amplitudes remain unchanged for the most part. The effect of the load on the response is then analyzed by comparing the results at the nominal level of torque ($T = 30\ Nm$) with those obtained at $T' = 0.75T$ and $T'' = 1.25T$. As shown in the previous paragraph the parameter influencing more the amplitudes of the responses is actually the variation of the contact mesh stiffness at different loads. Those variations at the considered load levels are shown in Figure 170 while the comparison of the resulting STE are visible in Figure 171. The comparison of the FFT of the variation of the contact mesh stiffness exciting the system and that of the STE can be appreciated in Figure 172 and show differences in both the values and

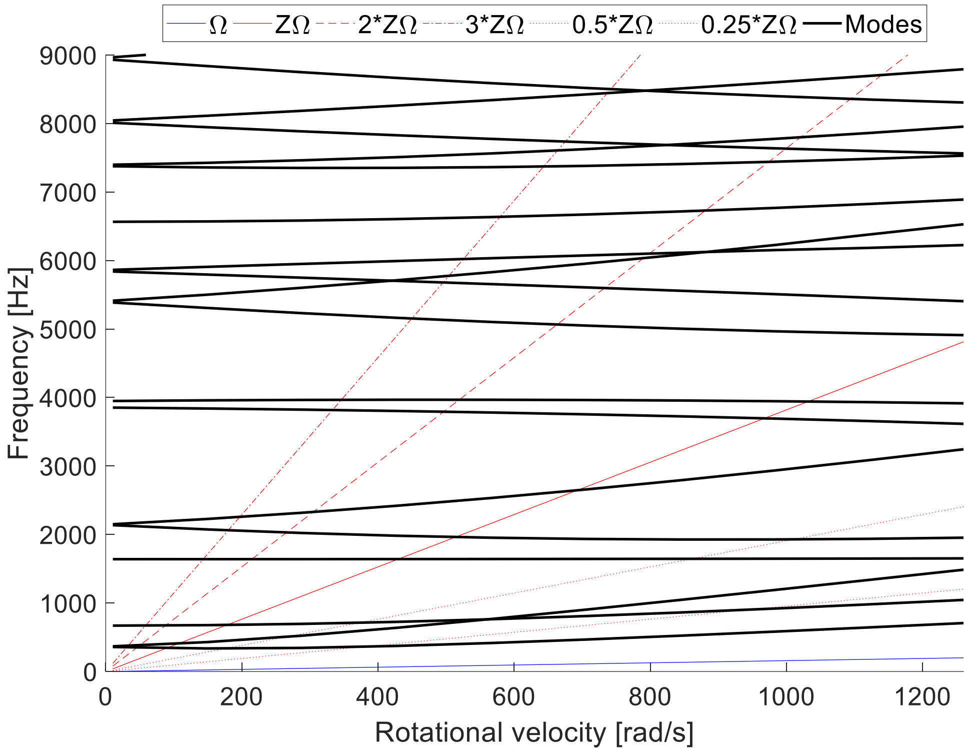

Figure 165: Campbell diagram with gyroscopic effect and stress stiffening

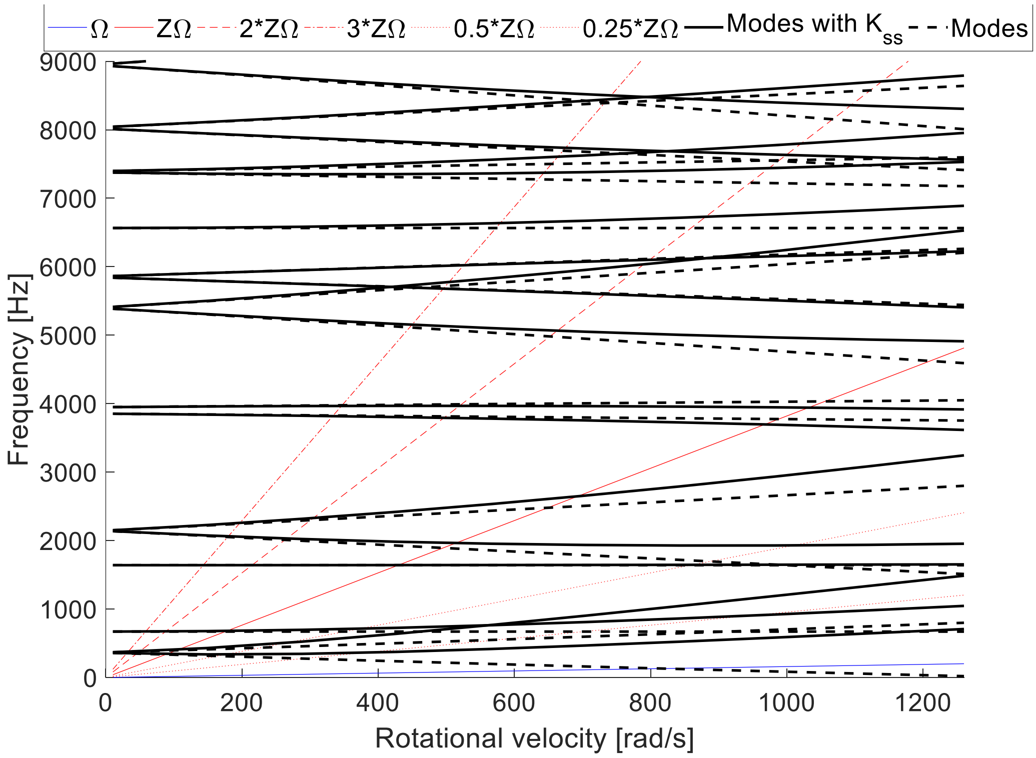

Figure 166: Comparison of the Campbell diagram with and without the stress stiffening effect

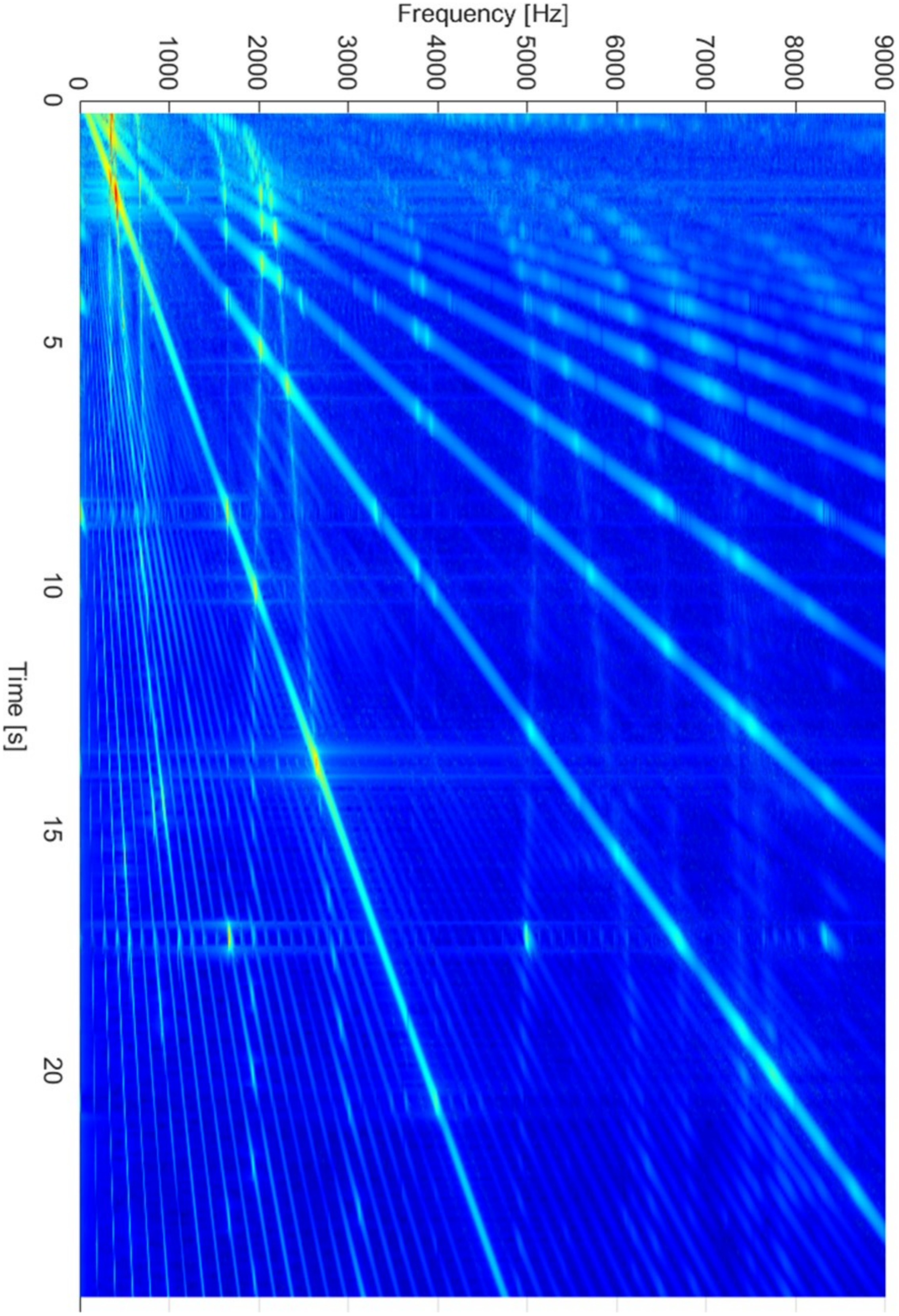

Figure 167: Spectrogram of the dynamic displacements in the axial direction

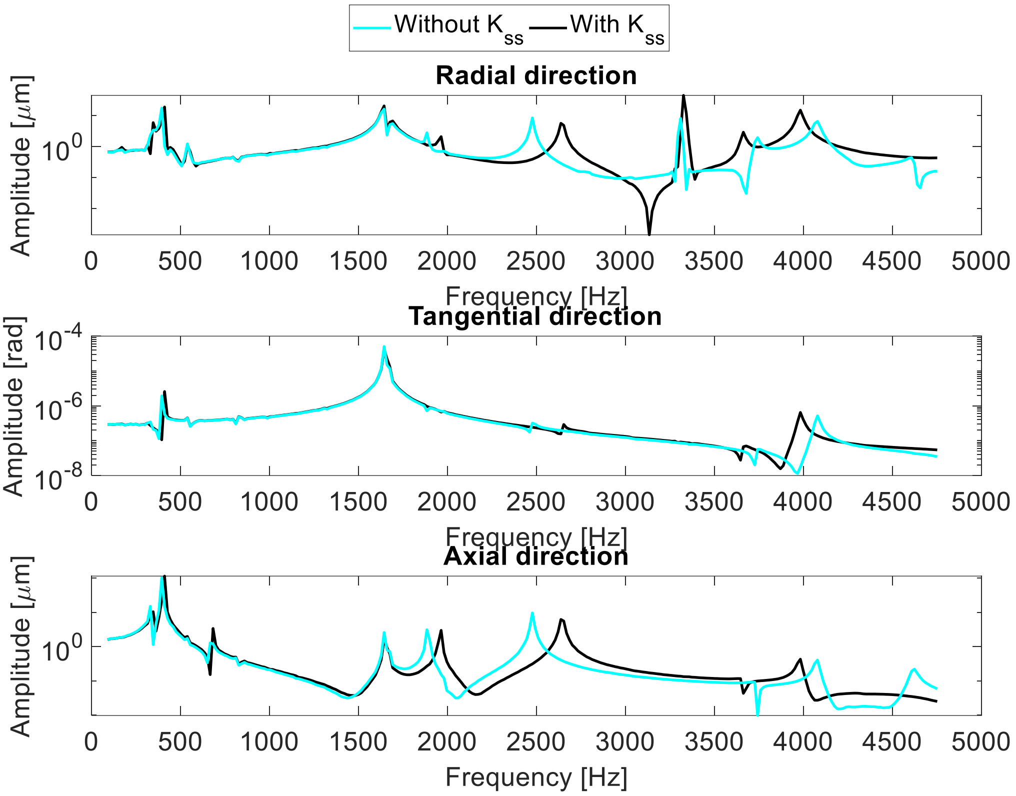

Figure 168: Comparison of the response on the order $Z\Omega$ with and without stress stiffening

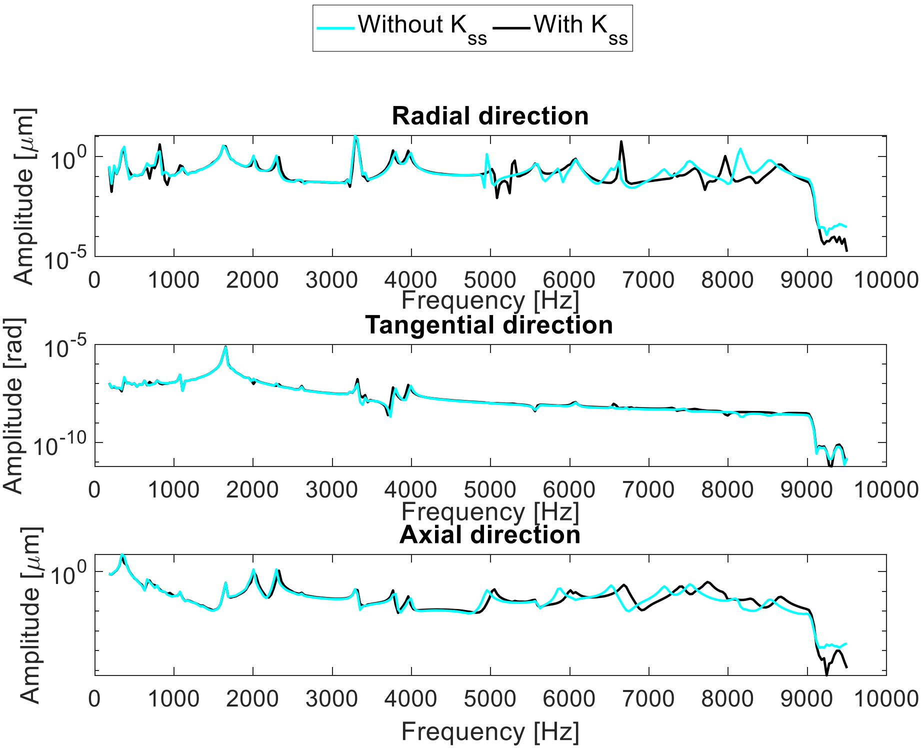

Figure 169: Comparison of the response on the order $2Z\Omega$ with and without stress stiffening

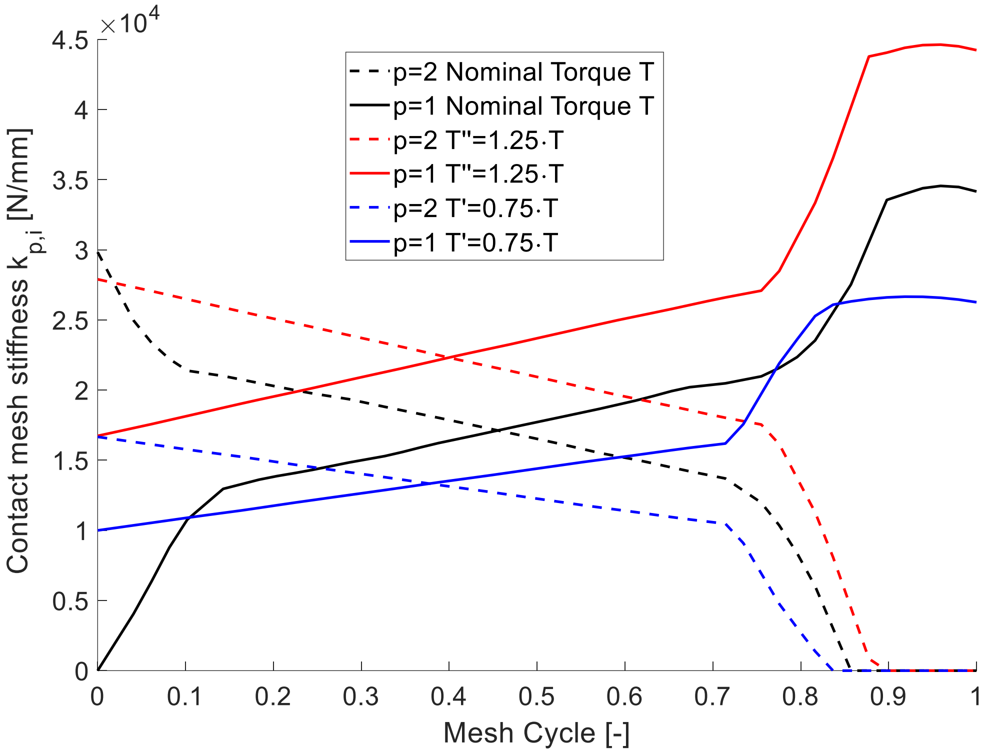

Figure 170: Contact mesh stiffness variation under different torques

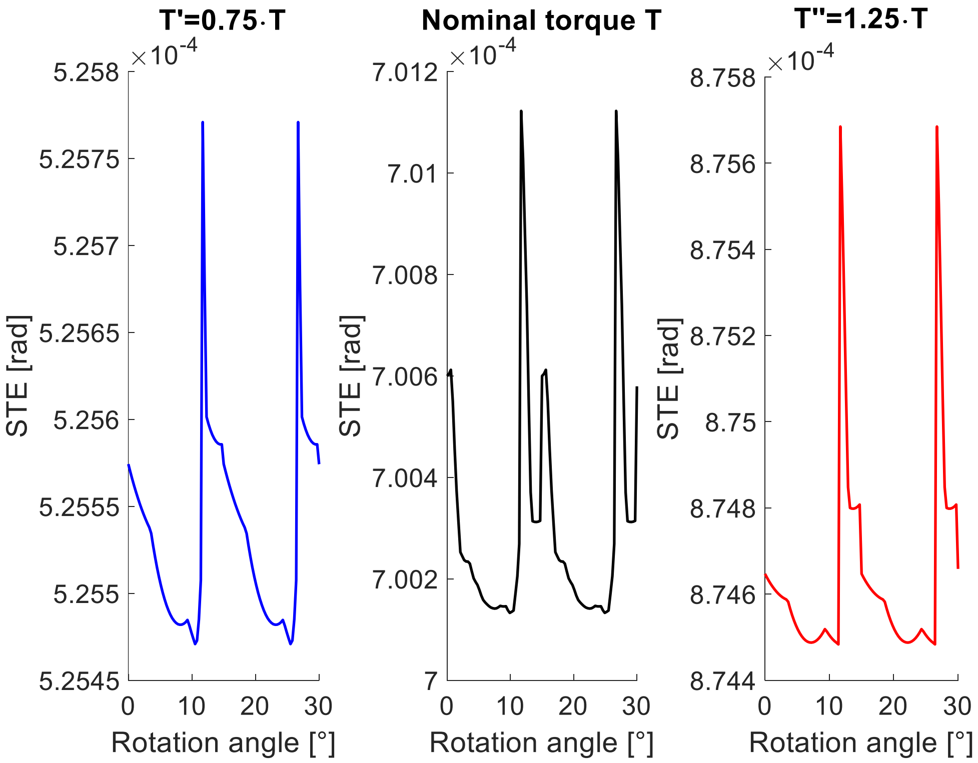

Figure 171: Variation of the STE under different torques

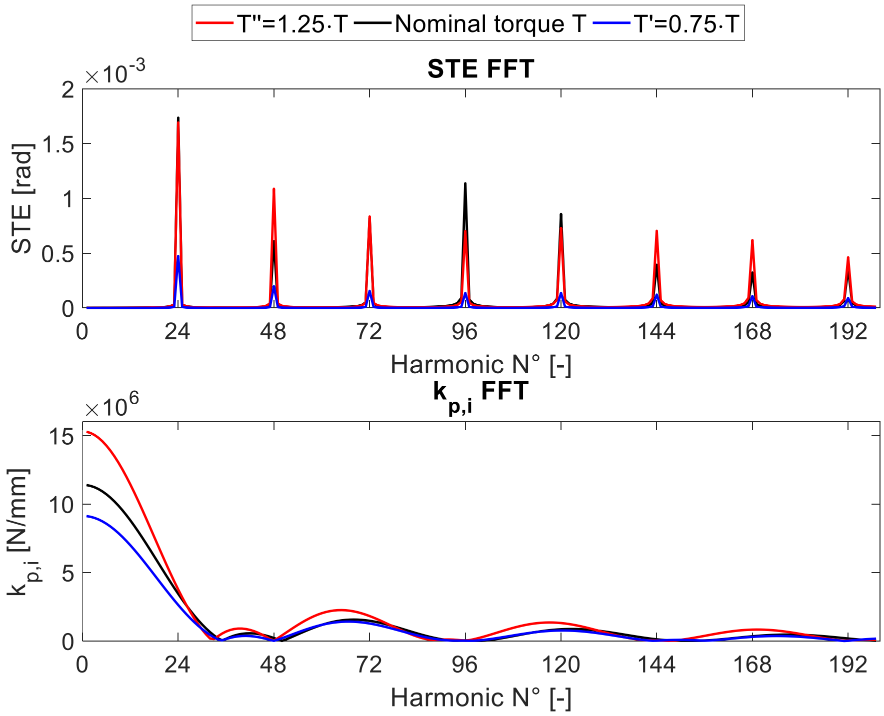

Figure 172: FFT of the excitation sources under different torques

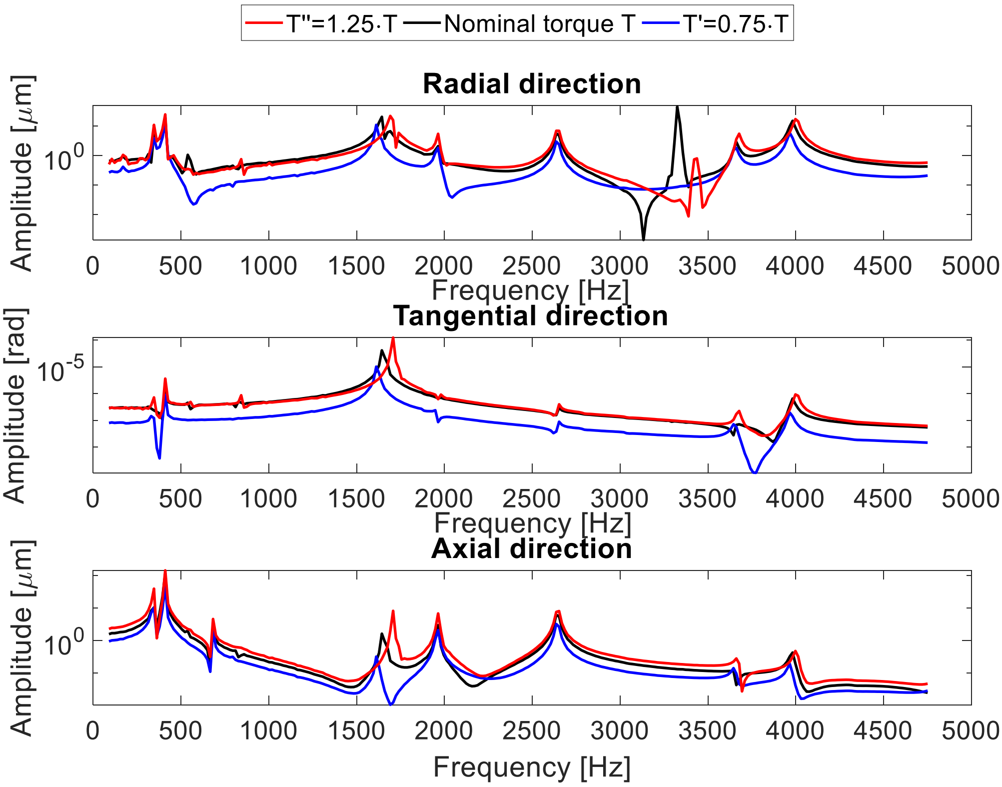

Figure 173: Comparison of the response on the order $Z\Omega$ under different torques

the distribution of the Fourier coefficients. After obtaining the dynamic displacements for the different cases the related spectrograms are computed and the order Z is extracted for thedifferent directions of displacement of the gear as experienced by the sensor nodes. This result is shown in Figure 173 and as expected the vibration levels are higher as the load and the excitation source increases although not in a uniform manner. The comparison of the response order $2Z$ is dropped since the higher and more meaningful levels of vibration are found in the order Z where the excitation is higher as highlighted by the comparison of the responses in Figure 168 and Figure 169 from the previous analysis. Next the effect of the introduction of TPM in the gear microgeometry is analyzed. Since the macroscopic quantities defining the gear and its FE discretization remain unchanged the same matrices defining the dynamic behavior will be used throughout this comparison, since recomputing the reduced matrices for each case would only bring insignificant changes in the dynamic response due to the small quantities of material removed when the microgeometry is changed. The type

Table 11: TPM cases

TPM 1 – Parabolic tip relief	
Δ_{p}	$0.0032\ mm$
l_p	$0.96\ mm$
TPM 2 – Linear tip relief	
Δ_t	$0.0040\ mm$
l_t	$1.92\ mm$

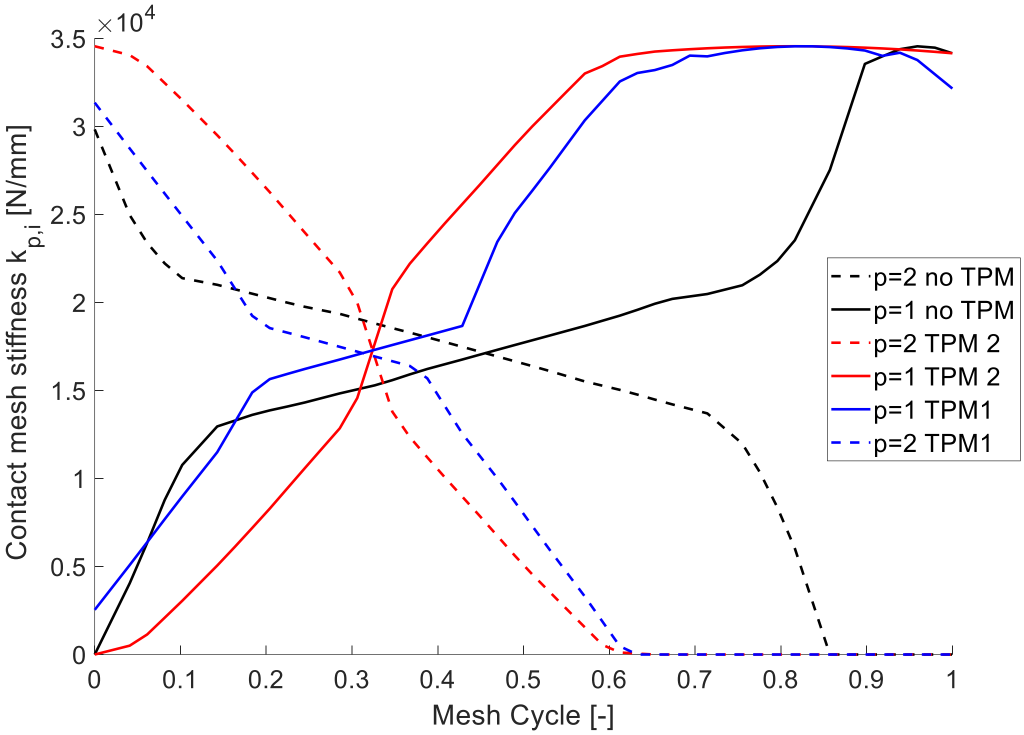

Figure 174: Variation of the contact mesh stiffness under different TPM

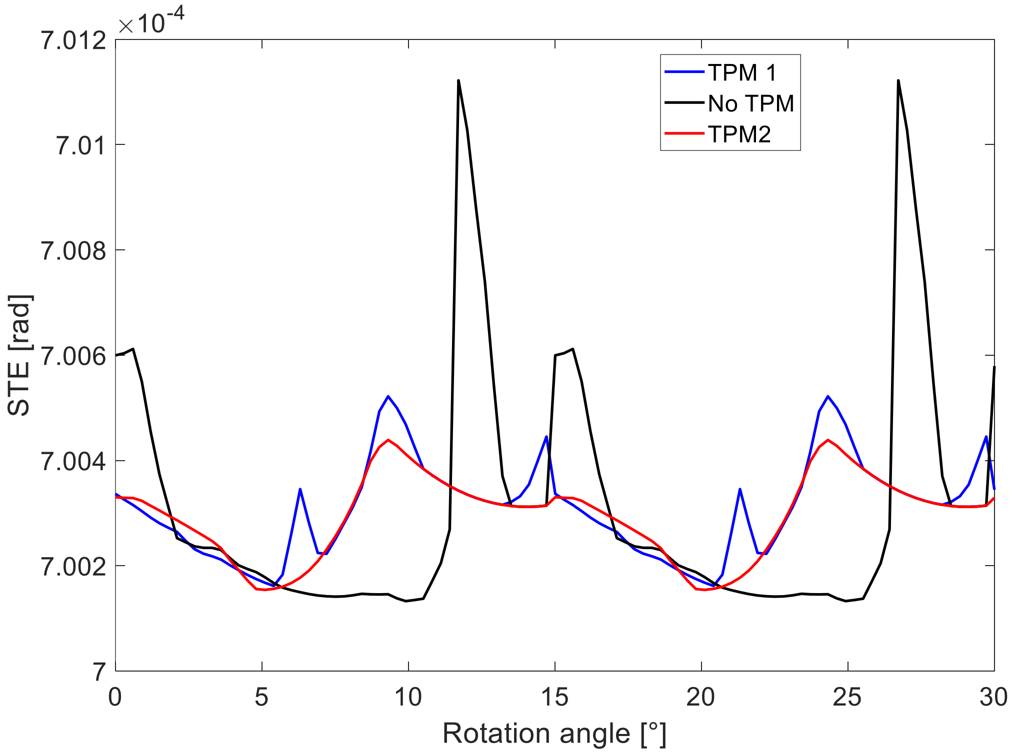

Figure 175: Variation of the STE under different TPM

and amount of modification applied are listed in Table 11. The resulting variation of the contact mesh stiffness exciting the system for the different TPM cases is visible in Figure 174 and their effect on the resulting STE is instead shown in Figure 175. The FFT of those excitation sources is visible in Figure 176. Due to the fact that the application of TPM to the gear smooths the STE and reduces its peak-to-peak value the FFT of the STE shows a great reduction when TPM are applied and moreover the second case considered, in which the amount of material removed is higher, shows also a higher reduction in the Fourier coefficients. However, the FFT of the contact mesh stiffness shows an opposite trend since increasing the amount of the modification increases the period of mesh cycle in which a single pair of teeth is in contact thus leading to an increase in the resulting Fourier coefficients. The comparison of the order Z extracted from the dynamic displacements for the different directions is shown in Figure 177 in which it can be seen that the vibration amplitudes are generally higher for the case where no TPM was applied, confirming the common knowledge that applying TPM to the flanks can smooth the operation of the transmission. However, although the FFT are quite different from each other, the response shows similar amplitudes, except for the results in

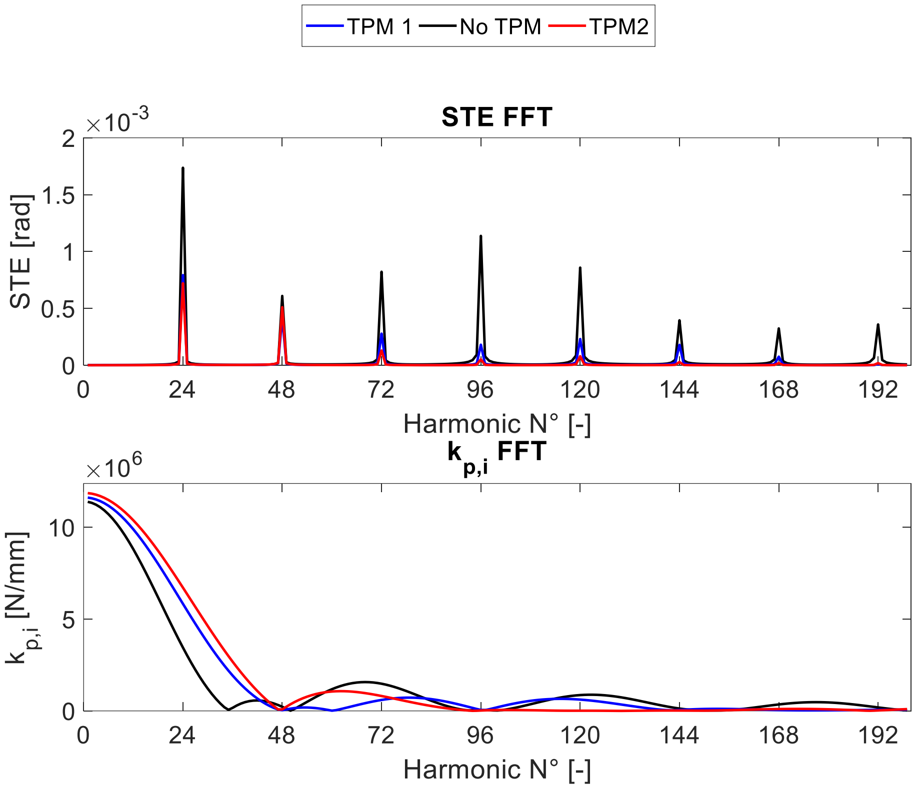

Figure 176: FFT of the excitation sources under different TPM

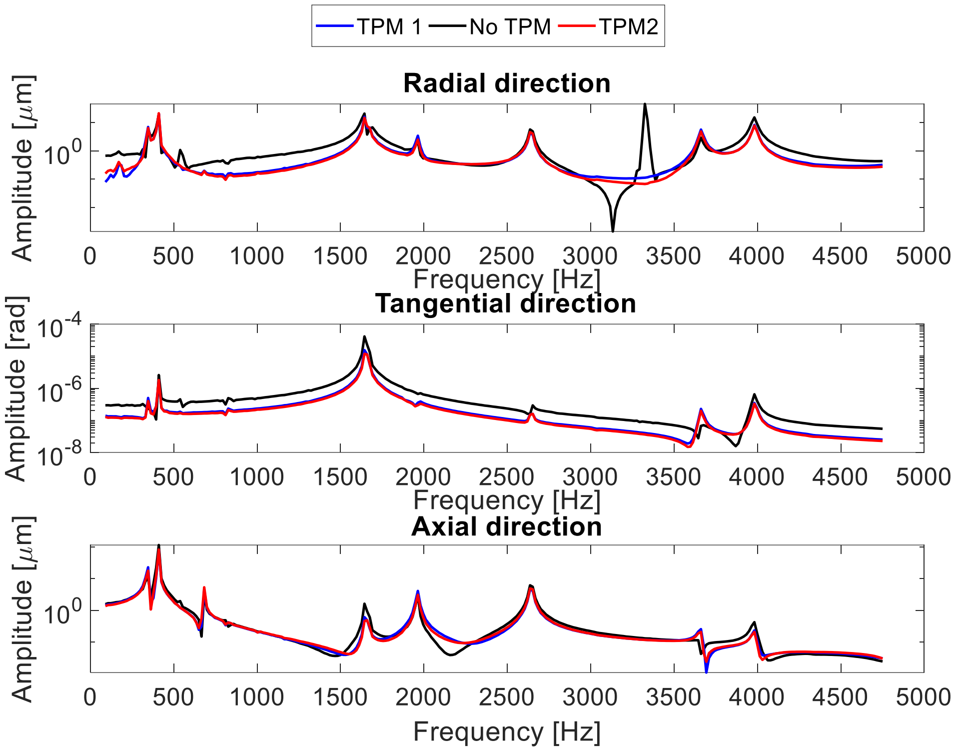

Figure 177: Comparison of the response on the order $Z\Omega$ under different TPM

the tangential direction which show an overall reduction of the vibration levels. The main difference between the various cases is the resonance in the radial direction in the $3 \div 3.5\ kHz$ range which is caused by the crossing of the torsional mode shape with the excitation order $\frac{1}{2}Z\Omega$ as visible from the spectrograms in Appendix B. This particular resonance is completely eliminated when TPM are applied.

VII. Conclusions and future work

In this work, after a brief history of the field, the literature and its state of the art have been analyzed starting from the studies that have been done to understand the sources of excitation up to the different dynamic models, from the simplest to the most advanced, that have been proposed have been discussed.

The first step of this work has been the definition of a 2D tool to study the engagement between gear pairs in quasi static conditions. After the definition of the most important parameters concerning the macro-geometry of the gears the operative deflections under load have been detailed. Those comprehend the deflections due to the flexibility of the tooth such as its bending and shear deflections, the deformation due to the fillet and an analytical model to consider the local deflection due to contact. Next the deflections of the gear body have been studied which include its torsional displacement and the effect of the application of the load to one tooth as it influences the others due to the compliance of the foundations which are now considered flexible instead of rigid. Those deflections are then included in an iterative nonlinear scheme which seeks the equilibrium position of the engaging teeth pairs as they deflect under the applied external load on the transmission. In order to fully take into consideration also the local contact conditions a non-Hertzian rough frictionless contact model is detailed and verified against Hertz solution for the cylinder-cylinder contact problem. This model is then extended to the contact between teeth and the notion of tooth profile modifications such as the linear or parabolic tip relief is then introduced. Several TPM are then analyzed to study their effect on the contact pressures when in tip corner contact conditions. Next this approach is applied to determine the STE and load sharing coefficients and the pressure distribution on the engaged flanks during the entire duty cycle of a tooth. The effect of the load and different parameters combinations of the amount of material removed and length of TPM is shown is investigated. This model is hence novel since usually in literature semi-analytical models are used only linearly, while in this case both the actual point of application of the load and the load applied to each tooth itself is found through a nonlinear iteration scheme, which is furthermore coupled to a contact model which is non-Hertzian in nature and that therefore can capture correctly edge contacts and pressure distributions where the curvature of the tooth profile is not an ideal involute. To achieve this level of detail a very refined FE model would be needed using the already available tools and also most commercial software employ Hertzian contact models which cannot capture at all the pressure peaks during tip-corner contact for example.

The proposed approach is however only applicable to spur gears and for TPM which are constant throughout the facewidth since the both the iterative contact detection and the contact model work in only in 2D. To surpass those limitations a modified approach is then introduced. The analytical displacements of the tooth are hence substituted with the results of a discretization considering it as a clamped-free of Timoshenko beam elements and the iterative contact detection is also upgraded with a mesh to mesh intersection algorithm capable of handling general 3D profiles. Also, the contact model is renewed with a 3D version with the same properties of the previous one, although the discretization changes from step-wise to piece-wise linear. This contact model is then compared against Hertz results on sphere-sphere and ellipsoid-ellipsoid contact as well as against literature results for a crowned roller with edge contact in which the non-Hertzian properties are highlighted. Results are then shown for different helix angles with different loads and profile modifications and the peak pressure maps of the flanks during contact are discussed also with crowning modifications along the facewidth.

The proposed approaches have advantages in terms of speed against commercial codes or general-purpose non-linear solvers since they're specialized for gears and do not rely on finite element discretizations to obtain the loaded deflections but use instead analytical formulas or simpler beam elements. Furthermore, they feature detailed contact models which do not use Hertzian hypotheses and are capable of accurately determining the actual contact conditions even in extreme situations without having to rely on extremely refined surface discretizations which make the solution process extremely slow.

In order to validate with experimental data the proposed approaches, a test bench has been designed capable to determine the STE under quasi static conditions. Its structural parts and the system to load the gears with a constant torque are described and further details are given on the measurement system which features a device to uncouple the shafts bending deflections under load from the torsional ones which are then read by a pair of high precision rotary encoders while the torque is recorded by a torque meter. After describing the necessary safety measures implemented results are shown for a pair of test gears. The obtained results are only preliminary due to the poor quality of the test gears and the highlighted flaws in the design of the bench and will be updated in the future when the new parts and better test gears will be available.

Finally, a scheme to study the dynamic response of compliant gears is detailed. As a first step the finite element model used to discretize the gear geometry with hexahedral elements is discussed which features a combination of selective reduced integration and an enhanced assumed strain field in order to remove shear and volumetric locking as well as removing spurious modes. This FE model is applied to a parametric discretization of the gear geometry and is then applied to a reduced order scheme which uses the Craig-Bampton reduced FE matrices, computed at several different rotation angles, in a model capable of quickly obtaining the dynamic displacements accounting for the complete flexibility and flexible mode shapes of the gear with the possibility of considering also eventual contact loss. This model is firstly applied to a gear with a rigid web and the gyroscopic effect is introduced. The importance of employing the correct contact mesh stiffness is the highlighted as well as the effect of damping. Then, a gear with a compliant thin web is analyzed and the effect of the stress stiffening phenomenon is described and introduced in the dynamic model. The effect of the load and of different tooth profile modifications applied to the flanks are finally studied.

The main drawbacks of the proposed scheme is that the pre-process phase is rather long and computationally intensive and that the time discretization is variable and can't be chosen directly but is the result of the combination of the rotational speed and the number of angular positions in which it's decided to split the mesh cycle. However, if the macro geometry of the gear doesn't change, the matrices can be reused for different load and micro geometry setups with minimal effort ensuring the possibility to study different parameters combinations with ease. Also, most dynamic phenomena don't happen at slow speeds and therefore a satisfying trade-off between the number of mesh cycle discretizations and the speed range can usually be found. In any case the advantages far outweigh the disadvantages since this scheme allows the computation of the dynamic behavior for the entire speed range with a single sweep in hours, which can take instead several months of calculations with the software that have this capability. Indeed, only some fixed rotational velocities, if any, are usually analyzed in the design phase for the extreme time-consuming nature of those analyses if a reduced scheme is not employed and the flexible behavior is important for the designer. Even at the lowest settings, commercial software capable of studying gear dynamics with compliant bodies take around $6-7\ s$ to solve each timestep, while the proposed model only takes in general less than $0.005\ s$ for a single timestep. All the simulations detailed in Chapter VI have around $3 \cdot 1e6$ timesteps resulting in a simulation time of around $4\ hours$ for each one, including the preprocessing work which consists of computing the actual mesh stiffness at a defined level of torque, meshing and computing the relevant FE matrices and performing the matrices reduction. For a commercial software, the same number of timesteps would be solved in $5000\ hours$, making it practically impossible to perform such simulation. This rough estimate doesn't even consider that those commercial tools employ a fixed timestep, making the number of required timesteps to fulfill the speed sweeps here presented even higher, increasing even more the required computational effort. Still there is room for improvement. In the future of this work the first step will be the inclusion of the driven gear in the system and eventually the extension to the entire drivetrain. Once that will be done more serious nonlinear analyses will be available by implementing an instantaneous load dependency of the mesh contact stiffness and it will then be possible to compare the obtained results with those available literature for the cases where contact loss happens in particular conditions. Another aspect to be considered is the nature of the damping, since without experimental data available beforehand a better approach would be to implement a frequency-independent damping to better understand the correlation between the variation of the applied contact mesh stiffness and the dynamic response. The proposed scheme will also then be applicable to helical and bevel gears by properly choosing the nodes where the contact mesh stiffness will be attached and its movement in time.

References

[1] M. Burrows and G. Sutton, "Interacting Gears Synchronize Propulsive Leg Movements in a Jumping Insect," *Science,* vol. 341, no. 6151, pp. 1254-1256, 2013.

[2] H. N. Ozguven and D. R. Houser, "Mathematical models used in gear dynamics - a review," *Journal of Sound and Vibration,* vol. 121, no. 3, pp. 383-411, 1988.

[3] B. Abersek, J. Flasker and S. Glodez, "Review of mathematical and experimental models for determination of service life of gears," *Engineering Fracture Mechanics,* vol. 71, pp. 439-453, 2004.

[4] L. Prasil and J. Mackerle, "Finite element analyses and simulations of gears and gear drives a bibliography 1997-2006," *International Journal for Computer-Aidea Engineering and Software,* vol. 25, no. 3, pp. 196-219, 2008.

[5] *Fundamental rating factors and calculation methods for involute spur and helical gear teeth,* ANSI/AGMA 2001-C95, 2001.

[6] *Calculation of load capacity of spur and helical gears,* ISO 6336, 2006.

[7] A. Fisher, "Factors in Calculating the Load Carrying Capacity of Helical," *Machinery,* vol. 98, pp. 545 - 552, 1961.

[8] A. A. Ross, *High speed gears. Technical report,* American Gear Manufacturers Association, 1927.

[9] W. A. Tuplin, "Gear tooth stresses at high speed," *Proceedings of the Institution of Mechanical Engineers,* vol. 163, no. 1, pp. 162-167, 1950.

[10] S. L. Harris, "Dynamic loads on teeth of spur gears," *Proceedings of the Institution of Mechanical Engineers,* vol. 172, no. 1, pp. 87-112, 1958.

[11] P. Velex and M. Ajmi, "On the modelling of excitations in geared systems by transmission errors," *Journal of Sound and Vibration,* vol. 290, pp. 882-909, 2006.

[12] P. Velex and M. Ajmi, "Dynamic tooth loads and quasi-static transmission errors in helical gears- Approximate dynamic factor formulae," *Mechanism and Machine Theory,* vol. 42, pp. 1512-1526, 2007.

[13] P. Velex, M. Chapron, H. Fakhfakh, J. Bruyère and S. Becquerelle, "On transmission errors and profile modifications minimising dynamic tooth load in multi-mesh gears," *Journal of Sound and Vibration,* vol. 379, pp. 28-52, 2016.

[14] C. Weber, "The deformation of load gears and the effect on their load-carrying capacity. Technical Report n.3," *British Department of Scientific and Industrial Research,* 1949.

[15] C. Weber and K. Banaschek, Formanderung und profilrucknahme bei gerad-und schragverzahnten antriebstechnik, Brunswick: F. Vieweg, 1953.

[16] H. R. Hertz, "On contact between elastic bodies," *Collected Works,* vol. 1, 1895.

[17] G. Lundberg, "Elastische Beruhrung zweier Halbraume," *Forschung auf dem Gebiete des Ingenieurwesens,* vol. 10, no. 5, pp. 201-211, 1939.

[18] J. Ishikawa, *Bull of T.I.T,* vol. 197, no. 3, 1957.

[19] J. Shi, X. Ma, C. Xu and S. Zang, "Meshing stiffness analysis of gear using the Ishikawa method," *Applied Mechanics and Materials,* Vols. 401-403, pp. 203-206, 2013.

[20] A. Y. Attia, "Deflection of spur gear teeth cut in thin rims," *ASME paper,* Vols. 63-WA-14, pp. 1-9, 1964.

[21] R. W. Cornell, "Compliance and stress sensitivity of spur gear teeth," *Journal of Mechanical Design,* vol. 103, no. 2, pp. 447-459, 1981.

[22] W. J. O'Donnel, "Stress and deflection of built-in beams," *ASME paper,* Vols. (62-WA-16), 1963.

[23] P. Sainsot, P. Velex and O. Duverger, "Contribution of gear body to tooth deflections - A new bidimensional analytical formula.," *Journal of Mechanical Design,* vol. 126, pp. 748-752, 2004.

[24] Y. Cai and T. Hayashi, "The linear approximated equation of vibration of a pair of spur gears," *Journal of Mechanical Design,* vol. 116, pp. 558-564, 1994.

[25] K. Umezawa, "The meshing test on helical gears under tooth load transmission (3rd report, the static behaviours of driven gear)," *Bulletin of JSME,* vol. 17, no. 112, pp. 1348-1355, 1974.

[26] K. Umezawa, T. Suzuki and T. Sato, "Vibration of power transmission helical gears: Approximate equation of tooth stiffness," *Bulletin of the JSME,* vol. 29, no. 251, pp. 1605-1611, 1986.

[27] Y. Cai, "Simulation on the rotational vibration of helical gears in consideration of the tooth separation phenomenon: A new stiffness function of helical involute tooth pair," *Journal of Mechanical Design,* vol. 117, pp. 460-469, 1995.

[28] K. L. Wang and H. S. Cheng, "A numerical solution to the dynamic load, film thickness and surface temperatures in spur gears, Part I: Analysis," *Journal of Mechanical Design,* vol. 103, pp. 177-187, 1981.

[29] J. H. Steward, "The compliance of solid, wide-faced spur gears," *Journal of Mechanical Design,* vol. 112, pp. 590-595, 1990.

[30] G. Deng, T. Nakanishi and K. Inoue, "Bending load capacity enhancement using an asymmetric tooth profile," *JSME International Journal Series C,* vol. 46, no. 3, pp. 1171-1177, 2003.

[31] T. Lin, H. Ou and R. Li, "A finite element method for 3D static and dynamic contact/impact analysis of gear drives," *Computer Methods in Applied Mechanics and Engineering,* vol. 196, pp. 1716-1728, 2007.

[32] N. L. Pedersen and M. F. Jorgenses, "On gear tooth stiffness evaluation," *Computers and Structures,* vol. 135, pp. 109-117, 2014.

[33] M. H. Arafa and M. M. Megahed, "Evaluation of spur gear mesh compliance usign the finite element method," *Proceedings of the Institution of Mechanical Engineers, Part C: Journal of Mechanical Engineering Science,* vol. 213, pp. 569-579, 1999.

[34] W. Hu and Z. Chen, "A multi-mesh mpm for simulating the meshing process of spur gears," *Computers and Structures,* vol. 81, pp. 1991-2002, 2003.

[35] J. D. Wang and I. M. Howard, "Error analysis of finite element modeling of involute spur gears," *Journal of Mechanical Design,* vol. 128, pp. 90-97, 2006.

[36] S. He, R. Gunda and R. Singh, "Effect of sliding friction on the dynamics of spur gear pair with realistic time-varying stiffness," *Journal fo Sound and Vibration,* vol. 301, pp. 927-949, 2007.

[37] S. Li, "Finite element anayses for contact strenght and bending strenght of a pair of spur gears with machining errors, assembly errors and tooth modifications," *Mechanism and Machine Theory,* vol. 42, pp. 88-114, 2007.

[38] A. Y. Tesfahuneng, F. Rosa and C. Gorca, "The effects of the shape of tooth profile modifications on the transmission error, bending and contact stress of spur gears," *Proceedings of the Institution of Mechanical Engineering Part C: Journal of Mechanical Engineering Science,* vol. 224, pp. 1749-1758, 2010.

[39] V. Nikolic, C. Dolicanin and D. Dimitrijevic, "Dynamic model for the stress and strain state analysis of a spur gear transmission," *Journal of Mechanical Engineering,* vol. 58, no. 1, pp. 56-67, 2012.

[40] L. Prasil and J. Mackerle, "Finite element analyses and simulations of gears and gear drives a bibliography 1997-2006," *International Journal for Computer-Aided Engineering and Software,* vol. 25, no. 3, pp. 196-219, 2008.

[41] R. G. Parker, S. M. Vijayakar and T. Imajo, "Non-linear dynamic response of a spur gear pair: Modelling and experimental comparisons," *Journal of Sound and Vibration,* vol. 237, no. 3, pp. 435-455, 2000.

[42] M. Ajmi and P. Velex, "A model for simulating the quasi-static and dynamic behaviour of solid wide-faced spur and helical gears," *Mechanism and Machine Theory,* vol. 40, pp. 173-190, 2005.

[43] R. Guilbault, C. Gosseling and L. Cloutier, "Helical gears, effect of tooth deviations and tooth modifications on load sharing and fillet stresses," *Journal of Mechanical Design,* vol. 128, no. 2, pp. 444-456, 2005.

[44] J. Wei, W. Sun and L. Wang, "Effect of flank deviation on load distributions for helical gear," *Journal of Mechanical Science and Technology,* vol. 25, no. 7, pp. 1781-1789, 2011.

[45] D. R. Houser, F. Oswald and M. Valco, "Comparison of transmission error predictions with noise measurements for several spur and helical gears," *AIAA/ASME/SAE/ASEE 30th Joint Propulsion conference,* 1994.

[46] R. G. Munro, L. Morrish and D. Palmer, "Gear transmission error outside the normal path of contact due to corner and top contact," *Proceedings of the Institution of Mechanical Engineers,* vol. 213, pp. 389-400, 1999.

[47] G. Bonori, M. Barbieri and F. Pellicano, "Optimum profile modifications of spur gears by means of genetic algorithms," *Journal of Sound and Vibration,* vol. 313, pp. 603-616, 2008.

[48] T. F. Conry and A. Seireg, "A mathematical programming method for design of elastic bodies in contact," *Journal of Applied Mechanics,* vol. 38, no. 2, pp. 387-392, 1971.

[49] T. F. Conry and A. Seireg, "A mathematical programming technique for the evaluation of load distribution and optimal modifications of gear systems," *Journal of Engineering and Industry,* vol. 95, no. 4, pp. 1115-1122, 1973.

[50] M. Maatar and P. Velex, "Quasi-static and dynamic analysis of narrow-faced helical gears with profile and lead modifications," *Journal of Mechanical Design,* vol. 119, pp. 474-480, 1997.

[51] J. Bruyere and P. Velex, "Derivation of optimum profile modifications in narrow-faced spur and helical gears using a perturbation method," *Journal of Mechanical Design,* vol. 135, no. 7, pp. 071009-1-8, 2013.

[52] J. Bruyere and P. Velex, "A simplified multi-objective analysis of optimum profil modification in spur and helical gears," *Mechanism and Machine Theory,* vol. 80, pp. 70-83, 2014.

[53] J. Bruyere, X. Gu and P. Velex, "On the analytical definition of profile modifications minimising transmission error variation in narrow-faced spur helical gears," *Mechanism and Machine Theory,* vol. 92, pp. 257-272, 2015.

[54] C. C. Wang, "Rotational vibration with backlash: Part 1," *Journal of Mechanical Design,* vol. 100, pp. 363-373, 1978.

[55] C. C. Wang, "Rotational vibration with backlash: Part 2," *Journal of Mechanical Design,* vol. 103, pp. 387-397, 1981.

[56] B. M. Bahgat, M. O. M. Osman and T. S. Sankar, "On the spur-gear dynamic tooth-load under consideration of system elasticity and tooth involute profile," *Journal of Mechanisms, Transmissions and Automation in Design,* vol. 105, pp. 302-309, 1983.

[57] H. N. Ozguven and H. D. R, "Dynamic analysis of high speed gears by using the loaded static transmission error," *Journal of Sound and Vibration,* vol. 125, no. 1, pp. 71-83, 1988.

[58] A. Kubo, K. Yamada, T. Aida and S. Sato, "Research on ultra high speed gear devices," *Bulletin of the JSME,* vol. 38, pp. 2692-2715, 1972.

[59] A. Kahraman and R. Singh, "Non-linear dynamics of a spur gear pair," *Journal of Sound and Vibration,* vol. 142, no. 1, pp. 45-79, 1990.

[60] A. Kahraman and R. Singh, "Interactions between time-varying mesh stiffness and clearance non-linearities in a geared system," *Journal of Sound and Vibration,* vol. 146, no. 1, pp. 135-156, 1991.

[61] G. W. Blankenship and A. Kahraman, "Steady state forced response of a mechanical oscillator with combined parametric excitation and clearance type non-linearity," *Journal of Sound and Vibration,* vol. 185, no. 2, pp. 743-765, 1995.

[62] P. Velex and M. Maatar, "A mathematical model for analyzing the influence of shape deviations and mounting errors on gear dynamic behaviour," *Journal of Sound and Vibration,* vol. 191, no. 5, pp. 629-660, 1994.

[63] R. G. Munro, "The D.C. component of gear transmission error," *Proceedings of the 1989 International Power Transmission and gearing conference,* pp. 467-470, 1989.

[64] S. Theodossiades and S. Natsiavas, "Non-linear dynamics of gear-pair systems with periodic stiffness and backlash," *Journal of Sound and Vibration,* vol. 229, no. 2, pp. 287-310, 2000.

[65] S. Theodossiades and S. Natsiavas, "On geared rotordynamic systems with oil journal bearings," *Journal of Sound and Vibration,* vol. 243, no. 4, pp. 721-745, 2001.

[66] S. Theodossiades and S. Natsiavas, "Periodic and chaotic dynamics of motor-driven gear-pair systems with backlash," *Chaos, Solitons and Fractals,* vol. 12, no. 13, pp. 2427 - 2440, 2001.

[67] V. Elisaus, M. Mohammadpour, S. Theodossiades and H. Rahnejat, "Effect of teeth micro-geometrical form modification on contact kinematics and efficiency of high performance transmissions," *Proceedings of the Institution of Mechanical Engineers, Part K: Journal of Multy-body Dynamics,* vol. 231, no. 3, pp. 538-555, 2017.

[68] M. Amabili and A. Rivola, "Dynamic analysis of spur gear pairs: Steady-state response and stability of the sdof model with time-varying meshing damping," *Mechanical Systems and Signal Processing,* vol. 11, no. 3, pp. 375-390, 1997.

[69] H. H. Lin and C. H. Liou, "A parametric study of gear dynamics. Techincal Report NASA/CR-1998-206598," *NASA,* 1998.

[70] A. Kahraman and G. W. Blankenship, "Effect of involute tip relief on dynamic reponse of spur gear pairs," *Journal of Mechanical Design, Transactions of the ASME,* vol. 121, no. 2, pp. 313-315, 1999.

[71] A. Kahraman and G. W. Blankenship, "Effect of involute contact ratio on spur gear dynamics," *Journal of Mechanical Design, Transactions of the ASME,* vol. 121, no. 1, pp. 112-118, 1999.

[72] L. Vedmar and B. Henriksson, "A general approach for determining dynamic forces in spur gears," *Journal of Mechanical Design,* vol. 120, pp. 593-598, 1998.

[73] M. Vaishya and R. Singh, "Sliding friction-induced non-linearity and parametric effects in gears," *Journal of Sound and Vibration,* vol. 248, no. 4, pp. 671-694, 2001.

[74] M. Vaishya and R. Singh, "Strategies for modeling friction in gear dynamics," *Journal of Mechanical Design,* vol. 125, pp. 383-393, 2003.

[75] R. Maliha, C. U. Dogruer and N. H. Ozguven, "Nonlinear dynamic modeling of gear-shaft-disk-bearing systems using finite elements and describing functions," *Journal of Mechanical Design,* vol. 126, pp. 534-541, 2004.

[76] X. Dai, C. G. Cooley and R. G. Parker, "Dynamic tooth root strains and experimental correlations in spur gear pairs," *Mechanism and Machine Theory,* vol. 101, pp. 60-74, 2016.

[77] C. G. Cooley, R. G. Parker and S. M. Vijayakar, "A frequency domain finite element approach for three-dimensional gear dynamics," *Proceedings of the ASME 2009 IDETC/CIE,* pp. DETC2009-87525(1-11), 2009.

[78] R. G. Parker, V. Agashe and S. M. Vijayakar, "Dynamic response of a planetary gear system using a finite element/contact mechanics model," *Journal of Mechanical Design,* vol. 122, pp. 304-310, 2000.

[79] T. M. Ericson and R. G. Parker, "Planetary gear modal vibration experiments and correlation against lumped-parameter and finite element models," *Journal of Sound and Vibration,* vol. 332, pp. 2350-2375, 2013.

[80] A. Kahraman and S. M. Vijayakar, "Effect of internal gear flexibility on the quasi-static behavior of a planetary gear set," *Journal of Mechanical Design,* vol. 123, pp. 408-415, 2001.

[81] A. Singh, A. Kahraman and H. Ligata, "Internal gear strains and load sharing in planetary transmissions," *Journal of Mechanical Design,* vol. 130, pp. 1-10, 2008.

[82] A. Kahraman, H. Ligata and A. Singh, "Influence of ring gear rim thickness on planetary gear set behaviour," *Journal of Mechanical Design,* vol. 132, pp. 1-8, 2010.

[83] G. Liu, J. Hong and R. G. Parker, "Influence of simultaneous time-varying bearing and tooth mesh stiffness fluctuations on spur gear pair vibration," *Nonlinear Dynamics,* pp. 1-22, 2019.

[84] T. Eritnel and R. G. Parker, "An investigation of tooth mesh nonlinearity and partial contact loss in gear pairs using a lumped-parameter model," *Mechanism and Machine Theory,* vol. 56, pp. 28-51, 2012.

[85] T. Eritnel and R. G. Parker, "Three-dimensional nonlinear vibration of gear pairs," *Journal of Sound and Vibration,* vol. 331, no. 15, pp. 3628-3648, 2012.

[86] T. Eritnel and R. G. Parker, "Nonlinear vibration of gears with tooth surface modifications," *Journal of Vibration and Acoustics,* vol. 135, no. 5, pp. (051005)1-11, 2013.

[87] X. Dai, C. G. Cooley and R. G. Parker, "An efficient hybrid analytical-computational method for nonlinear vibration of spur gear pairs," *Journal of Vibration and Acoustics,* vol. 141, no. 1, pp. (011006)1-13, 2018.

[88] C. G. Cooley and R. G. Parker, "Vibration of high-speed rotating rings coupled to spatial space-fixed stiffness," *Journal of Sound and Vibration,* vol. 333, pp. 2631-2648, 2014.

[89] C. G. Cooley and R. G. Parker, "Limitations of an inexstensible model for the vibration of high-speed rotating elastic rings with attached space-fixed discrete stiffness," *European Journal of Mechanics A/Solids,* vol. 54, pp. 187-197, 2015.

[90] C. Liu, C. G. Cooley and R. G. Parker, "Parametric instability of spinning elastic rings excited by fluctuating space-fixed stiffnesses," *Journal of Sound and Vibration,* vol. 400, pp. 533-549, 2017.

[91] C. G. Cooley, C. Liu, X. Dai and R. G. Parker, "Techniques for the calculation of gear pair mesh stiffness," *Power Transmissions,* pp. 161-166, 2017.

[92] M. A. Hotait and A. Kahraman, "Experiments on the relationship between the dynamic transmission error and the dynamic stress factor of spur gear pairs," *Mechanism and Machine Theory,* vol. 70, pp. 116-128, 2013.

[93] A. Palermo, D. Mundo, R. Hadjit and W. Desmet, "Multibody element for spur and helical transmission error and the dynamic stress factor of spur gear pairs.," *Mechanism and Machine Theory,* vol. 62, pp. 13-30, 2013.

[94] T. Lim and R. SIngh, "A review of gear housing dynamics and acoustics literature," *NASA Technical Report CR-185148,* 1989.

[95] T. Lim and R. Singh, "Vibration transmission through rolling element bearings, part II: System studies," *Journal of Sound and Vibration,* vol. 139, no. 2, pp. 201-225, 1990.

[96] T. Lim and R. Singh, "Vibration transmission through rolling element bearings, part III: Geared rotor system studies," *Journal of Sound and Vibration,* vol. 151, no. 1, pp. 31-54, 1991.

[97] E. Rigaud and J. Sabot, "Effect of elasticity of shafts, bearings, casing and couplings on the critical rotational speeds of a gearbox," *VDI Berichte,* pp. 833-845, 1996.

[98] J. Zhou, W. Sun and Q. Tao, "Gearbox low-noise design method based on panel acoustic contribution," *Mathematical Problems in Engineering,* vol. 2014, pp. (850549)1-10, 2014.

[99] Y. Guo, T. Eritnel, T. M. Ericson and R. G. Parker, "Vibro-acoustic propagation of gear dynamics in a gear-bearing-housing system," *Journal of Sound and Vibration,* vol. 333, no. 22, pp. 5762-5785, 2014.

[100] G. Niemann and H. Winter, Machine Elements, Berlin - New York: Springer, 1983.

[101] C. Fetvaci, "Computer simulation of involute tooth generation," *Mechanical Engineering,* pp. 503-526, 2012.

[102] C. S. Yang, "Mathematical model of a helical gear with asymmetric involute teeth and its analysis," *International Journal of Advanced Manufacturing Technology,* vol. 62, no. 5-6, pp. 448-456, 2005.

[103] F. L. Litvin, A. Fuentes, I. Gozalez-Perez, A. Piscopo and P. Ruzziconi, "Face gear drive with helical involute pinion: Geometry, generation by shaper and work, avoidance of singularities and stress analysis," *NASA Technical Report,* Vols. NASA-CR-2005-213443, pp. 1 - 55, 2005.

[104] D. Schwarz, "Fast and robust curve intersections," *Mathworks FileExchange,* 2017.

[105] Z. Chen and Y. Shao, "Mesh stiffness calculation of a spur gear pair with tooth profile modification," *Mechanism and Machine Theory,* vol. 62, pp. 63-74, 2013.

[106] K. L. Jhonson, Contact Mechanics, Cambridge: Cambridge University Press, 1985.

[107] J. J. Kalker, Three-Dimensional Elastic Bodies in Rolling Contact, Springer Netherlands, 1990.

[108] P. Wriggers, Computational contact mechanics, Berlin: Springer, 2002.

[109] R. S. Sayles, "Basic principles of rough surface rough contact analysis using numerical methods," *Tribology International,* vol. 29, no. 8, pp. 639 - 650, 1996.

[110] C. H. Venner, "Multilevel solution of the EHL line and point contact problems," *Ph.D Thesis, University of Twente,* 1963.

[111] F. B. Oswald, H. H. Lin and D. I. R, "Dynamic Analysis of Spur Gear Transmissions (DANST). PC Version 3.00 User Manual," *NASA Technical Report 107291,* pp. 1 - 26, 1996.

[112] Y. M. Mohan and T. Seshaiah, "Spur gear optimization by using genetic algorithm," *International Journal of Engineering Research and Applications ,* vol. 2, no. 1, pp. 331 - 318, 2012.

[113] A. L. Kapelevich and Y. V. Shekhtman, "Direct gear design: Bending stress minimization," *Gear Technology,* vol. 20, no. 5, pp. 44 - 47, 2003.

[114] N. Amini, B. G. Rosen and H. Westberg, "Optimization of gear tooth surfaces," *International Journal of Machine Tools and Manufacture,* vol. 38, no. 5-6, pp. 425 - 435, 1998.

[115] O. C. Ziekiewicz and R. L. Taylor, The finite element method for solid and structural mechanics, Oxford: Elsevier, Butterwhort-Heinemann, 2005.

[116] G. Genta, Vibration dynamics and control, New York: Springer, 2009.

[117] A. Carpinteri, Scienza delle costruzioni, Bologna: Pitagora Editrice, 1992.

[118] G. R. Cowper, "The shear coefficient in Timoshenko's beam theory," *Transactions of ASME, Journal of Applied Mechanics,* vol. 33, no. 2, pp. 335 - 340, 1966.

[119] R. H. MacNeal, Finite Elements: Their Design and Performance, New York: Marcel Dekker, 1993.

[120] T. Möller and B. Trumbore, "Fast. minimum storage ray-triangle intersection," *Journal of Graphics Tools,* vol. 2, no. 1, pp. 21 - 28, 1997.

[121] D. Meagher, "Octree Encoding: A new technique for the representation, manipulation and display of arbitrary 3-D objects by computer," *Rensselaer Polytechnic Institute,* Vols. Technical Report IPL-TR-80-111, 1980.

[122] Thomas, "Fast mesh-mesh intersection using ray-tri intersection with octree spatial partitioning," *Mathworks FileExchange,* 2015.

[123] F. Marmo and R. L, "A general approach to the solution of Boussinesq's problem for polynomial pressures acting over polygonal domains," *Journal of Elasticity,* vol. 122, pp. 75 - 112, 2016.

[124] F. Marmo, S. S and L. Rosati, "Analytical solution of the Cerruti problem under linearly distributed horizontal pressures over polygonal domains," *Journal of Elasticity,* vol. 124, pp. 27 - 56, 2016.

[125] F. Marmo, F. Toraldo, A. Rosati and L. Rosati, "Numerical solution of smooth and rough contact problems," *Meccanica,* vol. 53, pp. 1415 - 1440, 2018.

[126] J. J. Kalker and Y. Van Randen, "A minimum principle for frictionless elastic contact with application to non-Hertzian half-space contact problems," *Journal of Engineering Mathematics,* vol. 6, pp. 193 - 206, 1972.

[127] S. Boedo, "A corrected displacement solution to linearly varying surface pressure over a triangular region on the elastic hafl-space," *Tribology International,* vol. 60, pp. 116 - 118, 2013.

[128] J. M. de Mul, J. J. Kalker and B. Fredriksson, "The contact between arbitrarily curved bodies of finite dimensions," *Journal of Tribology,* vol. 108, no. 1, pp. 140 - 148, 1986.

[129] S. Baud and P. Velex, "Static and dynamic tooth loading in spur and helical geared systems - Experiments and model validation," *Journal of Mechanical Design,* vol. 124, no. 2, pp. 334 - 346, 2002.

[130] M. Benatar, M. Handschuh, A. Kahraman and D. Talbot, "Static and dynamic transmission error measurements of helical gear pairs with various tooth modifications," *Journal of Mechanical Design,* vol. 141, no. 10, p. 103301, 2019.

[131] A. Palermo, J. Anthonis, D. Mundo and W. Desmet, "A novel test rig with adjustable shaft compliance and misalignments," *International Conference on Condition Monitoring of Machinery in Non-Stationary Operations (CMMNO),* vol. 5, pp. 497 - 506, 2013.

[132] A. Gugliotta, Elementi finiti, Torino: Otto Editore, 2002.

[133] R. D. Cook, Concepts and applications of Finite Element Analysis, New York: Jhon Wiley & Sons, 2001.

[134] A. R. de Sousa, J. R. Natal, V. R. Fontes and C. J. de Sà, "A new volumetric and shear locking-free 3D enhanced strain element," *Engineering Computations,* vol. 20, no. 7, pp. 896 - 925, 2003.

[135] O. P. Jacquotte and J. Oden, "Analysis of hourglass instabilities and control in underintegrated finite element methods," *Computer Methods in Applied Mechanics and Engineering,* vol. 44, pp. 339 - 363, 1984.

[136] O. P. Jacquotte and J. Oden, "An accurate and efficient a posteriori control of hourglass instabilities in underintegrated linear and nonlinear elasticity," *Computer Methods in Applied Mechanics and Engineering,* vol. 55, pp. 105 - 128, 1986.

[137] D. P. Flanagan and T. Belytschko, "A uniform strain hexahedron and quadrilateral with orthogonal hourglass control," *International Journal for Numerical Methods in Engineering,* vol. 17, pp. 679 - 706, 1981.

[138] E. L. Wilson and A. Ibrahimbegovic, "Use of incompatible displacement modes for the calculation of element stiffnesses or stresses," *Finite Elements in Analysis and Design,* vol. 7, no. 3, pp. 229 - 241, 1990.

[139] R. L. Taylor, P. J. Beresford and E. L. Wilson, "A non-conforming element for stress analysis," *International Journal for Numerical Methods in Engineering,* vol. 10, no. 6, pp. 1211 - 1219, 1976.

[140] R. J. Guyan, "Reduction of stiffness and mass matrices," *AIAA Journal,* vol. 3, no. 2, pp. 380 - 380, 1965.

[141] F. L. Litvin, Gear geometry and applied theory, Englewood Cliffs: P. T. R. Prentice Hall, 1994.

[142] M. Barbieri, A. Zippo and F. Pellicano, "Adaptive grid-size finite element modeling of helical gear pairs," *Mechanism and Machine Theory,* vol. 82, pp. 17 - 32, 2014.

[143] R. L. Huston, Multibody dynamics, Stoneham: Butterworth, 1990.

[144] E. Bonisoli, C. Delprete and C. Rosso, "Proposal of a modal-geometrical-based master nodes selection criterion in modal analysis," *Mechanical Systems and Signal Processing,* vol. 23, no. 3, pp. 606 - 620, 2009.

[145] R. R. Craig and M. C. C. Bampton, "Coupling of substructures for dynamic analyses," *AIAA Journal,* vol. 6, no. 7, pp. 1313 - 1319, 1968.

[146] N. M. Newmark, "A Method of Computation for Structural Dynamics," *Journal of the Engineering Mechanics Division,* vol. 85, no. 3, pp. 67 - 94, 1959.

[147] M. Geradin and N. Kill, "A new approach to finite element modelling of flexible rotors," *Engineering Computations,* vol. 1, no. 1, pp. 52 - 64, 1984.

[148] R. H. MacNeal, The Nastran Theoretical Manual, Washington D.C.: NASA, 1976.

Appendix A

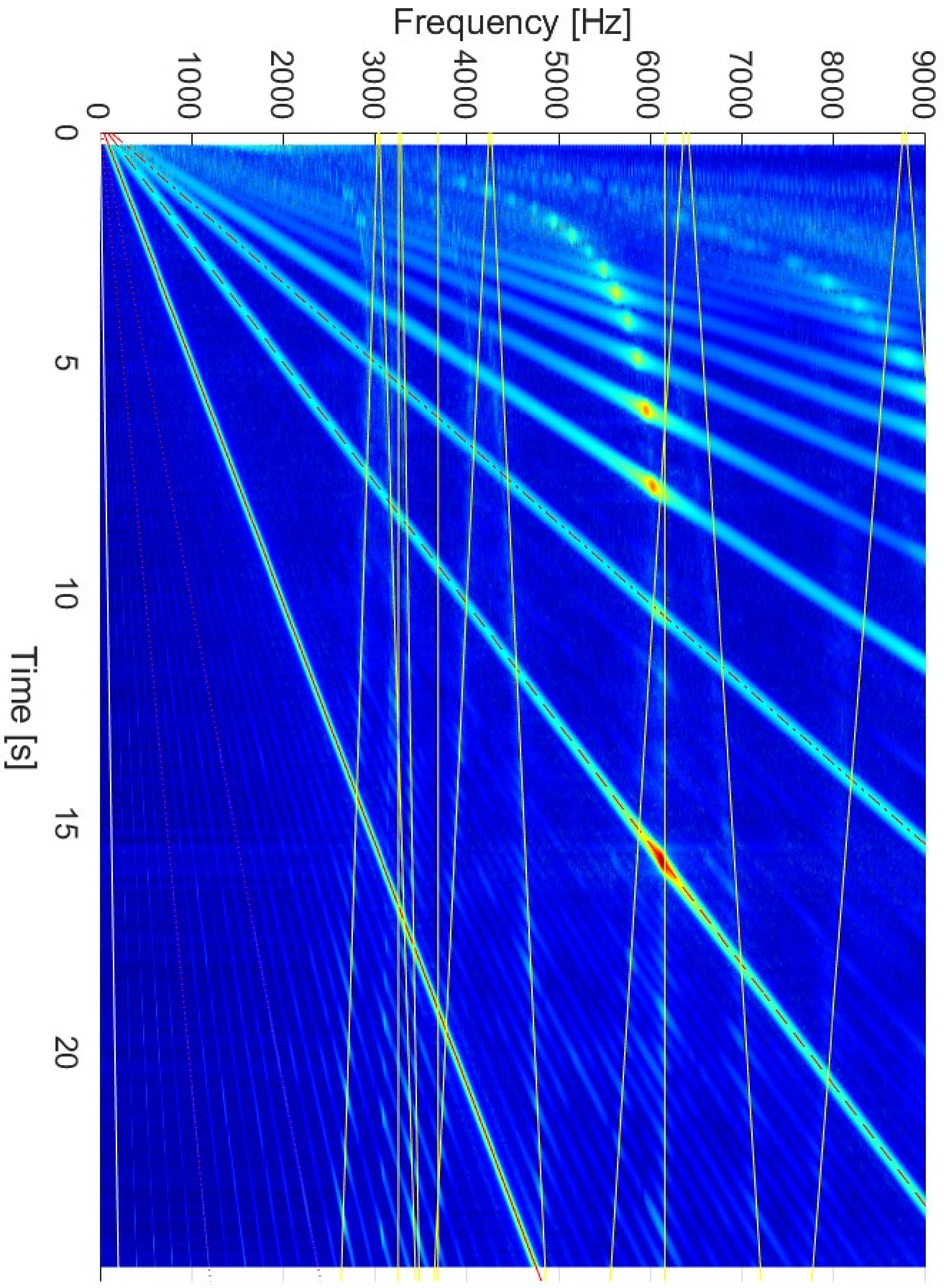

Figure 178: Overlap of the Campbell diagram with the spectrogram of the radial response

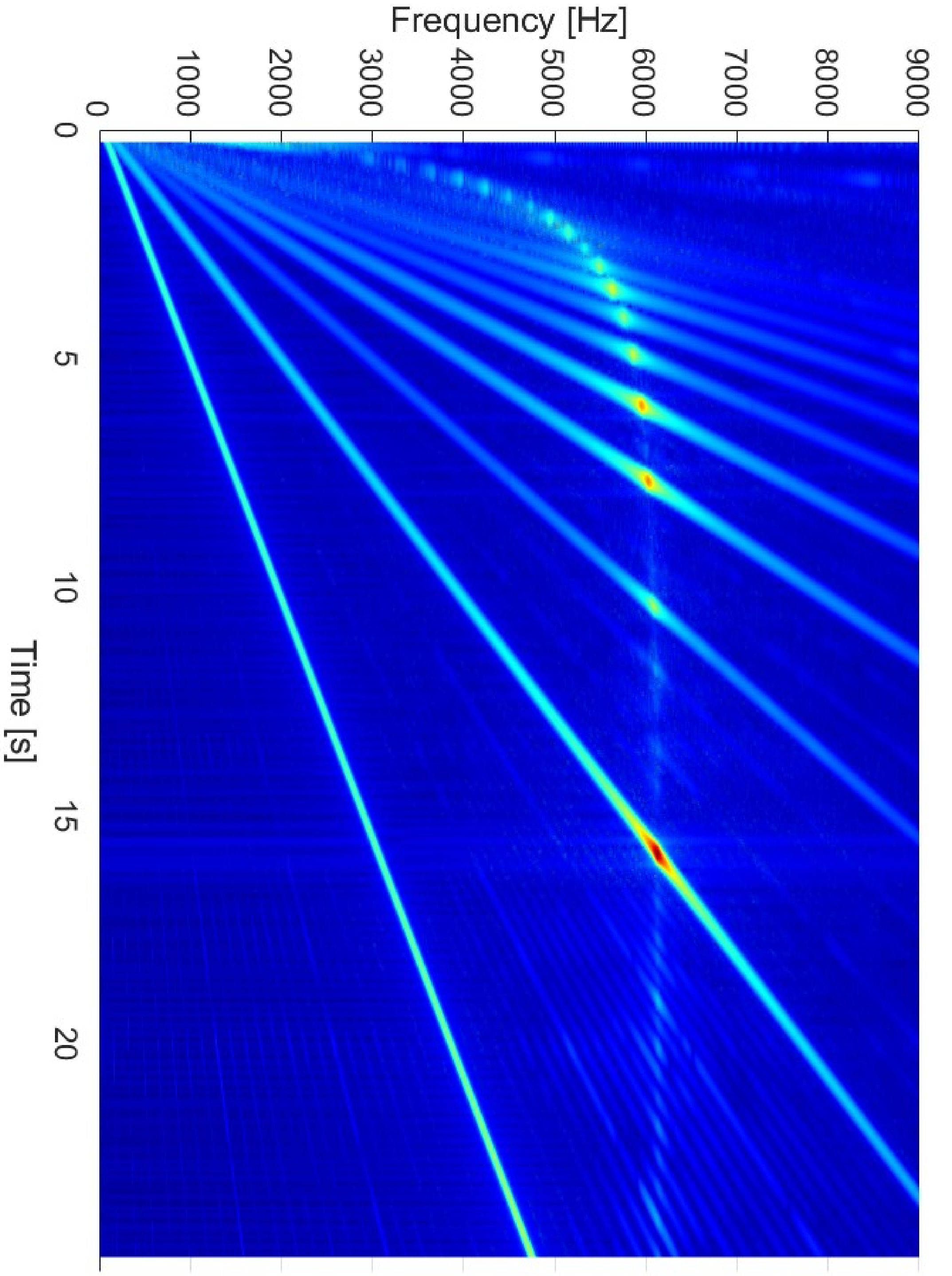

Figure 179: Spectrogram of the response in the tangential direction

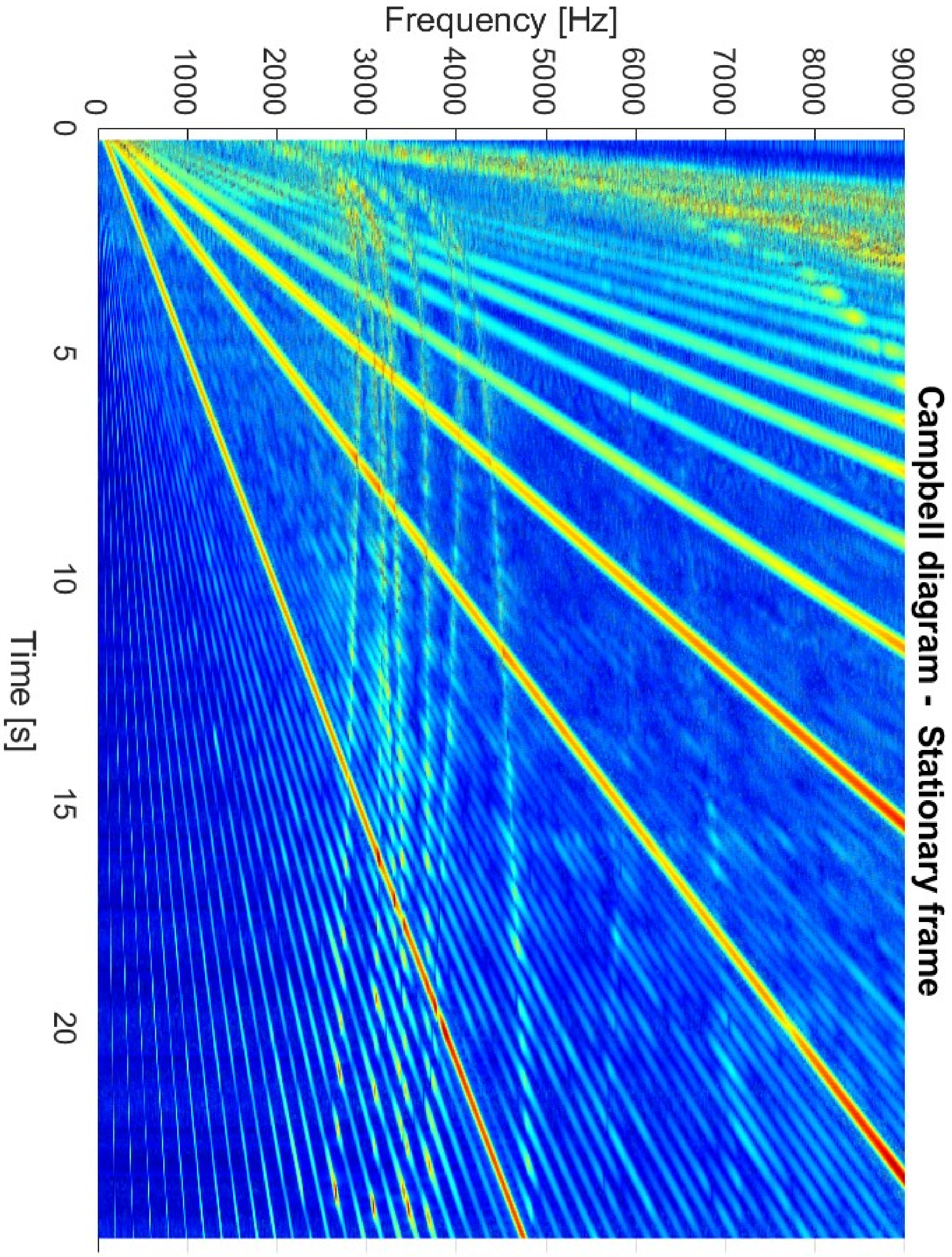

Figure 180: Spectrogram of the response in the axial direction

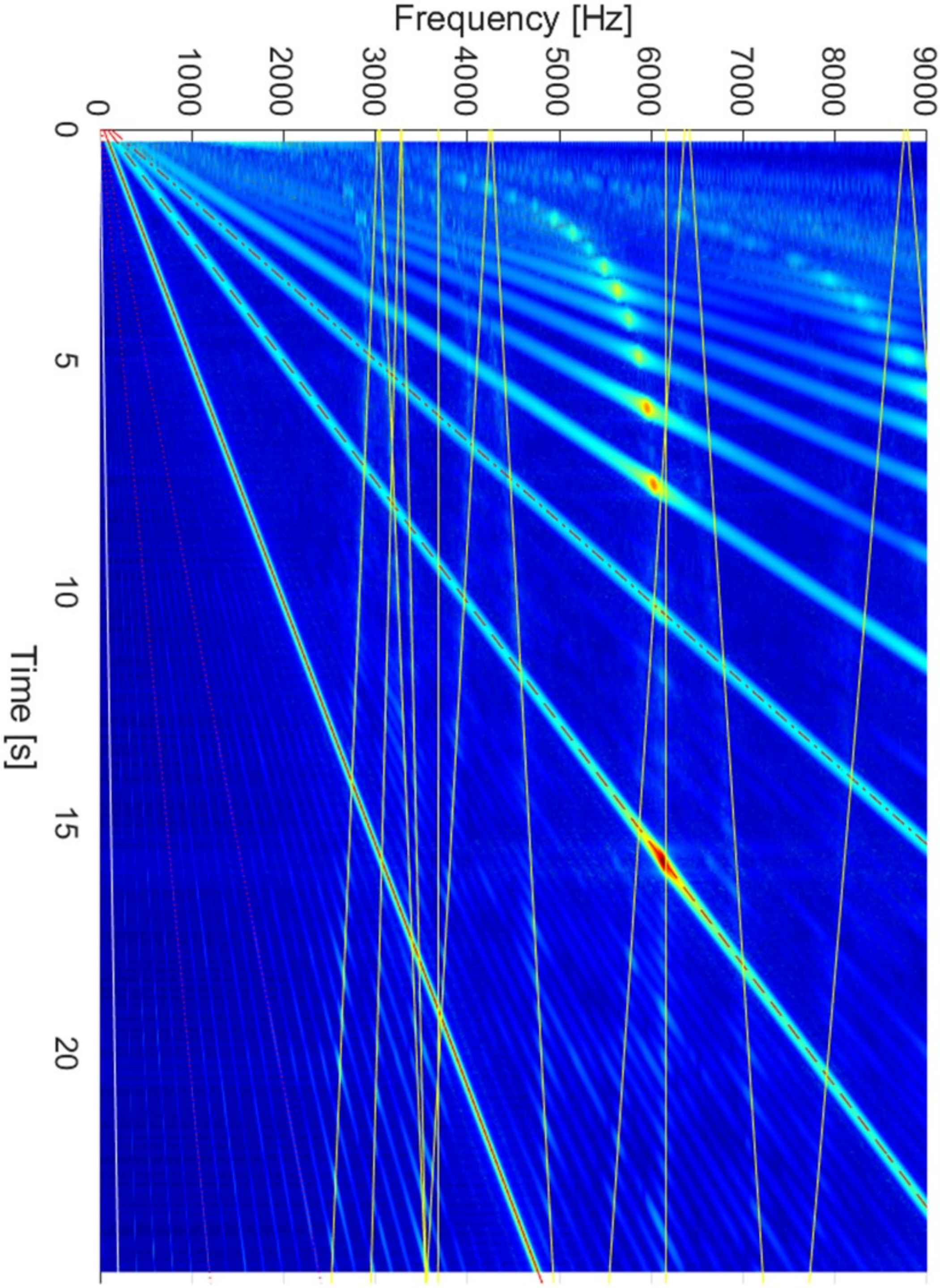

Figure 181: Overlap of the Campbell diagram with the spectrogram of the response in the radial direction including the gyroscopic effect

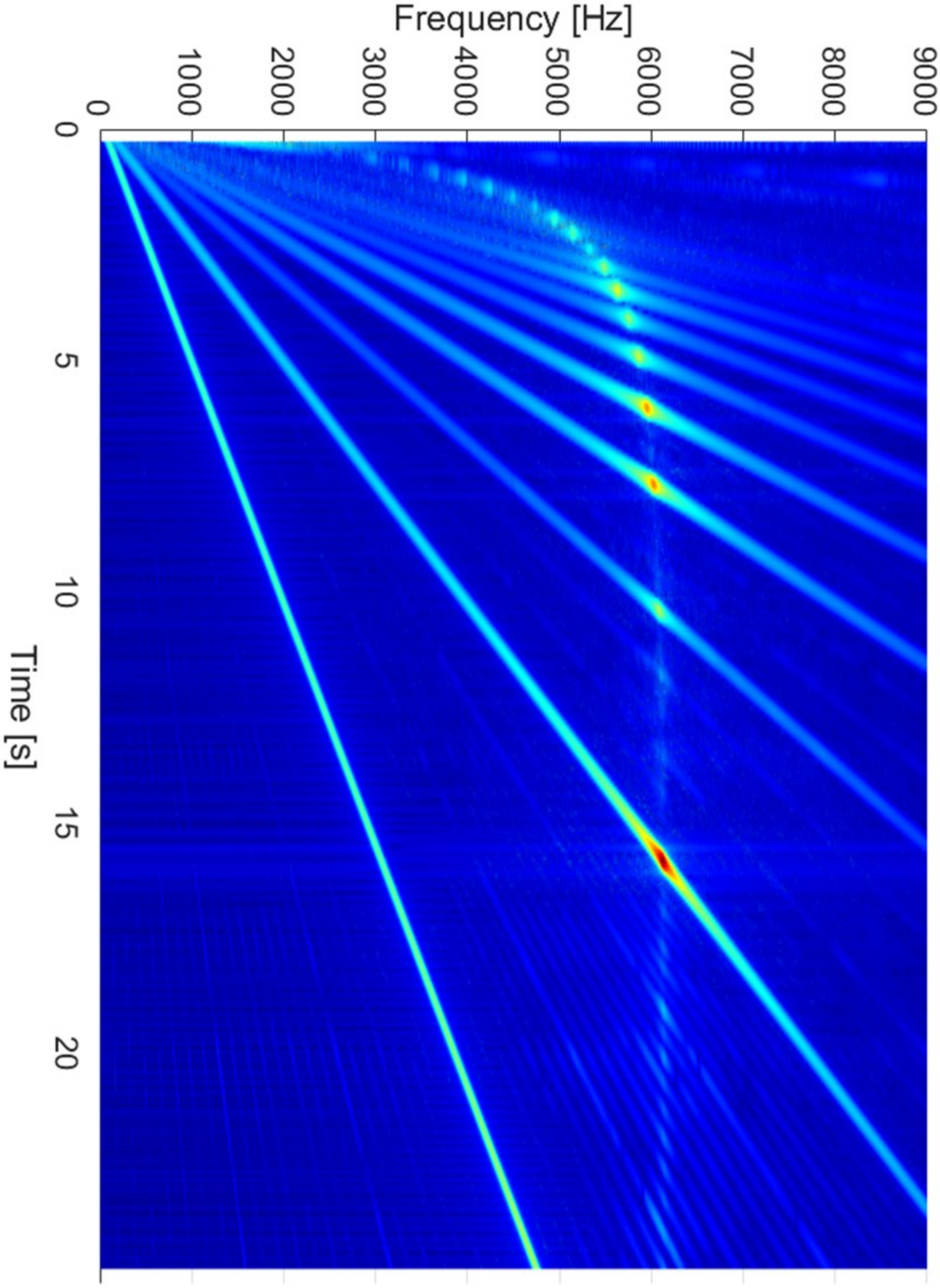

Figure 182: Spectrogram of the response in the tangential direction including the gyroscopic effect

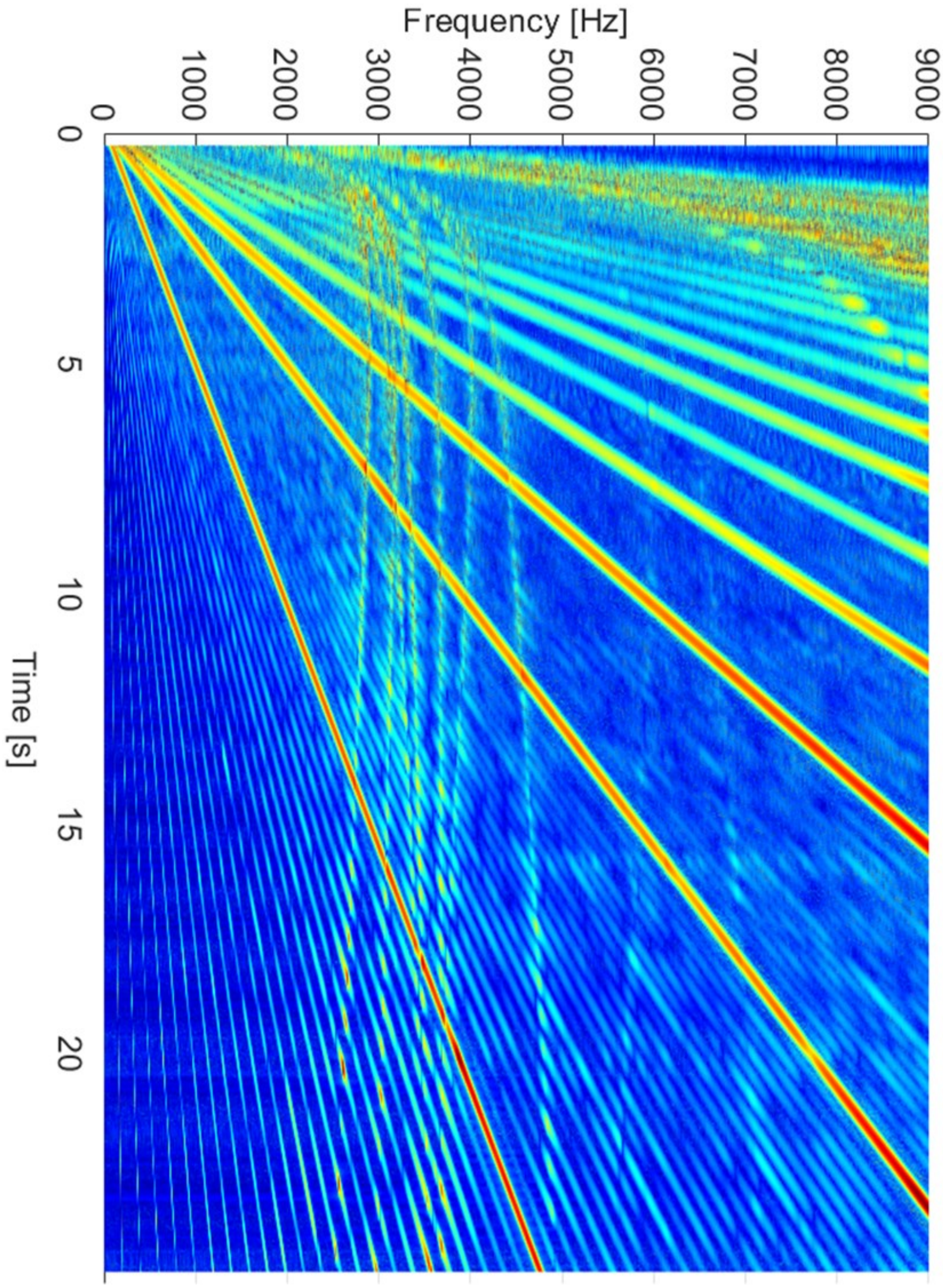

Figure 183: Spectrogram of the response in the axial direction including the gyroscopic effect

Appendix B

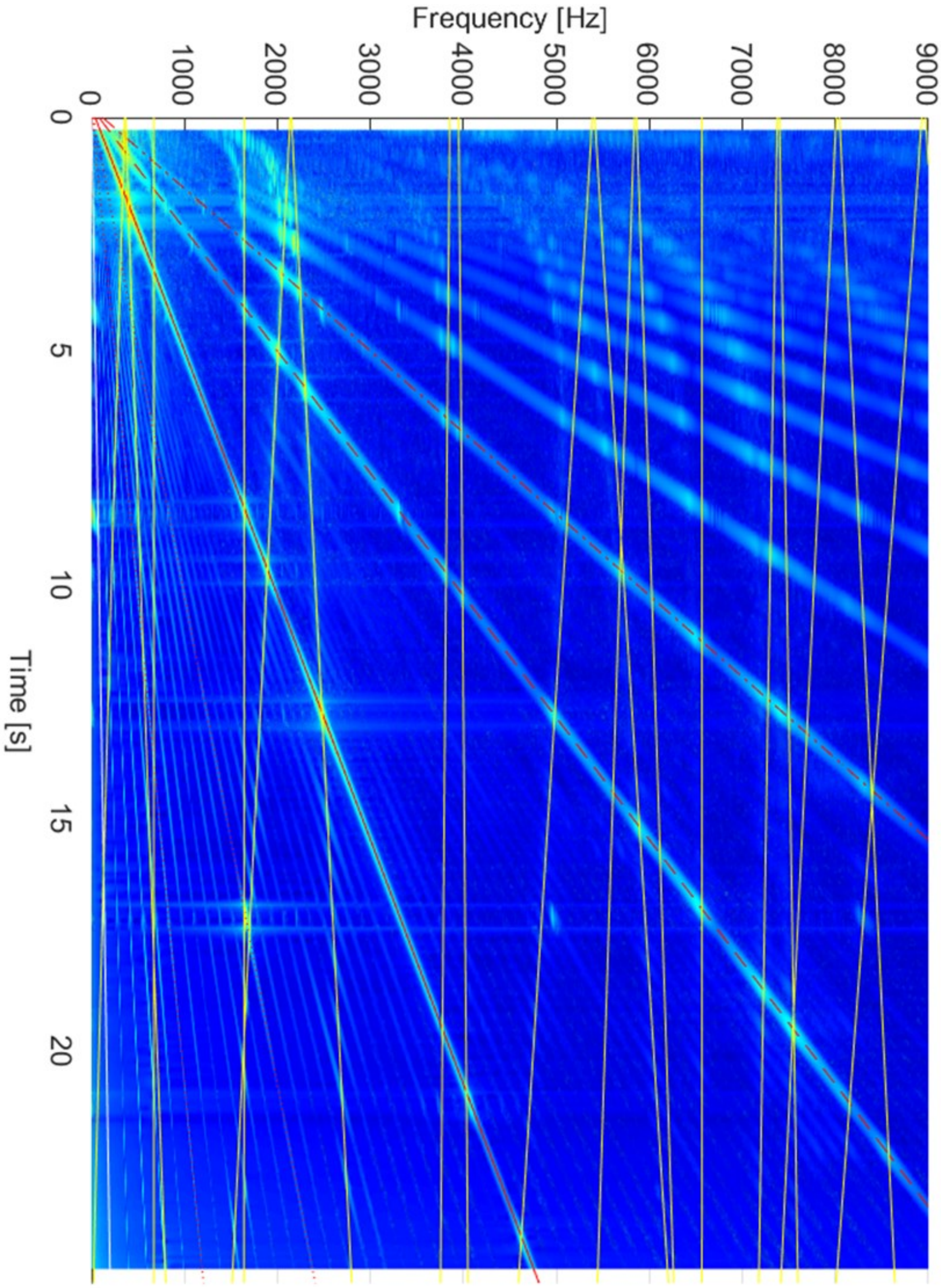

Figure 184: Overlap of the Campbell diagram with the spectrogram of the response in the axial direction including the gyroscopic effect

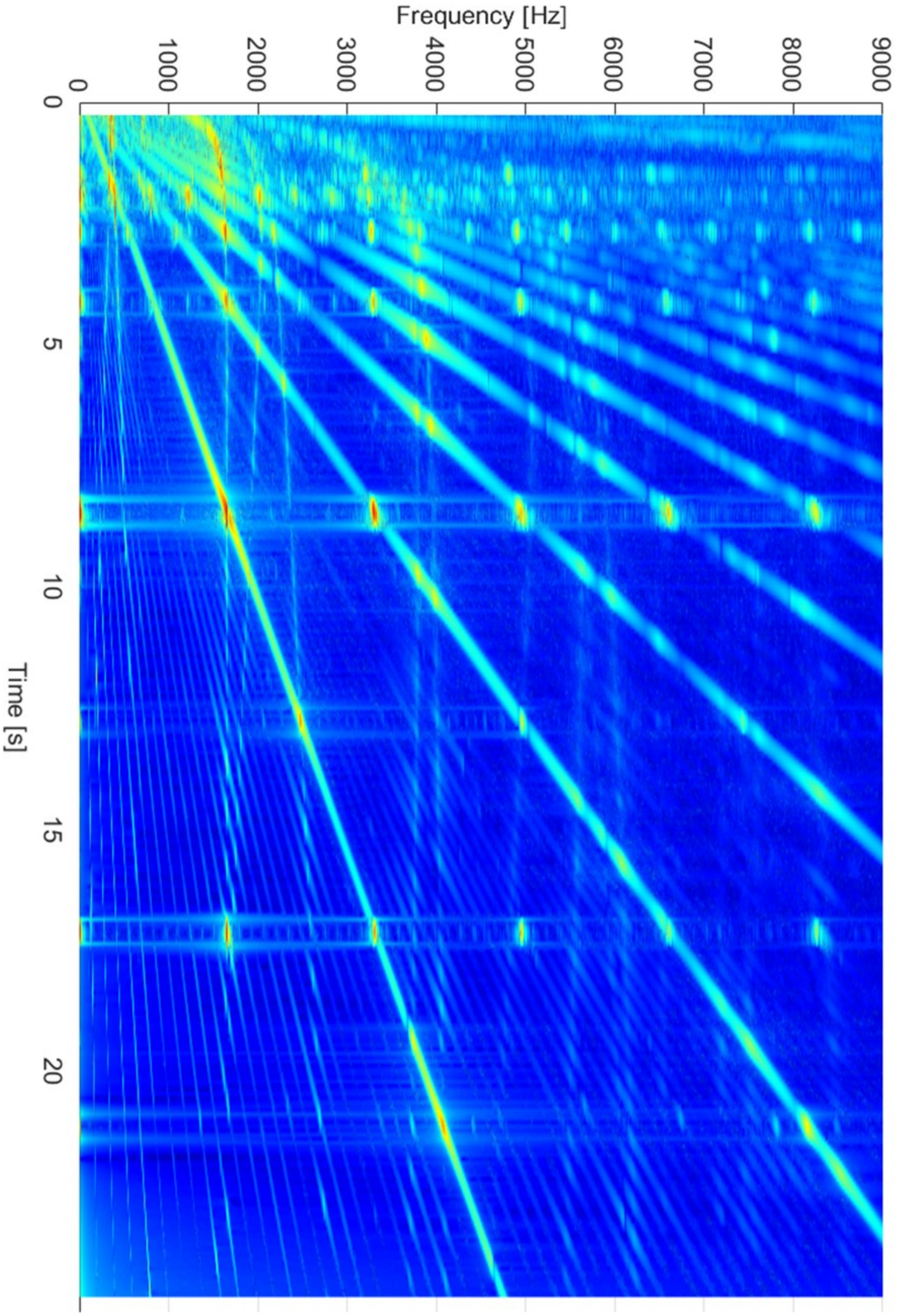

Figure 185: Spectrogram of the response in the radial direction including the gyroscopic effect

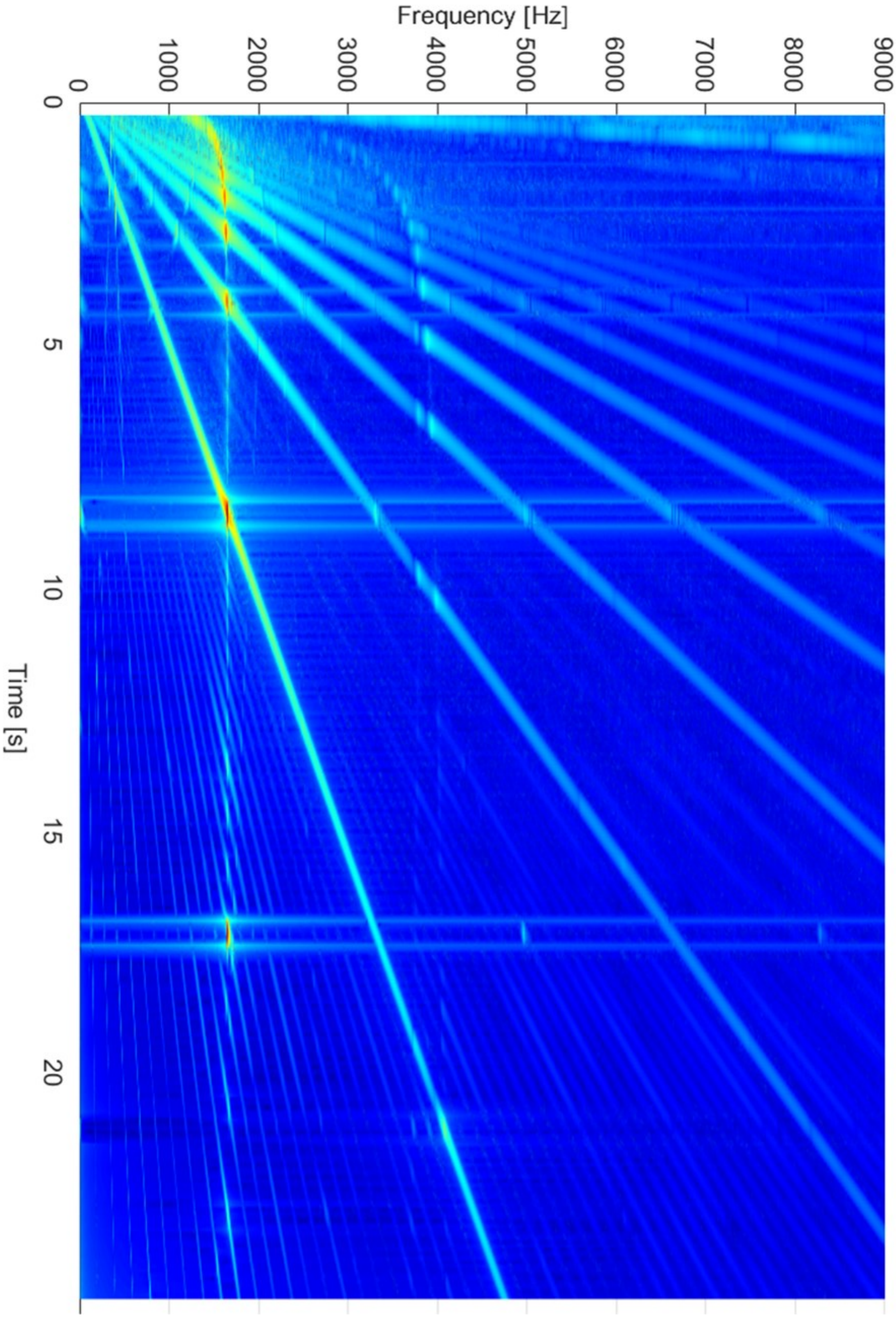

Figure 186: Spectrogram of the response in the tangential direction including the gyroscopic effect

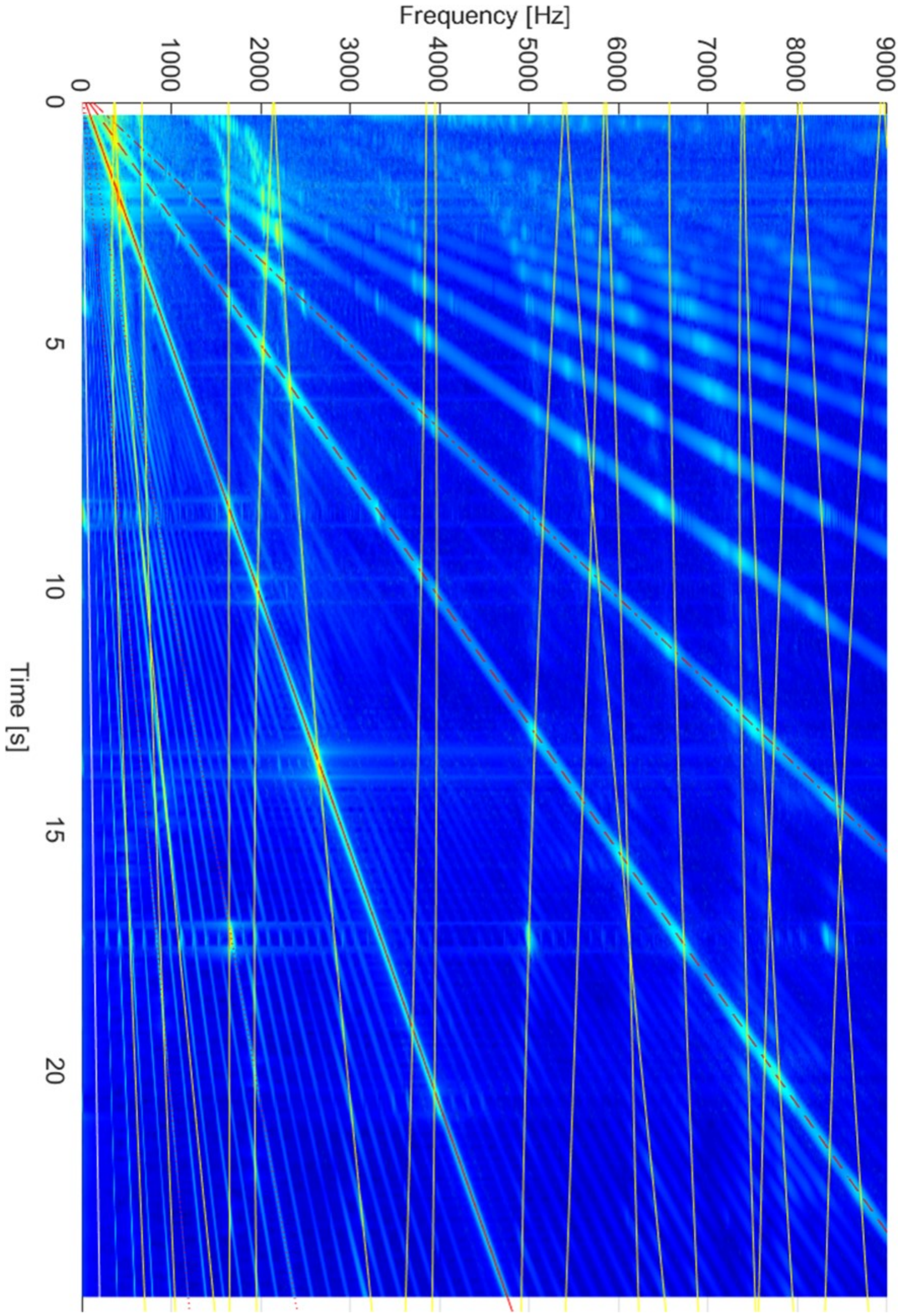

Figure 187: Overlap of the Campbell diagram with the spectrogram of the response in the axial direction including the gyroscopic and stress stiffening effects

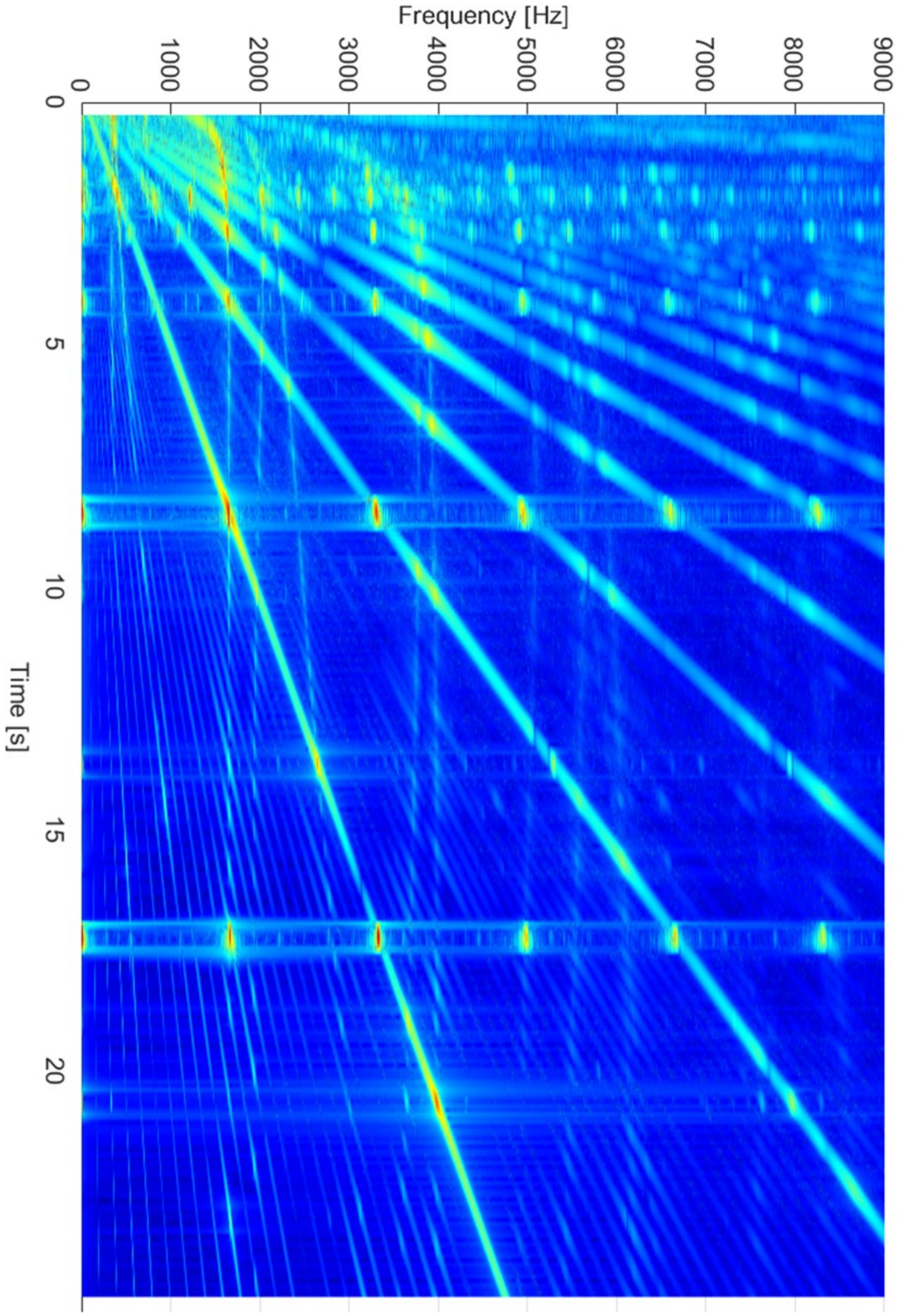

Figure 188: Spectrogram of the response in the radial direction including the gyroscopic and stress stiffening effects

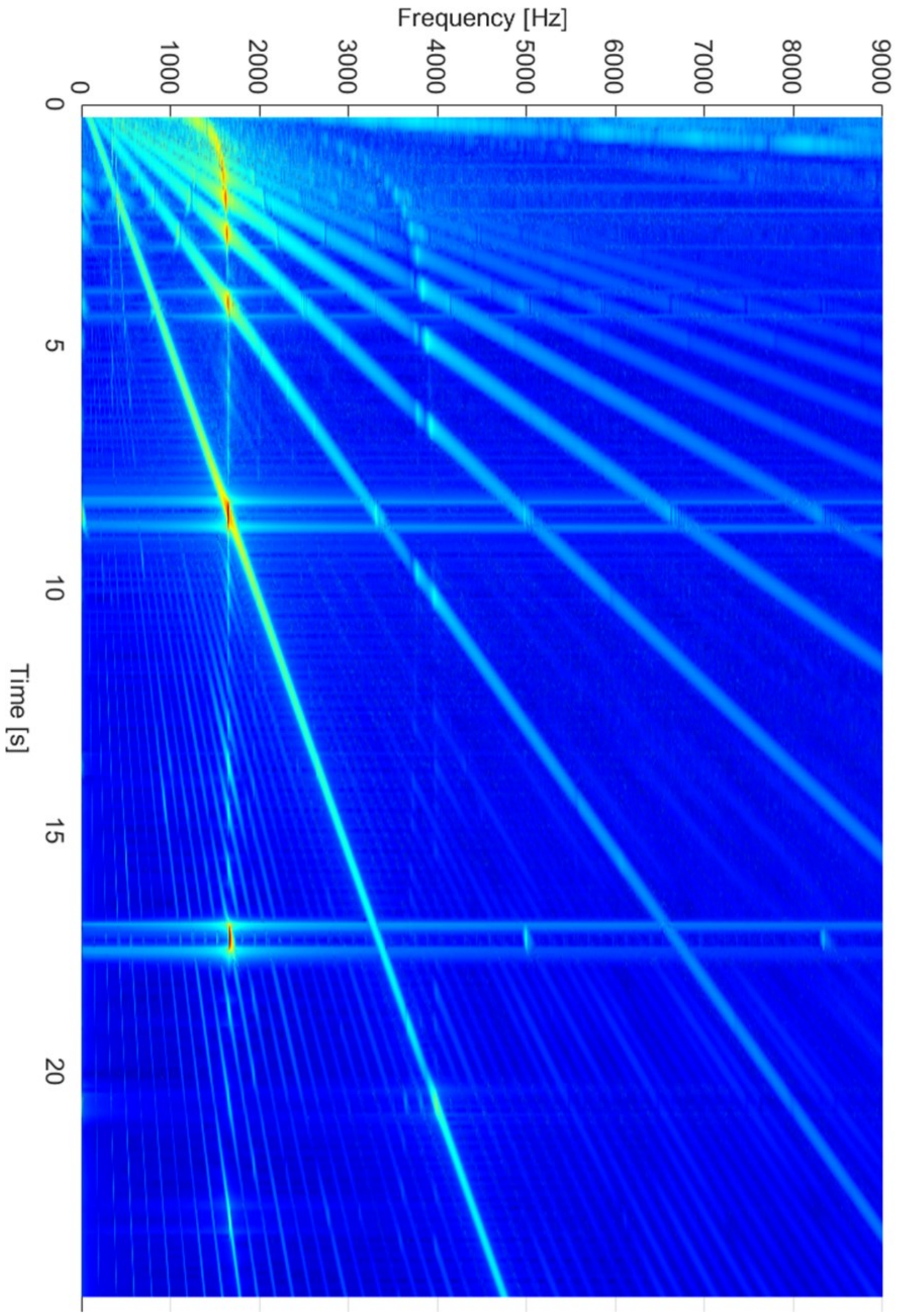

Figure 189: Spectrogram of the response in the tangential direction including the gyroscopic and stress stiffening effects